ALMA MATER STUDIORUM - UNIVERSITÀ DI BOLOGNA
Dipartimento di Fisica e Astronomia

DOTTORATO DI RICERCA IN
ASTROFISICA

Ciclo XXXIV

Tesi di Dottorato

CHEMICAL COMPOSITION OF MILKY WAY SATELLITES: MAGELLANIC CLOUDS AND SAGITTARIUS DWARF GALAXY

Presentata da: **Alice Minelli**

Coordinatore Dottorato:
Chiar.mo Prof. **Andrea Miglio**

Supervisore:
Prof. **Alessio Mucciarelli**

Esame finale anno 2022

Settore Concorsuale: 02/C1 – Astronomia, Astrofisica, Fisica della Terra e dei Pianeti
Settore Scientifico Disciplinare: FIS/05 – Astronomia e Astrofisica

Abstract

This PhD project is aimed at investigating the chemical composition of the stellar populations in the closest satellites of the Milky Way (MW), namely the Large and Small Magellanic Cloud (LMC and SMC, respectively) and the remnant of the Sagittarius (Sgr) dwarf spheroidal galaxy. Their proximity allows us to resolve their individual stars both with spectroscopy and photometry, studying in details the characteristics of their stellar populations. All these objects are interacting galaxies: LMC and SMC are in an early stage of a minor merger event, and Sgr is being disrupted by the tidal field of the MW. There is a plenty of literature regarding the chemical composition of these systems, however, the extension of these galaxies prevent a complete and homogeneous analysis.

Therefore, we homogeneously analysed stellar spectra belonging to MW and its satellites galaxies and we derived their chemical compositions. We highlighted the importance of a homogeneous analysis in the comparison among different galaxies or different samples, to avoid systematics due to different methods or physical assumptions.

The main results are summarised as follows.

(1) We compared the chemical composition of LMC and Sgr, finding that they have similar abundance ratios for all the elements, pointing out that the two galaxies have experienced similar chemical enrichment histories, and supporting the hypothesis that the progenitor of Sgr was a galaxy with a mass and star formation rate (SFR) similar to those of the LMC. Comparing them with the MW, we found lower [α/Fe] and iron-peak abundance ratios measured in LMC and Sgr, suggesting a lower SFR and a smaller contribution by massive stars in comparison to the MW. In particular we found that the most discrepant elements between LMC/Sgr and MW abundances are Sc, V and Zn. We proposed to use these iron-peak elements as new tool to identify objects accreted from systems with lower SFR than the MW.

(2) We tested the application of this new tool for chemical tagging with MW globular clusters (GCs), identifying NGC 6388 and NGC 6441 as accreted MW GCs.

(3) Thanks to the chemical tagging, we were able to recognize, among the LMC GCs, NGC 2005 as an accreted GCs, since its chemical abundances are different respect to the other LMC GCs. Its abundances are coherent with an environment

that experienced a less efficient star formation than the LMC.
(4) We better characterised the chemical composition of the SMC, analysing both GCs and field stars. The two samples of stars share the same abundance ratios in all the analysed elements, therefore they experienced similar chemical enrichment history. This information allows to properly use the metallicity of the field stars as a proxy of their age. We also compare the chemical composition of the SMC with the one of the MW and from the differences we concluded that SMC experienced a slower SFR, a lower contribution by massive stars, as found for the LMC.
(5) We analysed a sample of Sgr stars, selected using *GAIA* proper motions in order to be Sgr main body stars. The sample has allowed to derive the first unbiased metallicity distribution of Sgr, estimating a fraction of metal-poor stars of about 0.2%.

Publications

1. *An homogeneous comparison between the chemical composition of the Large Magellanic Cloud and the Sagittarius dwarf galaxy*
   Minelli A., Mucciarelli A., Romano D., Bellazzini M., Origlia L., Ferraro F. R., 2021, The Astrophysical Journal, 910, 114

2. *A New Set of Chisels for Galactic Archeology: Sc, V, and Zn as Taggers of Accreted Globular Clusters*
   Minelli A., Mucciarelli A., Massari D., Bellazzini M., Romano D., Ferraro F. R., 2021, The Astrophysical Journal, 918, 32

3. *A relic from a past merger event in the Large Magellanic Cloud*
   Mucciarelli A., Massari D., Minelli A., Romano D., Bellazzini M., Ferraro F. R., Matteucci F., Origlia L., 2021, Nature Astronomy, 5, 1247

4. *The chemical double helix of the Magellanic Clouds: I - the chemical composition of 206 Small Magellanic Cloud red giant stars*
   Mucciarelli A., Minelli A., Romano D., Ferraro F.R., Origlia L., in preparation

5. *The chemical double helix of the Magellanic Clouds: II - the chemical composition of three SMC globular clusters*
   Minelli A., Mucciarelli A., Romano D., Origlia L., Ferraro F.R., in preparation

6. *The first unbiased Metallicity Distribution of Sagittarius dSph: preliminary results*
   Minelli A., Bonifacio P., Mucciarelli A., Bellazzini M., Monaco L., in preparation

Contents

List of Figures

List of Tables

Chapter 1

Introduction

This PhD project is devoted to characterize the chemical composition of the stellar populations in the Milky Way (MW) satellites, focusing in particular on the Large and Small Magellanic Clouds (LMC and SMC, respectively) and the remnant of the Sagittarius dwarf galaxy (Sgr).

Galaxies in the Local Group (LG) are an excellent laboratory to study the evolution and the chemical enrichment history of the galaxies, using both deep photometry (deeper than the oldest main sequence turn off) and high resolution spectroscopy. Photometry allows us to constrain the full star formation history of a galaxy, thus tracing its evolution. The chemical composition derived by high-resolution spectroscopy is a crucial and independent constraint to further interpret the chemical evolution of a galaxy. Moreover, the advent of the 8-10 meter class telescopes has allowed us to observe with high-resolution spectroscopy stars fainter than the Red Giant Branch (RGB) Tip in these galaxies, hence studying stellar populations older than $\sim$ 1-2 Gyr.

In the LG there is a large variety of galaxy types, with a wide range of masses, ages, metallicities, gas contents, morphologies and star formation histories (SFH). The LG is dominated by two large spirals, namely the MW and M31, as represented in Fig, 1.1. Most of the other members are dwarf galaxies found in the proximity of the two large spirals in the majority of the cases, that evolved in interaction with other galaxies. Also, isolated dwarf galaxies have been observed (McConnachie, 2012). LG includes several types of dwarf galaxies, such as early-type dwarf spheroidals, late-type star-forming dwarf irregulars, very-low surface brightness dwarfs, ultra-faint dwarfs (UFDs), centrally concentrated actively star-forming galaxies and the extreme ultracompact dwarfs.

Dwarf galaxies play a relevant role in the hierarchical scenario of galaxy formation, as they are the natural candidates to be "building blocks" of larger systems. In this scenario, larger galaxies form through merging episodes of smaller systems, like

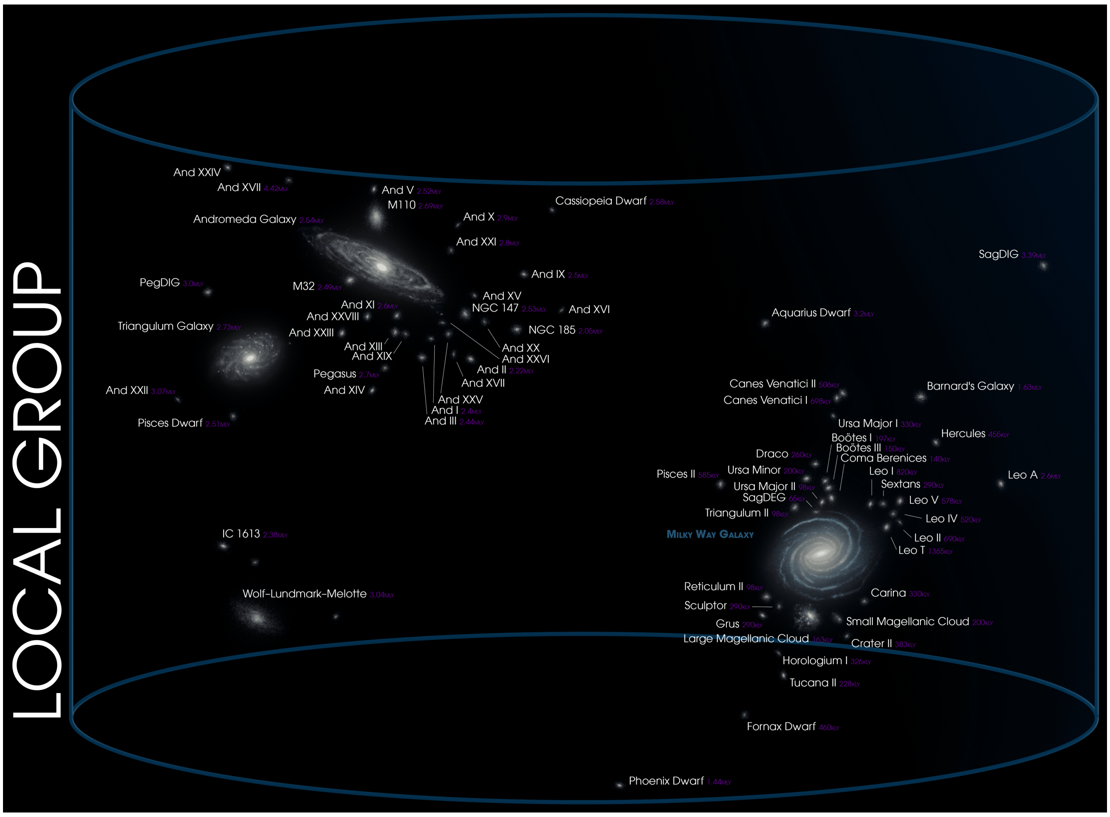

Figure 1.1: Scheme of the Local Group, where the two large spirals MW and M31 (Andromeda Galaxy) and the several dwarf galaxies around them are visible.

dwarf galaxies (White & Rees, 1978). For this reason, the general expectation is that the properties of the smaller systems will be reflected in the larger ones. Dwarf galaxies have relatively simple substructures and, since small systems are believed to be the first to collapse in the early Universe, galaxies like these should born first (Tolstoy et al., 2009). Moreover, they are typically low-metallicity systems, therefore they are assumed to be highly unevolved and they potentially host the first stars. For their importance, there are a lot of studies focused on these galaxies (see for a review Simon, 2019; Tolstoy et al., 2009; Annibali & Tosi, 2022).
In the LG are present also two emblematic cases of interactive systems: Sgr is a remnant of a dwarf galaxy disrupted by the tidal field of the MW, whereas the Magellanic Clouds (MCs) are on a early stage of a minor merger, but they are also in gravitation interaction with the MW. Therefore, the study of these close MW satellites is crucial to reconstruct the chemical enrichment history of these interacting systems, not well know yet.

1.1 The chemical tools: nucleosynthesis and abundance ratios

Chemical abundances are fingerprints of the formation and chemical enrichment history of stellar systems. Chemical abundance ratios reveal us the details of the chemical evolution of the analysed galaxies, highlighting the role played by the different nucleosynthesis channels. In fact, different elements are synthesized in stars with different mass progenitors and released into the interstellar medium (ISM) at different epochs from the onset of the star formation events. From the polluted gas, new stars were formed, and they maintain the memory of the past events in their chemical composition. Therefore, looking at the behaviour of the elemental abundance ratios as a function of the metallicity, each element displays a specific trend, reflecting its nucleosynthesis channels. This is visible in Fig. 1.2, where the abundance ratios as a function of [Fe/H] in MW stars of elements produced from different nucleosynthesis paths are shown.

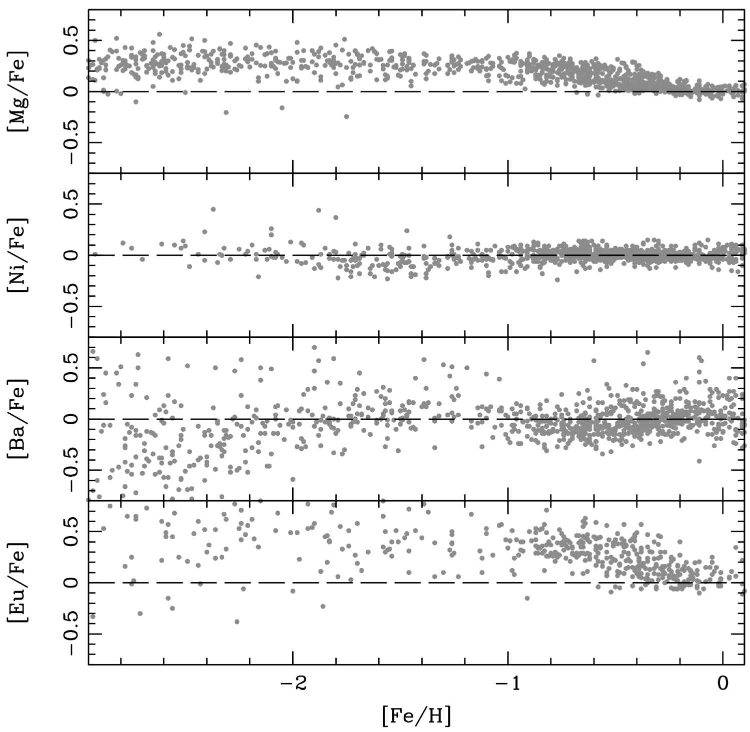

Figure 1.2: Elemental abundance ratios as a function of the metallicity for Mg (α-element), Ni (iron-peak element), Ba (slow neutron-capture element) and Eu (rapid neutron-capture element), from top to bottom panels respectively. Chemical abundances for MW field stars are from the works by Edvardsson et al. (1993); Burris et al. (2000); Fulbright (2000); Stephens & Boesgaard (2002); Gratton et al. (2003); Reddy et al. (2003, 2006); Barklem et al. (2005); Bensby et al. (2005); Forsberg et al. (2019).

Also, it is important to study the chemical composition of both field and globular clusters (GCs) stars, which give complementary information, since field stars provide high statistics, and metallicity distributions and abundances can be derived all over the galaxies, while for GC stars ages and metallicities can be derived simultaneously and with high precision.
Because the chemical abundances in a galaxy are the result of the evolution of their stellar content (in terms of star formation rate (SFR), initial mass function (IMF), infall and outfall processes...), stars accreted from an external galaxy (for instance after a merging episode) could exhibit a different chemical composition with respect to the host galaxy. This makes the study of the chemical composition a powerful tool to identify possible substructures in a galaxy and recognize past merging events (Freeman & Bland-Hawthorn, 2002). The reason is that the stars have memory of the chemical composition of the gas from which they were formed, and in a galaxy with different chemical enrichment history the gas has been enriched in a different way.

In the following, a briefly description of the characteristics of the main groups of elements is discussed. The main mechanisms of production of the elements are rehired in the periodic table in Fig. 1.3, color-coded according to the origin of the elements.

1.1.1 α-elements

The name of this group of elements is linked to their nucleosynthesis, since they formed through the capture of α particles (that are He nuclei, made of two protons and two neutrons) on seed nuclei (He and C).
The main elements belonging to this family are O, Ne, Mg, Si, S, Ca, and Ti. They are mostly synthesized in massive stars and released into the ISM mainly through Type II supernovae (SNe II), with only a minor component produced in Type Ia supernovae (SNe Ia) (Romano et al., 2010; Kobayashi et al., 2020). The α-elements can be gathered in two groups according to their formation mechanism: the hydrostatic elements (O and Mg), synthesized via hydrostatic C and Ne burning, mainly in stars with masses larger than 30-35 $M_{\odot}$and without contribution by SN Ia, and the explosive elements (Si, Ca and Ti), synthesized via explosive O and Si burning, mainly in stars with masses of 15-25 $M_{\odot}$ and in a smaller amount in SN Ia (Woosley & Weaver, 1995).

As seen in the first panel of Fig. 1.2, where [Mg/Fe] as a function of metallicity is shown, the behaviour described by α-elements is flat in the metal-poor regime, with [α/Fe] overabundant with respect to the solar value, followed by a decreasing trend starting from [Fe/H] ~ -1 dex. Such trend is due to the time delay between the onset of the SNe II and SNe Ia, the latter starting to pollute the ISM about 1 Gyr after the beginning of the star formation and producing mainly Fe and iron-peak

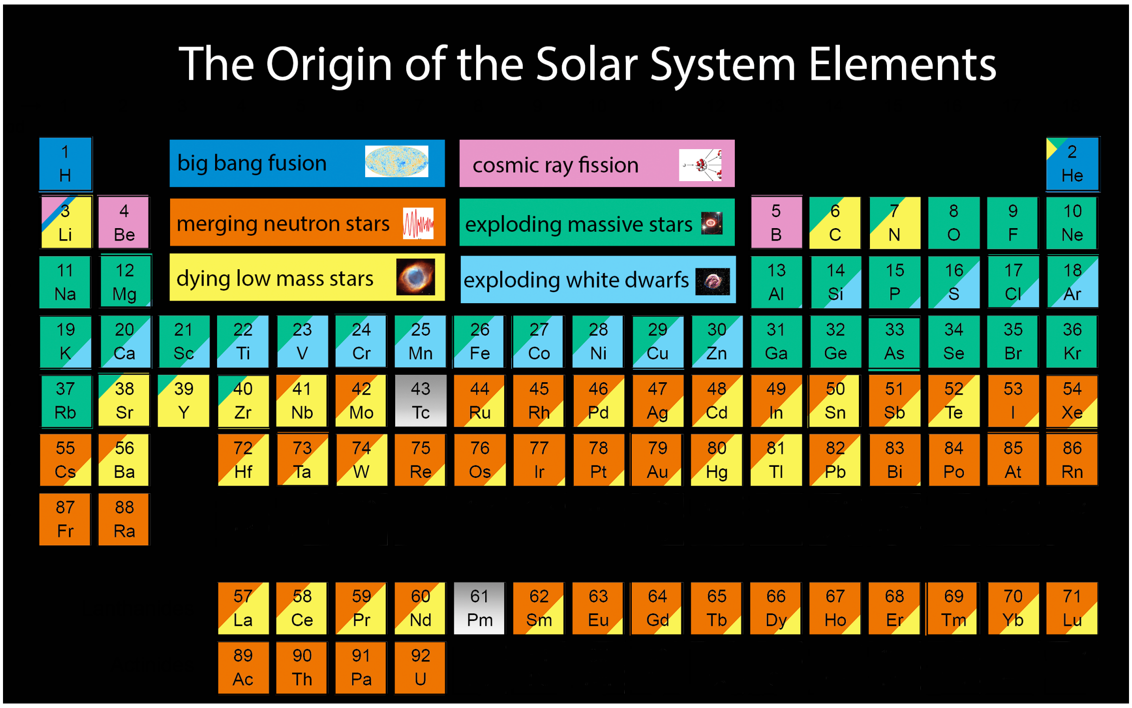

Figure 1.3: Periodic table color-coded by the origin of the elements in the Solar System. Different origins are listed in figure. Elements with more than one source have the approximate amount due to each process indicated by the amount of area. Tc, Pm, and the elements beyond U do not have long-lived or stable isotopes and are colored in gray or not included.
Graphic created by Jennifer Johnson, Astronomical image credits by ESA/NASA/AASNova.

elements (Tinsley, 1979; Matteucci & Greggio, 1986). This decrease of [α/Fe] is usually called *knee*. Its metallicity flags the metallicity reached by the system at the epoch when SNe Ia start to dominate the chemical enrichment. The α-*knee* is an important speedometer to measure the SFR, since it moves to higher metallicity if the star formation is larger. Furthermore, an increase of the number of formed high-mass stars, exploding as SNe II, implies an increasing in the amount of the produced α- elements, changing the constant value of [α/Fe] before the α-*knee*. Hence, the value of [α/Fe] before the *knee* is highly sensitive to the IMF of the galaxy. In Fig. 1.4 and 1.5 is reported the comparison among the MW and some dwarf spheroidal galaxies for [Mg/Fe] and [Ca/Fe] as a function of [Fe/H], where is visible the different location of the α-*knee*.

1.1.2 Odd-Z light elements: Na and Al

Na is mainly produced in massive stars through the hydrostatic C burning and partially during the H burning in Asymptotic giant branch (AGB) stars through

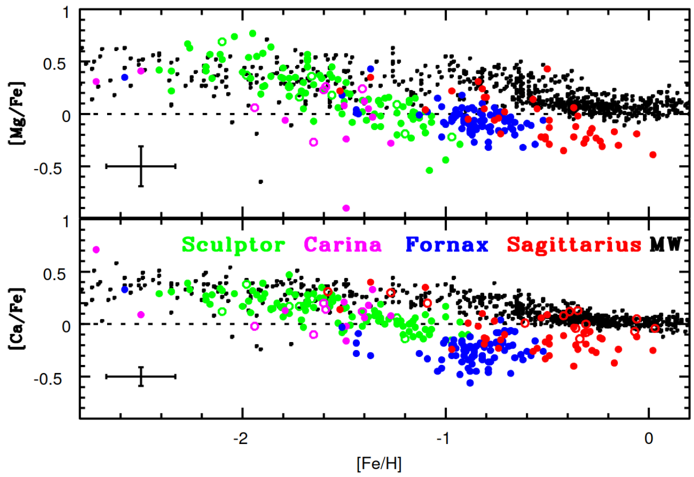

Figure 1.4: α-elements (Mg and Ca) in four nearby dwarf spheroidal galaxies: Sgr (red) from McWilliam & Smecker-Hane (2005); Monaco et al. (2005); Sbordone et al. (2007), Fornax (blue) from Shetrone et al. (2003); Letarte (2007), Sculptor (green) from Shetrone et al. (2003); Geisler et al. (2005); Hill (2010) and Carina (magenta) from Shetrone et al. (2003); Koch et al. (2008). Open symbols refer to single-slit spectroscopy measurements, while filled circles refer to multi-object spectroscopy. The small black symbols are a compilation of the MW disk and halo star abundances, from Venn et al. (2004).
Taken from Tolstoy et al. (2009).

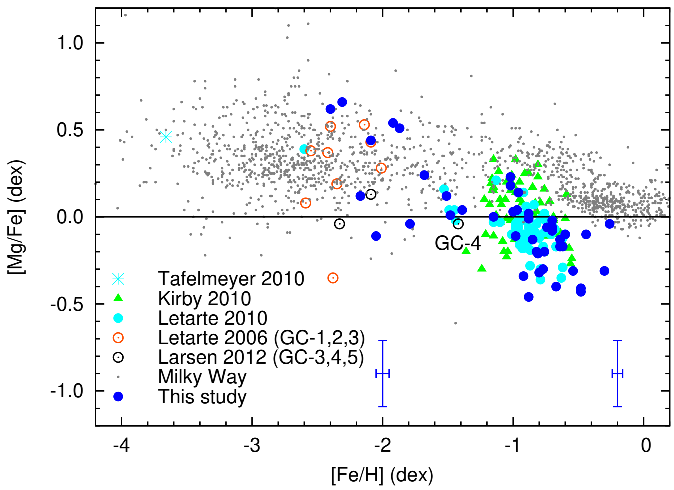

Figure 1.5: Distribution of [Mg/Fe] for a sample of RGB stars in the Fornax dSph as blue filled circles (Lemasle et al., 2014). The cyan filled circles are the data of Letarte et al. (2010), the cyan stars are the metal-poor star of Tafelmeyer et al. (2010) and the green triangles are the stars of Kirby et al. (2010), while orange and black empty circles are the stars in Fornax globular clusters from Letarte et al. (2006) and Larsen et al. (2012) respectively. MW halo stars from Venn et al. (2004) and Frebel (2010) and references therein are in small grey dots. Representative error bars are given for the metal-poor ([Fe/H] < -1.4 dex) and metal-rich ([Fe/H] > -1.4 dex) regimes.
Taken from Lemasle et al. (2014)

the NaNe cycle, with a small contribution from the s-process (Clayton, 2003).
Al is synthesized through the hydrostatic C and Ne burning, but a small amount is produced also during the H burning in the MgAl chain (Woosley & Weaver, 1995). For both elements, a very high star-to-star dispersion was observed in intermediate-age and old GCs, with abundances spanning up to 1 dex (Gratton et al., 2006; Bastian & Lardo, 2018). This is due to the presence of the so-called "multiple populations" (MPs) in GCs. The stars of the various sub-populations in a given GC show different anti-correlated abundances of light elements, the most prominent being the Na-O and C-N anti-correlations (Carretta et al., 2009a), and some clusters additionally show a Mg–Al anti-correlation (Carretta et al., 2009b; Pancino et al., 2017). An example of [O/Fe]-[Na/Fe] anti-correlation for MW GCs analysed by Carretta et al. (2009a,b) is reported in Fig. 1.6. Their appearance seems not to depend on the environment of the GCs and the type of the host galaxy, but it depends on the age and the mass of the GCs. Indeed, they have been observed only in clusters older than ~ 2 Gyr, with NGC 1978 (Martocchia et al., 2018) and Hodge 6 (Hollyhead et al., 2019) being the youngest systems where chemical variations have been detected to date. Moreover, the star-to-star abundance variations becoming more relevant with increasing cluster mass (Bragaglia et al., 2012; Schiavon et al., 2013; Milone et al., 2017).

1.1.3 Iron-peak elements

The iron-peak elements are the heaviest elements synthesized through thermonuclear reactions. This group includes mainly elements with Z between 21 and 30 (namely Sc, V, Cr, Mn, Fe, Co, Ni, Cu and Zn).
Thanks to the huge number of available atomic lines, which span the whole spectral range, Fe is probably the best known chemical element.
Elements belonging to this group are mainly produced during the explosive nucleosynthesis associated to SNe Ia, but contributions not negligible are also from SN II and hypernovae (HNe), that are associated to stars more massive than $\sim$ 25-30 $M_\odot$ and more energetic than normal SN II at least by a factor of 10. The details of nucleosynthesis vary across the group, and for some of them still not well understand, with the complication that the yield of some elements are metallicity dependent (see e.g. Romano et al., 2010).
Sc is produced in the innermost ejected layers of SN II, both during Ne burning and in explosive O and Si burning (Woosley & Weaver, 1995). V, Cr and Mn are synthesised mainly by outer incomplete explosive Si burning in massive stars, while Co is formed in complete Si burning in the deepest stellar layers (Woosley & Weaver, 1995; Limongi & Chieffi, 2003). In particular, Mn is produced more by SNe Ia than SNe II/HNe relative to Fe (Kobayashi & Nomoto, 2009). Also Ni is mainly produced in the zones which undergo complete explosive Si burning in

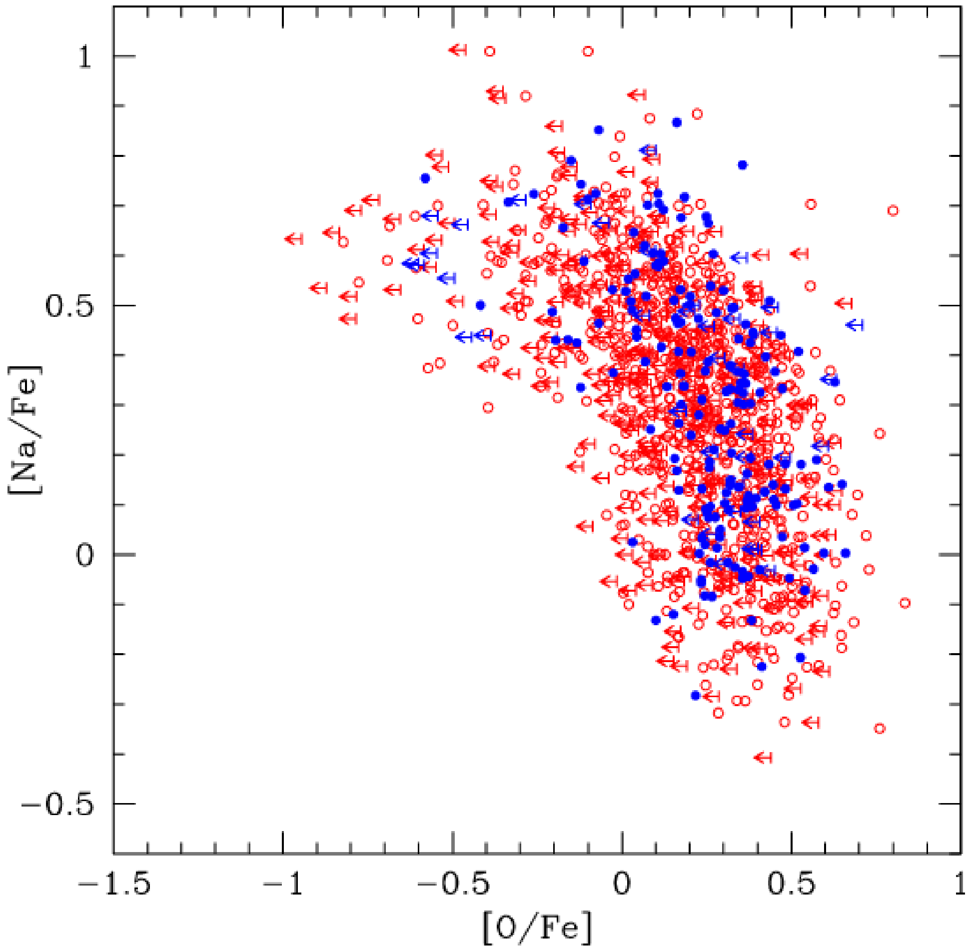

Figure 1.6: The Na-O anti-correlation for a total of 1958 (red circles) plus 214 (blue circles) individual RGB stars in 19 MW GCs, observed with GIRAFFE and UVES spectrographs respectively (data from Carretta et al., 2009a,b). Arrows indicate upper limits in oxygen abundances.
Taken from Carretta et al. (2009a)

stars (Limongi & Chieffi, 2003), but the yields of SNe-Ia are metallicity-dependent (Kobayashi et al., 2020). The Cu content of extremely metal-poor stars is basically determined by explosive nucleosynthesis in massive stars where it is made during the hydrostatic burning of the He core and of the C shell (Woosley & Weaver, 1995; Limongi & Chieffi, 2003). But as the metallicity grows, the contribution from the weak s-process operating in massive stars becomes increasingly important (Romano & Matteucci, 2007). Finally, Zn is almost totally produced by HNe (Nomoto et al., 2013).
In Fig 1.2, second panel, is represented the behaviour of Ni abundance ratio as a function of the metallicity. Its trend suggests that the origin of Ni is strictly linked to that of Fe from both SNe types.

1.1.4 Neutron-capture elements

The name of this group is linked to their mechanism of production, since they form through subsequent neutron-capture on a seed nucleus, usually an iron-peak element, followed by β decays (Burbidge et al., 1957).
All the elements with proton number Z larger than 30 belong to this group. They are distinguished in slow (s-) and rapid (r-) process neutron-capture elements according to the rate of neutron-captures with respect to the time-scale of the β decays.
The s-process elements, for which the rate of neutron-capture is slower than the radiative decay timescale, are grouped around three peaks of stability corresponding to the neutrons magic numbers (N=50, 82, 126). The light-s are the elements with atomic number $30 < Z \leq 40$ and the most commonly studied are Sr, Y and Zr. They are synthesised in AGB stars, but 32% of Sr, 22% of Y, and 44% of Zr can be produced from electron capture SNe (Kobayashi et al., 2020). The heavy-s elements are the elements up to Z = 84 and the s-process captures mainly occur during the thermal pulse stage of low-mass (1-3 $M_\odot$) AGB stars, where the main source of neutrons is the $^{13}C(\alpha,n)^{16}O$ reaction (Busso et al., 1999). In particular, the yields are strongly metallicity dependent, since as the metallicity increase, increase also the number of seed nucleus and decrease the number of neutrons per seed nucleus, in advance to the production of the light-s elements. The typical elements observed among the heavy-s ones are Ba (its behaviour in Fig 1.2, third panel), La and Nd. Lastly, there are the elements around Pb, the heaviest ones and the most difficult to measure. The only element sometimes detected is Pb. For the heavier neutron-capture elements, contributions from both Neutron star (NS) – Black Hole and NS–NS mergers and magneto-rotational SNe are necessary (Kobayashi et al., 2020).
The r-process elements are those forming when the neutron-capture process occurs in a very fast way. Their precise sites of production are still debated but require neutron-rich and high energy environments. These conditions can be found in low-mass SN II progenitors (Wheeler et al., 1998), in the NS mergers (Pian et al., 2017) and in the collapsars (Siegel et al., 2019). The most common element belonging to this group is Eu (its behaviour in Fig 1.2, last panel). Kobayashi et al. (2020) assert that it is not possible to explain the observed [Eu/Fe] ratios in the MW with NS mergers alone, and the contribution from magneto-rotational SNe is necessary.

1.2 Project goals

The principal aim of this PhD project is to shed light to some open questions about the property of the three more massive MW satellites, namely the Sgr, LMC and SMC. In particular to:

1. understand if the LMC and Sgr have had a similar chemical enrichment history,

as expected in light of the possible similar masses of the LMC and the Sgr progenitor, and their similar mean metallicity;

2. better characterize the chemical composition of SMC, analysing both field stars and GCs stars in homogeneous way;

3. derive the real metallicity distribution for Sgr, because the metallicity distributions available so far for this galaxy are biased by the presence of the massive, metal-poor GC M 54;

4. measure the chemical abundances for the main groups of elements (light, alpha, iron-peak, neutron-capture elements) that will allow to reconstruct the chemical enrichment histories of the galaxies and to estimate the role played by SNe II and SNe Ia and AGB stars to their chemical enrichment history;

5. search for the presence of metallicity gradient within the galaxies, which would point to spatially nonuniform star formation events, and for possible kinematically/chemically distinct substructures that could indicate accreted stellar populations;

6. search for very metal-poor stars ([Fe/H] < -2.5 dex), corresponding to the stars formed in the first bursts of star formation.

1.3 Thesis organization

This thesis is organized as follows:
Chapter 2 summarizes the main information concerning the SFH and chemical abundances of MW satellites galaxies (LMC, SMC and Sgr) on which this project is focused.
Chapter 3 presents the homogeneous comparison between the chemical composition of the LMC and the Sgr dwarf galaxy, in order to highlight similarities and differences among them and with the MW.
In Chapter 4 is discussed the identification of NGC 2005 as an accreted GC in the LMC, the only known case so far to be identified by its chemical fingerprints in the realm of dwarf galaxies.
Chapter 5 and 6 focus on the chemical characterization of the SMC, from the study of field stars and GCs respectively, and comparing them with the MW.
Chapter 7 describes the preliminary results derived from the analysis of a unbiased sample of Sgr main body field stars.
Chapter 8 discusses the use of some iron-peak element abundances (Sc, V, Zn) as chemical diagnostic to recognize accreted GCs in our Galaxy.
Finally, Chapter 9 presents the summary of the main results of this project and the future prospectives.

Chapter 2

LMC, SMC and Sgr: state of the art

Hereafter, the SFH and the chemical composition of the three nearest MW interactive galaxies, on which my PhD project is focused.

2.1 Large Magellanic Cloud

The LMC is classified as a barred spiral galaxy SB(s)m (de Vaucouleurs et al., 1991). It has a complex structure, with a central bar of high surface brightness and a circular symmetry stellar disc with spiral arms. It is located at a distance of ~ 50 kpc (Alves, 2004; Tully et al., 2016).
The LMC is gravitationally bound with the SMC, with which is on a early stage of a minor merger. The interaction starts around 4-5 Gyr ago, when the SMC was tidally captured by the LMC (Bekki et al., 2004; Bekki & Chiba, 2005). The MCs are also gravitationally bounded to the MW, but they are only at the first approach with the Galaxy, completing at the most one orbit around it (Besla et al., 2010; Besla, 2015). The LMC starts to experience significant tidal gas stripping only recently (nearly 1.5 Gyr ago, as derived by Guglielmo et al., 2014). An indication of these interactions is found in the Magellanic Bridge, a weak gas structure that connect the two Clouds, and in the Magellanic Stream, a stream made only by HI that draws the path of the Clouds, due to the tidal interaction with the MW (Hammer et al., 2015).

2.1.1 LMC star formation history

The LMC SFH is particularly complex, due to the strong gravitational interactions with the SMC and the MW. Stellar populations of different ages and metallicities are present in the galaxy. This is clearly seen from the prominent features visible in the color-magnitude diagrams (CMDs) of three LMC fields located at different distances from the LMC center moving toward the north (see Fig. 2.1). Isocrones of different ages are superimposed to the CMDs, highlighting the presence of an extended main sequence, made up of young stars, indicating that the star formation is still ongoing, and an extremely populated red giant branch (RGB), with the He-clump, composed of stars older than 1 Gyr.

The LMC SFH can be derived from CMDs of a fields located in different regions of the galaxy, in comparison with a synthetic CMD. The star formation started nearly

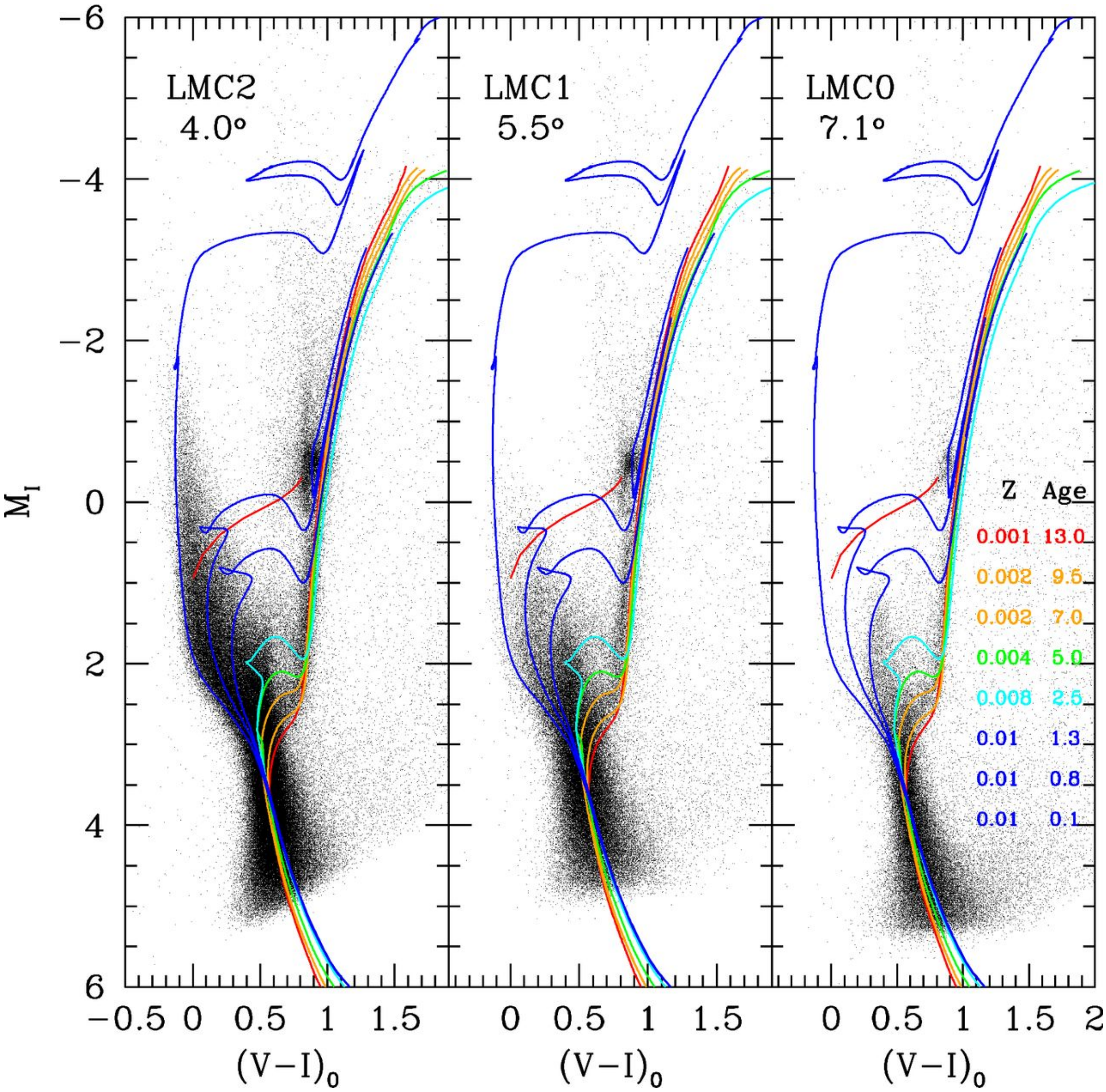

Figure 2.1: [(V-I)$_0$, M$_I$] CMDs for three LMC fields located at difference distances from the LMC center toward the north. Isochrones from Pietrinferni et al. (2004) of ages and metallicities as labelled have been superimposed. The three youngest isochrones have been chosen to indicate the adopted age of the end of the bulk of the star formation in fields LMC0 (1.3 Gyr), LMC1 (0.8 Gyr) and LMC2 (0.1 Gyr).
Taken from Meschin et al. (2014).

13 Gry ago, the period of the first burst in all the galaxies of the LG. All the works (Harris & Zaritsky, 2009; Rubele et al., 2012; Nidever et al., 2020) agree that, after the first burst, the LMC continued to form stars at a slow rate, until 4-5 Gyr ago, when a strong formation episode happened. This burst temporally coincides with the start of the tidal interaction with the SMC. During the last period, numerous star formation bursts have been observed in correspondence with closest passages among clouds (Bekki et al., 2004). In Fig. 2.2 is reported the representation of the LMC SFH derived by Meschin et al. (2014) in the three different analysed regions of the galaxy, derived form the analyses of the CMD reported in Fig. 2.1. These SFHs show common features, in the form of epochs of enhanced or decreased star-forming activity, whose intensity varies consistently and smoothly across the three fields, indicating a strong galactocentric stellar population gradient in the sense that younger populations are more concentrated inward.
Similar information can be derived from the study of LMC GCs, from which age and metallicity can be infer simultaneously with high accuracy, allowing to derive the age-metallicity relation (AMR) of the galaxy. Three distinct groups of GCs have been observed. The first it is composed by the oldest and metal-poor GCs ([Fe/H] < -1.0 dex), forming at the beginning, during the first star formation burst (Brocato et al., 1996; Olszewski et al., 1991; Olsen et al., 1998; Grocholski et al.,

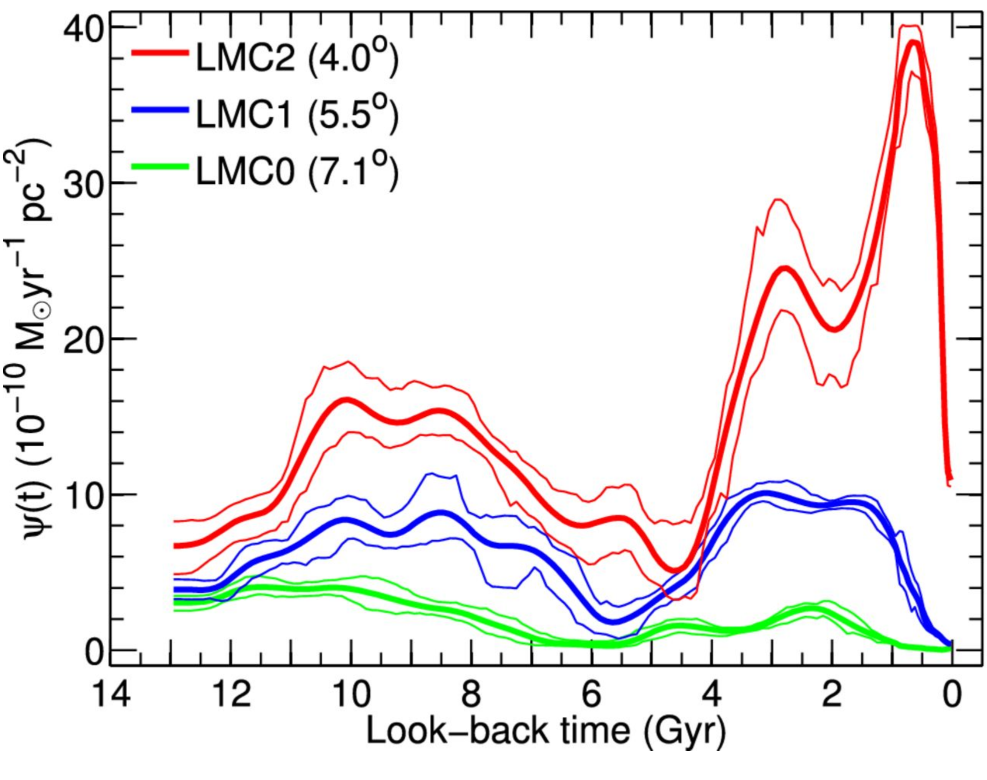

Figure 2.2: Comparison of the SFH of the LMC in the three studied fields. The thin lines represent the uncertainties. Taken from Meschin et al. (2014)

2006; Johnson et al., 2006; Mucciarelli et al., 2010; Mateluna et al., 2012). The predominant group of GCs are more metallic and with an age between 1 and 3 Gyr (Gallart et al., 2003; Ferraro et al., 2004). They are the ones born after the beginning of the gravitational interaction between the Clouds. Only one GC, namely ESO 121, have been found with ad age between 3 and 10 Gyr ago (Geisler et al., 1997; Mackey et al., 2006). The lack of GCs in this age range is called *Age Gap*. A possible explanation is that the GCs formed in that period have been stripped from the galaxy or destroyed due to the tidal interaction with the SMC. The last group of GCs is composed by the youngest GCs, with an age smaller than 1 Gyr (Brocato et al., 2003; Grocholski et al., 2006).
Therefore also the distribution of the LMC GCs confirms the SFH derived from field stars.

2.1.2 Chemical composition of the LMC

The chemical composition of the LMC stars has been studied using both low and high-resolution spectra. For many decades, low-resolution spectra observing the spectral region around the Ca II triplet have been the only tool to investigate the metallicity of stellar populations older than 1 Gyr. High-resolution spectra were obtained only for the brightest stars, sampling the stellar populations younger than 200-300 Myr. With the advent of the 8-10 meter class telescopes, also RGB stars (therefore stellar populations older than 1 Gyr) can be observed with high-resolution spectroscopy.

Field stars

Extended studies based on low-resolution spectra have been made for LMC field stars, where the metallicity can be derived from the CaII triplet. Cole et al. (2005) analysed 373 RGB star spectra located in the central region of the LMC bar and they found that the metallicity distribution (reported in Fig. 2.3) can be described as the sum of two Gaussians, one for the metal-poor population, peaked at -1.08 dex (including 11% of the total stars), and the other for the metal-rich one, with a peak at -0.37 dex. Carrera et al. (2008a, 2011) studied stars located in different regions of the galaxy and they derived the presence of a metallicity gradient outside 6° from the LMC center, with the oldest stellar population (12-13 Gyr) uniformly distributed, while the young one (younger than 3-4 Gyr) decrease its presence moving outwards, leading to a decreasing of the mean metallicity in the external regions.

Thanks to the 8-10 meter class telescopes, high-resolution spectra are available also for LMC RGB stars allowing us to study with high details the chemical composition of stellar populations older than ∼1 Gyr. In particular, measured abundance ratios related to different groups of elements provide the opportunity to estimate the contribution of SNe Ia, SN II and AGB stars to the chemical enrichment history

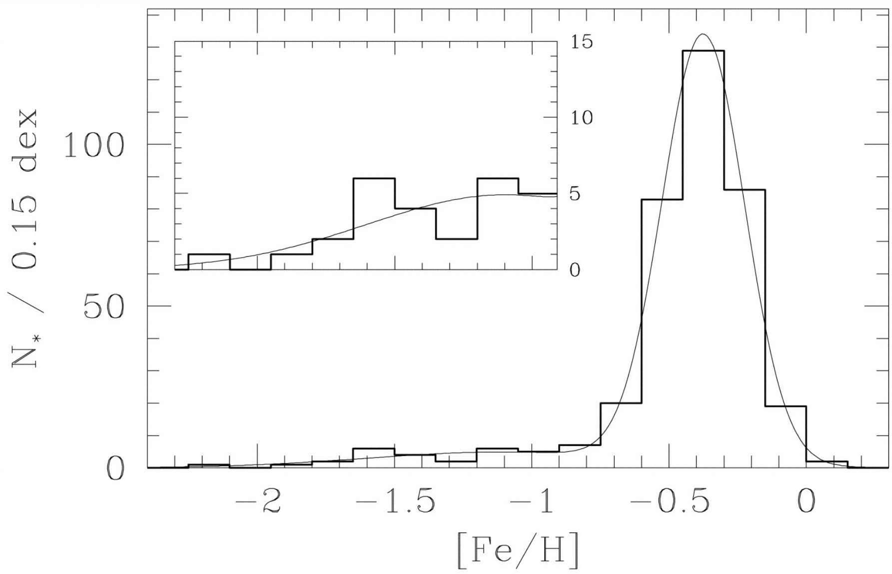

Figure 2.3: Metallicity distribution of LMC RGB stars of the bar field analysed by Cole et al. (2005). The smooth curve is the sum of two Gaussians that best match the data. The inset shows an expanded view of the region [Fe/H] < -0.9 dex.
Taken from Cole et al. (2005).

of the galaxy.
Concerning the metallicity distribution, Lapenna et al. (2012) studied 89 LMC disk stars and found the presence of two stellar populations, a metal-poor component peaked at –1.07 dex including the 16% of the total stellar population, and a metal-rich component peaked at –0.48 dex, in good agreement with the results found by Cole et al. (2005). Similar results have been found by Song et al. (2017), where they analysed about 300 RGB stars located near the LMC bar, even if with slight different values of the metallicity peaks (–0.66 dex for the metal-rich component and –1.2 dex for the metal-poor one).
Evidence of the presence of a metallicity gradient appears also from high-resolution studies, such as Gallart et al. (2008) and Meschin et al. (2014), proposing an Outside-In disk evolution model.
The chemical abundances of the α-elements are derived by Pompéia et al. (2008), who analysed 59 LMC disk RGB stars, Lapenna et al. (2012), and Van der Swaelmen et al. (2013), who studied 106 RGB stars, located in the bar. All the three works agree on the α-elements abundance ratios, which describes a decreasing trend as a function of the metallicity of the stars and a depletion with respect to the MW stars at similar metallicity, in agreement with a slower SFR characterizing the LMC in its first period (in Fig. 2.4 an example of the α-trend derived by Van der Swaelmen et al., 2013). But an higher spread is found the in bar α-abundances with respect to the disk ones.

Pompéia et al. (2008) and Van der Swaelmen et al. (2013) derived also the abun-

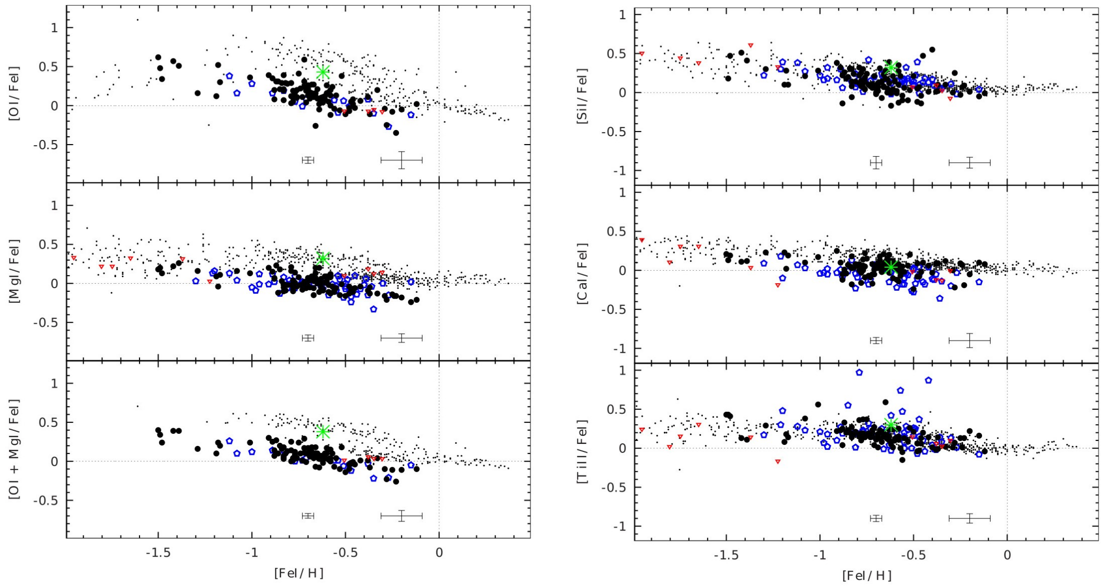

Figure 2.4: Left panel: from first to third raw [OI/FeI] vs [FeI/H], [MgI/FeI] vs [FeI/H], and [OI+MgI/2 FeI] vs [FeI/H]. Right panel: from first to third raw [SiI/FeI] vs [FeI/H], [CaI/FeI] vs [FeI/H], and [TiII/FeI] vs [FeI/H]. Represented data: LMC bar abundances (black filled circles) and LMC inner disk (blue open pentagons) from Van der Swaelmen et al. (2013), LMC GCs (red downward triangle) from Johnson et al. (2006); Mucciarelli et al. (2008, 2010), MW stars (black tiny dots) from Bensby et al. (2005); Reddy et al. (2003, 2006) for thin e thick disc, from Fulbright (2000); Stephens & Boesgaard (2002); Reddy et al. (2006) for the halo. In each panel, typical random (left) and systematic (right) error bars on both coordinates are provided for LMC samples by Van der Swaelmen et al. (2013).
Taken from Van der Swaelmen et al. (2013).

dances of other elements. They found that the iron-peak elements show a decreasing trend with the metallicity, and they are under-abundant in comparison to the MW stars of similar [Fe/H]. Instead, the neutron-capture elements exhibit an increasing trend, with abundance ratio higher respect to the MW one in a metal-rich regime, with slight differences between the disk and the bar of the LMC. They explained the enhancement in neutron-capture elements as an higher contribution by low mass AGB stars. The abundance differences observed in the bar respect to the disk are link to an increasing in the bar star formation between 2 and 5 Gyr ago, while the disk maintain a constant rate (Van der Swaelmen et al., 2013).
Furthermore, there are recent results based on the *APOGEE* survey (Nidever et al., 2020; Hasselquist et al., 2021), where they derived the α-elements abundances and they observed a decreasing trend in the [α/Fe] – [Fe/H] plane until a metallicity of –1.2 dex, in agreement with the other literature works. But, at higher metallicities, they found ad increasing trend, as shown in Fig. 2.5. They interpreted this trend as an early low efficient star formation, followed by a strong burst occurring in more

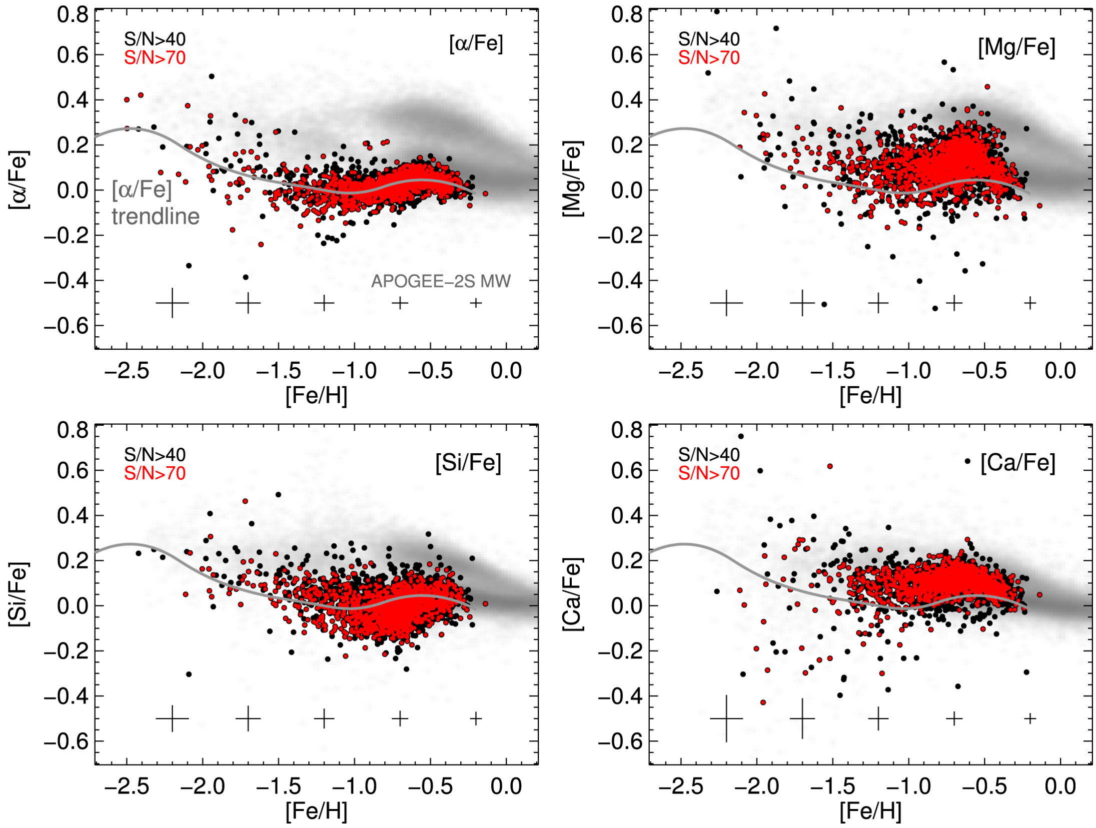

Figure 2.5: The α-abundances for the *APOGEE* LMC stars with S/N $>$ 40 (black circles) and S/N $>$ 70 (red circles). The density of *APOGEE* MW disk field stars with similar $T_{\rm eff}$, logg, and S/N as the LMC stars is shown in gray scale for reference. The trend line of the parameter-level [α/Fe] (upper left panel) is shown in each panel as a fiducial. Taken from Nidever et al. (2020)

recent times, when many SNe II drove up the α-element abundances.
Hasselquist et al. (2021) derived the abundances also for some iron-peak and neutron-capture elements, finding results in agreement with the ones just mentioned.
Finally, there is the work of Reggiani et al. (2021) focused on the chemical abundances of metal-poor stars, where they analysed 9 metal-poor giant stars belonging to the LMC in a metallicity range of $-$ 2.4 $<$ [Fe/H] $<$ $-$ 1.5 dex. They derived that the chemical abundances are similar to MW stars in α, light, and iron-peak elements, but are enhanced relative to the MW in the r-process element Eu. They argued these patterns as the product of their isolated chemical evolution which implies a slow SFR with extended era for metal-poor star formation, in combination with r-process nucleosynthesis occurring on a timescale longer than SN II one, but shorter than or comparable to SN Ia one.

Globular clusters

Focusing on high-resolution works, Mucciarelli et al. (2009b, 2010) analysed RGB

star spectra belonging to three old LMC GCs, namely NGC 1786, NGC 2210 and NGC 2257. They derived the metallicity and the abundance ratio for light odd-Z, α, iron-peak, and neutron-capture elements. They found a metallicity of – 1.75 dex for NGC 1786, – 1.65 dex for NGC 2210, and – 1.95 dex for NGC 2257. They observed the presence of chemical anomalies in Na, O, Mg, and Al and they concluded that the old, metal-poor stellar population of the LMC GCs closely resembles the MW GCs in many chemical abundance patterns such as the iron-peak, the α, and heavy s-process elements, while [Eu/Fe] is enhanced ($\sim +0.70$ dex) in all the clusters, as happens in metal-poor field stars (Reggiani et al., 2021).
These results are not in agreement with the ones derived by Johnson et al. (2006) and Mateluna et al. (2012), which analysed four different old GCs, namely Hodge 11, NGC 1898, NGC 2005 and NGC 2019. They found that [Ca/Fe], [Ti/Fe], and [V/Fe] in the LMC are significantly lower than what is seen in the Galactic GCs.

Different abundance behaviours were found in intermediate-age LMC GCs. Mucciarelli et al. (2008) analysed a sample of 27 RGB stars located in four GCs, namely NGC 1651, NGC 1783, NGC 1978, and NGC 2173. The four GCs have a metallicity between – 0.51 dex (NGC 2173) and – 0.30 dex (NGC 1651). All the analyzed abundance patterns behave similarly in the four clusters and also show negligible star-to-star scatter within each GC. In particular, the measurement gives slightly subsolar [Na/Fe] and a more significant [Al/Fe] depletion. The [α/Fe] abundance ratios are nearly solar, while the iron-peak elements well trace those of the Fe. S-process neutron-capture elements behave in a peculiar way: light s-elements give subsolar [Y/Fe] and [Zr/Fe] abundance ratios, while heavy s-elements give enhanced [Ba/Fe], [La/Fe], and [Nd/Fe] with respect to the solar values. Also, the [Eu/Fe] abundance ratio turns out to be enhanced. The observed cluster stars do not show any sign of the anti-correlation in light elements present in all the Galactic and old LMC GCs, indication of a different formation/evolution scenario for the LMC massive clusters younger than $\sim$ 3 Gyr with respect to the old ones.
The same results are found by Mucciarelli et al. (2011) for NGC 1866, a young and massive LMC GC.

2.2 Small Magellanic Cloud

The SMC is an irregular galaxy characterized by an ongoing star formation activity, located at a distance of $\sim$ 60 kpc (Tully et al., 2016). Like the LMC, it has experienced a violent and complex SFH due to the gravitational interaction with the LMC and MW, forming a triple system (for more details see Section 2.1).
As a consequence of the tidal interaction, the LMC stripped a large number of stars from the SMC ($\sim$ 5% of the LMC's mass comes from the SMC; Olsen et al., 2011).

2.2.1 SMC star formation history

Numerous works are present in literature regarding the SFH of the SMC, and based on the study of CMDs of different regions of the galaxy.
Dolphin et al. (2001) observed a field located $\sim 2°$ northwest from the center of the SMC and they found a continuum star formation with a burst between 5 and 8 Gyr ago.
Harris & Zaritsky (2004) derived a global SFH based on the *Magellanic Cloud Photometric Survey*. They found that ∼50% of the stars that ever formed in the SMC are older than 8.4 Gyr and that the SMC formed relatively few stars between 8.4 and 3 Gyr ago. They found a rise in the mean SFR during the most recent 3 Gyr, with burst at 2.5 Gyr and 0.4 Gyr, which are temporally coincident with past perigalactic passages of the SMC with the MW, and at 0.06 Gyr. However this study is based on CMD that are not deep enough to sample also the old and intermediate-age stars.
McCumber et al. (2005) studied a HST field located nearly the SMC center, and found an increasing in SFR between 4 and 12 Gyr ago and at 1.7 Gyr
Chiosi & Vallenari (2007) derived the SFH from CMDs of stars located in three different central regions of the SMC and they found similar features in all the fields, such as a slow SFR until 6 Gyr, followed by bursts at 6 Gyr, 3 Gyr and 300-400 Myr ago.
The most complete work, reaching the oldest main sequence turn-off (MSTO), was performed by Noël et al. (2009), where they studied the CMDs in 12 different regions of the SMC located between 1.3° to 4.0° from the SMC center. The derived SFH in each region is reported in Fig. 2.6. They found in all the fields three main episodes of enhanced SFR at 1.5 – 2.5 Gyr, 4 – 5 Gyr and 10 Gyr ago (the last splits in two peaks at 8 Gyr and 12 Gyr ago in the western fields), with different relative importance depending on the position in the galaxy. They derived the presence of another star formation burst peaked at 0.2 – 0.5 Gyr ago, but only in the eastern fields and in the most central one located to the south.
Lastly, Sabbi et al. (2009) derived the SFH in six different regions of the SMC characterised by very different star and gas densities. The six fields were observed with the HST/ACS camera and the photometry reaches the magnitudes of the oldest MSTO. They found that the SMC was already forming stars $\sim$ 12 Gyr ago, but in the first few billion years the star formation activity was low. The SMC formed stars over a long interval of time until 2 – 3 Gyr ago, with an increase in the star-forming activity approximately between 4 and 6 Gyr ago. Finally they found that stars younger than $\sim$ 100 Myr have a very inhomogeneous distribution, indicating that recent star formation has locally developed.

From all these works come out the complexity of the SMC SFH, with the presence of numerous bursts in star formation due to the gravitational interaction with the LMC and the MW. This figure out also from the CMD of a central region of the

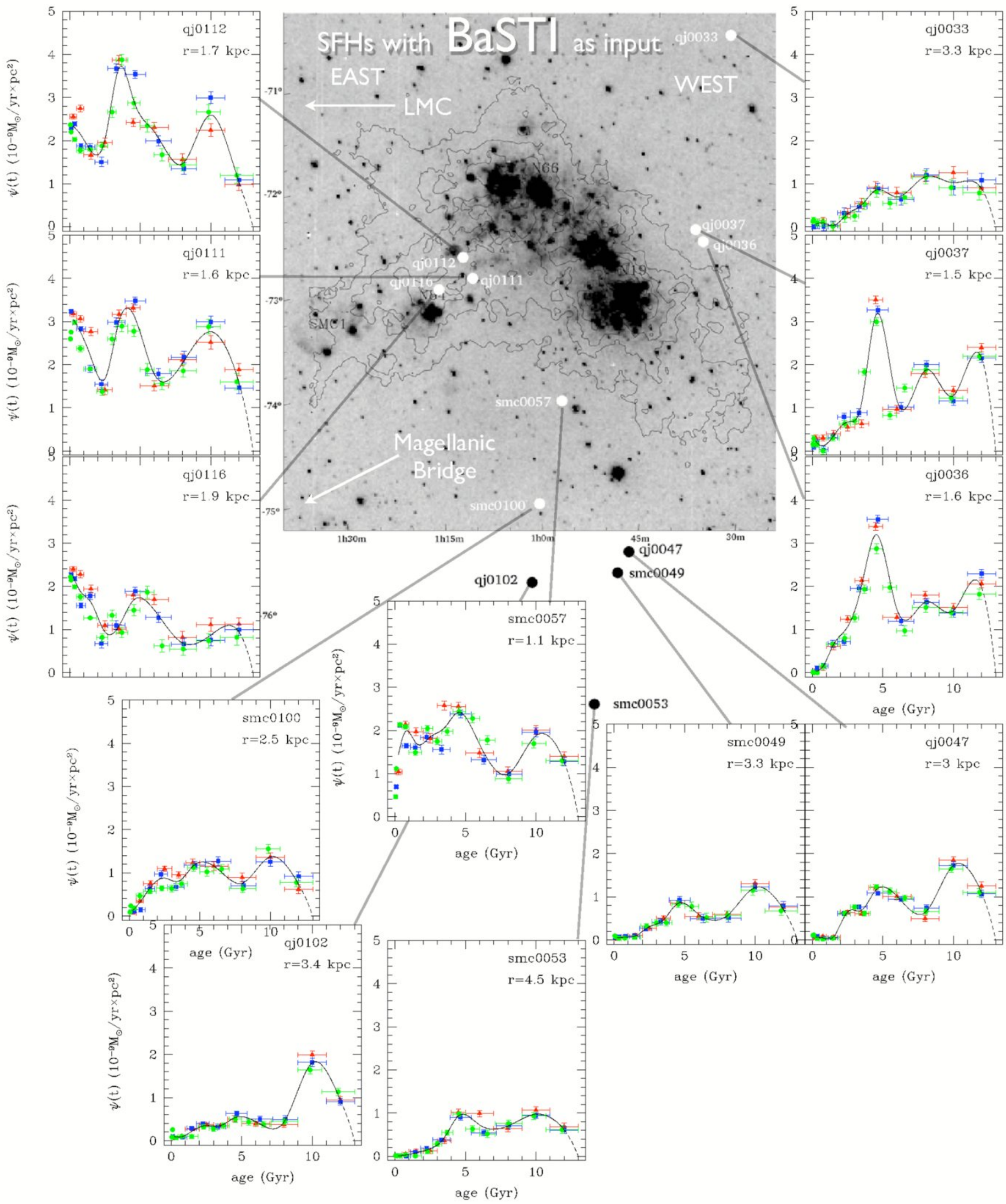

Figure 2.6: Derived SFR as a function of time for each SMC field. The different symbol and color depend on the set of age intervals and sampling adopted: red triangles are for age-1, blue squares are for age-2, and green circles are for age-3 (for more detail see Table 2 Noël et al., 2009). The final solution is the black line, obtained by fitting a cubic spline. North is top and east is to the left.
Taken from Noël et al. (2009).

SMC in Fig. 2.7, where a prominent main sequence and an evolved RGB are present, indicating the existence of young and old stars respectively.

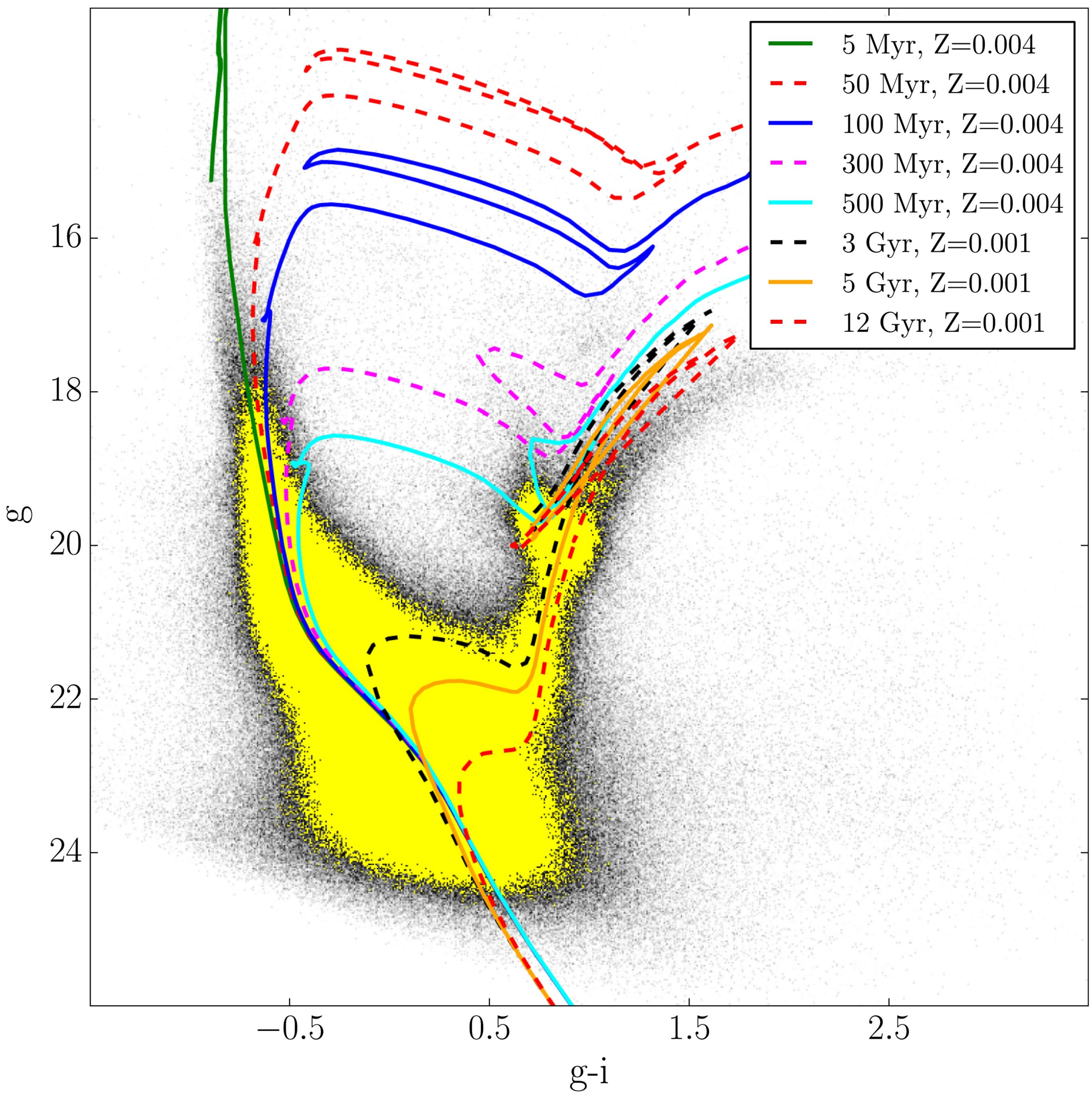

Figure 2.7: CMD of a field near the center of the SMC made with STEP survey (the SMC in Time: Evolution of a Prototype interacting late-type dwarf galaxy). The stellar isochrones are from Marigo et al. (2008): for metal abundance Z = 0.004, ages 5 Myr (green continuous line), 50 Myr (red dashed line), 100 Myr (blue continuous line), 300 Myr (pink dashed line) and 500 Myr (cyan continuous line); Z = 0.001, ages 3 Gyr (black dashed line), 5 Gyr (orange continuous line) and 12 Gyr (dashed red line). Assumed distance modulus and reddening E(B - V) are 18.9 and 0.04 mag, respectively.
Taken from Ripepi et al. (2014)

2.2.2 Chemical composition of the SMC

Thanks to its proximity, there are numerous works focus on the studies of both field stars and GC stars, but the majority of them analysed low-resolution spectra.

Field stars

Starting from low-resolution studies, where the metallicity was derived from the CaII triplet lines, Carrera et al. (2008b) analysed over 350 RGB stars located in 13 different positions in the SMC from 1° to 4° from its center. They found an average metallicity around – 1 dex in the innermost field. This value decrease moving outwards and towards west, indication of the presence of a metallicity gradient. These results are in agreement with the one derived by Dobbie et al. (2014b). They studied 3037 RGB field stars located in different regions of the galaxy, and they found a unimodal metallicity distribution with a peak at – 0.993 ± 0.006 dex, and they explained the metallicity gradient with an increasing of the fraction of metal-rich stars in the central regions of the galaxy. Finally, also Parisi et al. (2016) analysed 400 SMC field stars, and they found a metallicity distribution with only one peak at – 0.97 ± 0.01 dex, and the presence of a metallicity gradient, with the mean metallicity of field stars that decrease moving outwards (their distribution is reported in Fig. 2.8).

Concerning the high-resolution studies, the abundances of other elements can be

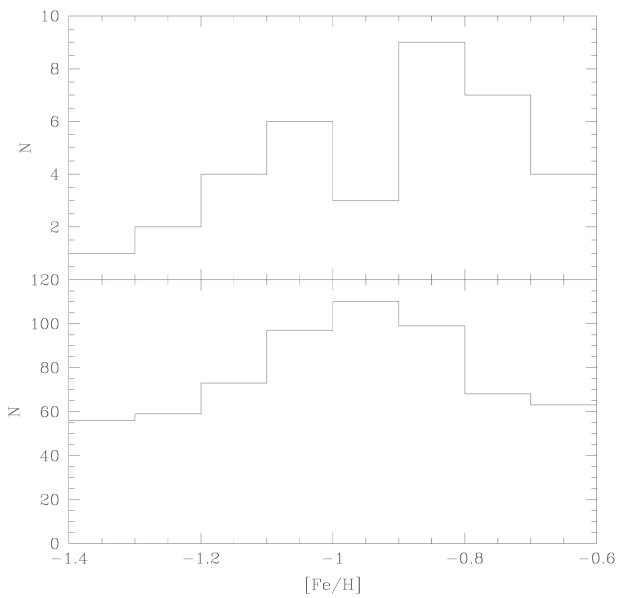

Figure 2.8: Metallicity distribution of SMC field giant stars (bottom) analysed by Parisi et al. (2016), compared to the GCs metallicity distribution (top) derived by Parisi et al. (2009, 2015).
Taken from Parisi et al. (2016).

derived from the spectra. Nidever et al. (2020) analysed a large sample of *APOGEE* data, and they derived the abundances for the α-elements, and they found that they are under-abundant with respect to the MW stars of similar metallicities in the metal-rich regime, with the α-*knee* more metal-poor than those of less massive MW dwarf galaxies such as Fornax, Sculptor, or Sagittarius. They provided a decreasing trend in the [α/Fe] abundance ratio until – 1.5 dex, followed by a *platò*, with perhaps a slight decrease beginning at [Fe/H] $\sim$ – 0.7 dex. In contrast, same from *APOGEE* data, Hasselquist et al. (2021) observed a weak increase in [Mg/Fe] beginning at [Fe/H] $\sim$ – 1.3, with a peak at [Fe/H] $\sim$ – 1.0, followed by a slight decrease. This trend is not observed in the other α-abundances. The observed trends in both works are explained by the authors as an indication of one or a series of star-bursts, but they are not sufficiently powerful to substantially enrich the gas already present with α-elements, on the contrary of the LMC.
Hasselquist et al. (2021) derived also the abundances of some iron-peak and neutron-capture elements and they found that the patterns of the SMC are similar to those of the LMC in all the elements. They interpreted the similarities between the SMC and LMC abundance patterns with a similar chemical enrichment history experienced by the two galaxies, but the LMC enriched to higher metallicities than the SMC by $\sim$ 0.4 dex, potentially a consequence of its larger mass.
Finally, the work by Reggiani et al. (2021) on the chemical abundances of metal-poor stars analysed also four SMC metal-poor giant stars (with metallicities of – 2.6 < [Fe/H] < – 2.0 dex), and they found results similar to the one explained for the LMC in Section 2.1.2.

Globular Clusters

Regarding GCs, SMC is the only dwarf galaxy in the LG containing populous intermediate-age star clusters of all ages, filling the *Age Gap* observed among the LMC GCs. From CaII triplet, Parisi et al. (2015) studied stars located in 15 GCs and they found evidence of bimodality in the GCs metallicity distribution, in contrast to SMC field stars, with peaks at [Fe/H] = – 1.1 dex and [Fe/H] = – 0.8 dex, where the last is more populated. They provided also the absence of a metallicity gradient within the galaxy. This result was confirmed also in Parisi et al. (2016), where they have a total of 29 SMC GCs previously analysed (Parisi et al., 2009, 2015). The distribution that they found is reported in Fig. 2.8, in comparison with the one that they derived for field stars.

Looking at the high-resolution studies of SMC GCs, the only one is the work by Dalessandro et al. (2016). They analysed 5 spectra acquired with UVES-FLAMES (Pasquini et al., 2002) belonging to NGC 121, an old and massive GC in the SMC. They derived the metallicity and the light-elements abundances in order to search for the light elements anti-correlation present in GCs. They found an average metallicity of – 1.28 dex. The position of these stars in both the [O/Fe]–[Na/Fe] and [Mg/Fe]–[Al/Fe] diagrams is consistent with that of Galactic and LMC old globular first generation stars, even if they do not follow exactly the distribution of MW and LMC GCs, especially in the [Mg/Fe]–[Al/Fe] diagram. This might be related to the different chemical evolution history of the SMC.

2.3 Sagittarius dwarf galaxy

Sgr was discovered by Ibata et al. (1994) as a large and extended group of co-moving stars in the direction of the Galactic centre.
The galaxy is a massive dwarf spheroidal that is currently merging with the MW. The main body of the system is a large low surface brightness elongated spheroid, located behind the Galactic Bulge at a distance of 26.3 ± 1.8 kpc (Monaco et al., 2004b). In addiction, two arms of its tidal stream are traced all over the sky, as visible in Fig. 2.9 (Belokurov et al., 2014).

Sgr is being embedded by the MW, and this process of disruption contributes to the build-up of the Galactic Halo in terms of dark matter, stars, and GCs (de Boer et al., 2015; Gibbons et al., 2017). The interaction started no less than 3 Gyr ago (Dierickx & Loeb, 2017) and it has likely collided with the MW disk at least once in the past (Purcell et al., 2011). It experienced pericentric passages which removed a significant fraction of gas and are consistent with delayed star formation

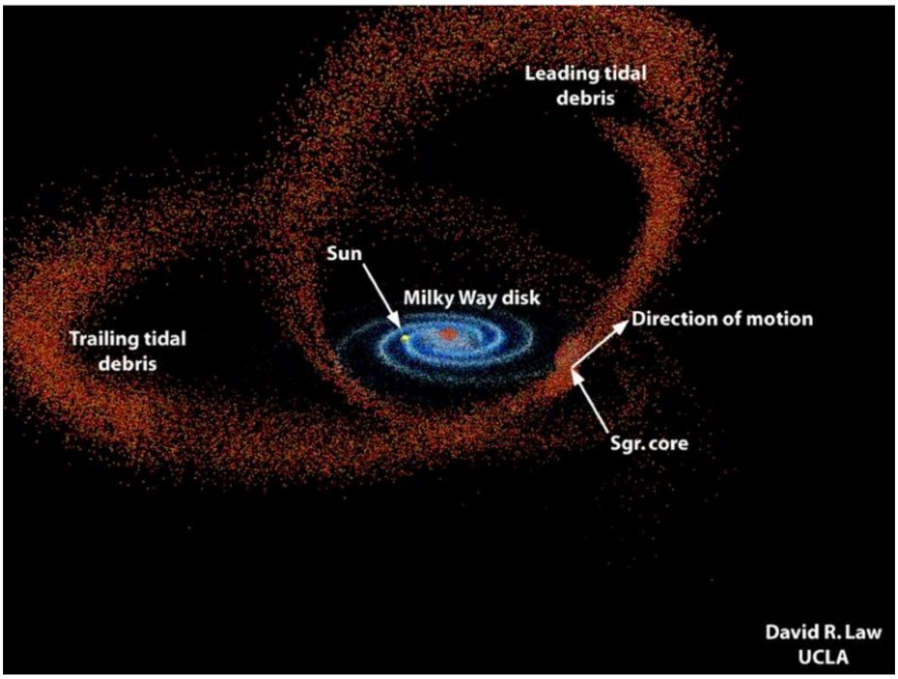

Figure 2.9: Representation of the stream of stars left behind as the Sgr is torn apart by the gravitational potential of the MW. Source: David R. Law, UCLA.

episodes (Mayer et al., 2001; Tepper-García & Bland-Hawthorn, 2018). Neutral gas has never been detected in Sgr (Koribalski et al., 1994; Burton & Lockman, 1999). Despite its proximity, a complete view of the properties of Sgr are still missing or uncertain, due to its location. Indeed, the main body of Sgr lies at low Galactic longitude and latitude, therefore the CMD from which candidates members should be selected is strongly affected by contaminants from foreground stars from the Bulge and the Thick Disc of the MW. The combination of high-metallicity and distance makes relatively easy to pick out good candidate members from the red (metal-rich) side of the RGB, as can be seen in the *Gaia* CMD of the Sgr center in Fig. 2.10, where the most prominent features are indicated. In this way, an observational bias against metal-poor stars is introduced.
Furthermore, the central region of the galaxy (where generally the most extensive and detailed studies focused) hosts a complex and composite stellar nucleus (Monaco et al., 2004a; Bellazzini et al., 2008) and a massive metal-poor GC M 54 (Bellazzini et al., 2008; Alfaro-Cuello et al., 2019), whose stellar content is not representative of the main body of Sgr (Siegel et al., 2007; Mucciarelli et al., 2017b; Alfaro-Cuello et al., 2019). Therefore, selecting main body Sgr stars is quite challenging.

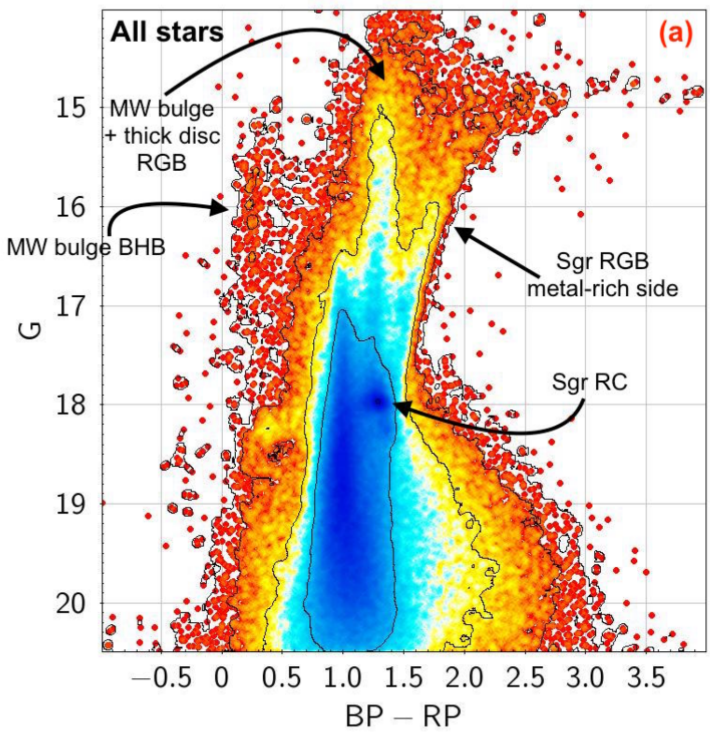

Figure 2.10: *Gaia* eDR2 CMD of a circular field with radius = 1.0° at the center of Sgr dSph. The innermost 12.0 arcmin are not included, to remove the contribution from the nuclear region, including the globular cluster M 54. The main evolutionary sequences are indicated.

2.3.1 Sgr star formation history

The violent interactions between Sgr and MW have significantly impacted on the stellar populations of Sgr contributing to shape its SFH. It is believed that pericentric passages are associated with burst in Sgr star formation (Mayer et al., 2001). Moreover, also the SFH of the MW disk was influenced by Sgr, triggering analogous bursts (Laporte et al., 2019; Ruiz-Lara et al., 2020). On the other hand, the tidal interaction between Sgr and the MW stripped away all the Sgr gas, stopping in this way the star formation.
The SFH of the Sgr is not well know until now and still uncertain, since it is challenging removing the MW foreground stars that contaminates the observed CMDs of the galaxy.
Siegel et al. (2007) analysed the *Hubble Space Telescope* photometry of the Sgr core region, where the massive, metal-poor GC M54 lies, and they derived the SFH of the central region of the galaxy from isochrones fitting procedure. They found that the dominant stellar population is formed by old metal-poor field stars and GCs, and from the observed multiple turnoffs they inferred the presence of at least two intermediate-aged star formations, aged at 4 and 6 Gyr. They found a prominent, ~ 2.3 Gyr old Sgr population, and finally evidence of a even younger ($\sim 0.1 - 0.8$ Gyr old) stellar population. The SFH that they derived is in Fig. 2.11.

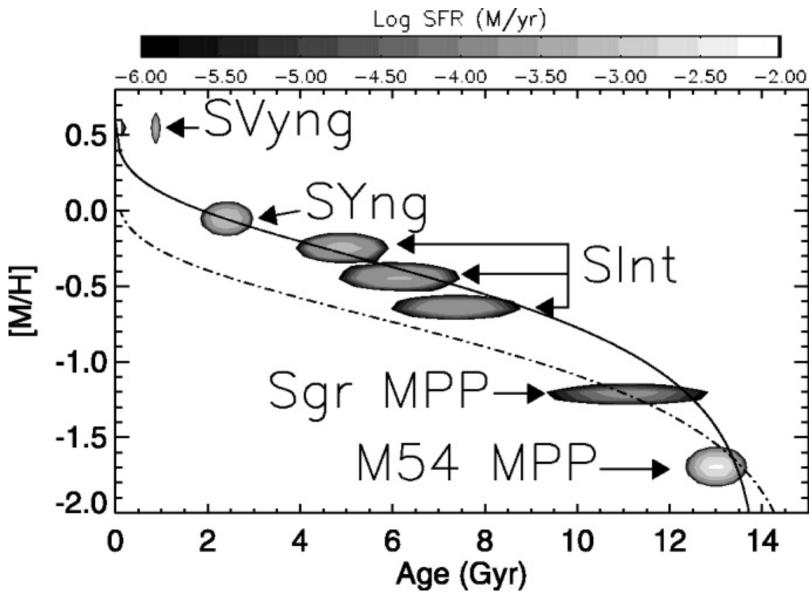

Figure 2.11: Simulated SFH of the Sgr core field. Distinct contributions are from the metal-poor M 54 population (M54 MPP), Sgr's metal-poor population (Sgr MPP), and Sgr's young (SYng) population. The intermediate Sgr population (SInt) is broad and composed of multiple bursts or continuous star formation. There appears to be some contribution from a very young Sgr population (SVYng). The dotted line is the AMR from Layden & Sarajedini (1997) using a simple closed-box model; the solid line an updated model with faster enrichment. Taken from Siegel et al. (2007).

Similar results are found by Bellazzini et al. (2006). They statistically decontaminated from the MW stars the CMD of a 1° × 1° field in the core of Sgr, and they found that the best fit age for the dominant stellar population is in the range between 5.5 and 9.5 Gyr ago, independently on the adopted theoretical models. Also in a previous work, Bellazzini et al. (1999) derived that the Sgr SFR had a peak from 8 to 10 Gyr ago, when the mean metallicity was in the range – 1.3/– 0.7 dex. After that maximum, the SFR rapidly decreased and ceased at a time $<$ 2 Gyr ago depending on the adopted model, since the gas reservoir was completely exhausted. They found also indication of a secondary peak in the SFR between 3 and 7 Gyr ago.
SFH of Sgr was derived also by Dolphin (2002) in his work on the dwarf spheroidals. For Sgr, he analysed CMD of the central region (0.2° from the center) and of an external one (2.4° from the center). He found evidence of star formation until $\sim$ 2 Gyr ago for the central field, while the outer filed shows only about half of the number of young stars with age $<$ 8 Gyr. The SFH is extended with a mean peak aged at 8.6 Gyr in the inner field and 9.8 Gyr in the outer field.
Moreover, the SFH was derived for the Sgr stream by de Boer et al. (2015). They analysed photometric and spectroscopic observations from the *Sloan Digital Sky Survey* and derived separately the SFH for the bright and the faint Sgr streams. Both stream components show a tight sequence in the plane of age versus [Fe/H], indicating that star formation within Sgr took place in a well-mixed medium, homogeneously enriched in metals. The tight sequence starts from old, metal-poor populations and extends to a metallicity of [Fe/H] $\sim$ – 0.7 at an age of $\sim$ 5 Gyr before star formation terminates. Superimposing in this plane the age and metallicity of GCs associated with the Sgr dwarf galaxy (Forbes & Bridges, 2010), they found that the GCs trace out the same tight sequence in age and metallicity space, indicating that the sequence observed in both streams is consistent with Sgr populations present elsewhere in the stream and main body. Therefore, they use the SFH derived from both stream components to study the SFH of the parent galaxy: Sgr has undergone an extended star formation history, with multiple peaks in SFR. It formed stars for at least 7 Gyr, since in the streams, SFR drop rapidly around 5–7 Gyr ago, probably caused by the infall of Sgr into the MW potential, coinciding with stripping of gas from the outskirts of Sgr, from which the streams were formed.

2.3.2 Chemical composition of the Sgr

In this section is reported a description of the chemical composition of the different components of Sgr, namely the Sgr main body, the Sgr Stream, the central stellar nucleus of the galaxy and the massive metal-poor GC M 54. The stellar nucleus and M 54 are considered two distinct objects according to Bellazzini et al. (2008), who derived that they formed independently from kinematical and surface brightness information. M 54 reached the nucleus of Sgr because of significant decay of the original orbit due to dynamical friction.

Main body

Regarding the main body of the galaxy, there are several works based on high-resolution spectra that infer the chemical abundances for different elements. Bonifacio et al. (2004) derived the abundances if O, Mg, Si, Ca and Fe for 10 giants. Monaco et al. (2005) analysed a sample of 15 RGB stars and derive the metallicity and the α-elements abundances. Sbordone et al. (2007) studied 12 giant star spectra and derived the abundances for 21 elements from O to Nd. All this works found that the dominant stellar population is composed by star with [Fe/H] > -0.5 dex, with a metal-poor tail reaching values of –1.52 dex (Monaco et al., 2005). The mean [α/Fe] trend as a function of the metallicity derived by Sbordone et al. (2007) is reported in Fig. 2.12. In metal-poor regime ([Fe/H] < -1 dex) all the elemental abundance ratios have values similar to the one observed in the Galactic Halo, but in metal-rich regime they are depleted in α-elements, Na, Al, Sc, V, Co, Ni, Cu, and Zn, and enriched in La, Ce, and Nd relative to the MW. This suggests that the Sgr stars where formed from a gas less enriched by SNe II and with a top-light IMF, with the lack of the most massive stars in comparison with the MW, and with a stronger contribution by AGB stars.

Stellar nucleus and M 54

Moving to the Sgr stellar nucleus and M 54, Carretta et al. (2010b) analysed 27 RGB stars belonging to the Sgr core and 76 RGB stars of M 54. They derived a mean metallicity of -0.62 ± 0.07 dex for the nucleus and -1.56 ± 0.02 dex for M 54. They derived also the abundances of light-elements and iron-peak elements and they observed the presence of anti-correlation O-Na and Mg-Al in M 54, but not in the nucleus. Concerning iron-peak elements, they found that for M 54 stars have on average a flat distribution around the solar abundance ratio, while for the nucleus stars a small deficiency in the iron-peak elements abundance ratios with respect to the solar ratios is visible. They explained these ratios with an extra contribution from metal-poor SNe Ia to the gas from which these stars formed.

Based on medium-resolution spectra, Mucciarelli et al. (2017b) derived the metallicity and the α-elements abundances for 235 stars located in the central regions of Sgr. The derived metallicity distribution has two peaks, the metal-poor one at ~ -1.5 dex (likely dominated by M 54), and the metal-rich one, at ~ -0.5 dex, for the main population of Sgr. By a selection in metallicity and distance from the center, they identified 61 stars belonging to M 54 and they derived $\langle$[Fe/H]$\rangle = -1.52 \pm 0.02$ dex. Regarding the α-elements abundances, M 54 is consistent with Sgr main body stars, they are enhanced in metal-poor regime and matched well with the ones of

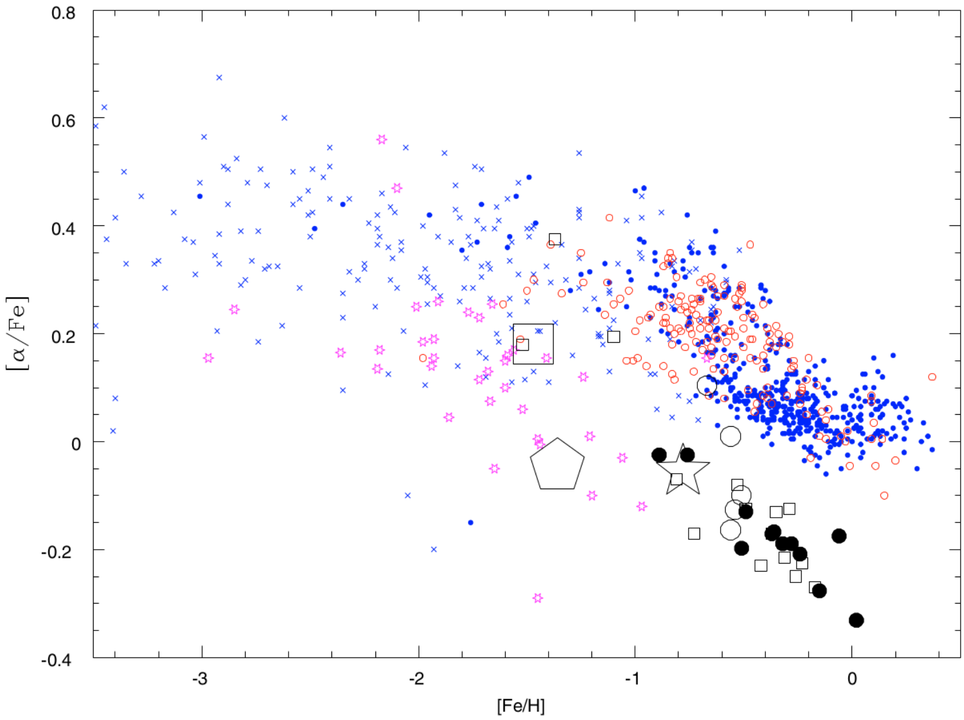

Figure 2.12: [α/Fe] (defined as mean of [Mg/Fe] and [Ca/Fe]) is plotted against [Fe/H] for various samples: Sgr dSph main body (large filled black dots) and Terzan 7 (large open dots) from Sbordone et al. (2007); Sgr dSph main body (open squares)from Monaco et al. (2005); LG dSph stars, namely Carina, Draco, Fornax, Leo I, Sculptor, Sextans, Ursa Major I (small open stars) from Shetrone et al. (2001, 2003); MW thin and thick disk (blue filled circles) and MW Halo stars (blue crosses) from Venn et al. (2004); MW thick disk stars (red open circles) from Reddy et al. (2006). Huge open symbols refer to mean values for GCs: Palomar 12 (star) from Cohen (2004), M 54 (square) from Brown et al. (1999) and Ruprecht 106 (pentagon) from Brown et al. (1997).
Taken from Sbordone et al. (2007).

the Galactic Halo stars, while in metal-rich regime they are underabundant with respect to the MW stars. To identify stars belonging to the nucleus of Sgr, Mucciarelli et al. (2017b) considered only the stars with [Fe/H] > -1 dex and they found evidence of a metallicity gradient, with the metallicity decreasing moving outward. The metallicity gradient corresponds to an age gradient.
A more recent work focusing on the central region of Sgr is the one by Alfaro-Cuello et al. (2019). They analysed *Multi-Unit Spectroscopic Explorer* data set that covers M 54 out to ∼2.5 half-light radius and they extracted the spectra of nearly 6600 cluster member stars. They derived the presence of different stellar subpopulations: (1) young metal-rich, with ages of 2.2 Gyr and an average metallicity of [Fe/H] = – 0.04 dex; (2) intermediate-age metal-rich, of 4.3 Gyr and [Fe/H] = – 0.29 dex; (3) old metal-poor, with ages 12.2 Gyr and metallicity [Fe/H] = – 1.41 dex. The young population is the most centrally concentrated, followed by the intermediate-

aged population, which is the dominant one in stellar number.

Moreover, Hansen et al. (2018) focused on the analysis of 13 metal-poor stars belonging to the Sgr main body, down to [Fe/H] ~ -3 dex. They analysed high-resolution spectra and they found high level of s-process enhancement and, most notably, also α-enhancement and strong contribution from r-process. These findings do not support a top-light IMF.

Stream

Hasselquist et al. (2017), Hayes et al. (2020) and Hasselquist et al. (2021) analysed numerous *APOGEE* high-resolution spectra belonging both to Sgr main body and to the streams, and they measure the abundance ratio of light, α, iron-peak and neutron-capture elements for a large sample of stars. They found that the Stream stars are on average more metal-poor than the main body ones, but their α-abundance patterns are similar to the one observed for the stars in the Sgr core, depleted respect to the MW stars with similar metallicities (found also by Carlin et al., 2018, , where they analysed high-resolution spectra of Sgr stream stars.). In particular Hayes et al. (2020) measured a difference in metallicity between Stream and core Sgr stars of ~ 0.6 dex, and they found a metallicity gradient in the Stream depending on the time at which the stars were stripped from Sgr, with stars less metallic in more ancient wraps of the Stream (derived also previously by Monaco et al., 2007, in their study focused on the Sgr stream stars).

Chapter 3

A homogeneous comparison between the chemical composition of LMC and Sgr

Based on the results published in
Minelli A., Mucciarelli A., Romano D., Bellazzini M., Origlia L., Ferraro F. R., 2021, The Astrophysical Journal, 910, 114

3.1 Introduction

LMC and Sgr exhibit some similarities in terms of stellar populations, with their stellar content dominated by an intermediate-age population with similar metallicity. The metallicity distributions of these two galaxies are both peaked at a metallicity of [Fe/H] $\sim -0.5/-0.3$ dex, as found by several spectroscopic works, see e.g. Pompéia et al. (2008), Lapenna et al. (2012), Van der Swaelmen et al. (2013), Song et al. (2017), Nidever et al. (2020) for LMC, and Monaco et al. (2005), Bellazzini et al. (2006), Sbordone et al. (2007), Carretta et al. (2010b), McWilliam et al. (2013), Hasselquist et al. (2017), Mucciarelli et al. (2017b) for Sgr. The age range of their dominant populations is $\sim$ 3-5 Gyr for LMC (Bekki & Chiba, 2005; Harris & Zaritsky, 2009; Rubele et al., 2012; Nidever et al., 2020) and $\sim$ 6-8 Gyr for Sgr (Layden & Sarajedini, 2000; Bellazzini et al., 2006; de Boer et al., 2015). Also, both galaxies have a metal-poor, old stellar component accounting for less than $\sim$10% of the total stellar content (see e.g. Monaco et al., 2003; Cole et al., 2005; Hamanowicz et al., 2016; Nidever et al., 2020).

The violent interactions between LMC and SMC and between Sgr and MW have significantly impacted on the stellar populations of LMC and Sgr contributing to shape their star formation histories. Some similarities between the chemical composition of the metal-rich component of LMC and Sgr have been already highlighted (Bonifacio et al., 2000, 2004; Monaco et al., 2005; Hasselquist et al., 2017; Muccia-

relli et al., 2017b), especially for the [α/Fe] abundance ratios that in the metal-rich stars of both galaxies are lower than those measured among the MW stars of similar [Fe/H], as expected for galaxies with lower star formation efficiencies (Matteucci & Brocato, 1990). Also, sub-solar abundance ratios of some iron-peak elements and super-solar abundances for some neutron-capture elements are common features of the metal-rich stars of LMC and Sgr (Pompéia et al., 2008; Van der Swaelmen et al., 2013). Their similar chemical patterns suggest that they have experienced analogous chemical enrichment histories and that the progenitor of Sgr could be as massive as the LMC (Niederste-Ostholt et al., 2012; de Boer et al., 2014; Gibbons et al., 2017; Mucciarelli et al., 2017b; Carlin et al., 2018).
Moreover, Bonifacio et al. (2004) stated that the derived high metallicity places Sgr clearly outside the metallicity–luminosity correlation valid for other LG galaxies (van den Bergh, 1999, and references therein) since it is underluminous for its metallicity. The capability of attaining a high metallicity is usually associated with the ability to retain the SNe ejecta and therefore one of the possible explanations that they gave is that Sgr was much more massive in the past, during the phase in which it raised its metallicity and has now lost much of its mass due to interaction with the MW.

However, in order to properly highlight similarities and differences between the chemical compositions of the two galaxies one needs to compare sets of chemical abundances obtained under the same assumptions (see e.g. Reichert et al., 2020). In fact, the adopted model atmospheres, temperature scale, atomic data, solar reference abundances can lead to systematics among different chemical analyses, hampering the possibility of a fully meaningful comparison of abundance patterns. The comparisons between the chemical patterns of LMC and Sgr performed so far are based on analyses that adopted different physical assumptions, limiting our capability to highlight real differences or similarities and allowing us to provide only a qualitative comparison.
To bypass this issue, in this study we present a homogeneous and self-consistent chemical analysis of high-resolution spectra for red giant branch (RGB) stars in LMC, Sgr and MW, with the twofold aim of comparing the chemical composition of LMC and Sgr, keeping the MW abundance pattern as a reference. This study is restricted to the dominant stellar components of the two galaxies, therefore stars with [Fe/H] > -1.0 dex. In particular, we measured chemical abundances for the main groups of elements (light, alpha, iron-peak, neutron-capture elements) to estimate the role played to their chemical evolution by massive stars, exploding either as SNe II or more energetic HNe, degenerate binary systems, exploding as SNe Ia and AGB stars.

3.2 Spectroscopic datasets

This work presents the homogeneous chemical analysis of three samples of high-resolution spectra collected with the optical spectrograph UVES-FLAMES (Pasquini et al., 2002) mounted at the Very Large Telescope of the European Southern Observatory*. The observations have been performed adopting the Red Arm 580 UVES setup, with a spectral resolution of 47000 and a spectral coverage between about 4800 and 6800 Å. All the spectra have been reduced with the dedicated ESO pipelines†, including bias subtraction, flat-fielding, wavelength calibration, spectral extraction and order merging. For each target the individual exposures have been sky-subtracted using the spectra of some close sky regions observed in the same exposure of the science targets.

- *LMC dataset* — It includes 30 RGB stars belonging to the LMC. Eleven of these stars have been originally selected as possible member stars of some LMC GCs but they revealed to be LMC field stars according to their radial velocity (RV) and metallicity (both discrepant with respect to those of the close GC). The spectra of the other stars have been retrieved from the ESO archive, selecting UVES-FLAMES observations pointed toward the LMC and considering only giant stars with signal-to-noise ratio (SNR) per pixel larger than ∼20 and with RVs between +170 and +380 $\mathrm{km\,s^{-1}}$ that is the range of RVs of the LMC stars (Zhao et al., 2003; Carrera et al., 2008a). The LMC spectra have SNR ranging from ∼20 to ∼60 at 6000 Å. The final sample is composed by stars located in different regions of the galaxy, distributed between $\sim 0.5°$ to $\sim 5°$ from the LMC center (van der Marel, 2001). No significant metallicity gradient is expected among the LMC stars within this distance from the center because the mean metallicity of the LMC field stars remains constant within 6° from the LMC center (Carrera et al., 2011).

- *Sgr dataset* — This dataset includes UVES-FLAMES spectra of 14 stars belonging to the upper RGB of the main body of Sgr. 12 of these stars have been already discussed by Monaco et al. (2005) that, however, provide only the abundances of Fe, Mg, Ca and Ti, while the remaining two stars are from the UVES-FLAMES sample by Carretta et al. (2010b). The study of Monaco et al. (2005) included other three RGB stars with [Fe/H] between – 1.5 and – 1.1 dex, all located within 3.2° from M 54 center but only the most metal-poor considered as likely member of M 54. Our chemical analysis, however, suggests that

*Based on observations collected under programs 071.B-0146, 072.B-0293, 072.D-0342, 074.D-0369, 076.D-0381, 078.B-0323, 080.D-0368, 081.D-0286,084.D-0933, 092.D-0244, 188.B-3002, 193.B-0936.

†http://www.eso.org/sci/software/pipelines/

these three stars are likely members of M 54, in virtue of their strong enhancement of Na and Al abundances typical of second-generation stars observed in globular cluster-like systems (Bastian & Lardo, 2018). Therefore we exclude these stars from our sample, focusing only on the metal-rich ([Fe/H] >-1.0 dex) component of Sgr.

- *MW dataset* — We defined a reference sample of 14 giant/sub-giant MW stars selected from Soubiran et al. (2016) and Smiljanic et al. (2016) and covering the same range of metallicity of the LMC/Sgr targets. The stars belong both to thin and thick disk of the Galaxy, and they have been selected in order to have observations with the Red Arm 580 UVES setup available in the ESO archive and with low color excess (E(B-V) $<$ 0.2 mag).

We highlight that the LMC and Sgr samples include the best spectra, in terms of SNR and spectral resolution, available in the ESO archive for these two galaxies but they cannot be considered as fully representative of the metallicity distributions of these galaxies. In fact, the LMC sample has been built with stars from different programs and in most cases selected as candidate cluster members. The Sgr stars by Monaco et al. (2005) have been selected along the reddest side of the Sgr RGB in order to maximize the detection of Sgr member stars, hence privileging the most metal-rich stars. The fact that the stars in our Sgr sample have metallicities on average higher than that of the LMC stars (see Section 3.5) is most likely due to this bias and does not reflect a real difference in the metallicity distributions. We are aware that the samples we are using are small and not fully representative of the complexity of the three galaxies. Currently, a complete chemical screening based on high-resolution spectra can be performed on small samples but a fully homogeneous comparison of the chemical abundances of different elements in these three galaxies is a crucial starting point also for future observations.

3.3 Atmospheric parameters

As a first step, effective temperatures (T_{eff}) and surface gravities (log g) for the observed targets have been derived by using the early third data release of the ESA/*Gaia* mission (Gaia Collaboration et al., 2016, 2021) and the near-infrared 2MASS survey (Skrutskie et al., 2006).

3.3.1 *Gaia* eDR3 photometric parameters

T_{eff} have been calculated by using the $(BP-RP)_0$ -T_{eff} transformation provided by Mucciarelli & Bellazzini (2020) and based on the infrared flux method T_{eff} estimated by González Hernández & Bonifacio (2009). The transformation was calibrated on

Gaia eDR2 data, but it remains valid also for the new data release. The (BP-RP) colors have been corrected for extinction with an iterative procedure following the scheme proposed by Gaia Collaboration et al. (2018b). The color excess adopted for the Sgr targets is E(B-V) = 0.14 ± 0.03 mag (Layden & Sarajedini, 2000). For the LMC targets we used the reddening maps by Skowron et al. (2021). Finally, for the MW sample color excesses are from Schlafly & Finkbeiner (2011). Because color-T_{eff} relations derived by Mucciarelli & Bellazzini (2020) have a dependence from the stellar metallicity, first we derived T_{eff} adopting [Fe/H] = − 0.5 dex for all the stars (a reasonable value for the LMC/Sgr dominant stellar populations), and subsequently we refined T_{eff} adopting for any star the appropriate metallicity obtained from the chemical analysis.

log g have been calculated by adopting the photometric T_{eff} described above, a stellar mass of 1 $M_{\odot}$ (a representative value for the stellar mass of stars belonging to the main LMC and Sgr stellar populations)[‡] and the G-band bolometric corrections computed according to Andrae et al. (2018). To transform apparent magnitudes in absolute magnitudes, we adopted the distance modulus of $(m-M)_0 = 17.10 \pm 0.15$ mag for Sgr (Monaco et al., 2004b) and $(m-M)_0 = 18.50 \pm 0.02$ mag for LMC (Alves, 2004). For the MW stars, their distances have been derived from *Gaia* eDR3 parallaxes corrected by the offset (+0.029 mas) provided by Gaia Collaboration et al. (2018c). Only for one star in the MW sample the ratio between parallax and its uncertainty is lower than 10, indicating that the distance errors are not symmetrical (Bailer-Jones, 2015). According to the typical parallax errors, the derived distance errors are of the order of 0.10 pc.

3.3.2 2MASS/SofI photometric parameters

For most of the targets we adopted the near-infrared photometry provided by the 2MASS survey but for the LMC targets observed close to globular clusters, for which we used our own SofI@NTT photometry (that is more precise than 2MASS photometry thanks to the higher spatial resolution) calibrated onto 2MASS photometric system. T_{eff} have been obtained using the $(J-K)_0$-T_{eff} relation provided by González Hernández & Bonifacio (2009) and defined onto 2MASS photometric system, and adopting the same color excesses discussed above. For log g the only difference with respect to the procedure based on the *Gaia* eDR3 photometry is the computation of the K-band bolometric corrections following the prescriptions by Buzzoni et al. (2010).

[‡]The precise value of the adopted stellar mass does not significantly affect the derived log g because a variation of $+1 M_{\odot}$ leads to a variation of +0.3 in log g.

3.3.3 Comparison between *Gaia* eDR3 and 2MASS/SofI photometric parameters

The two sets of parameters are in good agreement for Sgr and MW stars. For the MW targets the mean differences between 2MASS and *Gaia* eDR3 parameters are – 136 ± 40 K (σ = 150 K) and – 0.01 ± 0.02 (σ = 0.09) respectively for T_{eff} and log g, while for Sgr targets are – 89 ± 20 K (σ = 72 K) and – 0.050 ± 0.006 (σ = 0.02). Instead, for the LMC targets the mean differences are – 149 ± 74 K (σ = 405 K) and –0.13 ± 0.06 K (σ = 0.31 K). Applying a 3-σ rejection, the mean difference between T_{eff} from 2MASS and *Gaia* eDR3 decreases down to –100 ± 58 K (σ = 310 K) but still with a significant scatter.

3.3.4 Spectroscopic parameters

An additional clue to validate the photometric parameters (and understand which set of parameters is more correct) is to use the standard spectroscopic constraints, namely, the excitation equilibrium to set T_{eff} (all the Fe I lines provide within the uncertainties the same abundances regardless of the excitation potential χ) and the ionization equilibrium to set log g (neutral and single ionized Fe lines provide within the uncertainties the same average abundance). As demonstrated by Mucciarelli & Bellazzini (2020), the spectroscopic parameters derived following this approach well agree with those derived from the photometry for [Fe/H] > – 1.5 dex, while at lower metallicities the spectroscopic parameters are systematically biased and they should be avoided (or appropriately corrected following the relations by Mucciarelli & Bellazzini, 2020). All the stars discussed in this work have [Fe/H] > – 1.1 dex, hence the spectroscopic method can be used to derive the parameters or to check the photometric ones. Therefore, correct parameters should provide null (within the uncertainties) values for both the slope between the Fe I abundance and χ (σ_χ) and the difference between the average Fe I and Fe II abundances (ΔFe).

T_{eff} from *Gaia* eDR3 and 2MASS photometries provide values of σ_χ that are null (within ±1σ) for almost all the MW and Sgr targets, indicating that the two photometric T_{eff} are reliable. For the LMC stars, T_{eff} from *Gaia* eDR3 photometry are higher than the 2MASS T_{eff} by about 200-250 K and providing significant values of σ_χ (at a level of 3-4 σ or more), at variance to 2MASS T_{eff} that have σ_χ null at a level of 1-2 σ. This difference with the spectroscopic T_{eff} is found also when photometric T_{eff} are estimated adopting the recent relation provided by Casagrande et al. (2021). This suggests that the *Gaia* eDR3 T_{eff} are over-estimated, for the LMC targets only. We attribute this different behavior to the high stellar crowding conditions in the LMC, leading to possible problems in the background subtraction for LMC stars.

We decide to use spectroscopic parameters for the targets in all the three galax-

ies, necessary especially for LMC targets due to the issues with the *Gaia* eDR3 photometry and the large uncertainties in the 2MASS photometry. In this way we guarantee a homogeneous approach in the determination of the atmospheric parameters for the three samples.
An additional hurdle in the spectroscopic determination of the stellar parameters arises from the fact that in giant stars with T_{eff} < 4200 K, Fe II lines are more sensitive to T_{eff} than Fe I lines and ΔFe is more sensitive to T_{eff} rather than to log g . Therefore, the usual approach to derive T_{eff} from excitation equilibrium and log g from ionization equilibrium should be revised, because ΔFe can be cancelled or reduced mainly with small changes in T_{eff} (without significant changes in σ_χ) and not with large variations in log g. Starting from the photometric parameters, we changed T_{eff} and log g in order to reduce the large ΔFe observed in some stars and to have simultaneously a value of σ_χ null within $\pm 1\sigma$.

Finally, the microturbulent velocities (v_t) have been determined by minimizing the slope between the abundances from Fe I lines and the reduced equivalent widths.

The final atmospheric parameters are listed in Table 3.1, together with the coordinates, the 2MASS/SofI and *Gaia* eDR3 photometry, the color excess and the measured metallicity.

3.4 Chemical analysis

The lines used to derive the chemical abundances have been selected by comparing the observed spectra with synthetic spectra calculated with the code `SYNTHE` (Kurucz, 2005) in order to evaluate the level of blending for each transition. The synthetic spectra have been calculated using the atomic and molecular data listed in the Kurucz/Castelli linelists[§] and convoluted with a Gaussian profile in order to reproduce the observed broadening. Model atmospheres have been calculated for any star with the code `ATLAS9` (Kurucz, 1993, 2005) and assuming the stellar parameters derived from the *Gaia* eDR3 (for Sgr and MW) or 2MASS/SofI (for LMC) photometry. Initially we assumed a metallicity of [Fe/H] = − 0.5 dex for all the targets. Each linelist has been subsequently refined according to the metallicity and the stellar parameters obtained from the chemical analysis.

The final number of lines used to derive the abundances change star by star depending on the analysed species: FeI (∼ 150), FeII (∼ 15), O (∼ 1), Na (∼ 4), Mg (∼ 3), Al (∼ 2), Si (∼ 10), Ca (∼ 10), ScII (∼ 7), Ti (∼ 50), V (∼ 6), Cr (∼ 10), Mn (∼ 5), Co (∼ 5), Ni (∼ 40), Cu (∼ 1), Zn (∼ 1), YII (∼ 5), Zr (∼ 3), BaII (∼ 2), LaII (∼ 1), NdII (∼ 10), EuII (∼ 1).

Chemical abundances for species with unblended lines (Fe, Na, Al, Ca, Ti, Si, Cr,

[§]http://wwwuser.oats.inaf.it/castelli/linelists.html

Table 3.1: Main information about the stellar targets.

ID	Ra (Degrees)	Dec (Degrees)	J (mag)	K (mag)	G (mag)	BP (mag)	RP (mag)	E(B-V) (mag)	T_{eff} (K)	log g	v_t (km/s)	[Fe/H] (dex)
LMC												
NGC1754_248	73.58459	-70.43408	14.67	13.72	16.77	17.52	15.87	0.093	4030	1.00	1.5	-0.53
NGC1786_2191	74.80183	-67.76463	13.70	12.95	15.53	16.16	14.76	0.074	4400	1.60	1.7	-0.29
NGC1786_569	74.82006	-67.74430	14.76	13.88	16.68	17.40	15.85	0.068	4200	1.25	1.7	-0.50
NGC1835_1295	76.28288	-69.39264	14.19	13.36	16.11	16.66	15.21	0.069	4200	0.85	1.7	-0.49
NGC1835_1713	76.25366	-69.39896	14.12	13.25	16.07	16.73	15.21	0.069	4090	0.80	1.6	-0.58
NGC1898_2322	79.16116	-69.65028	14.27	13.29	16.43	17.05	15.42	0.048	3920	0.80	1.5	-0.43
NGC1978_24	82.19133	-66.24008	13.82	12.75	18.27	16.99	15.98	0.052	3960	0.60	1.7	-0.56
NGC2108_382	86.00623	-69.18082	14.18	13.10	16.33	17.13	15.38	0.132	3920	0.70	2.0	-0.55
NGC2108_718	85.96358	-69.19105	14.18	13.16	16.23	17.05	15.35	0.149	3930	0.75	2.1	-0.57
NGC2210_1087	92.96237	-69.13304	13.78	12.93	15.79	16.53	14.96	0.062	4100	1.20	1.8	-0.52
2MASS J06112427-6913117	92.85120	-69.21990	14.33	13.48	16.36	17.12	15.48	0.074	4090	0.90	2.1	-0.98
2MASS J06120862-6911482	93.03606	-69.19669	14.40	13.38	16.38	17.13	15.55	0.077	4110	0.90	1.8	-0.91
2MASS J06113433-6904510	92.89313	-69.08083	14.44	13.57	16.34	17.08	15.51	0.060	4100	0.95	1.7	-0.56
2MASS J06100373-6902344	92.51558	-69.04289	14.49	13.57	16.44	17.20	15.59	0.058	4120	1.05	1.6	-0.62
2MASS J06122296-6908094	93.09576	-69.13594	14.50	13.63	16.33	17.00	15.55	0.062	4500	1.50	1.7	-0.95
2MASS J06092022-6908398	92.33421	-69.14439	14.53	13.50	16.58	17.40	15.71	0.065	4080	0.90	1.7	-0.45
2MASS J06103285-6906230	92.63706	-69.10633	14.53	13.83	16.53	17.11	15.67	0.064	4540	1.60	1.8	-0.33
2MASS J06122229-6913396	93.09298	-69.22767	14.55	13.56	16.65	17.42	15.77	0.071	4000	0.95	1.9	-0.69
2MASS J06114042-6905516	92.91859	-69.09769	14.56	13.69	16.61	17.37	15.75	0.060	4050	1.00	1.7	-0.75
2MASS J06110957-6920088	92.78991	-69.33578	14.58	13.64	16.53	17.26	15.70	0.076	4070	1.00	2.1	-0.63
2MASS J05244805-6945196	81.20025	-69.75546	14.59	13.58	16.72	17.14	15.68	0.063	4040	0.95	1.5	-0.84
2MASS J05235925-6945050	80.99690	-69.75140	14.73	13.86	16.78	17.57	15.90	0.049	4150	1.05	2.1	-0.35
2MASS J05225563-6938342	80.73190	-69.64287	14.78	13.96	16.77	17.29	15.88	0.036	4110	1.10	1.7	-0.26
2MASS J05242670-6946194	81.11131	-69.77203	14.87	14.01	16.87	17.65	16.02	0.046	4060	1.10	1.8	-0.36
2MASS J05225436-6951262	80.72653	-69.85732	14.88	14.24	16.97	17.61	16.06	0.091	4220	1.20	2.1	-0.57
2MASS J05244501-6944146	81.18757	-69.73737	14.96	14.15	16.88	17.64	16.07	0.064	4160	1.20	1.8	-0.72
2MASS J05235941-6944085	80.99753	-69.73572	15.00	14.51	17.07	17.67	16.29	0.049	4450	1.35	1.7	-0.43
2MASS J05224137-6937309	80.67245	-69.62527	15.13	14.16	16.94	17.55	16.14	0.030	4320	1.20	1.8	-0.58
2MASS J06143897-6947289	93.66241	-69.79135	15.51	14.63	17.29	17.96	16.53	0.072	4300	1.40	1.6	-0.33
2MASS J05224766-6943568	80.69869	-69.73249	15.57	15.19	17.07	17.50	16.35	0.053	4630	1.65	1.8	-0.33
Sgr												
2300127	283.94470	-30.59024	12.85	11.77	15.09	16.02	14.15	0.14	4010	0.80	1.7	-0.73
2300196	283.87830	-30.47219	13.37	12.34	15.67	16.61	14.72	0.14	4000	1.10	1.8	-0.30
2300215	283.82980	-30.50784	13.53	12.56	15.87	16.80	14.93	0.14	4040	1.10	1.9	-0.31
2409744	283.73282	-30.54539	13.24	12.22	15.62	16.61	14.65	0.14	4000	1.25	1.6	-0.20
3600230	283.44098	-30.43047	13.61	12.66	15.85	16.70	14.94	0.14	4100	1.30	1.6	-0.19
3600262	283.34311	-30.39651	13.72	12.73	15.93	16.82	15.01	0.14	4075	1.20	1.6	-0.29
3600302	283.43845	-30.51554	13.74	12.78	15.94	16.82	15.02	0.14	4060	1.20	1.6	-0.37
3800318	283.74289	-30.47235	13.16	12.16	15.52	16.37	14.50	0.14	3960	1.20	1.8	-0.36
3800558	283.74139	-30.44873	0.000	0.000	15.79	16.56	14.92	0.14	4265	1.30	1.5	-0.83
4214652	283.63782	-30.45532	13.22	12.25	15.37	16.23	14.48	0.14	4165	1.40	1.5	-0.27
4303773	283.50888	-30.60608	13.06	12.06	15.29	16.18	14.37	0.14	4020	1.05	1.6	-0.50
4304445	283.41928	-30.59531	13.38	12.47	15.53	16.35	14.64	0.14	4140	1.30	1.8	-0.42
4402285	283.33243	-30.62788	13.75	12.75	15.85	16.71	14.96	0.14	4125	1.30	1.5	-0.31
4408968	283.30374	-30.53438	13.93	12.94	16.06	16.94	15.17	0.14	3990	1.25	1.5	-0.08
MW												
HD749	2.90891	-49.65628	6.05	5.39	7.62	8.15	6.94	0.015	4680	2.70	1.2	-0.40
HD18293 (nuHyi)	42.61800	-75.06707	2.53	1.80	4.33	5.01	3.55	0.047	4270	2.25	1.3	0.18
HD107328	185.08612	3.31229	2.96	2.20	4.60	5.21	3.84	0.016	4550	2.45	1.8	-0.34
HD148897 (* s Her)	247.63937	20.47890	2.95	1.97	4.80	5.50	3.98	0.052	4295	1.20	1.7	-1.08
HD190056	301.08188	-32.05636	2.82	2.03	4.57	5.23	3.80	0.153	4375	2.20	1.1	-0.51
HD220009	350.08609	5.38104	2.89	1.99	4.65	5.31	3.87	0.054	4410	2.25	1.1	-0.55
GES J18242374-3302060	276.09888	-33.03495	10.11	9.42	11.77	12.35	11.04	0.164	4945	3.05	1.6	-0.02
GES J18225376-3406369	275.72394	-34.11022	10.73	10.05	12.44	13.02	11.71	0.125	4870	2.95	1.2	-0.12
GES J17560070-4139098	269.00287	-41.65274	11.08	10.45	12.94	13.48	12.12	0.204	5015	2.85	1.5	-0.27
GES J18222552-3413578	275.60632	-34.23277	11.10	10.37	12.85	13.46	12.10	0.112	4715	3.00	1.2	-0.03
GES J02561410-0029286	44.05890	-0.49131	11.49	10.90	13.13	13.60	12.41	0.055	4865	2.95	1.1	-0.71
GES J13201402-0457203	200.05844	-4.95570	12.03	11.40	13.59	14.10	12.92	0.038	4875	3.00	1.0	-0.49
GES J01203074-0056038	20.12810	-0.93438	12.30	11.56	14.02	14.62	13.28	0.029	4525	2.95	1.2	-0.25
GES J14194521-0506063	214.93840	-5.10184	12.55	11.85	14.10	14.64	13.42	0.037	4720	3.10	1.0	-0.33

Ni, Zr, Y and Nd) have been derived from the measured equivalent widths (EWs) of selected lines by using the code `GALA` (Mucciarelli et al., 2013).

EWs have been measured with `DAOSPEC` (Stetson & Pancino, 2008) through the wrapper `4DAO` (Mucciarelli, 2013). A visual inspection on the fitted lines has been performed in order to identify possible lines with unsatisfactory fit. For these few lines (less than 1% of the total) the EWs have been re-measured using the `IRAF` task *splot*.

For the species for which only blended lines (O, Sc, V, Mn, Co, Cu, Ba, La, Eu) or transitions located in noisy/complex spectral regions (Mg, Zn) are available, the chemical abundances have been derived with our own code `SALVADOR` that performs a χ^2-minimization between the observed line and a grid of suitable synthetic spectra calculated on the fly using the code `SYNTHE` and varying only the abundance of the corresponding element.

Atomic data (excitation potential χ, log gf, hyperfine/isotopic splitting and damping constants) for the used lines are from the Kurucz/Castelli database, improved for some specific transitions with more recent or more accurate data (see Mucciarelli et al., 2017a, for some additional references). Solar reference abundances are from Grevesse & Sauval (1998) but for oxygen for which the value quoted by Caffau et al. (2011) is adopted.

In the following, we discuss in details the procedure adopted to derive chemical abundances for a few problematic species.

- *Oxygen*: only the forbidden line at 6300.3 Å is available for this element in the optical range. This spectral region is contaminated by several telluric lines. For each target we calculated a synthetic spectrum for the Earth transmission using the code *TAPAS* (Bertaux et al., 2014) and in case of contamination of the O line the observed stellar spectrum has been divided by the Earth atmosphere spectrum.
  Oxygen abundance is derived using spectral synthesis because the forbidden line is blended with a Ni line. In principle, the oxygen abundance can be sensitive to the C and N abundances because of the molecular equilibrium. However, the UVES spectra do not allow to directly measure these abundances and the assumption of specific C and N abundances for mixed RGB stars is sensitive to metallicity and stellar mass. We thus adopted solar-scaled C and N abundances but we checked how O abundance changes for different assumptions of C and N abundances. Indeed, according to the C and N abundances measured for RGB stars brighter than the RGB Bump in these galaxies (see, e.g., Smith et al. (2002) for the LMC, Hasselquist et al. (2017) for Sgr and Gratton et al. (2000) for MW), [C/Fe] is depleted and [N/Fe] is enhanced. Fig. 3.1 shows for a representative target star the variation of [O/H] as a function of [C/Fe] depletion and corresponding [N/Fe] enhancement. [O/H] is poorly dependent on [N/Fe], while a mild dependence with [C/Fe] is found. In particular a [C/Fe] depletion (and a corresponding enhancement of [N/Fe]) by 0.5 dex decreases [O/H] by $\sim$ 0.1 dex.

- *Magnesium*: in the optical range the available Mg lines are those at 5528 and 5711 Å and the triplet at 6318-6319 Å . The first line is dominated by huge pressure-broadening wings, therefore excluded from our linelist. The second line is often used in chemical analyses of giant stars. On the other hand, this line is heavily saturated (and often insensitive to the Mg abundance) at [Fe/H] $> -$ 1.0 dex and low $T_{\rm eff}$ (<4500 K). In Fig. 3.2 we show some sets of synthetic spectra around the Mg line at 5711 Å and the Mg triplet at 6318-6319 Å for a representative giant star considering three different metallicity ([Fe/H] = $-$ 1.0, $-$ 0.5, + 0.0 dex). The line at 5711 Å becomes more saturated increasing the metallicity and the Mg abundance, becoming totally

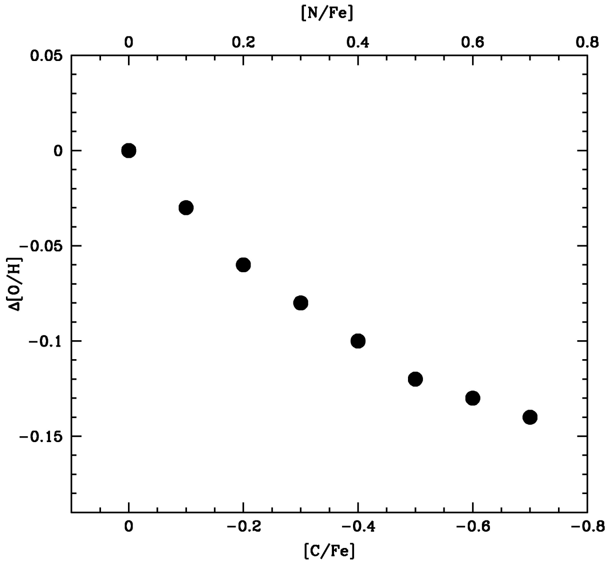

Figure 3.1: Variation of [O/H] as a function of the adopted [C/Fe] and [N/Fe] for a representative star of our sample.

insensitive to the abundance variations approaching solar metallicities. Instead, the weaker lines at 6318-19 Å are still sensitive to the Mg abundance until [Fe/H] $\sim$ 0.0 dex. Therefore, we suggest to avoid the use of the Mg line at 5711 Å in metal-rich giant stars and consider with caution abundances derived from this transition.
Only in a few targets (generally with [Fe/H] $<$ – 0.9/– 0.8 dex) the Mg line at 5711 Å is still sensitive to the abundance and it can be safely used. For all the other stars Mg abundances have been derived from the lines at 6318-6319 Å using spectral synthesis because these transitions are located on the red wing of a broad auto-ionization Ca line that affects the continuum location.

- *Sodium*: the two Na doublets used in this work (at 5682-5688 Å and 6154-6160 Å) are both affected by departures from local thermodynamic equilibrium. We applied the suitable NLTE corrections for each line by Lind et al. (2011), of the order of about – 0.15 dex for the first doublet and about – 0.05 dex for the second one.

- *Copper*: the only available line is that at 5205.5 Å (the other optical Cu line, at 5782 Å lies in the gap between the two chips of the 580 setup). At the metallicities/temperatures of our targets, the line is already on the flat part of the curve of growth and basically insensitive to the abundance. Hence, we exclude the abundances of Cu from our analysis and we discourage to use this Cu line for metal-rich giant stars similar to those analysed here.

- *Barium*: three Ba II lines are available in the spectra, located at 5853.7, 6141.7 and 6496.9 Å . The latter transition provides abundances systematically higher than the other two lines for all the targets. We check the atomic parameters of the three BaII lines on the solar-flux spectrum by Neckel & Labs (1984), and the line 6496.9 Å provides Ba abundance 0.2 dex higher than the other lines, therefore it has been excluded.

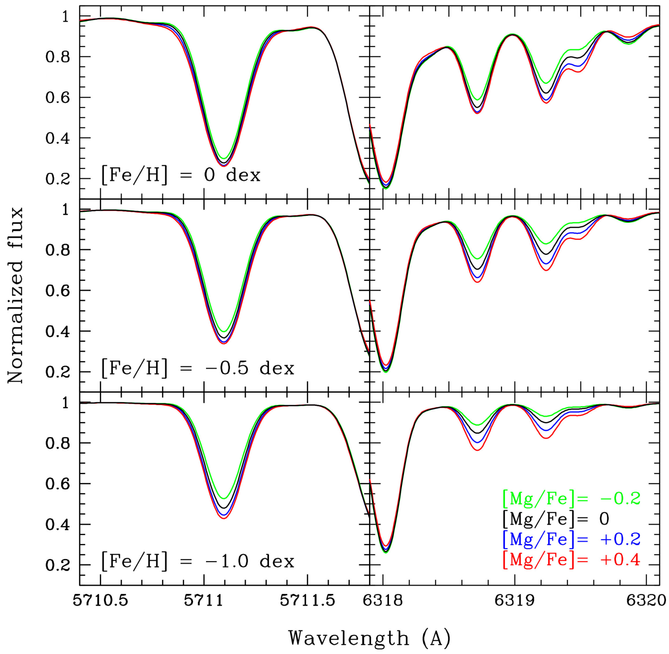

Figure 3.2: Synthetic spectra calculated for a representative giant star with T_{eff} = 4200 K, log g = 1.00 and v_t = 2.00 km/s at three different metallicities ([Fe/H]=—1.0,–0.5,+0.0 dex, lower, middle and upper panels, respectively), around the Mg line at 5711 Å and the Mg triplet at 6318-19 Å (left and right panels, respectively). For each metallicity, synthetic spectra have been computed with different Mg abundances, namely [Mg/Fe]=–0.2 (green lines), 0.0 (black lines), +0.2 (blue lines) and +0.4 dex (red lines).

3.4.1 Error Estimates

Abundance uncertainties have been computed by summing in quadrature the error related to the measurement process and those arising from the adopted atmospheric parameters. The errors due to the measurement have been derived according to the method adopted to obtain the abundances.

Internal errors relative to the EW measurements have been estimated as the line-to-line scatter divided by the root mean square of the number of used lines. For the elements for which less than 4 lines are available (namely Al, Na, Y and Zr) we adopt the standard deviation from Fe I lines as more realistic estimate of the

line-to-line scatter.
O, Mg, Sc, Co, V, Mn, Zn, Ba, La and Eu are the elements whose abundances are derived from spectral synthesis. The uncertainties of their measurement have been estimated by resorting to Monte Carlo simulation. We created synthetic spectra with representative values for the atmospheric parameters of the analysed stars, and we injected Poisson noise into them, according to the SNR of the observed spectra. For each line, 200 *noisy* spectra have been generated and the abundance derived adopting the same procedure used for observed spectra. Finally we calculated the internal measurement error as the standard deviation of the elemental abundance values derived from the 200 simulations.

The uncertainties arising from the atmospheric parameters have been computed by varying one only parameter at a time, keeping the other ones fixed, and deriving the abundance variation. This method provides a conservative estimate of the uncertainties because it does not take into account the correlations among the parameters. The applied variations are of 100 K, 0.1 dex, 0.1 km/s for $T_{\rm eff}$ log g and v_t, respectively. The variations correspond to the typical uncertainties of the atmospheric parameters.

Since our results are expressed as abundance ratios, also the uncertainties in the Fe abundance have been taken into account. When an abundance ratio [X/Fe]=[X/H]-[Fe/H] is considered, the uncertainties arising from atmospheric parameters partially cancel out because metallic lines of different species but the same ionization stage respond in a similar way to variations in these parameters. Therefore the final errors in [Fe/H] and [X/Fe] abundance ratios are calculated as follows:

$$\sigma_{[Fe/H]} = \sqrt{\frac{\sigma^2_{Fe}}{N_{Fe}} + (\delta^{\rm T_{eff}}_{Fe})^2 + (\delta^{log\ g}_{Fe})^2 + (\delta^{\eta}_{Fe})^2} \tag{3.1}$$

$$\sigma_{[X/Fe]} = \sqrt{\frac{\sigma^2_{X}}{N_{X}} + \frac{\sigma^2_{Fe}}{N_{Fe}} + (\delta^{\rm T_{eff}}_{X} - \delta^{\rm T_{eff}}_{Fe})^2 + (\delta^{log\ g}_{X} - \delta^{log\ g}_{Fe})^2 + (\delta^{\eta}_{X} - \delta^{\eta}_{Fe})^2} \tag{3.2}$$

where $\sigma_{X,Fe}$ is the dispersion around the mean of the chemical abundances, $N_{X,Fe}$ is the number of lines used to derive the abundances and $\delta^{i}_{X,Fe}$ are the abundance variations obtained modifying the atmospheric parameter *i*.

3.5 Results and discussion

This work provides for the first time a fully self-consistent comparison of the abundances for the main groups of elements (light-, α-, iron-peak, neutron-capture elements) among the metal-rich stars in LMC, Sgr and MW. Although these samples cannot be considered as fully representative of the metallicity distributions of the parent galaxies, in particular because of some selection bias in their definition (see Section 3.2), this work has the main advantage to remove most of the systematics (i.e. solar abundances, atomic data, model atmospheres), affecting the comparison of their abundances.

Tables 3.2-3.4 list the measured values of the elemental abundances with their error. In Figs. 3.3-3.8 we show the results obtained for the three samples, together with the abundances in Galactic field stars from the literature (see caption of Figs. 3.3-3.8 for references). Only for the works that do not adopt solar values determined with their own linelist, we re-scaled their abundances to our solar reference values. The latter measures are shown as a sanity check to verify that our heterogeneous sample of MW stars reproduces the main MW chemical patterns. Also, the use of both dwarf and giant stars and of different assumptions in the chemical analyses (i.e. atomic data, solar reference values, model atmospheres, among others) could hamper the direct comparison with the LMC and Sgr abundances derived here. The comparison between our abundances and those from the literature is satisfactory for almost all the elements, while we found offsets of about 0.1-0.2 dex for Na, Al, Co, V and Eu. These differences are mainly explained by the different transitions, atomic parameters and (in the case of Na) NLTE corrections adopted by different authors. The existence of these offsets enforces the importance of a homogeneous analysis for all the stars.

In this section we also compare our results with the abundances available in literature, i.e. Pompéia et al. (2008), Lapenna et al. (2012), Van der Swaelmen et al. (2013), Nidever et al. (2020) for the LMC and Monaco et al. (2005), Sbordone et al. (2007), Carretta et al. (2010b) and Mucciarelli et al. (2017b) for Sgr.

3.5.1 Light elements: Na and Al

Na and Al are mainly synthesized in massive stars through the hydrostatic C and Ne burning and only a small amount is produced during the H burning through the NeNa and MgAl cycles in AGB stars (Woosley & Weaver, 1995). Stars in the LMC and Sgr have similar [Na/Fe] and [Al/Fe] abundance ratios that are significantly lower (by 0.5 dex) than those measured in the MW sample (Fig. 3.3). These low values could suggest that the contribution by massive stars is similar in the two galaxies but significantly lower than that in the MW.

Low [Al/Fe] and [Na/Fe] abundances have been measured in Sgr stars also by Sbordone et al. (2007) and McWilliam et al. (2013), even if there are an offset of about -0.2 dex for Al and +0.3 dex for Na with respect to our values that are likely attributable to the different log gf (as in the case of Al) or NLTE corrections (as in the case of Na). Instead, the Sgr stars analysed by Carretta et al. (2010b)

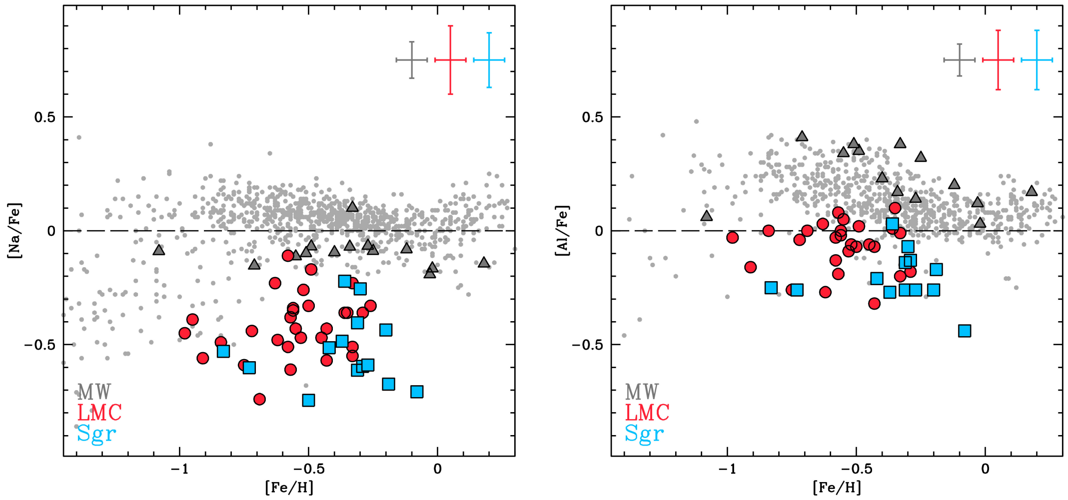

Figure 3.3: Behavior of the light elements [Na/Fe] and [Al/Fe] abundance ratios (left and right panel, respectively) as a function of [Fe/H] for LMC sample (red circles), Sgr sample (light blue squares) and MW sample (gray triangles). Abundances of Galactic stars from the literature are also plotted as a reference: Edvardsson et al. (1993); Fulbright (2000); Reddy et al. (2003, 2006); Bensby et al. (2005) for both the elements, and Stephens & Boesgaard (2002); Gratton et al. (2003) for Na.

exhibit higher [Na/Fe] values. This difference can be only partially explained by the different NLTE corrections for the Na lines.

3.5.2 α-elements

As explained in Section 1.1.1, the α-elements are mainly produced in SNe II, with only a minor component produced in SNe Ia that produce, instead, significant amounts of Fe on long timescales. Therefore, [α/Fe] ratios are used to trace the time-scales of the star formation in a given environment. We grouped the measured α-elements according to their formation mechanism: hydrostatic elements (O and Mg) that are synthesized mainly in stars with masses larger than 30-35 $M_{\odot}$, and explosive elements (Si, Ca and Ti) that are synthesized in stars with masses of 15-25 $M_{\odot}$.

Fig. 3.4 shows the behavior of the average abundance ratios of the two groups as a function of [Fe/H]. For both groups of elements, LMC and Sgr agree each other but with values of [α/Fe] lower than those measured in MW stars of similar [Fe/H]. This difference is more pronounced for the hydrostatic α-elements. Also, the hydrostatic α-elements show a clear decrease with increasing [Fe/H], reaching sub-solar values at [Fe/H] > -0.6 dex, at variance with the explosive elements that display a less pronounced decrease by increasing [Fe/H]. It is worth noticing that most of the Sgr stars have [Fe/H] > -0.5 dex and only two stars with [Fe/H] between –1.0 dex and

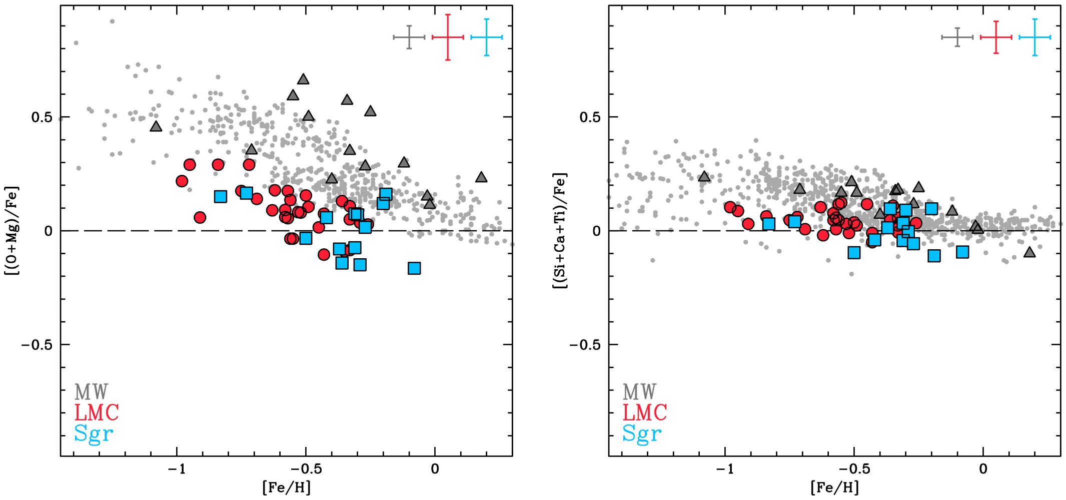

Figure 3.4: Behavior of the hydrostatic and explosive [α/Fe] abundance ratio (left and right panel, respectively) as a function of [Fe/H]. Same symbols of Fig. 3.3. The MW literature data for both groups of elements are from Edvardsson et al. (1993); Gratton et al. (2003); Reddy et al. (2003, 2006); Bensby et al. (2005), while for the explosive elements additional data are from Fulbright (2000); Stephens & Boesgaard (2002); Barklem et al. (2005).

–0.5 dex are in the Sgr sample. However, the abundance ratios for these two stars well match with those of the LMC stars of similar [Fe/H].

The low [α/Fe] ratios measured in LMC/Sgr point out that these stars formed from a gas already enriched by SNe Ia at [Fe/H] > -1 dex. Also, the larger difference between LMC/Sgr and MW measured for hydrostatic α-elements is consistent with galaxies having a lower number of stars more massive than $\sim$30 $M_{\odot}$, for instance galaxies with a lower star formation efficiency (like LMC and Sgr).
Comparing our abundances with the literature, no significant differences are found between the α abundances in the LMC sample and the ones derived by Pompéia et al. (2008), Lapenna et al. (2012) and Van der Swaelmen et al. (2013). Concerning Sgr, we find a general good agreement with the Mg, Ca and Ti abundances by Monaco et al. (2005) and with the Mg and Ca abundances by Mucciarelli et al. (2017b). A nice agreement is found also with the abundances by Sbordone et al. (2007) but Ti that is lower than our values by $\sim$0.3/0.4 dex, likely due to the large sensitivity of the Ti abundance to $T_{\rm eff}$. Our O, Si and Ti abundances match those by Carretta et al. (2010b), while their Mg are higher than ours by $\sim$0.3 dex, likely due to their selected Mg lines (see Section 3.4). Finally, we highlight the different behavior found by Nidever et al. (2020) that measured Mg, Si and Ca abundances from near-infrared *APOGEE* spectra of LMC giant stars. In their sample the [α/Fe] ratios show a flat run with [Fe/H], compatible with our result for Si and Ca but clearly different concerning Mg. The O and Mg abundances in our MW sample are

slightly higher by ∼0.15 dex than the literature data. We ascribe this difference to the different O and Mg lines used in the literature that are mainly based on dwarf stars. Because O and Mg abundances are derived by a few lines in both dwarf and giant stars, differences in the used diagnostics (in terms of the zero-point of their gf values or NLTE effects) are particularly evident for these elements. This difference between the abundances of our MW sample and the literature highlights again the importance of a homogeneous analysis.

3.5.3 Iron-peak elements

The iron-peak elements are the heaviest elements synthesized through thermonuclear reactions. They compose an heterogeneous group of elements in terms of nucleosynthesis. They form partly in massive stars, sometimes with a significant contribution by HNe (that are associated to stars more massive than ∼25-30 $M_{\odot}$ and more energetic by at least one order of magnitude with respect to normal SNe II). Not negligible amounts of Fe-peak elements can be produced also in SNe Ia (Leung & Nomoto, 2018, 2020; Lach et al., 2020). Moreover, further complicating matters, some of the iron-peak elements have a strong dependence of their yields on the metallicity (see e.g. Romano et al., 2010).

LMC and Sgr stars exhibit similar abundance patterns for all the measured iron-peak elements, as shown in Fig. 3.5.

Differences with respect to the MW stars are evident for Sc, V, Co, Ni and Zn abundances, showing in the cases of [Sc/Fe] and [Ni/Fe] a clear decrease of the abundance ratios by increasing [Fe/H]. A decreasing trend is also seen in [Zn/Fe] for the LMC sample, but the small number of Sgr stars with Zn measures prevents to properly identify a possible trend with [Fe/H].

The largest differences are observed for [V/Fe] and [Zn/Fe], whose values in LMC/Sgr stars are lower by 0.5-0.7 dex respect to MW stars of similar metallicity. In contrast, [Cr/Fe] and [Mn/Fe] show values comparable between LMC/Sgr and MW stars.

Even if the details of the nucleosynthesis of these elements are not fully known and for some of them the current evolutionary chemical models are not even able to reproduce the observed MW trends (Romano et al., 2010), the chemical patterns obtained for the three samples provide a scenario coherent with that drawn above based on the abundances of light and α-elements. In fact, a large amount of these elements is produced by massive stars, via SNe II, HNe and electron-capture SNe. The measured abundances in LMC and Sgr stars for most of the iron-peak elements are compatible with a scenario where the contribution by massive stars to the chemical enrichment of the parent galaxies is less important than in the MW. In particular, the low abundances of Zn would suggest a small or lacking contribution by stars

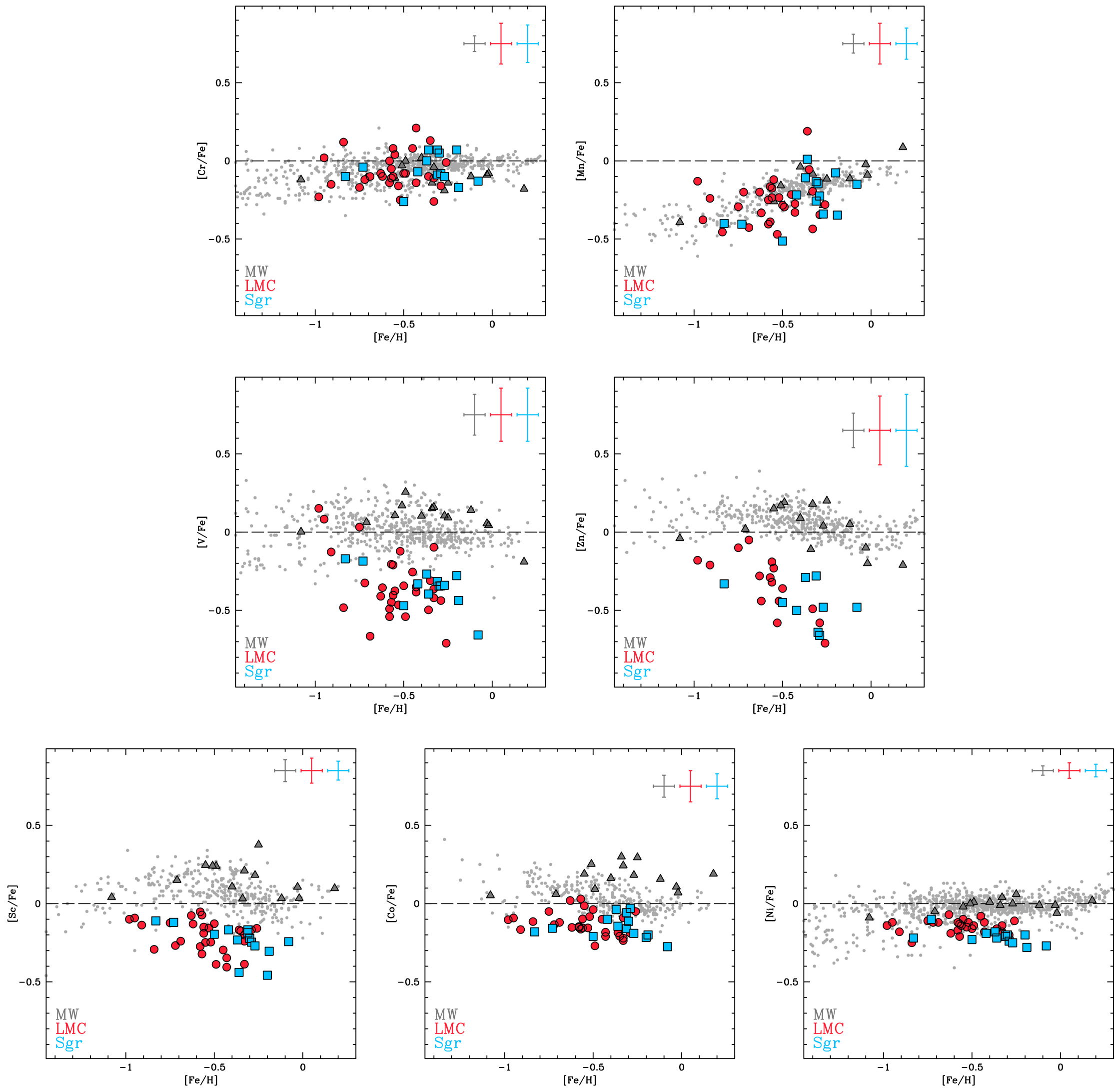

Figure 3.5: Behavior of the iron-peak [Cr/Fe], [Mn/Fe], [V/Fe], [Zn/Fe], [Co/Fe], [Ni/Fe] and [Sc/Fe] abundance ratios as a function of [Fe/H]. Same symbols of Fig. 3.3. The MW literature data are from the works of Edvardsson et al. (1993)(Ni), Fulbright (2000) (V, Cr, Ni), Stephens & Boesgaard (2002)(Cr, Ni), Gratton et al. (2003) (Sc, V, Cr, Mn, Ni, Zn), Reddy et al. (2003, 2006) (Sc, V, Cr, Mn, Co, Ni, Zn), Bensby et al. (2005)(Cr, Ni, Zn), Nissen et al. (2007)(Zn)

more massive than ~25-30 $M_{\odot}$, because this element is almost totally produced by HNe (Nomoto et al., 2013), while its production in SNe Ia is probably negligible.

As noted above, V and Zn exhibit the largest differences with respect to the MW stars with similar [Fe/H]. These abundance ratios are the most clean-cut chemical differences between LMC/Sgr and MW and in principle they could be used to distinguish, among the MW stars with [Fe/H] > -1 dex, those formed in smaller satellites that evolved similarly to the LMC/Sgr and were subsequently accreted and disrupted by the MW tidal field. Zn abundances lower than those in MW stars of similar metallicity have been measured also in Sculptor (Skúladóttir et al., 2017) and in other dwarf galaxies (Shetrone et al., 2001, 2003), but at lower metallicities than those discussed here.

3.5.4 Slow neutron-capture elements

Elements heavier than Fe are produced through neutron-capture processes on seed nuclei (Fe and iron-peak elements), and subsequent β decays (Burbidge et al., 1957). According to the rate of neutron-captures with respect to the time-scale of the β decays, we distinguish slow (s-) and rapid (r-)process elements. The s-process elements are grouped around three peaks of stability corresponding to the neutrons magic numbers (N=50, 82, 126). These elements are produced mainly by low-mass (1-3 $M_{\odot}$) AGB stars (whose yields are strongly metallicity dependent) with only a minor component produced in massive stars (see e.g. Busso et al., 1999).

We measured Y and Zr abundances among the elements belonging to the first-peak. The elements of this group are produced mainly in AGB stars with high metallicity, because the decrease of the number of neutrons per seed nucleus favors the formation of the lightest s-process elements (ls). As shown in the first two panels of Fig. 3.6, the three samples overlap each other, even if the large scatter, particularly in [Y/Fe] among the LMC and Sgr stars, makes it hard to compare these samples with the MW.

For the second peak, the heavy s-process elements (hs), we measured Ba, La (that are produced mainly through s-process) and Nd (that is produced by s-process for nearly 40% of the total, see e.g. Arlandini et al., 1999). The abundance behavior for these elements is illustrated in the corresponding panels of Fig. 3.6. Both in LMC and Sgr their abundance ratios are enhanced and higher than those measured in the MW stars, with the Sgr stars that show abundances higher than the LMC stars. The Sgr stars with [Fe/H]<–0.4 dex have [hs/Fe] compatible with those measured in LMC stars, while at higher [Fe/H] these abundance ratios increase significantly, reaching values of about +1 dex. In Fig. 3.7 we show the profile of the Zr and Ba lines in two pairs of LMC/Sgr stars with similar parameters and metallicity: the stars in the upper panel have similar Zr and Ba abundances, as demonstrated by their similar line strengths, while the the Sgr star shown in the lower panel exhibit Zr and Ba lines stronger than the those of the LMC star with similar parameters and metallicity.

The high heavy s-process element abundances measured in the most metal-rich Sgr stars seem to suggest a more significant contribution by metal-rich AGB stars in Sgr with respect to LMC. Also, LMC/Sgr stars have abundances of [hs/Fe] higher than

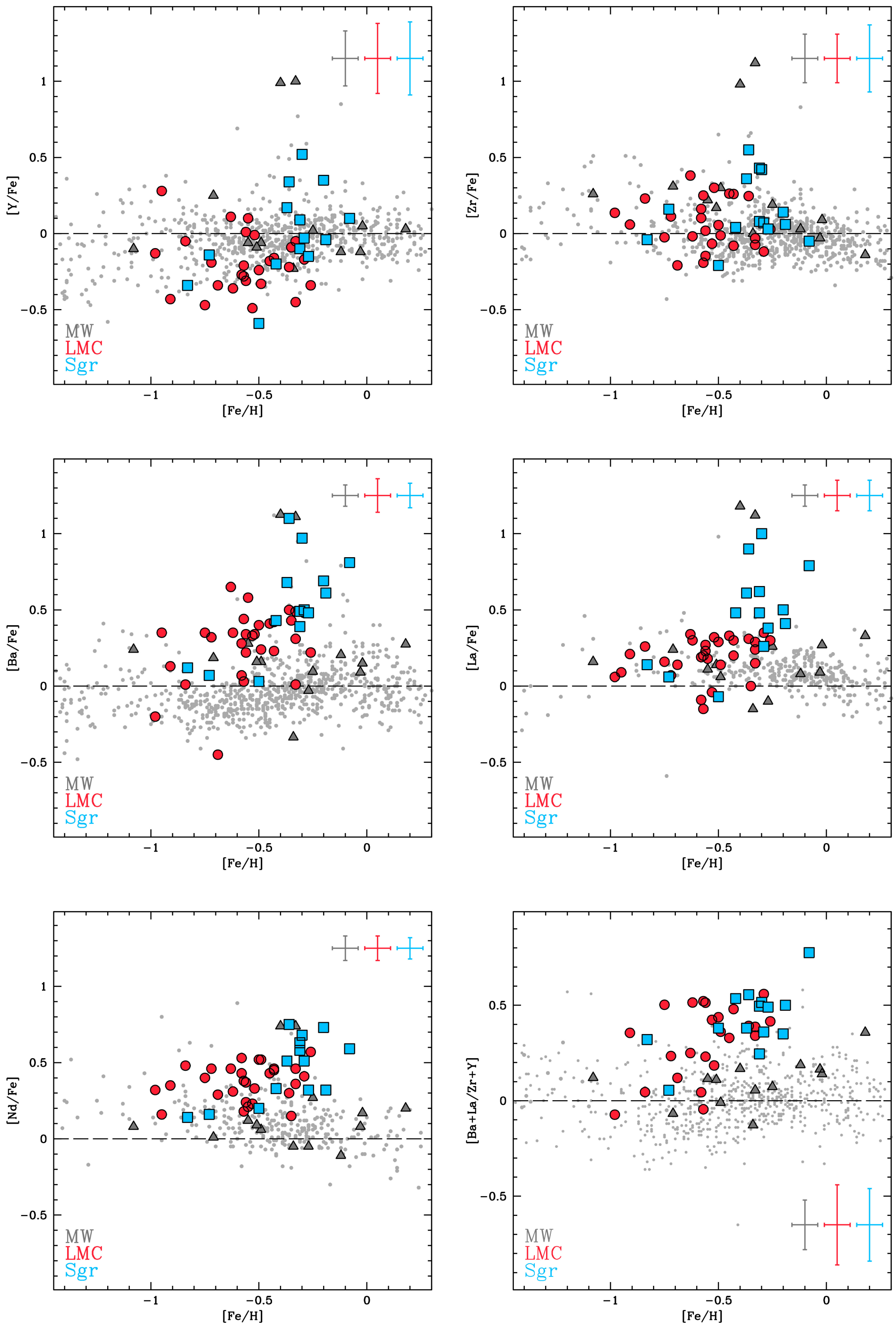

Figure 3.6: Behavior of the slow neutron-capture [Y/Fe], [Zr/Fe], [Ba/Fe], [La/Fe] and [Nd/Fe] as a function of [Fe/H]. In the last panel the comparison between ls and hs elements, where the ratio between the average value of Ba and La and the average value of Y and Zr is represented as a function of [Fe/H]. Same symbols of Fig. 3.3. The MW literature data are from Edvardsson et al. (1993, Y, Zr, Ba, Nd), Burris et al. (2000, Y, Zr, Ba, La, Nd), Fulbright (2000, Y, Zr, Ba), Stephens & Boesgaard (2002, Y, Ba), Reddy et al. (2003, Y, Zr, Ba, Nd), Reddy et al. (2006, Y, Ba, Nd), Barklem et al. (2005, Ba), Bensby et al. (2005, Y, Ba), Forsberg et al. (2019, Zr, La).

those measured in the MW, where the enhancement is moderate [¶]. Our abundances agree with those measured by Van der Swaelmen et al. (2013) for LMC stars and by Sbordone et al. (2007) for Sgr stars, despite some offsets due to the adopted atomic data.

In the last panel of Fig. 3.6 we plot the heavy-to-light s-process abundance ratios as a function of [Fe/H] in order to evaluate the relative contribution of the two groups of s-process elements that mainly arise from AGB stars of different metallicity. All the three galaxies shows an increase of this ratio by increasing [Fe/H] with a trend that is steeper in LMC and Sgr. This behaviour points out that the production of s-process elements in these two galaxies is dominated by AGB stars more metal-poor than in the MW. On the other hand, the production of heavy s-process elements is favored in less massive AGB stars, while elements of the first peak are produced in a similar amount in AGB stars regardless of their mass (see AGB models of Lugaro et al., 2012; Karakas & Lattanzio, 2014). Hence, the higher [hs/ls] ratios observed in LMC and Sgr with respect to the MW could suggest a lower contribution by the most massive AGB stars.

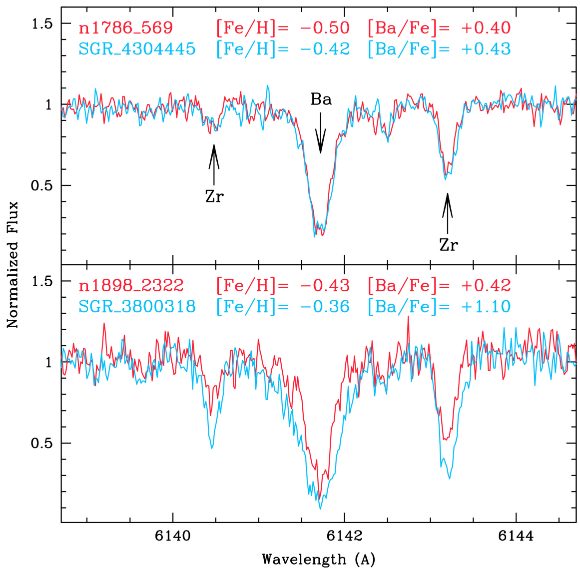

Figure 3.7: Comparison between the spectra of the two pairs of LMC and Sgr stars (red and blue lines, respectively) with similar stellar parameters and metallicities around the Ba II line at 6142 Å . The upper panel shows the comparison between two stars with similar Ba abundances (two Zr lines are also visible in the spectral range), while the lower panel shows the comparison between two stars characterized by a strong difference in both Zr and Ba abundances.

[¶]We note that in the MW sample, two stars (named HD749 and GES J14194521-0506063) are strongly enhanced in all the s-process elements abundances. They could be formed through mass transfer in a binary system. The study of the 3D motion using the information from the *Gaia* mission does not highlight anomalies in the kinematics of these stars.

3.5.5 Rapid neutron-capture elements

Rapid neutron-capture processes produce an half of the heaviest elements (see e.g. the seminal paper by Burbidge et al., 1957) but their precise sites of production are still debated, requiring neutron-rich, high energy environments. Among the possible sites, the most promising are low-mass SN II progenitors (in the range 8-10 $M_{\odot}$ see e.g. Wheeler et al., 1998), the NS mergers (Pian et al., 2017) and the collapsars (Siegel et al., 2019). We measured the abundance of Eu that is an almost pure r-process element.

As shown in the left panel of Fig. 3.8, both LMC and Sgr exhibit enhanced values of [Eu/Fe], comparable with those of the MW. The enhancement of [Eu/Fe] in LMC and Sgr in this range of metallicity has been already measured in previous works in a few stars (Bonifacio et al., 2000; Van der Swaelmen et al., 2013; McWilliam et al., 2013). A possible decrease of [Eu/Fe] by increasing [Fe/H] is visible among the LMC stars, while the same pattern is not clearly visible in Sgr. Comparable enhanced values of [Eu/Fe] in the three samples seem to suggest a similar production of r-process elements in these galaxies, in particular a similar rate of NS mergers per unit stellar mass, if NS mergers are the main contributors to the Galactic Eu abundances (see e.g. Matteucci et al., 2014).

Finally, we evaluate the abundance ratio between heavy s-process elements (considering the average of Ba and La abundances) and Eu, in order to estimate the contribution of the r-process to the production of other neutron-capture elements. As shown in the last panel of Fig. 3.8, [hs/Eu] exhibits a rapid increase by increasing [Fe/H] in all the three samples and in LMC/Sgr this increase occurs at lower metallicities that the MW. Theoretical models by Arlandini et al. (1999) and Burris et al. (2000) predict values of [Ba/Eu] of about –0.5 dex in case of pure r-process. The measured [hs/Fe] abundance ratios suggest that the role played by the r-process to the production of Ba and La decreases by increasing [Fe/H] and that in the metal-rich stars of LMC and Sgr the production of Ba and La is dominated by s-processes.

3.6 Summary

High-resolution UVES-FLAMES spectra of 30 LMC and 14 Sgr giant stars have been analysed, together with a reference sample of 14 MW giant stars selected in the same metallicity range of the LMC/Sgr stars. The three samples have been analysed with the same procedure in order to erase the main systematics of the analysis. From the homogeneous comparison we highlight differences and similarities in the chemical compositions of these three galaxies:

1. The metal-rich populations in LMC and Sgr show strong similarities in almost all the measured species, except for the heavy s-process elements Ba and La,

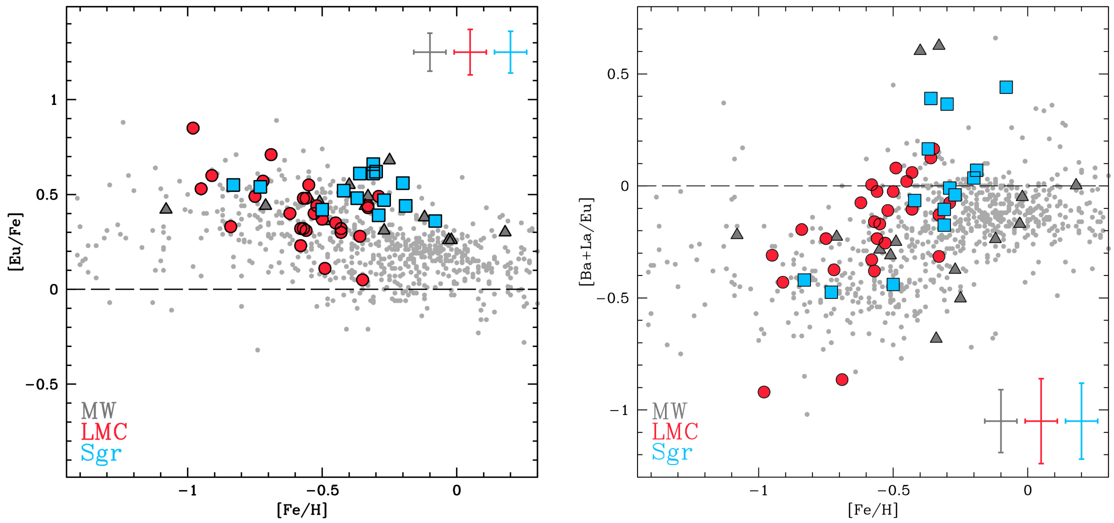

Figure 3.8: In the left panel, behavior of the [Eu/Fe] abundance ratio as a function of [Fe/H]. In the right panel, the ratio between the hs elements (average value between Ba and La abundances) and the Eu abundances, as a function of [Fe/H]. Same symbols of Fig. 3.3. The MW literature data are from Burris et al. (2000); Fulbright (2000); Reddy et al. (2003, 2006); Barklem et al. (2005); Bensby et al. (2005); Forsberg et al. (2019) for Eu.

with the stars of Sgr more enriched in both the abundance ratios with respect to LMC, suggesting a different contribution by AGB stars. Overall, their similar chemical compositions suggest similar chemical enrichment histories, coherently with a scenario where the progenitor of Sgr was a galaxy with a mass and a SFR similar to those of the LMC.

2. The comparison between LMC/Sgr and MW samples reveals that the former galaxies have different chemical abundances with respect to the MW stars for almost all the species. The abundance ratios for elements produced by massive stars exploding either as SNe II or HNe are systematically lower in LMC/Sgr with respect to the MW, pointing out that in these galaxies the contribution by massive stars to the chemical enrichment is less important. This can be explained in light of their low SFR, leading to a lower number of massive stars (poorly populating the IMF at the highest masses, see e.g. Yan et al., 2017; Jeřábková et al., 2018) and penalizing the elements produced by very massive stars. Also, the LMC and Sgr have masses comparable, as a order of magnitude, with that of Gaia-Enceladus (see Helmi, 2020), a massive dwarf galaxy that has been accreted by the MW $\sim$ 10 Gyr ago and that has contributed to built a large part of the Galactic Halo. The study of the chemical composition of these two galaxies can provide important insights to understand the chemical enrichment histories of galaxies of similar mass and star formation efficiency that have had an important role in the assembly of

the MW.

3. Among the measured elements, the most evident differences between LMC/Sgr and MW stars are measured for [V/Fe] and [Zn/Fe], where LMC/Sgr stars have abundance ratios lower than the MW stars of similar metallicity by as much as 0.5-0.7 dex. We suggest that these abundance ratios can be used to identify possible extra-galactic interlopers among the Galactic disk stars with [Fe/H]>–1.0 dex, i.e. stars accreted from LMC and Sgr or from galaxies that have experienced similar chemical enrichment histories. In other words, we suggest that [V/Fe] and [Zn/Fe] can be tools for a robust chemical tagging as powerful as the classical hydrostatic [α/Fe] ratios.

Table 3.2: LMC and Sgr chemical abundances.

ID	[Fe/H]	[FeII/H]	[Na/Fe]	[Al/Fe]	[O/Fe]	[Mg/Fe]	[Si/Fe]	[Ca/Fe]	[Ti/Fe]	[Sc/Fe]	[V/Fe]
					LMC						
NGC1754_248	-0.53±0.06	-0.56±0.22	-0.47±0.14	-0.09±0.14	0.25±0.06	-0.08±0.20	0.23±0.10	-0.03±0.13	-0.11±0.17	-0.16±0.05	-0.46±0.17
NGC1786_2191	-0.29±0.05	-0.31±0.16	-0.36±0.08	-0.18±0.08	0.14±0.06	-0.07±0.06	0.08±0.10	-0.04±0.05	-0.18±0.12	-0.17±0.07	-0.44±0.16
NGC1786_569	-0.50±0.05	-0.65±0.18	-0.33±0.11	-0.07±0.11	0.28±0.06	0.03±0.13	0.11±0.11	-0.01±0.06	0.01±0.14	-0.13±0.08	-0.34±0.16
NGC1835_1295	-0.49±0.06	-0.60±0.18	-0.17±0.15	0.02±0.15	0.14±0.08	0.07±0.27	0.13±0.11	0.10±0.07	-0.16±0.14	-0.39±0.08	-0.54±0.16
NGC1835_1713	-0.58±0.06	-0.64±0.19	-0.11±0.16	-0.13±0.16	0.06±0.08	–	0.21±0.11	0.06±0.10	-0.04±0.15	-0.27±0.14	-0.54±0.17
NGC1898_2322	-0.43±0.07	-0.42±0.26	-0.43±0.17	-0.07±0.16	0.18±0.08	-0.39±0.28	0.13±0.12	-0.07±0.11	-0.09±0.18	-0.41±0.08	-0.38±0.21
NGC1978_24	-0.56±0.05	-0.56±0.23	-0.34±0.16	-0.02±0.15	0.17±0.06	-0.24±0.19	0.14±0.10	0.13±0.17	0.08±0.17	-0.19±0.05	-0.40±0.16
NGC2108_382	-0.55±0.06	-0.52±0.24	-0.43±0.18	0.05±0.17	0.06±0.05	-0.13±0.11	0.18±0.10	0.18±0.12	0.01±0.18	-0.25±0.05	-0.37±0.19
NGC2108_718	-0.57±0.05	-0.58±0.22	-0.38±0.15	0.08±0.13	0.27±0.05	0.08±0.13	0.20±0.09	0.08±0.09	-0.11±0.18	-0.32±0.09	-0.20±0.18
NGC2210_1087	-0.52±0.05	-0.61±0.19	-0.26±0.14	-0.06±0.13	0.08±0.05	–	0.17±0.10	-0.06±0.10	-0.14±0.16	-0.25±0.06	-0.12±0.20
2MASS J06112427-6913117	-0.98±0.05	-0.99±0.18	-0.45±0.12	-0.03±0.18	0.24±0.08	0.19±0.18	0.20±0.10	0.14±0.07	-0.03±0.16	-0.10±0.08	0.15±0.18
2MASS J06120862-6911482	-0.91±0.05	-0.93±0.19	-0.56±0.10	-0.16±0.14	0.00±0.09	0.11±0.12	0.18±0.10	0.05±0.07	-0.14±0.16	-0.14±0.09	-0.13±0.17
2MASS J06113433-6904510	-0.56±0.05	-0.63±0.21	-0.35±0.12	0.00±0.11	0.22±0.05	0.05±0.16	0.24±0.11	-0.03±0.07	-0.07±0.15	-0.15±0.07	-0.21±0.16
2MASS J06100373-6902344	-0.62±0.04	-0.76±0.20	-0.48±0.12	-0.27±0.11	0.28±0.05	0.07±0.14	0.05±0.10	-0.06±0.06	-0.05±0.16	-0.13±0.07	-0.35±0.17
2MASS J06122296-6908094	-0.95±0.10	-0.94±0.12	-0.39±0.11	–	0.47±0.11	0.11±0.17	0.12±0.12	0.01±0.04	0.13±0.09	-0.09±0.12	0.08±0.12
2MASS J06092022-6908398	-0.45±0.05	-0.45±0.23	-0.47±0.19	-0.06±0.19	0.23±0.09	-0.20±0.35	0.18±0.11	0.11±0.10	0.06±0.16	-0.30±0.07	-0.25±0.18
2MASS J06103285-6906230	-0.33±0.08	-0.47±0.14	-0.23±0.10	-0.20±0.10	0.11±0.09	0.10±0.13	0.05±0.10	0.01±0.03	-0.08±0.10	-0.24±0.11	-0.10±0.13
2MASS J06122229-6913396	-0.69±0.05	-0.67±0.22	-0.74±0.21	0.00±0.03	0.14±0.06	–	0.28±0.11	-0.04±0.08	-0.22±0.17	-0.24±0.05	-0.66±0.21
2MASS J06114042-6905516	-0.75±0.04	-0.74±0.21	-0.59±0.11	-0.26±0.11	0.38±0.05	-0.03±0.13	0.13±0.10	0.08±0.10	-0.07±0.17	-0.12±0.12	0.03±0.18
2MASS J06110957-6920088	-0.63±0.04	-0.69±0.19	-0.23±0.14	0.03±0.14	0.09±0.06	–	0.24±0.10	0.11±0.11	-0.04±0.16	-0.08±0.07	-0.41±0.17
2MASS J05244805-6945196	-0.84±0.06	-0.81±0.26	-0.49±0.18	0.00±0.06	0.29±0.09	–	0.15±0.12	-0.00±0.14	0.04±0.17	-0.29±0.07	-0.48±0.19
2MASS J05235925-6945050	-0.35±0.05	-0.35±0.20	-0.36±0.21	0.10±0.21	0.11±0.10	-0.29±0.35	0.23±0.14	0.02±0.15	0.08±0.15	-0.17±0.09	-0.31±0.16
2MASS J05225563-6938342	-0.26±0.07	-0.27±0.22	-0.33±0.21	–	0.09±0.10	-0.03±0.25	0.32±0.14	-0.01±0.23	-0.21±0.17	-0.16±0.08	-0.71±0.18
2MASS J05242670-6946194	-0.36±0.05	-0.36±0.26	-0.36±0.18	0.01±0.18	0.13±0.07	–	0.18±0.12	0.01±0.10	-0.05±0.16	-0.17±0.07	-0.50±0.17
2MASS J05225436-6951262	-0.57±0.05	-0.54±0.20	-0.61±0.24	-0.19±0.23	0.26±0.10	-0.15±0.25	0.22±0.12	-0.13±0.09	-0.07±0.15	-0.07±0.09	-0.45±0.18
2MASS J05244501-6944146	-0.72±0.05	-0.82±0.22	-0.44±0.20	-0.04±0.15	0.29±0.09	–	0.22±0.14	-0.00±0.09	-0.04±0.16	-0.27±0.10	-0.32±0.19
2MASS J05235941-6944085	-0.43±0.07	-0.42±0.16	-0.57±0.15	-0.32±0.20	0.17±0.12	-0.02±0.35	0.05±0.12	-0.14±0.14	-0.06±0.12	-0.35±0.15	-0.35±0.18
2MASS J05224137-6937309	-0.58±0.07	-0.59±0.17	-0.51±0.21	-0.03±0.21	0.19±0.11	-0.00±0.25	0.15±0.12	0.02±0.13	-0.03±0.13	-0.05±0.10	-0.49±0.16
2MASS J06143897-6947289	-0.33±0.07	-0.36±0.19	-0.55±0.13	-0.01±0.17	0.05±0.11	–	0.22±0.15	-0.17±0.13	0.02±0.14	-0.20±0.08	-0.36±0.15
2MASS J05224766-6943568	-0.33±0.09	-0.33±0.13	-0.51±0.24	–	0.13±0.13	-0.30±0.21	0.23±0.12	0.04±0.10	-0.10±0.11	-0.39±0.12	-0.42±0.14
					Sgr						
2300127	-0.73±0.05	-0.77±0.21	-0.60±0.14	-0.26±0.15	0.28±0.08	0.05±0.20	0.08±0.11	0.01±0.12	0.03±0.16	-0.12±0.10	-0.19±0.19
2300196	-0.30±0.06	-0.45±0.22	-0.25±0.17	-0.07±0.16	0.07±0.08	–	0.15±0.10	0.09±0.15	0.03±0.17	-0.22±0.05	-0.34±0.18
2300215	-0.31±0.05	-0.23±0.24	-0.40±0.19	-0.14±0.18	-0.01±0.10	-0.14±0.25	0.08±0.11	0.03±0.16	-0.01±0.16	-0.17±0.07	-0.31±0.16
2409744	-0.20±0.06	-0.31±0.23	-0.44±0.18	-0.26±0.17	0.12±0.06	–	0.06±0.10	0.21±0.18	0.02±0.16	-0.46±0.04	-0.28±0.20
3600230	-0.19±0.05	-0.34±0.22	-0.67±0.16	-0.17±0.15	0.16±0.06	–	-0.03±0.11	-0.12±0.16	-0.18±0.16	-0.31±0.06	-0.44±0.18
3600262	-0.29±0.05	-0.44±0.22	-0.60±0.16	-0.13±0.15	0.14±0.07	-0.44±0.21	0.04±0.10	0.03±0.15	-0.08±0.16	-0.25±0.07	-0.34±0.18
3600302	-0.37±0.05	-0.48±0.21	-0.49±0.15	-0.27±0.14	0.07±0.05	-0.23±0.21	0.01±0.10	0.07±0.14	-0.04±0.16	-0.23±0.06	-0.27±0.19
3800318	-0.36±0.07	-0.41±0.24	-0.22±0.19	0.03±0.18	0.06±0.08	-0.34±0.16	0.20±0.10	0.07±0.17	0.02±0.18	-0.44±0.06	-0.40±0.17
3800558	-0.83±0.06	-0.99±0.15	-0.53±0.05	-0.25±0.07	0.35±0.07	-0.05±0.13	0.00±0.09	0.09±0.08	-0.00±0.13	-0.11±0.06	-0.17±0.10
4214652	-0.27±0.04	-0.46±0.19	-0.59±0.12	-0.26±0.11	0.16±0.07	-0.13±0.14	-0.10±0.09	0.05±0.13	-0.12±0.15	-0.27±0.06	-0.34±0.17
4303773	-0.50±0.05	-0.51±0.23	-0.75±0.14	–	0.10±0.07	-0.16±0.19	0.04±0.10	-0.10±0.13	-0.23±0.17	-0.20±0.06	-0.47±0.18
4304445	-0.42±0.04	-0.57±0.19	-0.51±0.13	-0.21±0.12	0.24±0.04	-0.12±0.11	0.04±0.10	-0.05±0.12	-0.11±0.15	-0.17±0.05	-0.33±0.17
4402285	-0.31±0.05	-0.46±0.20	-0.61±0.16	-0.26±0.13	0.14±0.06	0.01±0.19	0.02±0.09	-0.05±0.13	-0.10±0.15	-0.19±0.05	-0.31±0.17
4408968	-0.08±0.08	-0.15±0.24	-0.71±0.17	-0.44±0.16	-0.03±0.07	-0.30±0.21	0.13±0.09	-0.18±0.16	-0.23±0.16	-0.24±0.06	-0.66±0.17

Table 3.3: LMC and Sgr chemical abundances.

ID	[Cr/Fe]	[Mn/Fe]	[Co/Fe]	[Ni/Fe]	[Zn/Fe]	[Y/Fe]	[Zr/Fe]	[Ba/Fe]	[La/Fe]	[Nd/Fe]	[Eu/Fe]
					LMC						
NGC1754_248	-0.16±0.14	-0.47±0.16	-0.15±0.08	-0.15±0.04	-0.58±0.25	-0.49±0.25	-0.07±0.12	0.33±0.09	-0.04±0.09	0.23±0.06	0.40±0.12
NGC1786_2191	-0.16±0.08	-0.34±0.09	-0.19±0.06	-0.20±0.03	-0.58±0.12	-0.17±0.18	-0.12±0.11	0.48±0.05	0.35±0.05	0.41±0.06	0.49±0.09
NGC1786_569	-0.08±0.10	-0.28±0.08	-0.04±0.07	-0.16±0.04	-0.36±0.19	-0.24±0.22	0.06±0.13	0.40±0.07	0.29±0.07	0.52±0.08	0.37±0.10
NGC1835_1295	-0.08±0.13	-0.29±0.15	-0.27±0.19	-0.14±0.04	– ±–	-0.33±0.26	-0.01±0.15	0.24±0.13	0.14±0.09	0.52±0.10	0.11±0.14
NGC1835_1713	-0.00±0.13	-0.40±0.16	-0.15±0.11	-0.12±0.05	– ±–	-0.27±0.28	0.16±0.16	0.07±0.09	-0.09±0.09	0.43±0.06	0.32±0.13
NGC1898_2322	-0.14±0.13	-0.27±0.14	-0.18±0.10	-0.12±0.04	– ±–	-0.16±0.25	-0.08±0.15	0.42±0.09	0.30±0.09	0.46±0.06	0.30±0.12
NGC1978_24	0.08±0.13	-0.23±0.13	-0.10±0.09	-0.14±0.04	-0.32±0.25	0.01±0.25	0.02±0.13	0.22±0.09	0.27±0.07	0.37±0.07	0.48±0.09
NGC2108_382	0.04±0.13	-0.12±0.15	-0.01±0.10	-0.10±0.04	-0.23±0.18	0.10±0.25	– ±–	0.58±0.07	0.18±0.07	0.21±0.07	0.55±0.07
NGC2108_718	-0.11±0.13	-0.16±0.12	0.03±0.07	-0.13±0.04	-0.29±0.18	-0.21±0.23	-0.19±0.14	0.44±0.05	0.20±0.07	0.18±0.06	0.48±0.06
NGC2210_1087	-0.25±0.12	-0.23±0.13	-0.08±0.08	-0.12±0.04	-0.44±0.18	-0.01±0.22	0.30±0.12	0.34±0.06	0.32±0.07	0.33±0.04	0.44±0.09
2MASS J06112427-6913117	-0.23±0.14	-0.13±0.14	-0.10±0.10	-0.14±0.04	-0.18±0.25	-0.13±0.25	0.14±0.15	-0.20±0.11	0.06±0.12	0.32±0.11	0.85±0.11
2MASS J06120862-6911482	-0.15±0.11	-0.24±0.11	-0.17±0.08	-0.18±0.04	-0.21±0.18	-0.43±0.23	0.06±0.13	0.13±0.07	0.21±0.07	0.35±0.07	0.60±0.14
2MASS J06113433-6904510	-0.10±0.12	-0.17±0.11	-0.15±0.08	-0.14±0.04	-0.19±0.19	-0.31±0.23	-0.15±0.13	0.34±0.05	0.23±0.06	0.24±0.05	0.31±0.08
2MASS J06100373-6902344	-0.10±0.12	-0.33±0.17	-0.15±0.07	-0.19±0.04	-0.44±0.18	-0.36±0.23	-0.02±0.11	0.35±0.07	0.30±0.07	0.31±0.04	0.40±0.10
2MASS J06122296-6908094	0.02±0.07	-0.38±0.10	-0.09±0.08	-0.12±0.04	– ±–	0.28±0.11	– ±–	0.35±0.10	0.09±0.11	0.16±0.10	0.53±0.16
2MASS J06092022-6908398	0.08±0.12	-0.21±0.18	-0.10±0.17	-0.08±0.06	– ±–	-0.18±0.30	0.26±0.18	0.41±0.17	0.33±0.13	0.43±0.12	0.35±0.15
2MASS J06103285-6906230	-0.11±0.07	-0.19±0.11	-0.24±0.07	-0.19±0.04	-0.49±0.20	-0.05±0.18	-0.03±0.11	0.31±0.09	0.29±0.09	0.36±0.08	0.43±0.13
2MASS J06122229-6913396	-0.10±0.14	-0.43±0.14	-0.12±0.11	-0.12±0.05	-0.05±0.26	-0.34±0.28	-0.21±0.16	-0.45±0.14	0.14±0.08	0.29±0.07	0.71±0.12
2MASS J06114042-6905516	-0.17±0.14	-0.29±0.09	-0.05±0.07	-0.11±0.04	-0.10±0.26	-0.47±0.23	-0.02±0.11	0.35±0.06	0.16±0.07	0.40±0.06	0.49±0.09
2MASS J06110957-6920088	-0.08±0.11	-0.20±0.11	0.02±0.08	-0.07±0.05	-0.28±0.19	0.11±0.25	0.38±0.14	0.65±0.10	0.34±0.09	0.46±0.05	– ±–
2MASS J05244805-6945196	0.12±0.15	-0.45±0.16	-0.11±0.14	-0.25±0.05	– ±–	-0.05±0.33	0.23±0.17	0.01±0.09	0.26±0.12	0.48±0.08	0.33±0.12
2MASS J05235925-6945050	0.13±0.12	-0.05±0.16	-0.21±0.16	-0.18±0.08	– ±–	-0.09±0.33	– ±–	0.43±0.17	-0.00±0.13	0.15±0.12	0.05±0.16
2MASS J05225563-6938342	-0.01±0.23	-0.28±0.16	-0.05±0.16	-0.11±0.07	-0.71±0.40	-0.34±0.33	0.03±0.23	0.22±0.17	0.30±0.13	0.57±0.08	– ±–
2MASS J05242670-6946194	-0.10±0.13	0.19±0.17	-0.18±0.13	-0.16±0.06	– ±–	-0.22±0.25	0.25±0.29	0.50±0.09	0.31±0.08	0.30±0.08	0.28±0.12
2MASS J05225436-6951262	-0.05±0.13	-0.39±0.24	-0.16±0.14	-0.21±0.06	– ±–	-0.28±0.29	0.25±0.14	0.03±0.24	-0.15±0.13	0.38±0.09	0.32±0.16
2MASS J05244501-6944146	-0.12±0.14	-0.20±0.13	-0.13±0.10	-0.12±0.05	– ±–	-0.19±0.27	0.11±0.16	0.32±0.17	0.07±0.12	0.46±0.16	0.57±0.16
2MASS J05235941-6944085	0.21±0.17	-0.33±0.13	-0.21±0.20	-0.18±0.07	– ±–	– ±–	0.26±0.26	0.23±0.18	0.20±0.13	0.45±0.08	0.32±0.17
2MASS J05224137-6937309	-0.14±0.17	-0.25±0.17	-0.15±0.11	-0.17±0.06	– ±–	– ±–	0.10±0.19	0.28±0.18	0.19±0.13	0.53±0.07	0.23±0.17
2MASS J06143897-6947289	-0.26±0.14	– ±–	-0.09±0.12	-0.14±0.06	– ±–	-0.45±0.22	-0.07±0.13	0.01±0.18	0.24±0.13	– ±–	0.44±0.16
2MASS J05224766-6943568	0.07±0.12	-0.43±0.18	-0.22±0.15	-0.18±0.06	– ±–	– ±–	– ±–	0.49±0.18	0.15±0.14	0.46±0.11	– ±–
					Sgr						
2300127	-0.04±0.14	-0.41±0.10	-0.16±0.07	-0.10±0.04	– ±–	-0.14±0.27	0.16±0.21	0.07±0.08	0.06±0.12	0.16±0.04	0.54±0.11
2300196	0.05±0.11	-0.15±0.11	-0.11±0.11	-0.20±0.05	-0.64±0.24	0.52±0.27	0.42±0.26	0.97±0.10	1.00±0.09	0.68±0.06	0.62±0.12
2300215	0.07±0.13	-0.13±0.12	-0.06±0.11	-0.21±0.06	– ±–	0.09±0.25	0.43±0.28	0.39±0.17	0.62±0.13	0.63±0.06	0.61±0.15
2409744	0.07±0.12	-0.08±0.12	-0.22±0.10	-0.20±0.04	– ±–	0.35±0.24	0.14±0.28	0.69±0.08	0.50±0.08	0.73±0.08	0.56±0.09
3600230	-0.17±0.11	-0.35±0.11	-0.20±0.09	-0.28±0.04	– ±–	-0.04±0.23	0.06±0.22	0.61±0.08	0.41±0.07	0.32±0.05	0.44±0.09
3600262	-0.08±0.11	-0.22±0.12	-0.03±0.10	-0.24±0.04	-0.66±0.25	-0.03±0.24	0.07±0.21	0.50±0.06	0.26±0.07	0.51±0.05	0.39±0.07
3600302	0.00±0.12	-0.11±0.09	-0.04±0.08	-0.18±0.04	-0.29±0.25	0.17±0.22	0.36±0.22	0.68±0.07	0.61±0.07	0.51±0.05	0.48±0.09
3800318	0.07±0.13	0.01±0.20	-0.14±0.14	-0.22±0.04	– ±–	0.34±0.29	0.55±0.28	1.10±0.10	0.90±0.09	0.75±0.06	0.61±0.12
3800558	-0.10±0.10	-0.40±0.11	-0.18±0.09	-0.22±0.03	-0.33±0.19	-0.34±0.19	-0.04±0.19	0.12±0.08	0.14±0.08	0.14±0.07	0.55±0.11
4214652	-0.10±0.09	-0.34±0.12	-0.19±0.10	-0.25±0.04	-0.48±0.19	-0.15±0.21	0.03±0.20	0.48±0.09	0.38±0.08	0.32±0.05	0.47±0.11
4303773	-0.26±0.13	-0.51±0.12	-0.21±0.11	-0.23±0.04	-0.45±0.25	-0.59±0.26	-0.21±0.22	0.03±0.10	-0.07±0.09	0.20±0.08	0.42±0.12
4304445	-0.07±0.10	-0.22±0.08	-0.10±0.07	-0.19±0.04	-0.50±0.18	-0.20±0.22	0.04±0.20	0.43±0.06	0.48±0.06	0.33±0.05	0.52±0.07
4402285	-0.09±0.12	-0.26±0.10	-0.16±0.07	-0.20±0.03	-0.28±0.25	-0.10±0.22	0.08±0.20	0.49±0.07	0.48±0.07	0.58±0.06	0.66±0.08
4408968	-0.13±0.12	-0.15±0.12	-0.28±0.09	-0.27±0.04	-0.48±0.25	0.10±0.23	-0.05±0.26	0.81±0.08	0.79±0.07	0.59±0.07	0.36±0.08

Table 3.4: MW chemical abundances.

ID	[Fe/H]	[FeII/H]	[Na/Fe]	[Al/Fe]	[O/Fe]	[Mg/Fe]	[Si/Fe]	[Ca/Fe]	[Ti/Fe]	[Sc/Fe]	[V/Fe]
HD749	-0.40±0.07	-0.55±0.12	-0.09±0.12	0.23±0.09	0.25±0.08	0.20±0.08	0.08±0.09	0.06±0.06	0.07±0.09	0.11±0.09	0.10±0.13
HD18293 (nuHyi)	0.18±0.06	0.12±0.25	-0.14±0.16	0.17±0.12	0.23±0.10	–	0.04±0.07	-0.14±0.14	-0.20±0.14	0.10±0.04	-0.19±0.24
HD107328	-0.34±0.04	-0.46±0.13	-0.07±0.12	0.17±0.09	0.57±0.08	–	0.23±0.08	0.09±0.09	0.20±0.12	0.03±0.07	0.15±0.16
HD148897 (* s Her)	-1.08±0.08	-1.23±0.13	-0.09±0.03	0.06±0.07	0.58±0.07	0.32±0.05	0.23±0.11	0.28±0.06	0.19±0.11	0.04±0.11	0.00±0.10
HD190056	-0.51±0.04	-0.65±0.16	-0.10±0.11	0.38±0.10	0.66±0.08	–	0.22±0.08	0.18±0.10	0.24±0.14	0.24±0.05	0.17±0.17
HD220009	-0.55±0.04	-0.68±0.15	-0.11±0.10	0.34±0.09	0.59±0.07	–	0.18±0.08	0.10±0.10	0.22±0.13	0.25±0.06	0.11±0.17
GES J18242374-3302060	-0.02±0.06	-0.15±0.10	-0.17±0.09	0.03±0.07	0.23±0.06	-0.00±0.03	-0.00±0.08	0.06±0.06	-0.05±0.07	0.03±0.09	0.04±0.10
GES J18225376-3406369	-0.12±0.06	-0.27±0.11	-0.08±0.07	0.20±0.07	0.37±0.07	0.22±0.05	0.04±0.08	0.08±0.08	0.13±0.08	0.03±0.08	0.14±0.12
GES J17560070-4139098	-0.27±0.08	-0.39±0.09	-0.07±0.07	0.14±0.08	0.41±0.07	0.15±0.03	0.19±0.08	0.04±0.04	0.12±0.05	0.18±0.10	0.10±0.08
GES J18222552-3413578	-0.03±0.05	-0.12±0.16	-0.19±0.12	0.12±0.09	0.14±0.08	0.16±0.07	0.02±0.08	0.08±0.08	-0.05±0.11	0.11±0.07	0.05±0.14
GES J02561410-0029286	-0.71±0.07	-0.84±0.10	-0.15±0.07	0.41±0.07	0.41±0.07	0.29±0.04	0.26±0.08	0.04±0.04	0.24±0.06	0.15±0.09	0.06±0.09
GES J13201402-0457203	-0.49±0.06	-0.64±0.11	-0.07±0.06	0.35±0.06	0.56±0.06	0.44±0.25	0.15±0.08	0.05±0.05	0.30±0.08	0.24±0.08	0.26±0.12
GES J01203074-0056038	-0.25±0.04	-0.38±0.16	-0.09±0.15	0.32±0.11	0.52±0.10	–	0.25±0.08	0.12±0.12	0.19±0.13	0.38±0.05	0.09±0.16
GES J14194521-0506063	-0.33±0.05	-0.46±0.13	0.10±0.14	0.38±0.10	–	0.35±0.04	0.25±0.09	0.09±0.09	0.20±0.10	0.21±0.07	0.16±0.14
ID	[Cr/Fe]	[Mn/Fe]	[Co/Fe]	[Ni/Fe]	[Zn/Fe]	[Y/Fe]	[Zr/Fe]	[Ba/Fe]	[La/Fe]	[Nd/Fe]	[Eu/Fe]
HD749	0.02±0.04	-0.04±0.08	0.16±0.06	0.01±0.03	0.09±0.13	0.99±0.16	0.98±0.16	1.12±0.08	1.18±0.07	0.74±0.07	0.55±0.10
HD18293 (nuHyi)	-0.18±0.08	0.09±0.07	0.19±0.09	0.02±0.03	-0.21±0.11	0.03±0.20	-0.14±0.19	0.27±0.07	0.33±0.07	0.20±0.06	0.30±0.09
HD107328	-0.14±0.05	-0.20±0.09	0.30±0.07	-0.01±0.04	-0.11±0.10	-0.23±0.19	-0.00±0.18	-0.33±0.08	-0.15±0.05	-0.05±0.05	0.44±0.08
HD148897 (* s Her)	-0.12±0.10	-0.39±0.06	0.05±0.06	-0.09±0.04	-0.04±0.15	-0.10±0.18	0.26±0.17	0.24±0.10	0.16±0.11	0.08±0.07	0.42±0.16
HD190056	-0.03±0.09	-0.16±0.08	0.25±0.06	0.00±0.04	0.17±0.13	-0.09±0.21	0.17±0.20	0.16±0.08	0.14±0.07	0.09±0.04	0.46±0.10
HD220009	-0.11±0.09	-0.26±0.08	0.19±0.07	-0.02±0.03	0.15±0.10	-0.06±0.20	0.22±0.20	0.28±0.05	0.11±0.05	0.12±0.05	0.48±0.07
GES J18242374-3302060	-0.08±0.03	-0.09±0.07	0.07±0.08	-0.06±0.03	-0.20±0.11	0.05±0.14	0.09±0.13	0.15±0.07	0.27±0.06	0.17±0.07	0.26±0.08
GES J18225376-3406369	-0.10±0.05	-0.11±0.07	0.16±0.09	-0.01±0.03	0.05±0.11	-0.12±0.15	0.03±0.14	0.20±0.07	0.08±0.07	-0.11±0.07	0.38±0.09
GES J17560070-4139098	-0.19±0.04	-0.28±0.06	0.18±0.08	-0.00±0.03	0.04±0.12	–	0.03±0.11	-0.03±0.09	-0.10±0.07	-0.05±0.09	0.31±0.10
GES J18222552-3413578	-0.09±0.06	-0.02±0.08	0.11±0.09	-0.01±0.04	-0.10±0.08	-0.12±0.18	-0.03±0.16	0.09±0.04	0.09±0.05	0.08±0.06	0.26±0.08
GES J02561410-0029286	-0.11±0.04	-0.41±0.07	0.06±0.07	-0.05±0.03	0.02±0.11	0.25±0.14	0.31±0.12	0.18±0.08	0.24±0.07	0.01±0.08	0.44±0.10
GES J13201402-0457203	0.00±0.06	-0.28±0.06	0.09±0.07	0.01±0.03	0.19±0.11	-0.06±0.13	0.30±0.12	0.16±0.06	0.06±0.06	0.06±0.08	0.36±0.09
GES J01203074-0056038	-0.14±0.08	-0.11±0.11	0.29±0.07	0.06±0.04	0.20±0.11	0.02±0.22	0.19±0.20	0.09±0.07	0.26±0.06	0.27±0.06	0.68±0.08
GES J14194521-0506063	-0.04±0.07	-0.08±0.09	0.24±0.10	0.04±0.04	0.18±0.10	1.00±0.18	1.12±0.17	1.11±0.03	1.12±0.05	0.74±0.06	0.49±0.09

Chapter 4

A relic from a past merger event in the Large Magellanic Cloud

Based on the results published in
Mucciarelli A., Massari D., Minelli A., Romano D., Bellazzini M., Ferraro F. R., Matteucci F., Origlia L., 2021, Nature Astronomy, 5, 1247

4.1 Introduction

The LMC is the largest satellite orbiting the MW, with a total mass of $\sim 1{-}2.5\times10^{11}$ $M_\odot$ (Peñarrubia et al., 2016; Erkal et al., 2019) and a stellar mass of $\sim 3 \times 10^9$ $M_\odot$ (van der Marel & Kallivayalil, 2014). A satellite this massive is expected to host its own system of satellites. According to models of galaxy formation in the lambda cold dark matter theory, the number of these satellites is in the range 4-40 (Guo et al., 2010; Sales et al., 2013), the most massive of them dominating the mass budget (with a mass ratio compared to the LMC of ~ 0.1). The SMC, with a total mass of $\sim 2 \times 10^9$ $M_\odot$ (Stanimirović et al., 2004), matches well this prediction. The precise measurement of their proper motion allowed for the first time a reasonably sound reconstruction of the orbital history of the system(Kallivayalil et al., 2006, 2013). According to the most recent analyses the MCs may have become bound to each other around ∼3 Gyr ago and had their last close encounter ∼150 Myr ago (Patel et al., 2020).

The other satellites of the LMC should be much smaller, with total masses from $\sim 10^8 M_\odot$ down to values typical of the UFDs (Simon, 2019) that are the lowest-luminosity, oldest, most dark matter-dominated galaxies known so far. Attempts to determine which of the known UFDs were accreted by the MW together with the LMC hugely benefited from the advent of the second data release of the *Gaia* mission (Gaia Collaboration et al., 2018a), as this enabled the possibility to determine their

3D kinematics (Gaia Collaboration et al., 2018c; Simon, 2018; Kallivayalil et al., 2018). Dynamical integration of the UFDs orbits led to the conclusion that 4 to 6 of them (depending on the details of the modeling, Erkal & Belokurov, 2020; Patel et al., 2020) are indeed current satellites of the LMC. However, nothing is known about the past population of LMC satellites, that may be already disrupted within the host galaxy halo. So far, the only traces of accretion of matter from another galaxy by the LMC are associated with the complex interaction with the SMC (D'Onghia & Fox, 2016; Olsen et al., 2011).

Chemical tagging (Freeman & Bland-Hawthorn, 2002) is one of the few techniques that allows us to trace completely dissolved satellites, also in absence of any kinematically or spatially coherent relic, identifying stars and clusters that were lost long ago by means of their anomalous chemical composition, in contrast with the environment in which they live nowadays. However the power of the technique can be strongly hampered by the fact that spotting chemically anomalous stars in a given galaxy requires (a) high-resolution spectroscopy for large samples, and (b) extremely homogeneous chemical abundance analysis, as subtle differences in the assumptions on, e.g., astrophysical parameters, can wipe out (or spuriously introduce) the small abundance differences we are looking for. With the aim of digging into the past merging history of the largest MW satellite, here we attempt to overcome these problems by using old GCs as tracers and by deriving chemical abundances from high-resolution spectra with a strictly homogeneous analysis.

In this respect, GCs are a class of tracers that has been proven to be particularly effective in reconstructing the merger history of a galaxy such as the MW (Massari et al., 2019; Myeong et al., 2019; Kruijssen et al., 2020) or M31 (Mackey et al., 2019). This is because even a very low mass, low surface brightness dwarf galaxy, that may be dissolved by the tidal force of the main galaxy at its first peri-galactic passage, may host a dense stellar cluster able to survive in the same tidal field for many Gyr. Such a cluster will keep record of the characteristics of the environment in which it was born. In particular the chemical abundance pattern of its stars may be quite different from that of stars and clusters born in the main galaxy, due to the large differences in the star formation and chemical evolution between the hosting and the progenitor system.

Here we analyzed optical, high-resolution spectra of RGB in 11 old LMC GCs and in a reference sample of 15 MW GCs. These two datasets have been analyzed with the same methodology (i.e. atomic data, solar reference abundances, model atmospheres, temperature scale), thus removing any possible systematic error between the abundances of the two families of clusters. In particular, we derived the chemical abundance ratios for 13 species belonging to the main groups of elements, indicators of different production mechanisms and stellar progenitors.

4.2 Spectroscopic datasets

The LMC hosts the largest system of old GCs among the MW satellites, including 13 GCs (Olszewski et al., 1996) with ages comparable to those of the MW (Brocato et al., 1996; Olsen et al., 1998; Wagner-Kaiser et al., 2017). Chemical abundances of old LMC GCs based on high-resolution spectra of individual giant stars are available for about an half of the entire population (Hill et al., 2000; Johnson et al., 2006; Mucciarelli et al., 2010; Mateluna et al., 2012). These analyses are based on different methods and assumptions making the comparison among the LMC clusters and between MW and LMC clusters affected by several systematics (i.e. atomic data, solar reference abundances, model atmospheres, temperature scale...). In order to highlight similarities and differences in the chemical composition of giant stars in LMC and MW GCs, we homogeneously analyzed two samples of high-resolution, optical spectra.

1. LMC GCs dataset — This sample includes 11 out of 15 old LMC clusters, four of them (NGC 1466, NGC 1754, NGC 1835, NGC 1916) have never been analyzed before using high-resolution spectroscopy of individual stars (see Table 4.1). The dataset is composed of proprietary and archival data collected with the spectrographs FLAMES (Pasquini et al., 2002) and UVES (Dekker et al., 2000) at the Very Large Telescope of the European Southern Observatory and with the spectrograph MIKE (Bernstein et al., 2003) at the Magellan Telescope. Signal-to-noise ratios per pixel range from about 30-40 to 100. For nine GCs, observations with

Table 4.1: LMC GCs dataset information. Coordinates of the cluster centers are from the SIMBAD database. The number of analysed member stars for each cluster is listed according to the used instruments: U-FL for UVES-FLAMES, U for UVES, G for GIRAFFE/MEDUSA-FLAMES, M for MIKE. The program identification numbers of the ESO Programs are reported (Program ID: 080.D-0368, PI: Origlia; Program ID: 084.D-0933, PI: Mucciarelli; Program ID: 092.D-0244, PI: Mucciarelli). The clusters observed with the spectrograph MIKE are labeled as J06(Johnson et al., 2006). UVES-SV identifies observations performed during the UVES Science Verification.

Cluster	RA (J2000)	Dec (J2000)	N_{U-FL}	N_U	N_G	N_M	Programs
NGC 1466	03:44:33.0	–71:40:18.0	5	—	4	—	092.D-0244
NGC 1754	04:54:18.1	–70:26:32.6	5	—	—	—	084.D-0933
NGC 1786	04:59:07.5	–67:44:45.0	4	—	3	—	080.D-0933
NGC 1835	05:05:09.2	–69:24:21.0	4	—	—	—	092.D-0244
NGC 1898	05:16:45.4	–69:39:16.7	4	—	3	2	084.D-0933 + J06
NGC 1916	05:18:37.9	–69:24:22.9	4	—	—	—	092.D-0244
NGC 2005	05:30:08.5	–69:45:14.4	—	—	—	2	J06
NGC 2019	05:31:56.5	–70:09:32.5	—	—	—	3	J06
NGC 2210	06:11:31.3	–69:07:17.0	5	3	—	—	080.D-0368 + UVES-SV
NGC 2257	06:30:12.0	–64:19:36.0	3	3	3	—	080.D-0368, 66.B-0331
HODGE 11	06:14:22.9	–69:50:54.9	4	—	—	2	082.B-0458 + J06

the fiber-fed spectrograph FLAMES in the UVES+GIRAFFE combined mode have been secured. For all these clusters spectra with the Red Arm 580 UVES setup have been obtained, with a spectral resolution of 47000 and a spectral coverage between about 4800 and 6800 Å. Only for the clusters NGC 1466, NGC 1786, NGC 1898 and NGC 2257, a few of additional cluster stars have been observed with the GIRAFFE fibers. In fact, the small angular size (about 2 arcmin of diameter) of the LMC clusters and the physical size of the magnetic buttons sustaining the fibers prevent to allocate more than ∼8-10 FLAMES fibers on the cluster area in the same pointing. The adopted GIRAFFE/MEDUSA setups are HR11 (5597 - 5840 Å and resolution 29500) and HR13 (6120 - 6405 Å and resolution 26400).
For two clusters observed with FLAMES (namely, NGC 2210 and NGC 2257), additional archival data acquired with the slit spectrograph UVES are available. These observations have been secured with the Red Arm 580 UVES setup, adopting slits between 1 and 1.2 arcsec, providing spectral resolutions between 38000 and 45000.
Finally, we analyzed MIKE spectra for four GCs (NGC 1898, NGC 2005, NGC 2019, Hodge 11, previously analysed by Johnson et al., 2006), two of them in common with FLAMES. The MIKE spectra have been acquired with a slit of 1 arcsec, corresponding to a spectral resolution of 19000 and with a spectral range between 4500 and 7250 Å .

2. *MW GCs dataset* — A sample of giant stars in 15 MW GCs has been collected from archival data (see Table 4.2). The clusters have been selected in order to cover the entire range of metallicity of the Galactic halo/disk GCs system ([Fe/H] between –2.5 dex and –0.7 dex). All the spectra have been obtained with the multi-object spectrograph UVES-FLAMES adopting the same setup used for the LMC clusters. Signal-to-noise ratios per pixel range from about 70-80 to 150.

4.3 Atmospheric parameters

T_{eff} is the most crucial atmospheric parameter in the determination of chemical abundances. Temperatures can be inferred from suitable calibrations of broad-band colors or by requiring that no trend exists between the abundances of individual Fe lines and their excitation potential. The two methods can often provide discrepant results. In particular, the two approaches agree with each other for metallicities higher than –1.5 dex while the spectroscopic T_{eff} are overly low and under-estimated (down to about 300 K) for [Fe/H] < -1.5 dex, because of the inadequacies in the modeling of 1D/LTE radiative transfer in metal-poor giant stars (Mucciarelli & Bonifacio, 2020). Therefore, the use of spectroscopic T_{eff} leads to underestimate the abundances for metal-poor stars.

Due to the composite nature of the LMC dataset, homogeneous photometric information are not available for all the targets: for the proprietary data, near-

Table 4.2: MW GCs dataset information. Coordinates of the cluster centers are from the Harris catalog (Harris, 1996, 2010). The number of used stars and the identification numbers of the corresponding ESO Programs are also listed.

Cluster	RA (J2000)	Dec (J2000)	N_{stars}	Programs
NGC 104	00:24:05.67	–72:04:52.6	10	073.D-0211
NGC 288	00:52:45.24	–26:34:57.4	10	073.D-0211
NGC 1851	05:14:06.76	–40:02:47.6	23	188.B-3002
NGC 1904	05:24:11.09	–24:31:29.0	10	072.D-0507
NGC 2808	09:12:03.10	–64:51:48.6	12	072.D-0507
NGC 4590	12:39:27.98	–26:44:38.6	13	073.D-0211
NGC 5634	14:29:37.23	–05:58:35.1	7	093.B-0583
NGC 5824	15:03:58.63	–33:04:05.6	6	095.D-0290
NGC 5904	15:18:33.22	+02:04:51.7	14	073.D-0211
NGC 6093	16:17:02.41	–22:58:33.9	9	083.D-0208
NGC 6397	17:40:42.09	–53:40:27.6	12	073.D-0211
NGC 6752	19:10:52.11	–59:59:04.4	12	073.D-0211
NGC 6809	19:39:59.71	–30:57:53.1	13	073.D-0211
NGC 7078	21:29:58.33	+12:10:01.2	13	073.D-0211
NGC 7099	21:40:22.12	–23:10:47.5	19	073.D-0211 ; 085.D-0375

infrared JHK_s photometry is available, while for the archival data, optical ground-based or space-telescope photometry is in hand but in different photometric filters. Thanks to the high spectral resolution, the high number of lines and the good/high signal-to-noise ratio of the LMC spectra, T_{eff} can be derived spectroscopically with high precision for all the targets. Because the discrepancy between spectroscopic and photometric T_{eff} for clusters with [Fe/H] < -1.5 dex increases with decreasing the metallicity, we need to remove this effect in order to put all the T_{eff} on the same (unbiased) scale. The spectroscopic T_{eff} for clusters with [Fe/H]<-1.5 dex have been corrected according to the spectroscopic [Fe/H] (Mucciarelli & Bonifacio, 2020) in order to put them onto a photometric scale (González Hernández & Bonifacio, 2009), while spectroscopic T_{eff} for clusters with higher metallicity do not need any correction. A pure spectroscopic T_{eff} scale leads to systematically lower abundances for metal-poor stars. With the adopted procedure, the T_{eff} of all the stars are on the same scale. On the other hand, for the MW GCs homogeneous photometry is available (Stetson et al., 2019) and T_{eff} have been derived from the $(V-K_0)$-T_{eff} calibration (González Hernández & Bonifacio, 2009).

However, since one of the key results discussed here is based on the comparison of chemical abundances among LMC and MW clusters, it is particularly important to recall that T_{eff} for all the cluster stars are on the same scale (González Hernández & Bonifacio, 2009).

The log g have been estimated assuming for each cluster the T_{eff}-log g relation suitable for the red giant branch and derived from a theoretical isochrone (Dotter et al., 2008) with an age of 13 Gyr and metallicity and [α/Fe] from our chemical analysis. Because log g values have been derived according to the T_{eff} and metallicity of each star, the procedure to obtain this parameter is iterative. This approach avoids the uncertainties in log g arising from color excess and distance modulus of each individual cluster. The assumption of a different age is not critical: a change of 1 Gyr (that can be consider as a reasonable uncertainty in the ages of the target clusters) implies a variation of 0.01 in log g, with a negligible impact on the derived abundances.

v_t are derived by requiring no trend between abundances of the Fe lines and their reduced equivalent width, defined as the logarithm of the EW divide by the wavelength (Mucciarelli, 2011).

4.4 Chemical analysis

The chemical abundances of Fe, Si, Ca, Ti and Ni have been derived by comparing the measured EWs, derived with the code `DAOSPEC` (Stetson & Pancino, 2008), with the theoretical line strengths using the code `GALA` (Mucciarelli et al., 2013). For these species, we considered only transitions selected to be unblended according to the atmospheric parameters and metallicity of each individual star, privileging, when possible, the lines for which laboratory oscillator strengths are available.
Abundances of Sc, V, Mn, Co, Cu, Ba, La and Eu (whose transitions are affected by hyperfine/isotopic splitting) and of Zn (located in a crowded and noisy spectral region) have been derived through spectral synthesis, by performing a χ^2-minimization between observed and synthetic spectra.

All synthetic spectra used in this work have been computed with the code `SYNTHE` (Kurucz, 2005) including all the atomic and molecular transitions available in the Kurucz/Castelli database.
Model atmospheres for each star have been calculated with the code `ATLAS9` (Kurucz, 2005) under the assumptions of plane-parallel geometry, hydrostatic and radiative equilibrium and local thermodynamic equilibrium for all the species. For all the stars the model atmospheres have been computed assuming an α-enhanced chemical mixture, except for the stars of NGC 2005 and NGC 1898, for which solar-scaled model atmospheres have been used in accordance to the derived [α/Fe] abundance ratios. Still, we also verified that the use of α-enhanced model atmospheres in these two cases changes the measured abundance ratios only slightly, by less than 0.05 dex.

Note that we exclude from this discussion the light elements Na, O, Mg and Al because they are involved in the chemical anomalies due to the self-enrichment processes that characterized the early stage of life of the clusters (Gratton et al., 2006; Carretta et al., 2009a; Mucciarelli et al., 2009b; Bastian & Lardo, 2018). Therefore, their abundances cannot be easily used as tracers of the chemical composition of the parent galaxy. Indeed, we found evidence of star-to-star variations for the light elements Na, O, Mg and Al in the target clusters, as expected considering their mass and age. On the other hand, a null spread has been found for all the elements discussed in this work, so that any effect due to the internal evolution of the individual clusters does not affect our conclusions.

4.4.1 Uncertainties in the chemical abundances

The total uncertainty associated to a given abundance (in the form of [X/H]) in individual stars is obtained by taking into account internal errors and those arising from the adopted stellar parameters.

The uncertainty of [Fe/H] and [X/Fe] are obtained by summing in quadrature the different sources of error, using the equations in Section 3.4.1.

For each cluster, mean abundance ratios (and the corresponding standard errors) have been computed by averaging the abundances of the member stars weighted by the uncertainty (as described above). Since formal standard error on the weighted mean were in many case exceedingly small (of the order of ∼0.02–0.03 dex), due to the small number of stars per cluster (2-3), we decided to take the average error on individual measures as a conservative estimate of the uncertainty on the mean abundance.

Internal errors — Internal errors in [X/H] were estimated considering the line-to-line dispersion of the abundance mean divided by the root mean square of the number of lines. The dispersion of the mean reflects a combination of uncertainties in the measure, continuum location and in the atomic data.

When one only line is available, we considered as internal error the abundance variation due to the uncertainty in the measure process. For species for which equivalent width has been measured, we transformed in abundance the error associated to the Gaussian fit used to measure the equivalent width. For species measured from the spectral synthesis, we performed Monte Carlo simulations of the fitting procedure. For each star, a sample of 500 artificial spectra has been generated, by re-sampling the best-fit synthetic spectrum to the instrumental pixel-size and injecting Poissonian noise to reproduce the measured signal-to-noise. This sample of artificial spectra has been analyzed with the same approach adopted for the real spectra. The dispersion of the derived abundance distribution has been adopted as 1σ uncertainty.

Parameters errors — Abundance errors due to uncertainties in the atmospheric parameters were estimated by re-computing abundances varying the parameters by their uncertainties. The uncertainties in spectroscopic $T_{\rm eff}$ are estimated by applying a jackknife bootstrapping technique (Lupton, 1993), leading to errors from ∼50 up to ∼100 K, mainly depending on the signal-to-noise ratio of the spectrum. For the clusters with [Fe/H] <-1.5 dex, for which the correction to the photometric scale has been applied, we added in quadrature also the 1σ dispersion (36 K) associated to the calibration itself (Mucciarelli & Bonifacio, 2020). Temperatures were varied by the corresponding errors, gravities were modified by propagating the errors in T_{eff} on the adopted T_{eff}-log g relation and the v_t were re-computed adopting the new T_{eff} and log g. This approach allows to take into account the covariance existing between T_{eff} and log g (Cayrel et al., 2004), due to the physical relation existing between these two parameters, and between T_{eff} and v_t, due to the correlation between line strength and excitation potential.

Systematic errors — Chemical abundances can be affected by several sources of systematics, mainly the accuracy of the adopted atomic data, the used solar reference abundances, the used model atmospheres (and their physical assumptions), the zero-point of the used T_{eff} scale, and the method to infer stellar parameters. The chemical analysis of the two datasets discussed in this work (LMC and MW GCs) has been performed using the same approach in terms of these assumptions, in order to erase the main systematics and compare directly the abundances of the two families of clusters. Therefore, any possible source of systematic error arising from the analysis affects in the same way both the datasets, making the comparison between LMC and MW clusters more accurate and robust.

4.5 Chemical abundances

Fig. 4.1 shows the behaviour of [Si/Fe], [Ca/Fe], [Cu/Fe] and [Zn/Fe] as a function of [Fe/H] for the LMC and MW GCs samples. The average weighted abundance ratios for Fe, Si, Ca, Cu and Zn for the analysed LMC and MW old GCs with the corresponding standard errors are reported in Table 4.3. The LMC GCs draw well-defined sequences of each abundance ratio as a function of [Fe/H] that are distinct, in most cases, from those defined by the MW GCs, reflecting the different chemical evolution histories of the two galaxies (Lapenna et al., 2012; Van der Swaelmen et al., 2013; Nidever et al., 2020).

Among the LMC GCs, the metal-poor cluster NGC 2005 ([Fe/H] $= -1.75 \pm 0.04$ dex) is distinguished as a clear outlier. NGC 2005 is a relatively massive GC, M$\sim 2-3\ 10^5$M$_\odot$ (Mackey & Gilmore, 2003), located at ~ 0.23 kpc from the center of LMC. It exhibits abundance ratios that are systematically lower (in most cases at a level $>3\sigma$) than those measured in the LMC GCs with similar metallicities (see Fig. 4.2, data in Table 4.4) for almost all the species, including elements (Si, Ca, Sc, Ti, V, Mn, Co, Ni, Cu, Zn, Ba, La, Eu) forming from different nucleosynthesis channels (i.e. explosive and thermonuclear SNe, HNe, slow and rapid neutron-capture processes).

The 5 LMC GCs with [Fe/H] comparable with that of NGC 2005 (–1.75 <

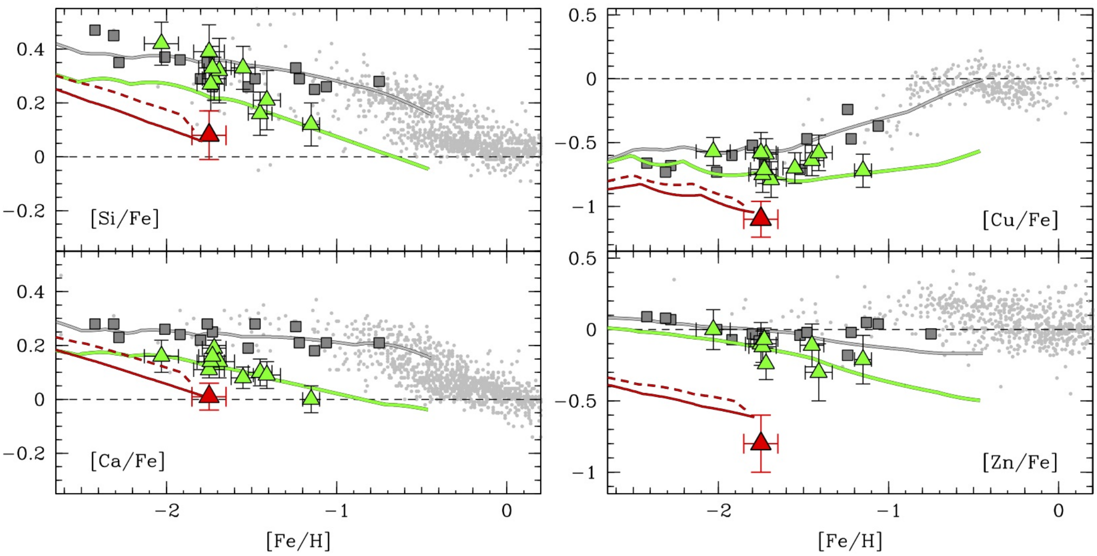

Figure 4.1: Behaviour of the [Si/Fe], [Ca/Fe], [Cu/Fe] and [Zn/Fe] abundance ratios as a function of [Fe/H] for the LMC (green triangles) and the MW (grey squares) clusters. The accreted LMC cluster NGC 2005 is highlighted as a red triangle. Solar neighbourhood stars (small grey circles, Bensby et al., 2014) are shown as reference. Error bars are computed as the mean value of the uncertainties in individual stars and displayed only for the LMC clusters (see Section 4.4.1). Superimposed chemical evolution models for the MW Halo (grey line), LMC (green line) and for two stellar systems with low star formation efficiencies, namely 0.075 Gy^{-1} over 1 Gyr and 0.15 Gy^{-1} over 0.5 Gyr (resulting in a star formation rate of $< 5 \cdot 10^{-4} M_{\odot} yr^{-1}$, red solid and dashed lines, respectively).

Table 4.3: Average weighted abundance ratios for [Fe/H], [Si/Fe], [Ca/Fe], [Cu/Fe] and [Zn/Fe] for the analyzed LMC and MW old GCs with the corresponding standard error and the dispersion of the weighted mean.

Cluster	[Fe/H] (dex)	σ	[Si/Fe] (dex)	σ	[Ca/Fe] (dex)	σ	[Cu/Fe] (dex)	σ	[Zn/Fe] (dex)	σ
					LMC					
NGC 1466	–1.55±0.02	0.05	+0.33±0.01	0.02	+0.08±0.03	0.08	–0.70±0.11	0.15	—	—
NGC 1754	–1.45±0.03	0.05	+0.16±0.02	0.04	+0.10±0.02	0.04	–0.64±0.07	0.15	–0.11±0.04	0.10
NGC 1786	–1.72±0.02	0.04	+0.29±0.05	0.09	+0.19±0.03	0.06	–0.59±0.05	0.09	–0.24±0.05	0.10
NGC 1835	–1.69±0.01	0.01	+0.32±0.05	0.10	+0.14±0.02	0.04	–0.79±0.08	0.15	—	—
NGC 1898	–1.15±0.02	0.05	+0.12±0.01	0.03	+0.00±0.03	0.07	–0.72±0.05	0.10	–0.21±0.15	0.23
NGC 1916	–1.75±0.03	0.05	+0.39±0.01	0.02	+0.11±0.03	0.04	–0.58±0.05	0.09	–0.10±0.08	0.11
NGC 2005	–1.75±0.04	0.06	+0.08±0.01	0.01	+0.01±0.03	0.04	–1.10±0.14	—	–0.80±0.20	—
NGC 2019	–1.41±0.05	0.08	+0.21±0.01	0.01	+0.09±0.04	0.08	–0.58±0.03	0.05	–0.30±0.20	—
NGC 2210	–1.74±0.02	0.06	+0.27±0.03	0.07	+0.14±0.01	0.03	–0.75±0.03	0.08	–0.12±0.07	0.15
NGC 2257	–1.73±0.02	0.04	+0.33±0.02	0.04	+0.16±0.03	0.05	–0.71±0.01	0.01	–0.07±0.13	0.21
HODGE 11	–2.03±0.04	0.09	+0.42±0.08	—	+0.16±0.01	0.02	–0.57±0.02	0.03	+0.00±0.05	0.10
					MW					
NGC 104	–0.75±0.01	0.03	+0.28±0.01	0.03	+0.21±0.02	0.07	—	—	–0.03±0.03	0.09
NGC 288	–1.24±0.01	0.04	+0.33±0.01	0.03	+0.27±0.01	0.03	–0.24±0.02	0.05	–0.18±0.04	0.14
NGC 1851	–1.13±0.01	0.04	+0.25±0.01	0.03	+0.18±0.01	0.05	—	—	+0.05±0.03	0.14
NGC 1904	–1.52±0.01	0.03	+0.26±0.01	0.02	+0.19±0.01	0.02	–0.71±0.01	0.04	–0.04±0.02	0.06
NGC 2808	–1.06±0.02	0.07	+0.26±0.01	0.04	+0.21±0.01	0.02	–0.37±0.04	0.12	+0.04±0.05	0.17
NGC 4590	–2.28±0.01	0.05	+0.35±0.04	0.06	+0.23±0.01	0.02	–0.68±0.02	0.04	+0.07±0.03	0.10
NGC 5634	–1.80±0.02	0.05	+0.29±0.01	0.04	+0.22±0.01	0.03	–0.52±0.04	0.11	–0.03±0.05	0.15
NGC 5824	–1.92±0.02	0.04	+0.36±0.03	0.08	+0.24±0.01	0.02	–0.60±0.04	0.11	–0.07±0.03	0.07
NGC 5904	–1.22±0.01	0.03	+0.29±0.01	0.03	+0.21±0.01	0.03	–0.47±0.02	0.06	–0.02±0.02	0.09
NGC 6093	–1.76±0.01	0.03	+0.35±0.01	0.04	+0.28±0.01	0.03	–0.58±0.01	0.03	–0.08±0.02	0.07
NGC 6397	–2.01±0.01	0.03	+0.37±0.02	0.08	+0.26±0.01	0.03	–0.73±0.04	0.09	+0.00±0.02	0.06
NGC 6752	–1.48±0.01	0.03	+0.29±0.01	0.03	+0.28±0.01	0.02	–0.47±0.01	0.06	–0.02±0.03	0.12
NGC 6809	–1.73±0.01	0.03	+0.26±0.01	0.04	+0.25±0.01	0.03	–0.66±0.01	0.05	–0.06±0.01	0.05
NGC 7078	–2.42±0.02	0.07	+0.47±0.04	0.09	+0.28±0.01	0.02	–0.66±0.03	0.07	+0.09±0.03	0.12
NGC 7099	–2.31±0.01	0.05	+0.45±0.01	0.02	+0.28±0.01	0.03	–0.73±0.03	0.10	+0.08±0.02	0.08

[Fe/H] < − 1.69 dex) have abundance ratios very similar each other, constituting a homogeneous group of clusters sharing the same chemistry. This demonstrates that these GCs formed in environments that have experienced a similar chemical enrichment history, likely the LMC itself. On the other hand, the strong chemical differences between NGC 2005 and this group of clusters is indicative of a completely different chemical enrichment path. This reveals that NGC 2005 cannot have formed in the same environment as the rest of the LMC clusters at that metallicity but it has rather born in a system that converted its gas into stars at a slower pace.

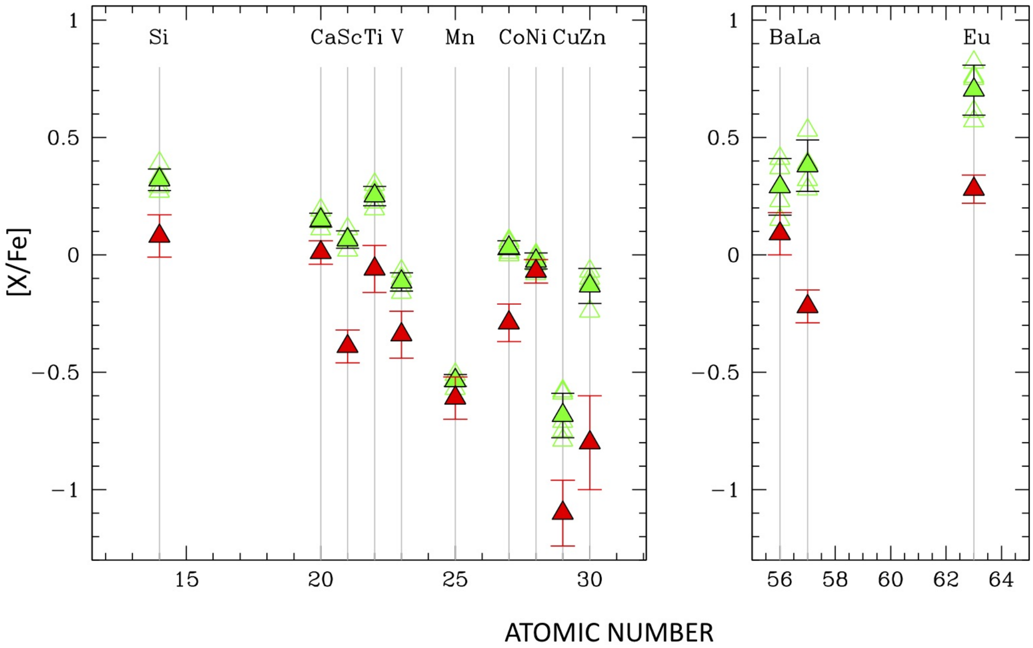

Figure 4.2: Abundance ratios measured for the accreted cluster NGC 2005 (red triangles) in comparison with those measured in the LMC old clusters with comparable metallicity (–1.75<[Fe/H]<-1.69 dex, green open triangles, namely NGC 1786, NGC 1835, NGC 1916, NGC 2210 and NGC 2257). The green filled triangles represent the average abundance ratios obtained for these five LMC GCs and the errorbars are the corresponding standard deviation.

4.6 Reliability of the NGC 2005 abundances

In this section we consider all the possible source of errors that can lead to a wrong value of chemical abundances, even if the previous analysis of NGC 2005 (Johnson et al., 2006) provides abundances consistent with our ones.

1. Atmospheric parameters

The two observed stars in NGC 2005 have atmospheric parameters comparable with those of the other stars in LMC clusters with similar metallicities, as expected because all the target stars belong to the brightest portion of the clusters red giant

Table 4.4: Average weighted abundance ratios for [TiII/Fe], [Ni/Fe], [Sc/Fe], [V/Fe], [Mn/Fe], [Co/Fe], [Ba/Fe], [La/Fe] and [Eu/Fe] for the LMC old clusters with metallicity comparable to NGC 2005, with the corresponding standard error and the dispersion of the weighted mean.

	NGC 1786		NGC 1916		NGC 2005	
element	mean	σ	mean	σ	mean	σ
$[TiII/Fe]$	0.23± 0.02	0.03	0.38± 0.02	0.03	-0.10±0.03	0.04
$[Ni/Fe]$	-0.09±0.01	0.03	-0.00±0.02	0.03	-0.06±0.04	0.05
$[Sc/Fe]$	0.04± 0.03	0.06	-0.01± 0.05	0.10	-0.39± 0.03	0.04
$[V/Fe]$	-0.09± 0.01	0.02	-0.21± 0.06	0.13	-0.42± 0.15	0.21
$[Mn/Fe]$	-0.55±0.06	0.13	-0.54±0.03	0.06	-0.66±0.03	0.04
$[Co/Fe]$	0.01± 0.03	0.06	-0.06± 0.05	0.09	-0.28± 0.02	0.03
$[Ba/Fe]$	0.32±0.08	0.16	0.42±0.06	0.12	0.05±0.06	0.08
$[La/Fe]$	0.34±0.08	0.17	0.40±0.08	0.13	-0.43±0.18	0.25
$[Eu/Fe]$	0.75±0.09	0.17	0.60±0.03	0.07	0.20±0.08	0.11
	NGC 2019		NGC 2210		NGC 2257	
element	mean	σ	mean	σ	mean	σ
$[TiII/Fe]$	0.20± 0.03	0.04	0.25± 0.03	0.08	0.37± 0.02	0.06
$[Ni/Fe]$	-0.14±0.06	0.10	-0.01±0.02	0.05	0.00±0.02	0.06
$[Sc/Fe]$	—	—	0.05± 0.02	0.07	0.12± 0.04	0.11
$[V/Fe]$	—	—	-0.17± 0.04	0.10	-0.19± 0.04	0.10
$[Mn/Fe]$	-0.54±0.07	0.12	-0.61±0.06	0.17	-0.51±0.04	0.09
$[Co/Fe]$	—	—	-0.02± 0.03	0.08	0.01± 0.03	0.08
$[Ba/Fe]$	0.20±0.08	0.13	0.12±0.04	0.11	0.30±0.05	0.11
$[La/Fe]$	0.19±0.05	0.08	0.28±0.07	0.18	0.34±0.03	0.07
$[Eu/Fe]$	0.71±0.06	0.10	0.64±0.04	0.11	0.77±0.05	0.12

branches (due to their distance, high-resolution spectroscopy in old LMC GCs is restricted to the brightest stars). We checked that there is no set of reasonable atmospheric parameters able to reconcile all the abundances of NGC 2005 with those measured in the other LMC metal-poor clusters. Because the analyzed transitions for the 13 measured species have different strengths, excitation potential and ionization stages, they have different (and sometimes opposite) sensitivity to the atmospheric parameters. Therefore, the variation of a given atmospheric parameter leads to an increase of some abundance ratios and the decrease of others, depending on the characteristics of the used transitions.

For example, a decrease of T_{eff} by 200 K (coupled with new, appropriate log g and v_t) for the stars in NGC 2005 provides [Si/Fe] comparable with those of the other clusters while [Ca/Fe] and [Ti/Fe] remain low. Furthermore, this new set of parameters provides values of [Zn/Fe] and [Cu/Fe] still significantly lower than those of the other LMC clusters. In order to increase these two abundance ratios, T_{eff} should be increased by 400-500 K, decreasing significantly the other abundance ratios. Also, such hot T_{eff} are incompatible with the position of the stars on the color-magnitude diagram. We therefore rule out that the peculiar chemistry of NGC 2005 could be driven by a particular choice of the atmospheric parameters of its stars, concluding that its deviations from the average trends defined by the other LMC clusters are genuine.

2. Line fitting

Fig. 4.3 shows some portions of the MIKE spectrum of the star NGC2005-S3, around four metallic lines of the species (namely Sc, Zn, La and Eu) that exhibit the largest differences between NGC 2005 and the clusters with similar [Fe/H] (see Fig. 4.2). The MIKE spectrum is compared with two synthetic spectra: the best-fit one and the one calculated assuming the average abundances measured in the other 5 LMC GCs. As is evident from this figure, the depth of the observed lines in NGC 2005 is not compatible at all with the abundances of the other LMC GCs with similar [Fe/H].

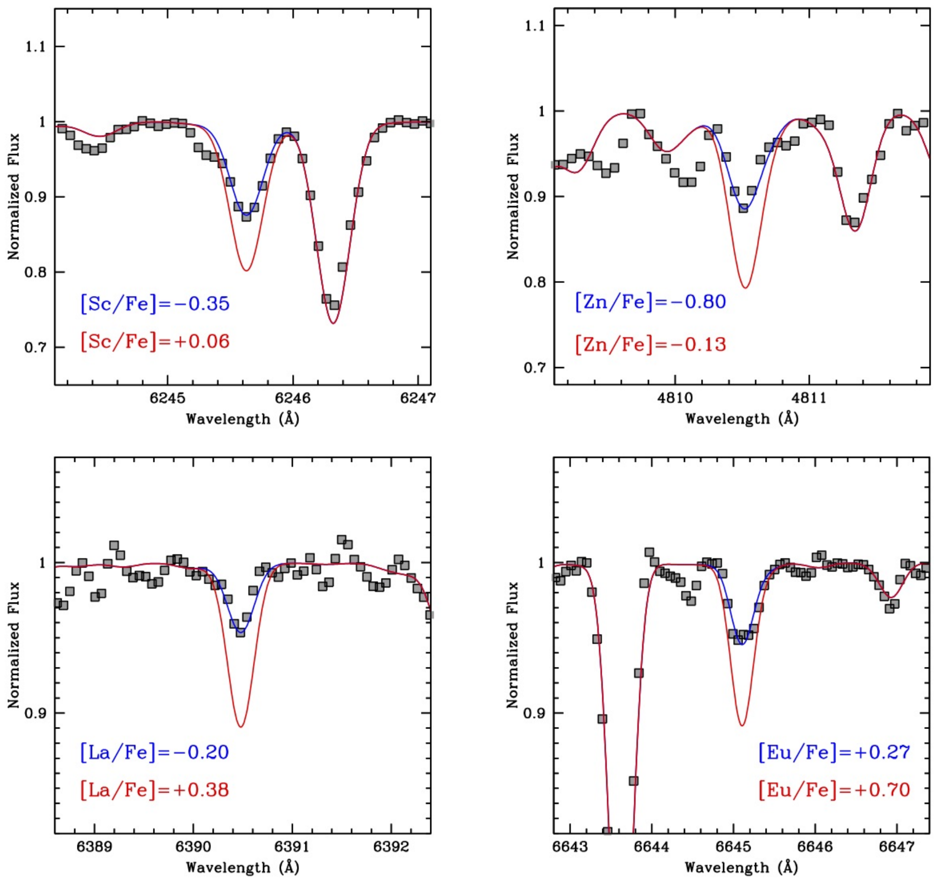

Figure 4.3: Portions of the MIKE spectrum of the star NGC2005-S3 (gray squares) around some metallic lines of interest for Sc, Zn, La and Eu, with superimposed the best-fit synthetic spectrum (blue lines) and a synthetic spectrum computed with the stellar parameters of this star but assuming the average abundances derived from the 5 LMC GCs with metallicity comparable to that of NGC 2005 (red lines).

On the other hand, Fig. 4.4 shows the comparison between the MIKE spectrum of the star NGC2005-S3 and the UVES spectrum of the star NGC2210-764 (which has atmospheric parameters and metallicity very similar to those of NGC2005-S3). A smoothing filter and a re-sampling have been applied to the UVES spectrum to mimic the spectral resolution and the pixel-size of MIKE spectra, allowing us to directly compare the line strength of metallic lines. As visible in Fig. 4.4 , Fe lines have similar strengths while Sc, La and Eu lines are shallower in the MIKE spectrum of NGC205-S3.

The uncertainty in the line fitting procedure and in the continuum location are not sufficient to justify such a stark discrepancy, not even in the case of the Zn line, that is one of the bluest transitions analyzed in this study, and for which the continuum location is more affected by the lines crowding.

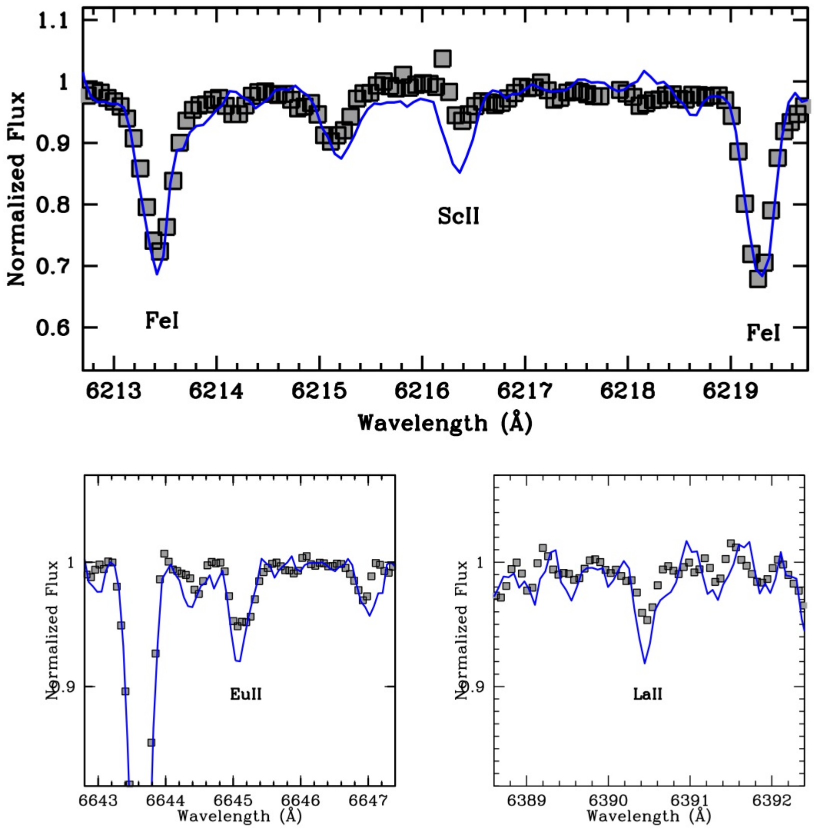

Figure 4.4: Portions of the MIKE spectrum of the star NGC2005-S3 (gray squares) around some metallic lines of interest for Sc, Fe, La and Eu, with superimposed the UVES spectrum of the star NGC2210-764, convoluted with a Gaussian profile to reproduce the MIKE spectral resolution and re-sampled to the MIKE pixel size (blue line).

3. Comparison between abundances from UVES and MIKE spectra
Among the LMC GCs with metallicity between –1.75 and –1.69 dex (see Fig. 4.1), NGC 2005 is the only for which the spectra have been obtained with the spectrograph MIKE, while the other 5 GCs have been observed with the spectrograph UVES.

We thus carry out some tests on the elemental abundances of NGC 2005 to exclude the possibility that the chemical peculiarity of this cluster is artificially caused by some systematic effect due to the use of different spectrographs.

To do so, we performed some checks on the abundances derived from UVES and MIKE. First, we considered two clusters, namely Hodge 11 and NGC 1898, for which both UVES and MIKE spectra are available (though no stars have been simultaneously observed with both the instruments). The number of available spectra obtained with the different spectrographs for the two GCs is reported in Table 4.1. Fig. 4.5 shows the differences between the average abundances as derived from UVES and MIKE spectra for these two clusters. No systematic difference exists for any of the measured elemental abundances, this demonstrating that the two instruments provide abundances that are fully compatible within the uncertainties.

As an additional sanity check, we further repeated the analysis of the UVES

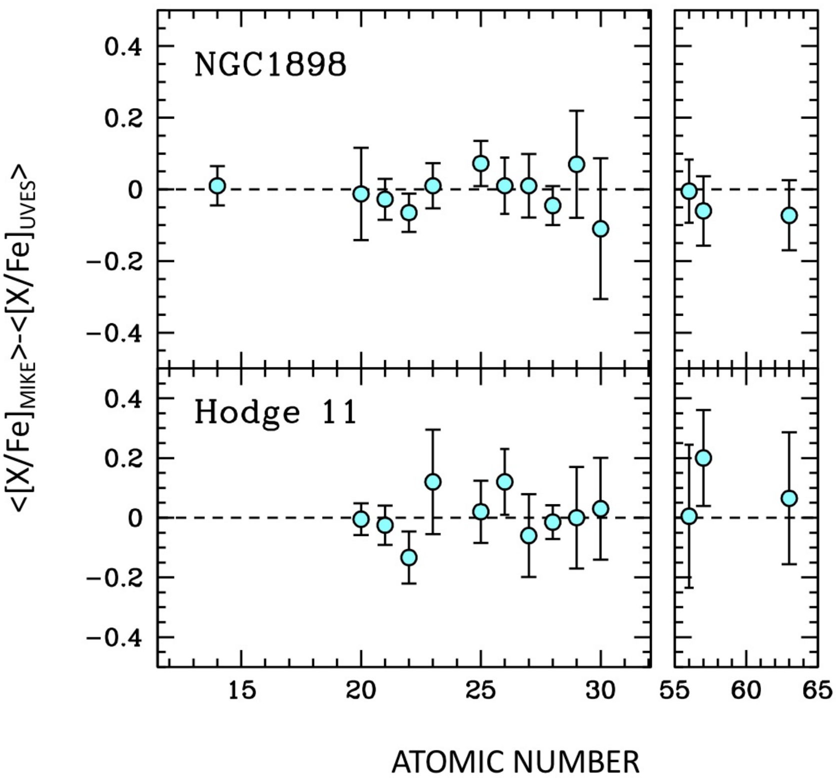

Figure 4.5: Differences between the average abundances derived from UVES and MIKE spectra for the clusters NGC 1898 (upper panel) and Hodge 11 (lower panel).

spectra of Hodge 11 and NGC 1898 by applying a smoothing filter, thus to reproduce the spectral resolution of the MIKE spectra, and by sampling the spectra to the pixel size of MIKE. This set of *MIKE-like* spectra allows to estimate whether some instrumental characteristics of the spectrograph (i.e. spectral resolution, efficiency and pixel size) can induce systematic differences in the derived abundances, for instance leading to over- or -under-estimate the continuum level or to significant variations in the derivation of the atmospheric parameters (temperatures and v_t have been derived spectroscopically). When these spectra are analyzed after fixing the stellar parameters obtained from the original UVES spectra, the average difference between the new and the original Fe abundances is -0.03±0.02 dex (σ= 0.05 dex). When the stellar parameters are re-derived, the average difference in [Fe/H] become -0.05±0.02 dex (σ= 0.05 dex), due to small changes in the stellar parameters themselves. In both cases, the characteristics of the MIKE spectra induce only a very small decrease of the Fe abundances, while the differences cancel out for the [X/Fe] abundance ratios.

Similarly to what we did in Fig. 4.2, Fig. 4.6 compares the average abundance ratios measured in two clusters with similar [Fe/H] but observed with the two spectrographs, namely NGC 1754 (observed with UVES) and NGC 2019 (observed with MIKE). Also for this pair of clusters, no significant differences are found and the abundance ratios of NGC 2019 are not systematically lower than those measured in NGC 1754.

Finally, we refer to the recent analysis of the Galactic benchmark star HD20 using both UVES and MIKE spectra (Hanke et al., 2020). Thanks to the very high S/N ratio of the spectra of this bright star (>400 for UVES and >1000 for MIKE), this comparison is adequate to highlight intrinsic differences solely due to the instruments (and not induced by the noise). The agreement between the abundances of Ti, Fe and Nd (the species with the largest number of available lines in the analysis) derived from the same lines and measured with UVES and MIKE is found to be excellent, thus excluding again significant systematics between the two instruments.

All these checks demonstrate that the abundances derived from MIKE and UVES are fully consistent with each other within the uncertainties and that the low abundance ratios measured in NGC 2005 are not an instrumental artifact.

4.7 Origin of the anomalous chemistry of NGC 2005

In order to determine the characteristics of NGC 2005 most likely progenitor, we computed chemical evolution models for different galactic environments. The analyzed data allowed us to produce models and calibrate them with respect to MW-like and LMC-like environment, and for systems evolving with less efficient star forma-

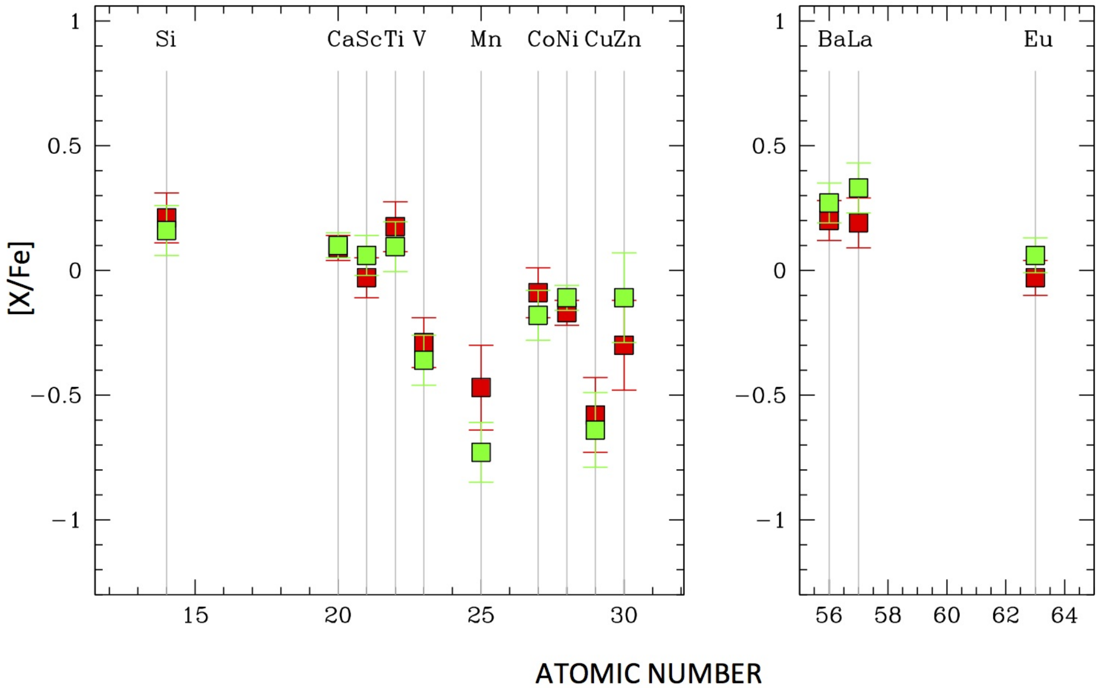

Figure 4.6: Abundance ratios measured for the clusters NGC 2019 (measured with MIKE, red square) and NGC 1754 (measured with UVES, green square).

tions. We purposely focused on elements with highly accurate stellar yields and that are representative of different nucleosynthesis channels (Table 4.3 and Fig. 4.1): Si and Ca (mainly produced through α-capture processes), Cu (mainly produced through slow neutron-capture processes) and Zn (mainly built in HNe high-energy explosions).

In Fig. 4.1 are superimposed the adopted chemical evolution models for the MW Halo (grey line), LMC (green line) and for NGC 2005 progenitor (red lines). Our models for the LMC reproduce reasonably well the data for all the LMC GCs but NGC 2005, which is always under-abundant at fixed metallicity. We run several chemical evolutionary models for the putative NGC 2005 parent galaxy. The ones that fit best the peculiar chemistry of NGC 2005 unavoidably require systems evolving with very low star formation efficiency, e.g., of dwarf spheroidal galaxies (Tolstoy et al., 2009). Although it is very difficult to set precise limits to the mass of the progenitor based on the chemistry alone, the very low [Zn/Fe] abundance measured in NGC 2005 with respect to the other LMC GCs suggests it formed from a gas poorly enriched from massive stars. In fact, in the framework of our models, Zn comes mainly from low-metallicity, massive ($> 30\mathrm{M}_{\odot}$) stars exploding as HNe (Romano et al., 2010). If the formation of such massive stars is suppressed, less Zn is formed, this resulting in a lower [Zn/Fe] ratio overall. It has been recently shown(Yan et al.,

2020) that the very low star formation rates expected in low-luminosity, metal-poor stellar systems lead to a lower upper mass limit for the galaxy-wide IMF. Indeed, if we consider star formation rates lower than $\sim 5 \cdot 10^{-4}\mathrm{M}_{\odot}\mathrm{yr}^{-1}$ and an upper mass limit of 40 $M_{\odot}$ for the galaxy-wide IMF, a remarkably good fit of the observed [Zn/Fe] ratio for NGC 2005 is obtained. All the other abundance ratios are fitted well within their errors under the same premises. These models for NGC 2005 are to be compared with the model for the LMC GCs that assumes a star formation rate of the order 1-1.5 $\mathrm{M}_{\odot}\mathrm{yr}^{-1}$ during the early LMC evolution and a galaxy-wide IMF upper mass limit of 100 $\mathrm{M}_{\odot}$.

4.8 Do observed counterparts of the progenitor of NGC 2005 exist?

The chemical abundance patterns measured in NGC 2005 and in the other LMC GCs demonstrate that the former originated in an environment characterized by a significantly less efficient star formation than that of the LMC. This is typical of dwarf spheroidal (dSph) satellites of the MW (Tolstoy et al., 2009). Thus it is natural to search among them, when looking for an existing galaxy similar to the putative progenitor of NGC 2005.

There are only two dSphs currently orbiting the MW that were able to form GCs: Sgr and Fornax. However, the abundance pattern of the Sgr is very similar to that of the LMC, as we found in our previous work (see Chapter 3), and as such it is not compatible with the chemical composition of NGC 2005. On the other hand, Fornax seems to fit all the properties of the progenitor galaxy of NGC 2005. In fact, the abundance pattern of NGC 2005 is remarkably similar to that of Fornax stars of the same metallicity. As we show in Fig. 4.7, other two dSph galaxies, namely Draco and Ursa Minor (Shetrone et al., 2001; Letarte et al., 2006; Cohen & Huang, 2009, 2010; Letarte et al., 2010; Lemasle et al., 2014; Ural et al., 2015) provide a good chemical match when compared to NGC 2005, but they have a stellar mass comparable to NGC 2005 itself ($\simeq 3 \times 10^5$ $\mathrm{M}_{\odot}$, McConnachie, 2012). Instead, Fornax has a stellar mass large enough ($\simeq 2 \times 10^7$ $\mathrm{M}_{\odot}$, McConnachie, 2012) to host a population of 5 old GCs, four of them being in the same mass range as NGC 2005 ($\gtrsim 1.3 \times 10^5$ $\mathrm{M}_{\odot}$, Leung et al., 2020). In general, dwarf galaxies with mass comparable to Fornax typically host between 0 and 6 globular clusters (Prole et al., 2019). The mass ratio between Fornax and LMC is $\frac{M_{For}}{M_{LMC}} < 0.01$, for both stellar and total (dynamical) mass. Therefore, the merging of a progenitor galaxy of NGC 2005 similar to the Fornax dSph with the LMC would classify as a minor merger, with negligible consequences on the structure of the LMC and negligible probability to leave a long-lived relic, except for a dense cluster with chemical composition not compatible with being born in the LMC. For this reason, the RV of NGC 2005 is similar to that of other clusters

in its surroundings, hence any (possible) strong anomaly due to its association with an accreted satellite has been washed out after many orbits within the gravitational potential of the LMC.
We conclude that the properties of the hypothesized progenitor galaxy of NGC 2005, now dissolved into the LMC, are fully compatible with well known existing galaxies, the Fornax dSph providing the best suited local example.

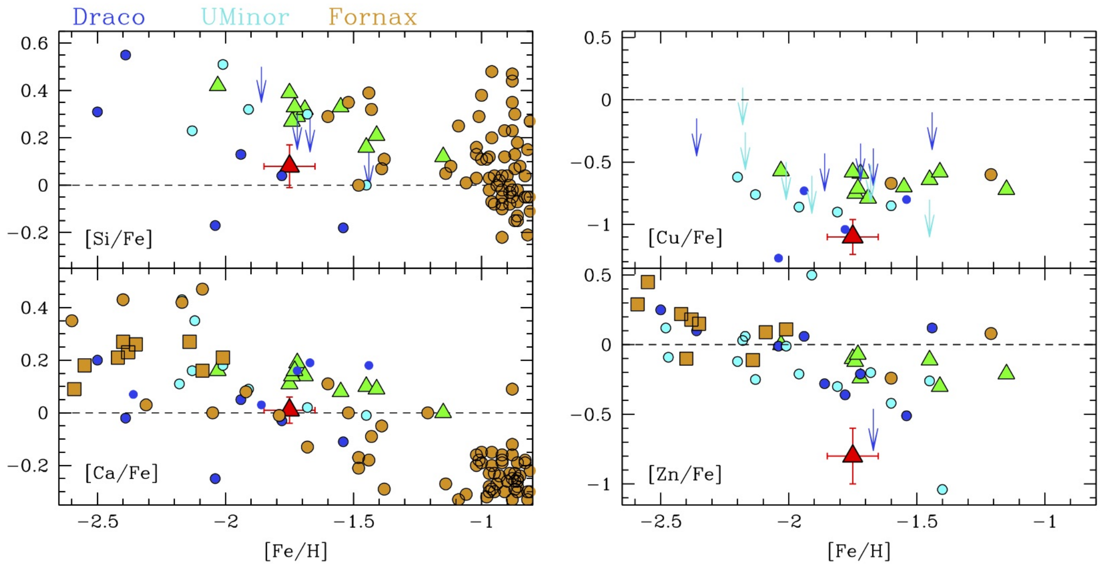

Figure 4.7: Behaviour of the [Si/Fe], [Ca/Fe], [Cu/Fe] and [Zn/Fe] abundance ratios as a function of [Fe/H] for the accreted LMC cluster NGC 2005 (red triangle) and the LMC clusters (green triangles) and the field stars in the dwarf spheroidal galaxies Fornax, Draco and Ursa Minor (orange, blue and cyan points, respectively; arrows indicate upper limits) and individual stars in the Fornax clusters (orange squares, Shetrone et al., 2001; Letarte et al., 2006; Cohen & Huang, 2009, 2010; Letarte et al., 2010; Lemasle et al., 2014; Ural et al., 2015).

4.9 Chemical evolution models

The trends of the abundance ratios of different chemical elements as a function of time (as traced by metallicity) in a given stellar system can be used to infer the structure formation timescale as well as the role of any gas inflow/outflow and the shape of the prevailing IMF. However, in order to do so, one needs to work out the proper chemical evolution model, tailored to the specific object under scrutiny.

The chemical evolution model for the MW adopted in this work is described extensively in previous papers (Chiappini et al., 2001; Romano et al., 2010). It assumes that the inner Galactic halo forms at early times from the accretion of unprocessed gas that triggers a very efficient star formation, of the order of $\sim$10 $M_\odot$ yr^{-1} on a Gyr timescale. The Galactic disc forms later on at a slower pace, but since our MW GCs data trace only the first $\sim$1 Gyr of Galactic evolution, in the following we omit all the details regarding the formation of the disc component – the interested reader is referred to the original papers. As we will see in the following, it is very important to calibrate the main ingredients of the chemical evolution model against a valid reference template; the MW provides indeed a very good anchor.

The models for the LMC and the putative NGC 2005 parent galaxy rest on previous work for dwarf Galactic satellites (Romano & Starkenburg, 2013; Romano et al., 2015). As for the LMC, we implement in the model the global SFH derived from observational pointers independent from chemical indicators (i.e., long-period variable star counts, which agree with previous studies by Rezaeikh et al., 2014). According to the adopted SFH, most LMC stars (about 75 per cent of the total stellar population) form during the first $\sim$3 Gyr of evolution. The star formation rate peaks at SFR $\sim$ 1–1.5 $M_\odot$ yr^{-1} during the first 1.5 Gyr of evolution, and steadily declines afterwards. As for the dwarf NGC 2005 progenitor, there are not independent SFH indicators that can be accessed, hence we assume a star formation burst forming 2×10^5 $M_\odot$ of stars in either 0.5 or 1 Gyr. The star formation of NGC 2005's progenitor galaxy is found to proceed at a much slower pace than that of the LMC, namely, <2.5–5 $\times$ 10^{-4} $M_\odot$ yr^{-1} (with the highest values corresponding to the shortest-duration burst).

In all models, cold gas of primordial chemical composition is accreted at an exponentially decreasing rate:

$$\frac{\mathrm{d}M_{\mathrm{inf}}(t)}{\mathrm{d}t} \propto \mathrm{e}^{-t/\tau} \tag{4.1}$$

where $M_{\mathrm{inf}}(t)$ is the mass accreted at time t and $\tau = 1$, 0.5 and 0.005 Gyr are the e-folding times for the MW, LMC and UFD NGC 2005 progenitor, respectively. We note that this smooth infall law produces results that are in qualitative agreement with those obtained by adopting much more complex accretion histories from cosmological simulations (Colavitti et al., 2008; Romano & Starkenburg, 2013).

The SFR is implemented according to the Kennicutt-Schmidt law (Schmidt, 1959; Kennicutt, 1998). In the model for the MW it reads

$$\psi(t) \propto \sigma_{\mathrm{gas}}^{k}(t), \tag{4.2}$$

where $\sigma_{\mathrm{gas}}(t)$ is the surface gas density at a given time and $k = 1.5$. In the models for dwarf galaxies it is

$$\psi(t) \propto M_{\mathrm{gas}}^{k}(t), \tag{4.3}$$

where $M_{\mathrm{gas}}(t)$ is the gas mass at a given time and $k = 1$.

As for the Galactic halo, the galaxy-wide IMF is the canonical one used in previous work (Kroupa, 2002), with $x = 1.7$ in the high-mass domain. A slightly steeper galaxy-wide IMF ($x = 1.9$ in the high-mass domain) is found to fit better the LMC data at relatively high metallicities; therefore, in Fig. 4.1 we show the results obtained with this IMF choice. Furthermore, in order to reproduce the chemical abundance ratios measured in NGC 2005, we find that it is necessary to require also a reduction of the upper mass limit of the IMF, from 100 to 40 $M_{\odot}$. These assumptions are justified, at least qualitatively, in the framework of the integrated galactic IMF theory by the low star formation rates and metal-poor environments that characterize dwarf and UFD galaxies (Yan et al., 2020).

4.9.1 Nucleosynthesis prescriptions

The most important ingredients of chemical evolution models are the stellar yields, namely, the amounts of different chemical elements that stars produce and eject into the ISM at their deaths. The chemical evolution models adopted in this study track the evolution of the abundances of several elements from hydrogen to europium, allowing us to study the evolution of elements that are produced by various nucleosynthetic processes in stars of different masses and initial chemical composition. The instantaneous recycling approximation is relaxed, i.e. we consider in detail the stellar lifetimes. In this way, different chemical elements are correctly restored to the ISM at different times, according to the lifetimes of their stellar progenitors.

We adopt grids of stellar yields calibrated against the MW data; in particular, with the adopted prescriptions for single low- and intermediate-mass stars (Karakas, 2010), massive stars (Nomoto et al., 2013) and SNe Ia (Iwamoto et al., 1999) (thermonuclear explosions of white dwarfs in binary systems, Matteucci & Greggio, 1986; Matteucci & Recchi, 2001), we are able to reproduce very well the average trends of the abundance ratios of several elements, including [Si/Fe], [Ca/Fe], [Zn/Fe], and [Cu/Fe], as a function of [Fe/H] in the Galactic halo (Romano et al., 2010). In particular, regarding the high-mass stars, we use a mixture of “normal” SNe II, which explode releasing energies of the order of 10^{51} ergs, and HNe, characterized by much larger explosion energies. In particular, by considering HNe explosions it is possible to explain the run of [Zn/Fe] with [Fe/H] in halo stars (Kobayashi et al., 2006; Romano et al., 2010). We obtain a good fit to the data presented in this study by assuming that as many as 95 per cent of stars with $m > 20$ $M_{\odot}$ explode as HNe for [Fe/H]< -2.5, while the HNe fraction goes to zero for [Fe/H]> -1 dex. In order to fit the MW GC data at best, we further adopt zero-point shifts of -0.2 dex for both [Si/Fe] and [Zn/Fe] (well inside the range allowed by theoretical uncertainties and observational systematics that may affect the ratios). The same stellar nucleosynthesis prescriptions (and zero-point shifts) are then adopted in the models for the LMC and NGC 2005's parent galaxy. Interestingly, it is found that the best agreement between model predictions and relevant data is obtained with a galaxy wide IMF that varies in qualitative agreement with the predictions of the integrated galactic IMF theory (Yan et al., 2020).

4.10 Summary

We performed a homogeneous analysis of the chemical composition of 13 old LMC GCs finding that the cluster NGC 2005 exhibits systematically lower abundance ratios with respect to the clusters with similar metallicities. The peculiar chemical composition of NGC 2005 suggests that this cluster originated in a galaxy that formed its stars with a much less efficient star formation compared to the LMC. This evidence suggests a low-mass galaxy progenitor, as massive as the dwarf spheroidal galaxies currently orbiting the MW or even lighter, characterized by low SFR (Tolstoy et al., 2009). NGC 2005 is the surviving witness of the ancient merger event leading to the dissolution of its parent galaxy into the LMC, the only case known so far identified by its chemical fingerprints in the realm of dwarf galaxies. Our findings thus support the predictions on the self-similar nature of the process of galaxy formation by the standard cosmology on our closest satellite, and open a new way to investigate the assembly history of galaxies beyond the MW via the chemical tagging of their GC systems.

Chapter 5

The chemical composition of 206 Small Magellanic Cloud red giant stars

Based on the results in
Mucciarelli A., Minelli A., Romano D., Ferraro F.R., Origlia L., 2022 submitted

5.1 Introduction

The SMC is the second most massive MW satellite after the LMC, with a total mass of $\sim 2 \cdot 10^9 M_\odot$ (Stanimirović et al., 2004). The two Clouds are gas-rich irregular galaxies, gravitationally bound each other and likely at the first passage of the MW (Besla et al., 2007, 2010; Besla, 2015; Kallivayalil et al., 2013). The history of the stellar populations of the SMC is intimately linked to the interplay of these three galaxies.

The CMD of different SMC fields (see e.g. Harris & Zaritsky, 2004; Noël et al., 2007; Cignoni et al., 2012, 2013) reveal the mixture of stellar populations in this galaxy, with prominent RGB and He-Clump, signatures of stellar populations older than 1-2 Gyr, and the presence of an extended blue main sequence, signatures of younger stellar populations.

The SFH of the SMC has been extensively investigated through the use of synthetic CMDs both using ground-based (Zaritsky et al., 2002) and Hubble Space Telescope photometry (Dolphin et al., 2001; Noël et al., 2007; Sabbi et al., 2009; Cignoni et al., 2012, 2013). Our current picture is the star formation activity in the SMC started slowly ~13 Gyr ago, with a prolonged period of low star formation activity until ~4-6 Gyr ago, when a new, vigorous burst of star formation occurred, likely forming most of the stars that we observe today.

Thanks to their proximity and the possibility to resolve individual stars both with photometry and spectroscopy, the MCs are an excellent opportunity to study the local cosmology and in particular the chemical enrichment histories and SFH of gas-rich and interacting galaxies, at variance with the dwarf spheroidal galaxies populating the LG that are gas-poor and isolated systems.

At variance with the LMC stars whose chemical composition has been widely studied using high-resolution spectroscopy (Hill et al., 2000; Pompéia et al., 2008; Mucciarelli et al., 2010; Lapenna et al., 2012; Van der Swaelmen et al., 2013; Nidever et al., 2020; Mucciarelli et al., 2021a), the chemical composition of the SMC stars has received less attention, despite the proximity of this galaxy (∼62 kpc, Graczyk et al., 2014).

For decades, the only high-resolution spectroscopic studies on SMC stars were mainly focused on bright supergiant stars and Cepheids, hence sampling stellar populations younger than ∼200 Myr (see e.g. Spite et al., 1989a,b; Hill et al., 1997; Romaniello et al., 2008). Most of the information about the metallicity distribution of the SMC RGB stars came from low-resolution spectroscopy in I-band, using the calibrated strength of the Ca II triplet as a proxy of [Fe/H] (Carrera et al., 2008b; Dobbie et al., 2014b,a; Parisi et al., 2016) Only recently, chemical analyses of high-resolution spectra in SMC RGB stars have been presented (Nidever et al., 2020; Reggiani et al., 2021; Hasselquist et al., 2021), allowing us to investigate in details the chemical composition of these stellar populations.

In this Chapter, we present the chemical analysis of 206 RGB stars members of the SMC observed with the high-resolution spectrograph FLAMES mounted at the ESO Very Large Telescope.

5.2 Observations and data reduction

5.2.1 SMC sample

A total of 320 stars in the direction of the SMC have been observed (ID program 086.D-0665, PI: Mucciarelli) with the multi-object spectrograph FLAMES (Pasquini et al., 2002) in the GIRAFFE-MEDUSA mode that allows us the simultaneous allocation of 132 high-resolution (R∼20000) fibers over a patrol field of about 25 arcmin diameter. Three different fields have been observed, centered around three GCs, namely NGC 121, NGC 339 and NGC 419 (hereafter these fields will be indicated as FLD-121, FLD-339 and FLD-419, respectively). Fig. 5.1 shows the spatial location of the three FLAMES fields superimposed to the map of the SMC stars obtained with the eDR3 of the *Gaia*/ESA mission (Gaia Collaboration et al., 2016, 2021).

The fields are located in different positions of the SMC: FLD-419 is located ∼ 1.5° eastern from the SMC center (Ripepi et al., 2017), FLD-339 is located ∼ 1.4° southern-eastern from the SMC center, while FLD-121 is in the SMC outskirt, ∼ 2.4°

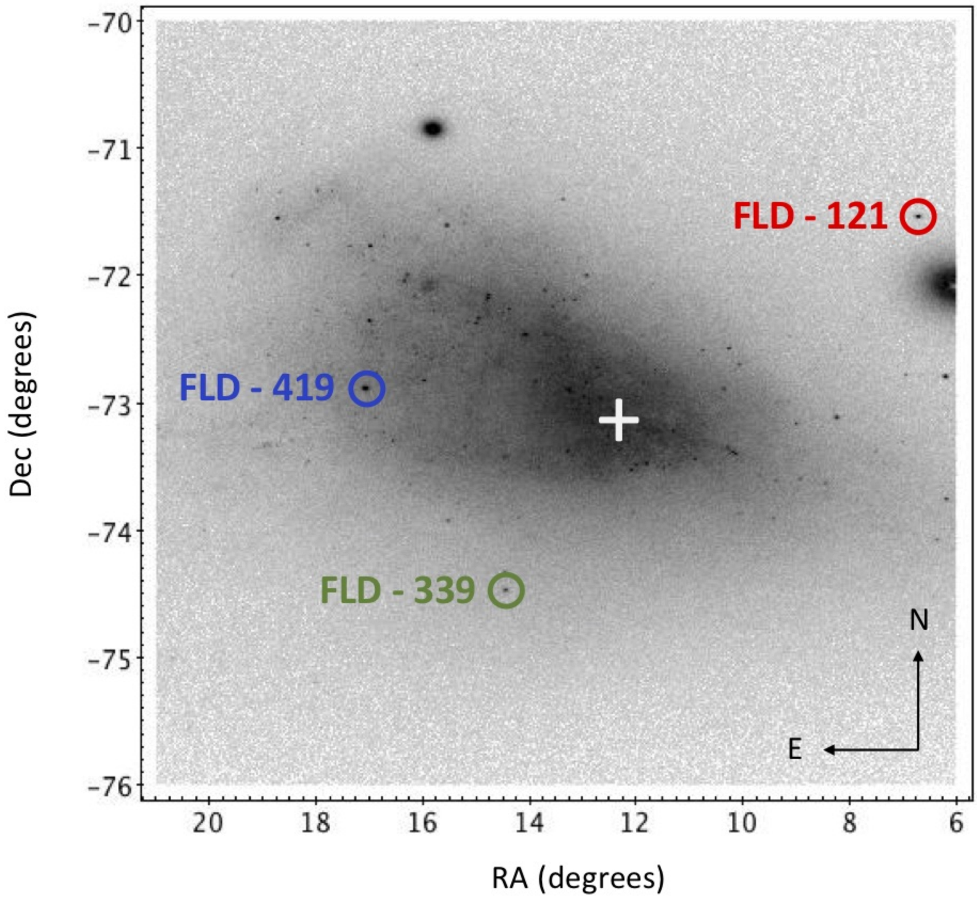

Figure 5.1: Spatial distribution of the fields observed with FLAMES (marked with red circles) superimposed to the map of the SMC stars from *Gaia* eDR3 (Gaia Collaboration et al., 2016, 2021). The white plus symbol marks the position of the SMC center derived by Ripepi et al. (2017) using Classic Cepheids observed within the Vista Magellanic Clouds Survey.

western from the SMC center.

The adopted GIRAFFE-MEDUSA grating setups are HR11, with a spectral resolution of 24200 and ranging from 5597 to 5840 Å , and HR13, with a spectral resolution of 22500 and a spectral coverage between 6120 and 6405 Å . These two setups allow to measure lines of the main groups of elements, like odd-Z (Na), α (O, Mg, Si, Ca and Ti), iron-peak (Sc, V, Fe, Ni, Cu) and s-process elements (Zr, Ba, La). The UVES fibers have been allocated to targets belonging to the three globular clusters and discussed in separated works (Dalessandro et al., 2016, and the work described in the next Chapter).
Table 5.1 lists the exposure times and the number of individual exposures for each setup and field.

Table 5.1: SMC observed fields. Coordinates of the FLAMES pointing, number of exposures and exposure times for the two FLAMES gratings, adopted color excess (Schlafly & Finkbeiner, 2011) and the number of observed SMC stars analyzed in this work.

Field	RA (J2000)	Dec (J2000)	HR11	HR13	E(B-V) (mag)	N_{SMC}
FLD-419	01:08:17.7	−72:53:02.7	6x2700sec	4x2700sec	0.089	91
FLD-339	00:57:48.9	−74:28:00.1	9x2700sec	5x2700sec	0.042	78
FLD-121	00:26:49.0	−71:32:09.9	7x2700sec 1x2200sec	5x2700sec	0.028	37

The spectroscopic targets have been originally selected from near-infrared (K_s, J-K_s) CMDs, using the SofI@NTT catalogs (Mucciarelli et al., 2009a, for NGC 339 and NGC 419, and unpublished proprietary photometry for NGC 121) for the region within 2.5 arcmin from the cluster center and the 2MASS database (Skrutskie et al., 2006) for the external regions. The targets have been selected according to the following criteria: (1) stars fainter than the RGB Tip (K_s=12.62, Cioni et al., 2000); (2) stars brighter than K_s= 14 for FLD-339 and FLD-419, and brighter than K_s= 14.4 for FLD-121, in order to guarantee a SNR per pixel larger than 20-30 in both setups and in all the observed fields. Due to the poorness of SMC RGB stars in the SMC outskirts, a fainter magnitude threshold has been adopted for FLD-121 in order to enlarge the number of observed SMC stars; (3) isolated stars, i.e. stars without close stars brighter than $K_s< K_s^{star}$+1.0 within 2" ; (4) for the targets from the 2MASS catalog (the majority of the observed targets) only stars with J and K_s magnitudes flagged as *A* (photometric uncertainties smaller than 10%) have been selected.

All the targets have been recovered in the *Gaia* eDR3 catalog. Fig. 5.2 shows the position in the (G, BP-RP) CMDs of the observed targets resulted to be SMC stars according to their RV, see Section 5.3.3.

The spectra have been reduced with the dedicated ESO GIRAFFE pipeline*, including bias-subtraction, flat-fielding, wavelength calibration with a standard Th-Ar lamp and spectral extraction. The contribution of the sky has been subtracted from each spectrum by using a median sky spectrum, as obtained by combining ∼15-20 spectra from fibers allocated to sky positions within each exposure.

5.2.2 MW globular clusters control sample

As discussed in Chapter 3, the comparison between abundances obtained from different works can be hampered by various systematics characterizing the chemical analyses, for instance related to the method used to infer the stellar parameters, the

*http://www.eso.org/sci//software/pipelines/

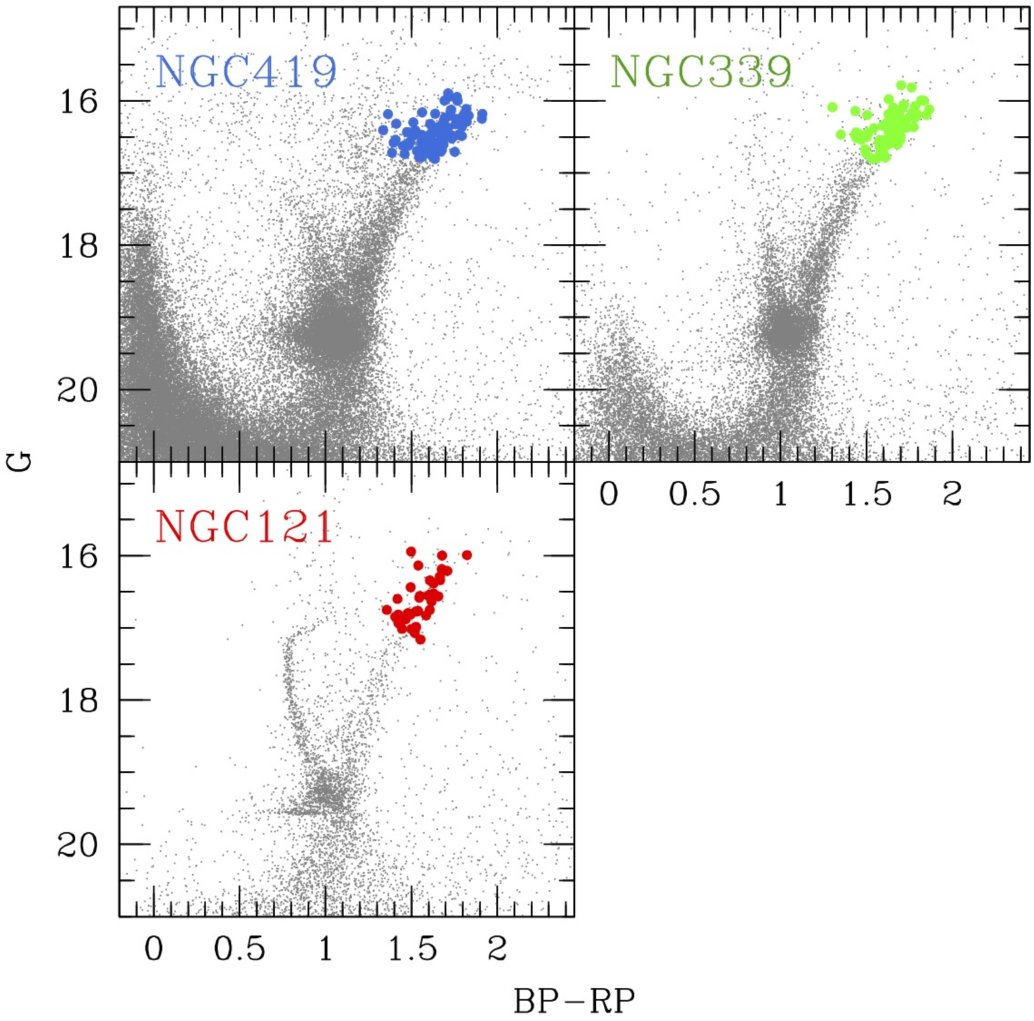

Figure 5.2: Position of the spectroscopic targets of the SMC field stars (grey dots) in the (G, BP-RP) CMDs. In the CMD of FLD-121 is visible the main sequence of the globular cluster 47 Tucanae.

adopted atomic data, model atmospheres and solar reference abundances. For this reason, when chemical analyses of extra-galactic stars are performed, it is crucial to analyze a control sample of MW stars analyzed in an homogeneous way.

In order to highlight and quantify possible differences and similarities between SMC and MW stars, we defined a control sample of MW stars analysed with the same method and assumptions used for the SMC stars (i.e. temperature scale, atomic data, solar reference abundances). We analyzed some MW GCs covering the same metallicity range of the SMC stars ([Fe/H] between ~ -2.2 and ~ -0.5 dex) and for which FLAMES spectra obtained with the GIRAFFE set-ups HR11 and HR13 are available in the ESO archive (ID programs: 072.D-0507 and 083.D-0208, PI: Carretta). The selected GCs are NGC 104, NGC 1851, NGC 1904, NGC 4833 and

NGC 5904. We restrict the analysis only to the stars with T_{eff} and log g comparable with those of the SMC stars studied here. Only for O and Na that exhibit large star-to-star variations in each of these GCs, we analyzed stars belonging to the so-called first population and selected according to Carretta et al. (2009a). The O and Na abundances of these first population stars can be considered as a good proxy of the chemical composition of the MW field at those metallicities.

5.3 Spectral analysis

5.3.1 Line selection

A first set of unblended metallic lines has been selected by visual inspection of suitable synthetic spectra calculated with the code `SYNTHE` (Sbordone et al., 2004; Kurucz, 2005), using the typical atmospheric parameters of the observed stars (see Section 5.3.2), adopting `ATLAS9` model atmospheres (Castelli & Kurucz, 2003) and including all the atomic and molecular transitions in the Kurucz/Castelli linelist†. The synthetic spectra have been convoluted with Gaussian profiles in order to reproduce the spectral resolution of the adopted GIRAFFE gratings. We privileged transitions with laboratory oscillator strengths. Only for the Sc II line at 6245.6 Å , for the Si I lines at 6155.1 and 6237.3 Å , and for the Cu I line at 5782 Å we adopted solar oscillator strengths. All the used lines are listed in Table 5.2 together with the corresponding log gf and excitation potential χ. We adopted an iterative process to define the linelist. A preliminary linelist has been defined by adopting a metallicity [M/H] = –1.0 dex for all the used synthetic spectra, according to the mean metallicity of the SMC derived from the Ca II triplet analysis by Carrera et al. (2008b); Dobbie et al. (2014b,a); Parisi et al. (2016). After a first chemical analysis, new and appropriate linelists have been defined for each star according to their metallicity, and for a few stars strongly enhanced in s-process elements (see Section 5.5).

5.3.2 Atmospheric parameters

T_{eff} and $\log g$ have been estimated from the photometry. In particular, T_{eff} have been obtained from the broad-band color $(G - K_s)_0$ adopting the $(G - K_s)_0$-T_{eff} transformation provided by Mucciarelli et al. (2021b). We adopted G magnitudes from *Gaia* eDR3 and K_s from 2MASS. G magnitudes have been corrected for extinction following the prescription by Gaia Collaboration et al. (2018b), while K_s magnitudes adopting the extinction coefficient by McCall (2004). The color excess values E(B-V) are from the infrared dust maps by Schlafly & Finkbeiner (2011) and listed in Table 5.1.

† http://wwwuser.oats.inaf.it/castelli/linelists.html

Table 5.2: List of all the used lines, with the corresponding log gf, excitation potential χ and the reference of the data origin.

Wavelength	Ion	log gf	χ	REF
5590.720	27.00	-1.870	2.042	Fuhr et al. (1988)
5598.480	26.00	-0.087	2.521	Fuhr & Wiese (2006)
5601.277	20.00	-0.523	2.526	Smith & Raggett (1981)
5611.356	26.00	-2.990	3.635	Fuhr et al. (1988)
5615.644	26.00	0.050	3.332	Fuhr & Wiese (2006)
5618.632	26.00	-1.276	4.209	Fuhr & Wiese (2006)
5624.542	26.00	-0.755	3.417	Fuhr & Wiese (2006)
5633.946	26.00	-0.320	4.991	Fuhr & Wiese (2006)
5638.262	26.00	-0.840	4.220	Fuhr & Wiese (2006)
5647.234	27.00	-1.560	2.280	Fuhr et al. (1988)
5648.565	22.00	-0.260	2.495	Martin et al. (1988a)
5650.689	26.00	-0.960	5.085	Fuhr & Wiese (2006)
5651.469	26.00	-2.000	4.473	Fuhr et al. (1988)
5652.318	26.00	-1.920	4.260	Fuhr & Wiese (2006)
5653.867	26.00	-1.610	4.386	Fuhr & Wiese (2006)
5661.345	26.00	-1.756	4.284	Fuhr & Wiese (2006)
5662.516	26.00	-0.573	4.178	Fuhr & Wiese (2006)
5670.8**	23.00	-0.420	1.081	Martin et al. (1988a)
5679.023	26.00	-0.900	4.652	Fuhr & Wiese (2006)
5682.633	11.00	-0.706	2.102	NIST

Uncertainties in T_{eff} have been estimated by propagating for any individual star the photometric error in the adopted color and the error in the color excess, assuming conservatively an uncertainty of 50% in E(B-V). These uncertainties have been added in quadrature to the typical error associated to the $(G - K_s)_0$-T_{eff} transformation (46 K), estimated as 1σ dispersion of the fit residuals, and that dominates the total T_{eff} errors (typically ∼50-60 K).

The log g values have been calculated through the Stefan-Boltzmann relation adopting the photometric T_{eff}, a true distance modulus $(m - M)_0 = 18.965 \pm 0.025$ (Graczyk et al., 2014), the bolometric corrections by Andrae et al. (2018) and a stellar mass of 1.0 $M_\odot$. Uncertainties in log g are of the order of 0.1, including the uncertainties in T_{eff}, distance modulus and stellar mass.

v_t are usually derived spectroscopically by erasing any trend between Fe abundance and the reduced equivalent widths (defined as the logarithm of the EW normalized to the wavelength). Because of the small number of available lines in the adopted spectral ranges, v_t derived spectroscopically risk to be uncertain or unreliable. In order to avoid the risk of significant fluctuations in the derived v_t (with an impact on the derived abundances), this parameter has been estimated adopting the log g - v_t relations provided by Mucciarelli & Bonifacio (2020) and based on the spectroscopic v_t derived from high-resolution spectra of giant stars in 16 Galactic GCs. The uncertainty in v_t has been estimated by adding in quadrature the error arising from the uncertainty in log g and that of the adopted log g - v_t relation.

5.3.3 Radial velocities

RVs have been measured by using the code DAOSPEC (Stetson & Pancino, 2008) that performs a line fitting assuming a Gaussian profile. The code is automatically launched by using the software 4DAO (Mucciarelli, 2013) that allows a visual inspection of all the fitted lines in order to directly evaluate the quality of the fitting procedure. RVs have been measured by the position of about 100 metallic lines for each star. The internal uncertainty is estimated by dividing the dispersion of the mean by the root mean square of the number of used lines and it is of the order of 0.1-0.3 km/s in both gratings. The accuracy of the wavelength calibration has been checked by measuring the position of the strong emission sky line at 6300.3 Å in the HR13 grating, finding no significant offset. No sky emission lines are available in the HR11 setup and we cannot directly checked the accuracy of the wavelength calibration. However, the RVs obtained from the two setups agree each other excluding any offset for the two setups and confirming the accuracy also of the HR11 spectra.

5.3.4 Chemical abundances

The chemical abundances of Na, Mg, Si, Ca, Ti, Fe and Ni have been derived from the measure of the equivalent widths (EWs) of unblended lines by using the code GALA (Mucciarelli et al., 2013). EWs have been measured by using the code DAOSPEC (Stetson & Pancino, 2008). The model atmospheres have been calculated with the last version of the ATLAS9 code[‡].

For species whose lines are affected by blending (O, Mg) or by hyperfine/isotopic splitting (Sc, V, Cu, Ba and La), abundances have been derived using our own code SALVADOR that performs a χ^2-minimization between the observed lines and a grid of synthetic spectra calculated with the code SYNTHE (Sbordone et al., 2004) and including all the atomic and molecular lines available in the Kurucz/Castelli linelists.

5.3.5 Abundance uncertainties

In the determination of the uncertainties in each derived abundance ratio we take into account two main sources of error, namely the errors arising from the measurement procedure (EW or spectral synthesis) and those arising from atmospheric

[‡]http://www.oact.inaf.it/castelli/castelli/sources/atlas9codes.html

parameters. These two sources of uncertainties have been added in quadrature, according to the equations reported in Section 3.4.1. Because we are interested to the error in a given abundance ratio [X/Fe], the errors in [X/H] and [Fe/H] have been combined in quadrature.
(1) Uncertainties related to the measurement procedure are computed as the dispersion of the mean normalized to the root mean square of the number of used transitions. For the elements measured from the EWs and for which one only line is available, the `DAOSPEC` uncertainty associated to the Gaussian fitting procedure is assumed as internal error.
(2) For the elements (O and La) for which one only transition has been measured using spectral synthesis, the internal error has been estimated by means of Monte Carlo simulations (same procedure described in Section 4.4.1.)
(3) Uncertainties due to atmospheric parameters have been estimated by repeating the analysis by varying each time a given parameter of the corresponding 1σ error and keeping fixed the other parameters.

5.4 RV and metallicity distribution

According to previous spectroscopic studies of SMC stars (Harris & Zaritsky, 2006; Carrera et al., 2008b; Dobbie et al., 2014b; Hasselquist et al., 2021) we identified as SMC stars those stars with RV larger than 100 km/s for a total of 206 stars out of the 320 observed stars.

Fig. 5.3 show the RV and [Fe/H] distributions of the three SMC fields.
In FLD-419 Fe abundances range from – 1.46 dex to – 0.68 dex, with only one star with [Fe/H] = – 2.18 dex. Excluding this star, the [Fe/H] distribution peaks at [Fe/H] = – 1.04 ± 0.02 dex, with a dispersion σ = 0.17 dex.
In FLD-339 all the stars have [Fe/H] between – 1.57 dex and – 0.52 dex, with a mean value of [Fe/H] = – 0.99 ± 0.02 dex and a dispersion σ = 0.18 dex.
The metallicity distribution of the stars in FLD-121 shows a main peak at [Fe/H] ∼ – 1.0 dex, consistent with the distributions observed in the other two fields, and a metal-poor tail reaching [Fe/H] = – 2.18 dex and lacking in the other two distributions (with the only exception of one only metal-poor star in FLD-419).

The total metallicity distribution peaks at [Fe/H] = – 1.06 dex (σ = 0.26 dex), compatible with both those obtained from Ca II triplet and that provided by Nidever et al. (2020). Reggiani et al. (2021) analysed four metal-poor SMC stars in common with our FLD-121 field obtaining [Fe/H] lower by ∼ – 0.25 dex than our ones reaching a value of [Fe/H] = – 2.60 dex, while the lower [Fe/H] reached in this sample is [Fe/H] ∼ – 2.2 dex. These differences can be mainly explained as due to the different v_t used in the two works, with the values derived by Reggiani et al. (2021) higher by 1 km/s than our ones.

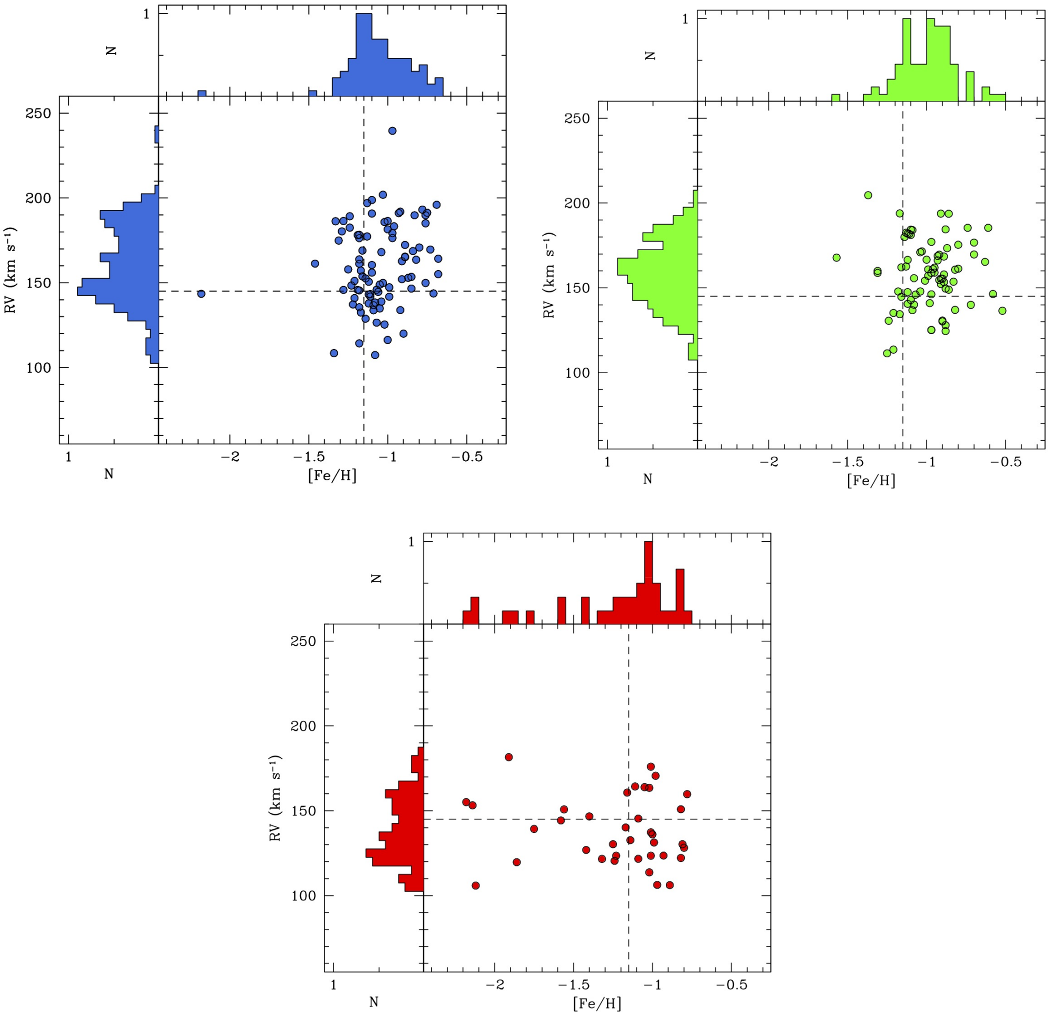

Figure 5.3: For each observed field (FLD-419 in blue, FLD-339 in green and FLD-121 in red), the main panel shows the behavior of RVs as a function of [Fe/H] for the observed SMC stars, while the normalized histograms of [Fe/H] and RV are shown. The dashed lines mark the position of the main peaks in the RV and [Fe/H] distribution in FLD-419 as a reference.

Fig. 5.4 shows the spectra of two SMC giant stars with very similar atmospheric parameters but a large (~ -1.5 dex) difference in [Fe/H].

5.5 Results

We derived abundances of Na, O, Mg, Si, Ca, Sc, Ti, V, Fe, Ni, Cu, Zr, Ba and La for 206 SMC RGB stars. Fig. 5.5-5.10 show the behavior of different abundance ratios as a function of [Fe/H] for the analyzed SMC stars, highlighting stars belonging to the different SMC fields. These abundance ratios are compared with those obtained

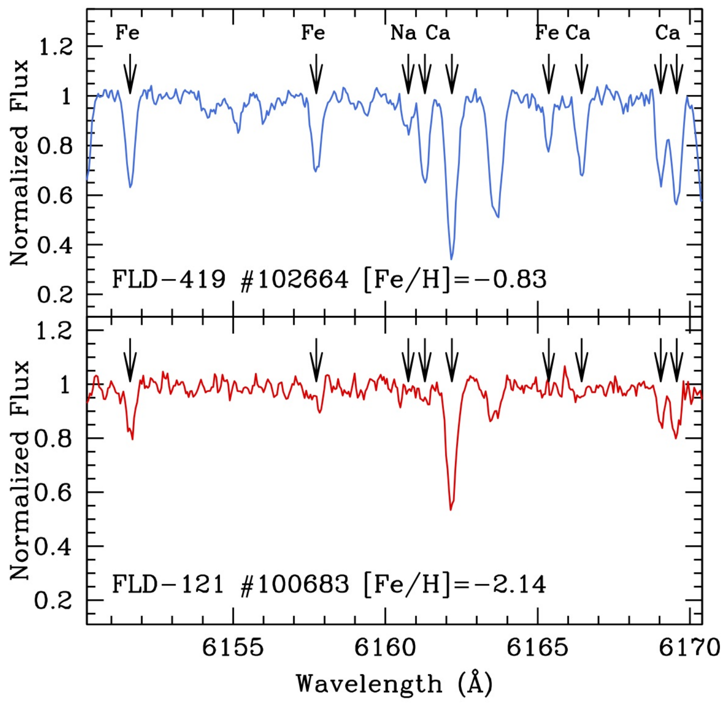

Figure 5.4: Comparison between the spectra of the stars FLD-419 #102664 (upper panel) and FLD-121 #100683 (lower panel) with very similar atmospheric parameters but different Fe content. Arrows mark the position of some metallic lines of interest.

for the control sample of 5 Galactic GCs, adopting the same assumptions in the chemical analysis (i.e. atomic data, solar reference values, model atmospheres, T_{eff} scale), therefore allowing a direct comparison with the SMC stars without the main systematics of the analyses. Additionally, we show abundance ratios for Galactic field stars from the literature as reference.

5.5.1 Na

Sodium is mainly produced in massive stars during the hydrostatic C and Ne burning, with a smaller contribution by AGB stars. In Galactic stars, [Na/Fe] increases by increasing [Fe/H] until solar values at [Fe/H] > -1 dex. Fig. 5.5 shows the distribution of [Na/Fe] of the observed targets. The bulk of the SMC stars exhibits sub-solar [Na/Fe] abundance ratios at any metallicities, with an average value of about -0.5 dex, similar to the typical [Na/Fe] measured in LMC stars (see Chapter 3, and Van der Swaelmen et al., 2013). The low [Na/Fe] values measured in the SMC stars point out a lower contribution by massive stars. Below [Fe/H] < -1.5 dex the upper limits that we provided for [Na/Fe] do not allow to provide firm conclusions for metal-poor stars.

5.5.2 α-elements

As already discussed in the introduction (Section 1.1.1), α-elements are produced mainly in massive stars exploding as SNe II, while a minor fraction is synthesized in SNe Ia. Due to the time delay between the enrichment of the two classes of SNe, the metallicity of the *knee* (marking the onset of the chemical contribution by SNe Ia) can be used as a proxy of the star formation efficiency of the galaxy.

O and Mg (the so-called hydrostatic α-elements) are produced mainly in stars with masses larger than ~30-35 $M_{\odot}$. On the other hand, Si, Ca and Ti (explosive α-elements) are produced in less massive stars (~15-25 $M_{\odot}$) and with a smaller (but not negligible) contribution by SNe Ia (see e.g. Kobayashi et al., 2020). Fig. 5.5 and 5.6 show the behavior with [Fe/H] of individual [α/Fe] abundance ratios, while Fig. 5.7 shows the run of the average values of hydrostatic and explosive [α/Fe]. These abundance ratios in the SMC stars clearly show a decrease by increasing the metallicity, moving from enhanced values for the most metal-poor stars ([Fe/H] < – 1.5 dex) down to solar-scaled values in the dominant population.

The most metal-poor stars exhibit [α/Fe] values compatible with those measured in our MW GCs control sample, and in agreement with the results by Nidever et al. (2020) and Reggiani et al. (2021) for SMC stars of similar metallicity. The subsequent decrease of [α/Fe] at higher [Fe/H] indicates that these stars formed from a gas enriched by SNe Ia. For stars with [Fe/H] > – 1.5 dex the difference in [α/Fe] between SMC and MW stars becomes more significant. In particular, the difference with the values measured in MW GCs is more pronounced for hydrostatic α-elements, suggesting a lower contribution to the chemical enrichment by stars with masses larger than 30-35 $M_{\odot}$.

The paucity of SMC stars with [Fe/H] < – 1.3 dex makes hard to properly identify the metallicity of the *knee* but this should be located at [Fe/H] lower than –1.5 dex, while Nidever et al. (2020) proposed the it is located at [Fe/H] < – 2.2 dex. However, the general behaviour of the measured [α/Fe] does not completely agrees with that obtained by Nidever et al. (2020) finding a flat run of [α/Fe] between [Fe/H] –1.5 and –0.5 dex.

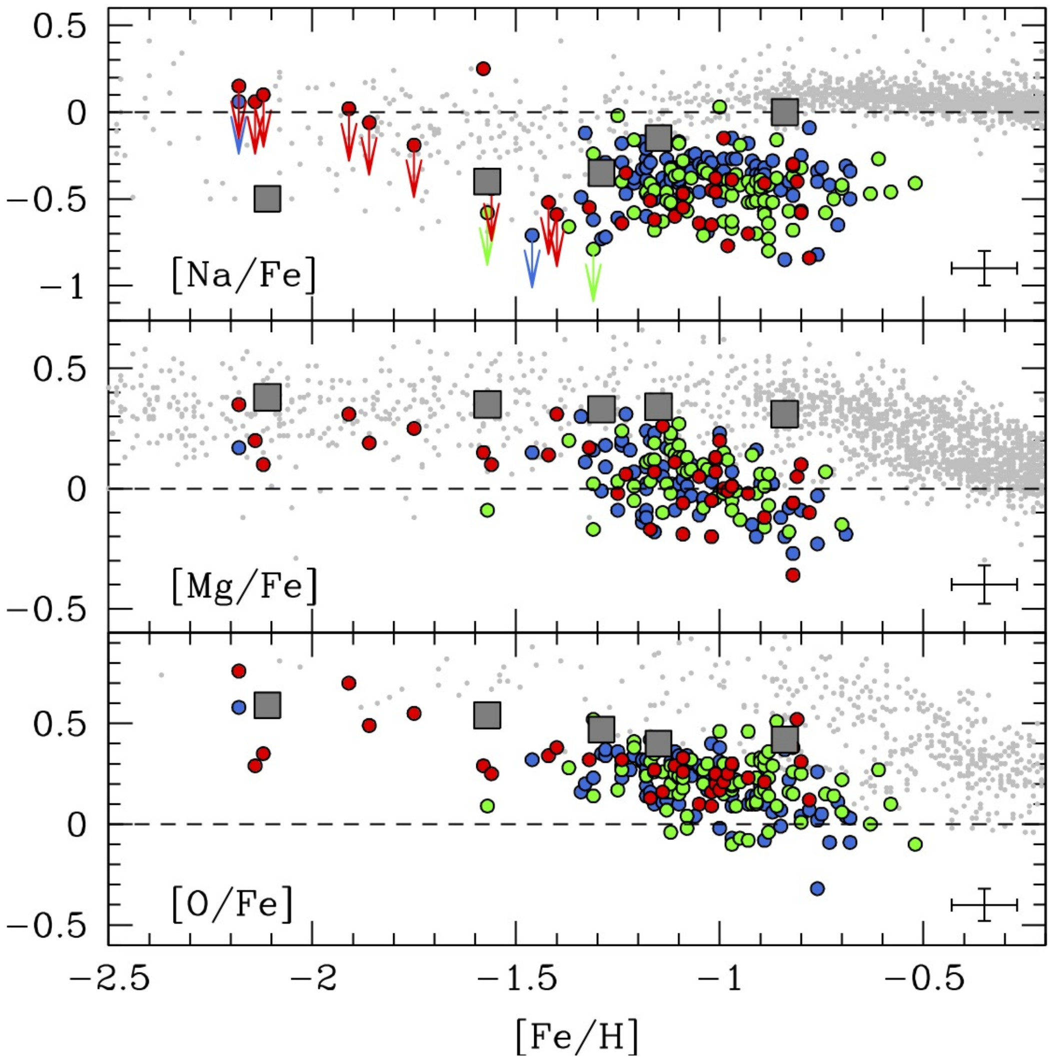

Figure 5.5: Behavior of the light element [Na/Fe] and α-elements [O/Fe] and [Mg/Fe] abundance ratios as a function of [Fe/H] for SMC stars located in the fields FLD-419, FLD-339 and FLD-121 (blue, green and red circles, respectively). Arrows indicate upper limits. The errorbars in the bottom-right corner indicate the typical uncertainties. Grey squares are the average values for the five Galactic GCs of the control sample. Abundances of Galactic stars from the literature are also plotted as a reference: Edvardsson et al. (1993); Gratton et al. (2003); Reddy et al. (2003, 2006) for all the elements, Fulbright (2000); Stephens & Boesgaard (2002); Adibekyan et al. (2012); Bensby et al. (2014); Roederer et al. (2014) for Na and Mg, Bensby et al. (2005) for O and Mg, Barklem et al. (2005) for Mg.

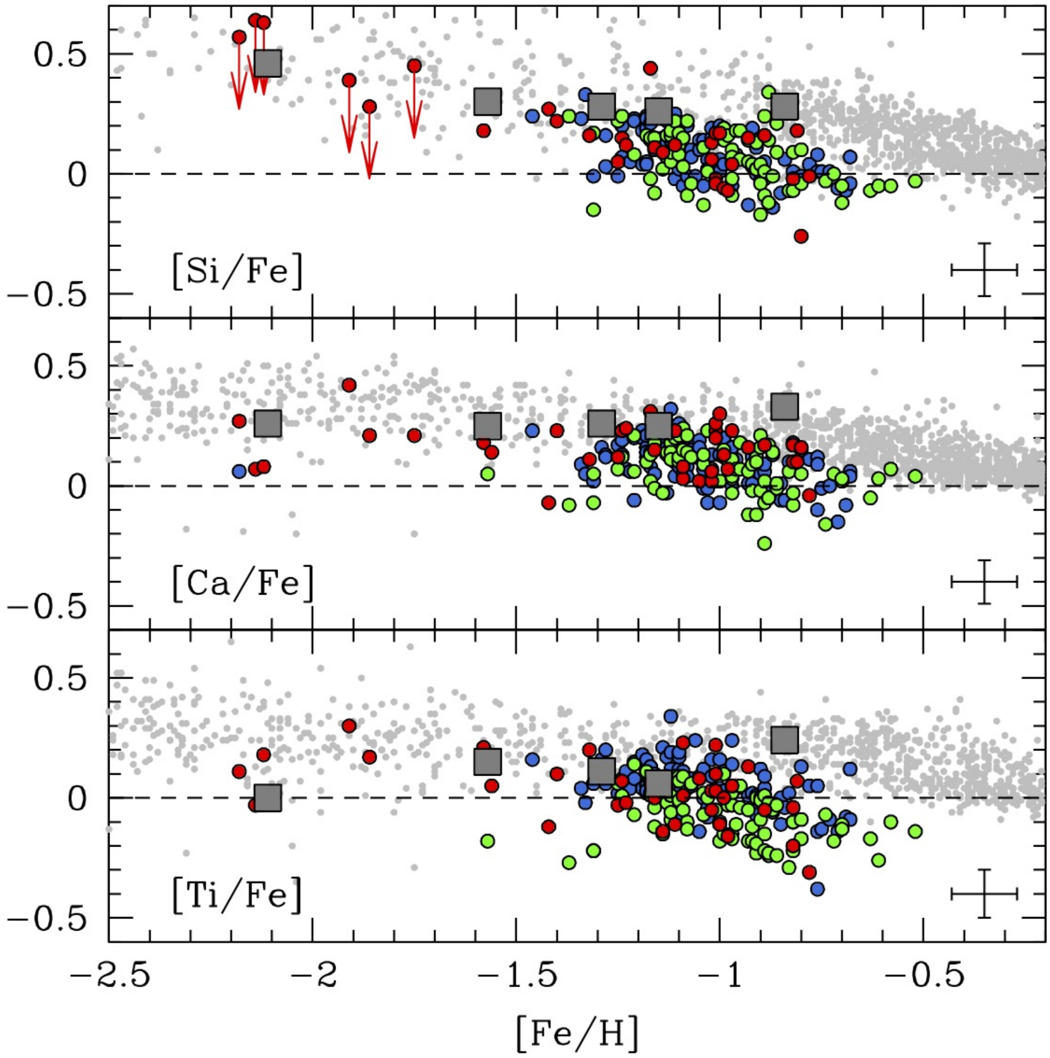

Figure 5.6: Behavior of the α-elements [Si/Fe], [Ca/Fe] and [Ti/Fe] abundance ratios as a function of [Fe/H]. Abundances of Galactic field stars are from Edvardsson et al. (1993); Fulbright (2000); Stephens & Boesgaard (2002); Gratton et al. (2003); Reddy et al. (2003, 2006); Roederer et al. (2014) for all elements, Adibekyan et al. (2012) for Ca and Si, Barklem et al. (2005) for Ca and Ti. Same symbols of Fig. 5.5.

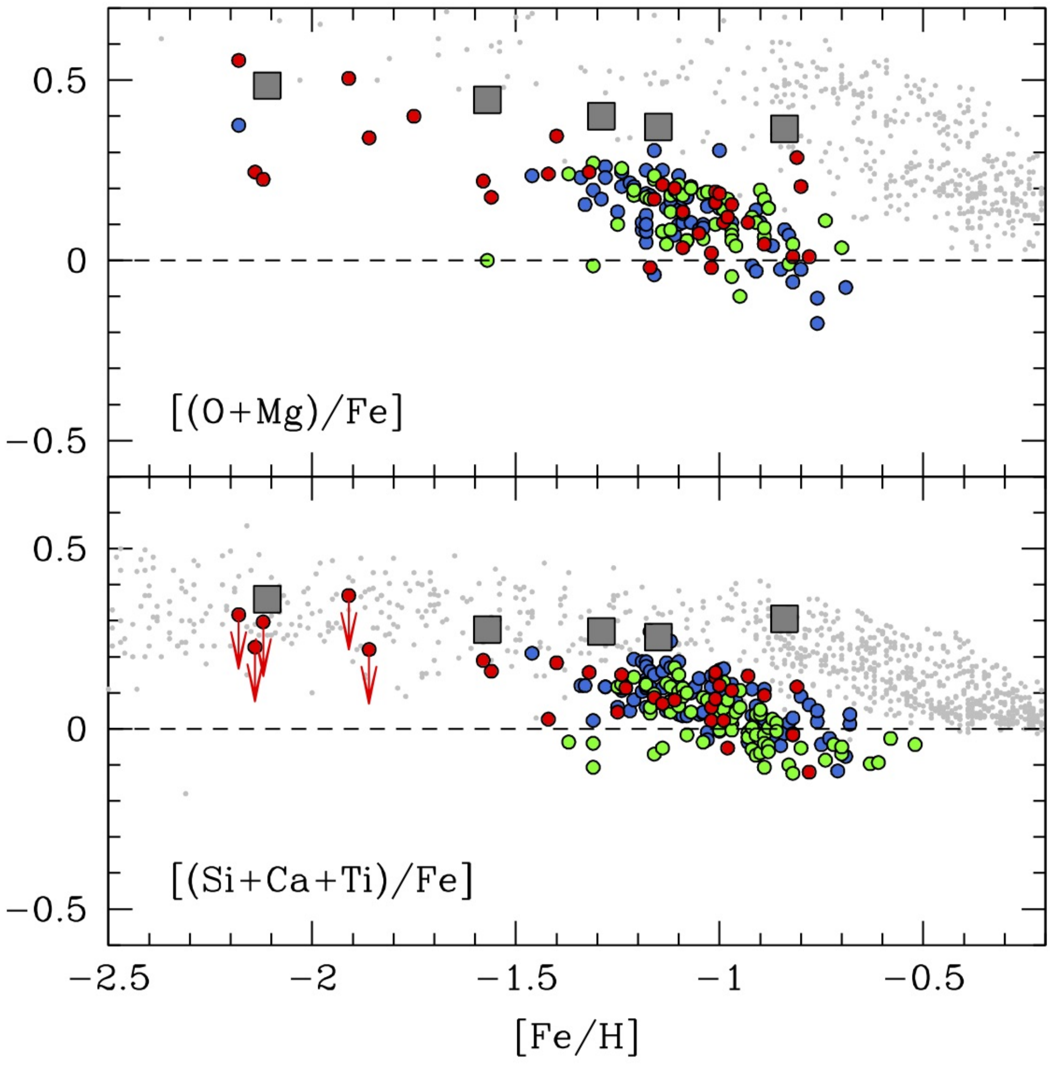

Figure 5.7: Behavior of the hydrostatic and explosive average [α/Fe] abundance ratios as a function of [Fe/H]. Same symbols of Fig. 5.5.

5.5.3 Iron-peak elements

Iron-peak elements are produced mainly in massive stars, both in SNe II and HNe, through different nucleosynthesis paths (Limongi & Chieffi, 2003; Romano et al., 2010; Kobayashi et al., 2020). Also, a not negligible contribution by SNe Ia can contribute to produce some of these elements (Leung & Nomoto, 2018; Lach et al., 2020).

As discussed in Chapter 3, abundances of some iron-peak elements (i.e. Zn, Sc and V) are extremely different in metal-rich dwarf stars (like LMC and Sagittarius) with respect to the MW stars. The metal-rich SMC stars have abundances of Sc and V, that are produced mainly by massive stars via SNe II, HNe and electron-capture SNe, significantly lower than the MW stars (see Fig. 5.8). On the other hand, SMC stars with [Fe/H] < -1.5 dex have Sc and V abundances compatible with those measured in the control sample.

The SMC stars have [Ni/Fe] values compatible with those measured in the GCs of the control sample until [Fe/H] ~ -1.0 dex, while for higher metallicities this abundance ratio slightly decreases, reaching values around [Ni/Fe] ~ -0.2 dex (see Fig. 5.9). This mild trend resembles that observed in Chapter 3 for [Ni/Fe] in LMC/Sgr at higher [Fe/H]. The decrease of [Ni/Fe] at higher metallicities is not observed in MW stars, where [Ni/Fe] remains constant, and it could suggest a lower contribution by SNe-Ia in the SMC.

Cu abundances, derived from the only line at 5782 Å exhibit a large star-to-star dispersion (see Fig. 5.9) and it is difficult to establish the real trend of this abundance ratio for the SMC stars. However, it is clear that the most metal-rich SMC stars have [Cu/Fe] lower than that measured in MW stars, indicating a lower contribution by s-process occurring in massive stars (Romano & Matteucci, 2007).

5.5.4 Neutron-capture elements

Elements heavier than the iron-peak group are produced through neutron-capture process on seed nuclei, followed by β decays. The neutron-capture elements measured here (namely Zr, Ba and La) are produced mainly by slow process occurring in low-mass (1-3 $M_{\odot}$) AGB stars, and in a minor amount in massive stars (Busso et al., 1999). However, at low metallicities these elements are produced also through rapid processes, occurring in rare and energetic events like neutron star mergers or collapsars (Kobayashi et al., 2020).

Fig. 5.10 displays the behavior with [Fe/H] of individual neutron-capture elements abundance ratios. The SMC stars show [Zr/Fe] and [La/Fe] abundance ratios similar, within the star-to-star scatter, to those observed in MW stars, and slightly higher [Ba/Fe]. Generally, these results suggest that the enrichment by AGB stars in the SMC has been comparable to that in the MW. Finally, we identified a few stars exhibit high [Ba/Fe] and [La/Fe] values (> 1 dex) that could be the result of mass transfer from a AGB companion star in binary systems.

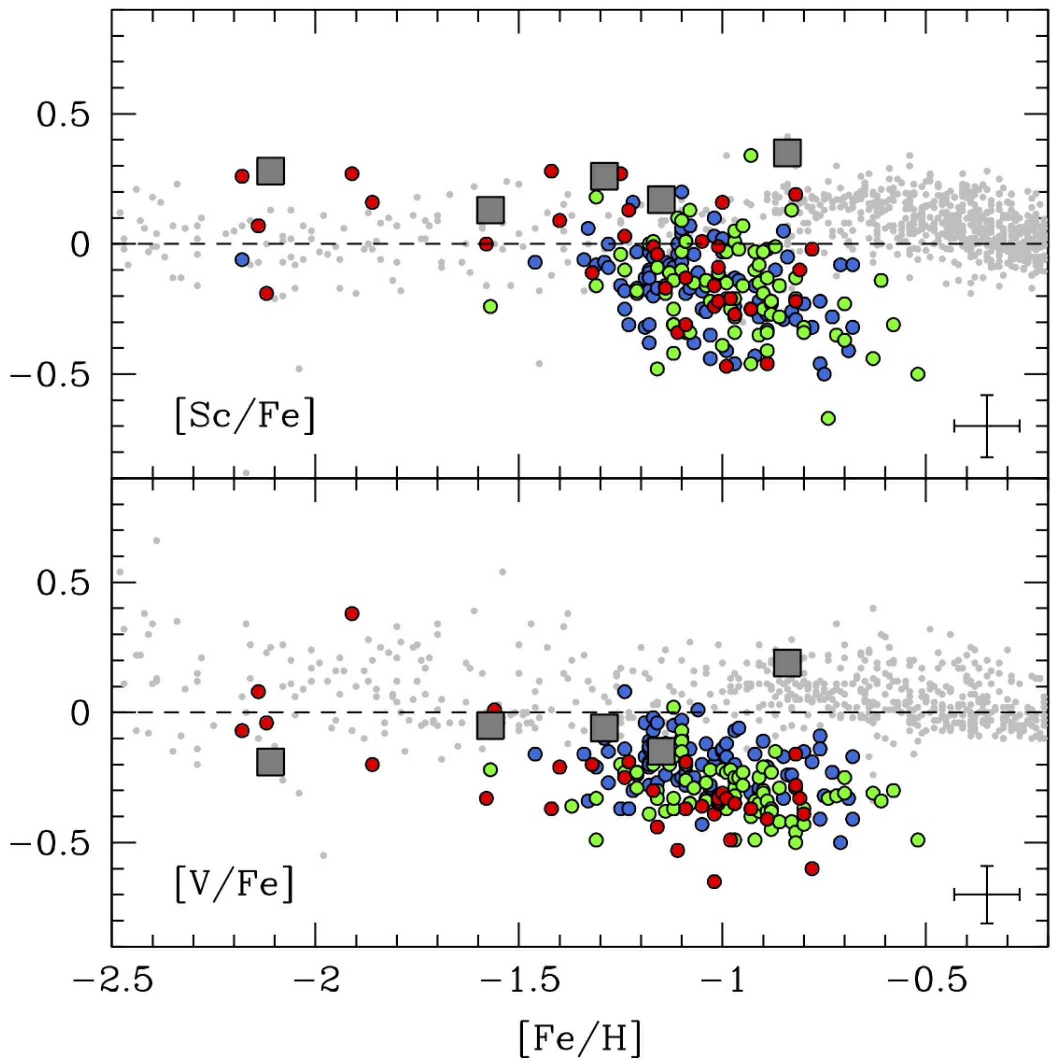

Figure 5.8: Behavior of the iron-peak elements [Sc/Fe] and [V/Fe] abundance ratios as a function of [Fe/H]. Abundances of Galactic field stars are from Gratton et al. (2003); Reddy et al. (2003, 2006); Roederer et al. (2014) for both elements, Fulbright (2000) for V, Adibekyan et al. (2012) for Sc. Same symbols of Fig. 5.5.

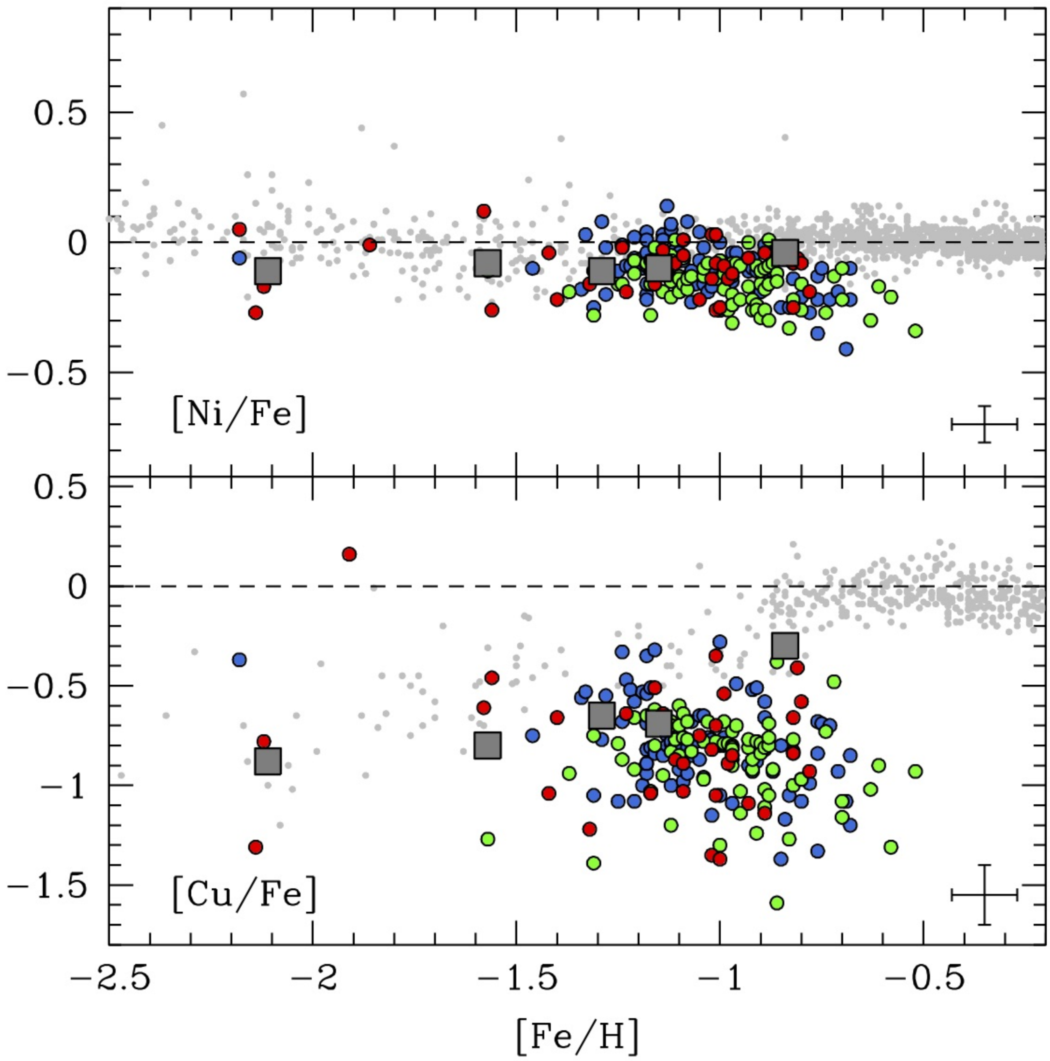

Figure 5.9: Behavior of the iron-peak elements [Ni/Fe] and [Cu/Fe] abundance ratios as a function of [Fe/H]. Abundances of Galactic field stars are from Reddy et al. (2003, 2006); Roederer et al. (2014) for both elements, Edvardsson et al. (1993); Fulbright (2000); Stephens & Boesgaard (2002); Gratton et al. (2003); Bensby et al. (2005); Adibekyan et al. (2012) for Ni, Bihain et al. (2004); Yan et al. (2015) for Cu. Same symbols of Fig. 5.5.

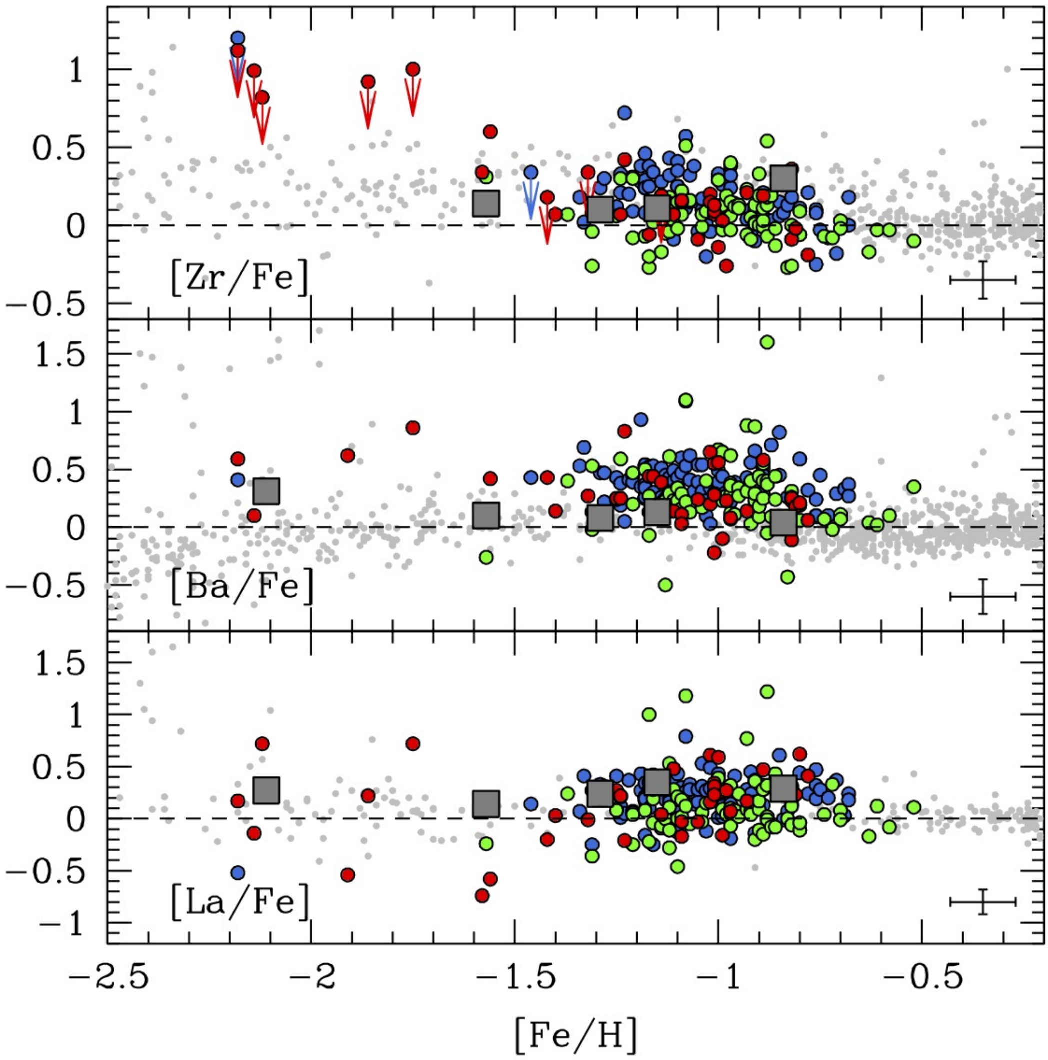

Figure 5.10: Behavior of the neutron-capture-elements [Zr/Fe], [Ba/Fe] and [La/Fe] abundance ratios as a function of [Fe/H]. Abundances of Galactic field stars are from Mishenina et al. (2013); Roederer et al. (2014) for all the elements, Edvardsson et al. (1993); Fulbright (2000); Reddy et al. (2003) for Zr and Ba, Burris et al. (2000); Battistini & Bensby (2016) for Zr and La, Stephens & Boesgaard (2002); Barklem et al. (2005); Bensby et al. (2005) for Ba.

5.6 Summary

The intermediate/old SMC stellar populations are dominated by metal-intermediate stars (– 1.4 dex < [Fe/H] < – 0.6 dex) and the metallicity distribution is peaked at ∼–1.0 dex with a metal-poor tail (down to ∼ – 2.2 dex) detected only in the most external field.

The information obtained from the FLAMES/GIRAFFE high-resolution spectra allow us to draw a scheme of the chemical evolution of the SMC, at least for the stellar populations older than ∼1-2 Gyr.
The abundance ratios of the most metal-poor stars of the sample, with [Fe/H] < – 1.5 dex are compatible with those measured in Galactic stars halo, as already pointed by Nidever et al. (2020), Reggiani et al. (2021) and Hasselquist et al. (2021), as well as with those measured in the LMC old clusters of similar metallicities (Johnson et al., 2006; Mucciarelli et al., 2010; Mateluna et al., 2012; Mucciarelli et al., 2021a) and in metal-poor stars of dwarf spheroidal galaxies as Sculptor (Hill et al., 2019). These similarities support the idea that in different environments of the Local Group the initial conditions at the time of the first star formation episodes were the same. Moving to the most metal-rich stars of the sample, with [Fe/H] > – 1.5 dex, the main component of SMC reveals lower abundance ratios for the elements produced by massive stars, both from SNe II and HNe, suggesting that in the contribution by massive stars to the chemical enrichment of the SMC is less important. These trends are similar to the ones observed for LMC metal-rich stars (see Chapter 3). Concerning the neutron-capture elements, their abundance ratios are similar to the MW ones also at metallicity higher than –1.5 dex, suggesting that enrichment by AGB stars in the SMC has been comparable to that in the MW.

Chapter 6

The chemical composition of three SMC globular clusters

Based on the results in
Minelli A., Mucciarelli A., Romano D., Origlia L., Ferraro F.R., 2022, submitted

6.1 Introduction

The SMC is an irregular galaxy characterized by an ongoing star formation activity. The galaxy has experienced a complex and violent SFH, influenced by the gravitational interaction with the LMC (started about 4-5 Gyr ago, Bekki et al., 2004; Bekki & Chiba, 2005) and the MW (it is likely at its first peri-Galactic passage, Besla et al., 2010; Besla, 2015). Indeed, the tidal interaction occurring among these galaxies have probably triggered the main star formation episodes in the Magellanic Clouds (Harris & Zaritsky, 2009; Rubele et al., 2012; Nidever et al., 2020). As explained in the previous Chapter, it is important to study the chemical enrichment history of the SMC since it is influenced by gravitational interactions and matter exchanges with LMC and MW. In particular, studying star clusters with different ages and abundances is interesting because they are prime indicators of a galaxy's chemical evolution, ideal tracers of the AMR of the galaxy, due to the opportunity to derive both age and [Fe/H].

Another information that we can detect concerning the GCs is the presence of anti-correlations in light elements, that is stars belonging to the same GC with similar metallicity but different chemical abundances in light elements. The abundance variations are due to self-enrichment processes that occur in the GCs. Therefore GCs host populations with abundance variations in light elements, which are typically referred to as multiple populations (MPs) The elements involved in these anti-correlations are C-N, O-Na and Mg-Al (Carretta et al., 2009a,b; Pancino et al., 2017). In particular in MW GCs it is observed that the second generation of stars have N, Na and Al enhanced while C, O and Mg depleted in comparison to the first generation of stars. The anti-correlation is stronger in C and N abundances, followed by O and Na (Cannon et al., 1998; Carretta et al., 2009a). The origin of the MPs is still unclear. From previous works based on MW and LMC GCs, we know that the mass (Carretta et al., 2010a; Bragaglia et al., 2012; Schiavon et al., 2013; Milone et al., 2017) and the cluster age (Martocchia et al., 2018, 2019) play a key role in the formation of the MPs. In particular, the star-to-star light element abundance variations became larger in massive and old GCs.

In this work, we homogeneously analyzed high-resolution spectra of RGB stars belonging to three GCs (NGC 121, NGC 339 and NGC 419) which cover a wide range of ages and metallicities, in order to study the evolution of the metallicity with the age. We derived chemical abundances for the main groups of elements (light, alpha, iron-peak, neutron-capture elements), for the purpose to estimate the role played by massive stars (exploding SNe II), degenerate binary systems (exploding as SNe Ia) and AGB stars. Furthermore, we looked for the MPs in these GCs, searching for the presence of chemical anomalies in light elements. The presence of MPs is expected for NGC 121 and NGC 339, where from previous photometric works it was found a fraction of 30% (Dalessandro et al., 2016; Niederhofer et al., 2017a) and 25% (Niederhofer et al., 2017b) of second generation stars, respectively. Instead, for NGC 419 no MPs was detected (Cabrera-Ziri et al., 2020).
Moreover, we compare the chemical abundances derived in GCs from this study, with the ones for SMC field stars (described in Chapter 5) and the MW GCs chemical abundances (analysed in the work on LMC GCs, described in Chapter 4). The analysis of the three samples of targets were made with the same method and the same atomic data and solar reference values, therefore they can be considered homogeneous.

6.2 Spectroscopic datasets

The aim of this work is to study the chemical evolution of the SMC with time, and also to search for chemical anomalies in GCs. Therefore, we study the chemical abundances of elements belonging to the main groups (light, α, iron-peak, and neutron-capture elements) in stars located in GCs with different ages. The adopted dataset is composed by high-resolution spectra of RGB stars belonging to three GCs (namely NGC 121, NGC 339 and NGC 419), chosen in order to cover the whole range of SMC GCs age. Their location within the SMC is represented in Fig. 5.1 of the previous Chapter.
The spectra were collected with the multi-object optical spectrographs FLAMES (Pasquini et al., 2002) mounted at the Very Large Telescope of the European South-

ern Observatory, under the program 086.D-0665 (PI: Mucciarelli). The observations concerning the UVES-FLAMES spectrograph have been performed adopting the Red Arm 580 UVES setup (spectral resolution of 47000 and spectral coverage $\sim$ 4800 – 6800 Å). The observations made with GIRAFFE spectrograph were obtained using MEDUSA configuration, with HR11 (5597 – 5840 Å and R = 24200) and HR13 (6120 – 6406 Å and R = 22500) gratings. The exposure times and the number of individual exposures for each setup and field are reported in Table 5.1 in the previous Chapter. After the reduction, performed with the dedicated ESO pipelines* (including bias subtraction, flat-fielding, wavelength calibration, spectral extraction and order merging), the individual exposures have been cleaned from the sky contribution by subtracting the spectra of some close sky regions observed at the same time of the science targets. Subsequently, single exposures of the same target have been combined in an individual spectrum for each star.
The stars have been selected from near-infrared SofI@NTT photometric catalog in the brighter portion of the RGB ($K_s \sim$ 13–14). The criteria applied for the selection are described in Section 5.2.1. Among the analysed stars, an additional check was performed taking into account their values of RVs and metallicities, and if they are in agreement among themselves the stars is considered to be a cluster member, otherwise, the stars were rejected. It is to be noted that the GIRAFFE spectra belonging to NGC 419 show an offset between the RVs of HR11 and HR13 spectra, probably arose from calibration problems. In Fig. 6.1 is shown the position in the (K, J-K) CMDs of the observed targets resulted to be SMC GCs stars.
The dataset includes:

- *NGC 121* — The oldest SMC GCs, with an age of 10.5 ± 0.5 Gyr and a metallicity of – 1.46 ± 0.10 dex (Glatt et al., 2009). The observed targets are five RGB stars observed with UVES.

- *NGC 339* — This is an intermediate-age cluster with age 6 ± 0.5 Gyr and [Fe/H] = – 1.12 ± 0.10 dex according to Glatt et al. (2009). We observed four RGB stars with UVES and three with GIRAFFE.

- *NGC 419* — NGC 419 is the youngest and most metallic GC between the three, having 1.4 ± 0.2 Gyr and [Fe/H] = – 0.67 ± 0.12 dex (Glatt et al., 2009). Its dataset includes five RGB stars observed with UVES and three observed with GIRAFFE.

Additionally, in order to have an homogeneous comparison with the MW, the sample of MW GCs analysed in the work described in Chapter 4 and list in Table 4.2 have been taken into account. The chemical analysis was made with the same assumption adopted for the SMC stars.

*http://www.eso.org/sci/software/pipelines/

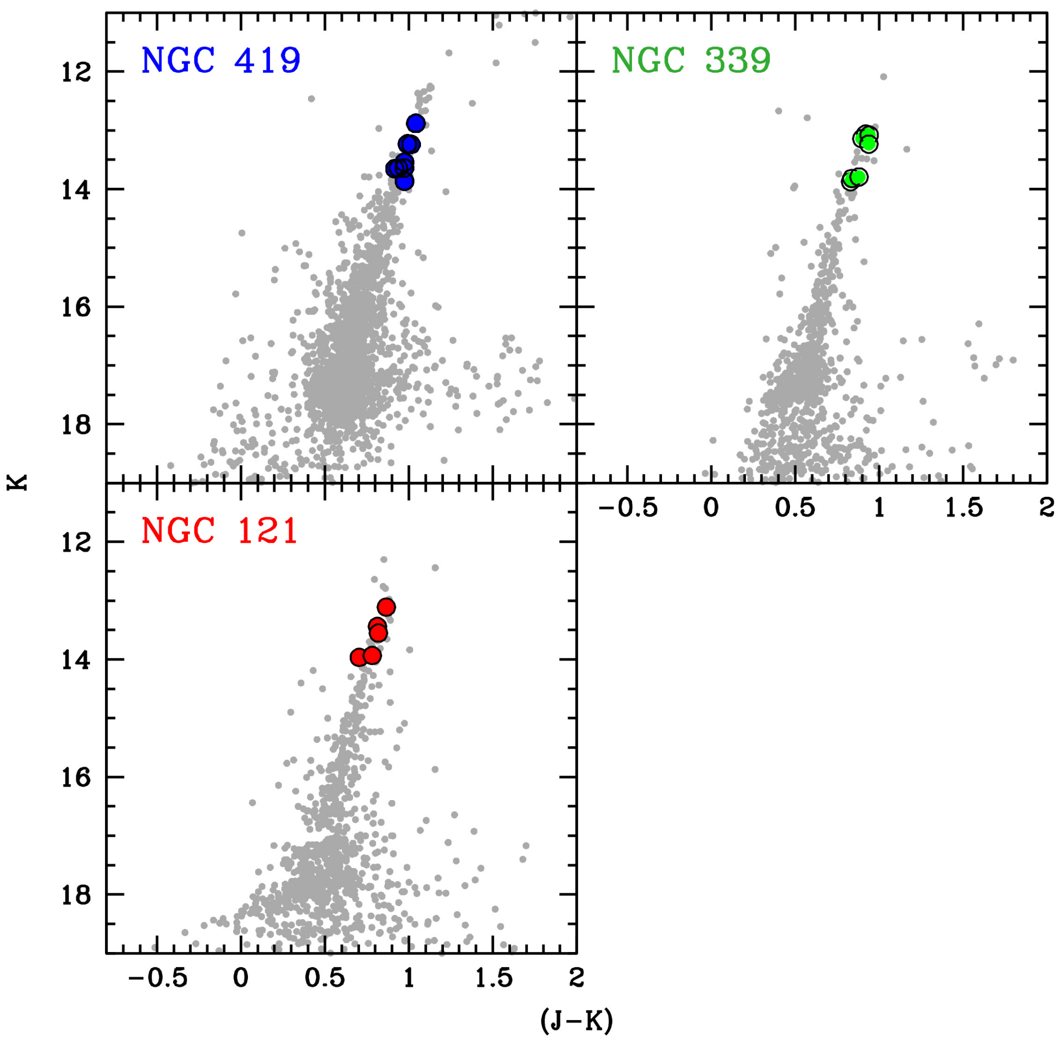

Figure 6.1: (K, J-K) CMDs of the SMC GCs stars (grey dots) with the position of the analysed target (colored circles).

6.3 Atmospheric parameters

T_{eff} has been derived from SofI@NTT photometry, using the $(J-K)_0$-T_{eff} relation provided by González Hernández & Bonifacio (2009). Since the relation needs as input a value for the metallicity of the stars, as a first step we adopted the [Fe/H] values available in the literature (in some cases they are photometric metallicities). The color excess E(B-V) are from the reddening maps by Schlafly & Finkbeiner (2011) (see Chapter 5).

Because of the low spectral noise (SNR $\sim$ 20 - 35) and the high number of Fe lines available (100 - 160 lines) in the UVES spectra allow to find an accurate value of T_{eff}

spectroscopically, we decided to derive it from the spectra as an additional check of the photometric T_{eff}. We used the code GALA (Mucciarelli et al., 2013), which find the best value of T_{eff} by erasing any trend between the abundance from Fe I lines and their excitation potential. Instead, the lower spectra coverage and resolution of the GIRAFFE spectra does not allow to measure enough Fe I lines to estimate a reliable T_{eff}.
As sanity check, we compare the photometric T_{eff} with the one obtained spectroscopically for the UVES spectra. For the stars belonging to NGC 339 the two values are similar within the errors. Instead, the spectroscopic temperature is on average 200 K higher than the photometric one for the UVES spectra of the stars belonging to NGC 419. Therefore, we decide to use the spectroscopic T_{eff} for all the UVES spectra, while we used reasonably the photometric T_{eff} for the GIRAFFE targets, applying a correction of +200 K to the photometric T_{eff} derived for NGC 419.

The log g is then derived from the T_{eff} by using an appropriate isochrone (in terms of age and metallicity) for each GC, computed with the Dartmouth Stellar Evolution Database (Dotter et al., 2008). As a first step we adopt the age and metallicity derived by Glatt et al. (2009) to calculate the isochrone, refining the metallicity value with the one derived in our analysis in each iteration. The final values chosen for the isochrones are: 10.5 Gyr and [Fe/H] = − 1.15 dex for NGC 121 stars, 6 Gyr and [Fe/H] = − 1.2 dex for the target belonging to NGC 339 and 1.4 Gyr and [Fe/H] = − 0.6 dex for NGC 419 stars. All of them are solar scaled according to our results for the α-elements abundances.

Finally, the v_t for UVES spectra have been determined spectroscopically with GALA, minimizing the slope between the abundances from Fe I lines and the reduced EWs. For the GIRAFFE spectra, the derived v_t risk to be affected by uncertainties due to the low number of available Fe lines. Therefore we compute them from the log g-v_t relation provided by Mucciarelli & Bonifacio (2020).

The final values, with the related errors, are listed in Table 6.1.

6.4 Chemical analysis

With the aim of reject blended and/or saturated atomic lines, we selected lines for the analysis from the comparison among the observed spectra and synthetic ones computed with the appropriate atmospheric parameters and metallicity by using the code SYNTHE (Kurucz, 2005). Atomic and molecular data (such as excitation potential χ, log gf, damping constants and hyperfine/isotopic splitting) used for synthetic spectra are taken from the Kurucz/Castelli linelists[†], with some exceptions for more recent or more accurate data for some transitions of Fe, Si, Ca, Ti, Ba and Eu (see Mucciarelli et al., 2017a, for additional references). The produced

[†] http://wwwuser.oats.inaf.it/castelli/linelists.html

Table 6.1: Adopted atmospherical parameters for SMC GCs stars. The ID numbers are referred to SofI@NTT photometric catalog. The spectrograph used for the observation of the stars is reported in the last column.

ID	T_{eff}	log g	v_t	spectra
		NGC 121		
9	3990±50	0.53±0.07	1.60±0.06	UVES
14	4070±50	0.66±0.07	1.80±0.09	UVES
18	4110±50	0.73±0.07	1.70±0.11	UVES
31	4250±50	0.97±0.07	1.60±0.07	UVES
35	4240±50	0.95±0.07	1.40±0.07	UVES
		NGC 339		
219	4140±100	0.72±0.07	1.80±0.15	GIRAFFE
466	4000±100	0.50±0.07	1.90±0.15	GIRAFFE
535	4000±30	0.50±0.07	1.70±0.05	UVES
835	4000±100	0.50±0.07	1.90±0.15	GIRAFFE
893	4050±30	0.58±0.07	1.60±0.05	UVES
958	4210±40	0.83±0.07	1.50±0.06	UVES
1076	4290±30	0.97±0.07	1.50±0.04	UVES
		NGC 419		
345	4320±100	1.41±0.07	1.56±0.15	GIRAFFE
616	4050±100	0.98±0.07	1.72±0.15	GIRAFFE
727	4270±70	1.33±0.07	1.60±0.08	UVES
732	4110±70	1.07±0.07	1.50±0.08	UVES
852	4145±60	1.13±0.07	1.70±0.11	UVES
885	4190±100	1.20±0.07	1.64±0.15	GIRAFFE
1384	4150±60	1.13±0.07	1.70±0.07	UVES
1633	4240±60	1.28±0.07	1.60±0.09	UVES

synthetic spectra are convoluted with a Gaussian profile in order to reproduce the observed broadening of GIRAFFE and UVES spectra. Model atmospheres have been calculated with the code `ATLAS9` (Kurucz, 1993, 2005). In order to account for the different blending conditions due to different resolution, we derived individual linelists for UVES and GIRAFFE spectra and since stars belonging to the same GC have similar chemical abundances and atmospheric parameters, one linelist for each GC is produced.

The final linelists include transitions of elements belonging to the main groups, such as light, α, iron-peak and neutron-capture, in particular, 22 elements for UVES spectra and 15 elements for GIRAFFE spectra. The average number of line used for UVES spectra are reported in Section 3.4, while for GIRAFFE spectra the number is smaller due to their shorter spectral range: FeI ($\sim$ 35), O ($\sim$ 1), Na ($\sim$ 4), Mg ($\sim$ 1), Si ($\sim$ 5), Ca ($\sim$ 5), Ti ($\sim$ 10), V ($\sim$ 6), Cr ($\sim$ 4), Co ($\sim$ 1), Ni ($\sim$ 10), Cu ($\sim$ 1), Zr ($\sim$ 3), BaII ($\sim$ 1), LaII ($\sim$ 1).
For species with unblended lines (Fe, Na, Al, Ca, Ti, Si, Cr, Ni, Zr, Y and Nd),

we measured the EWs of the selected lines with `DAOSPEC` (Stetson & Pancino, 2008) through the wrapper `4DAO` (Mucciarelli, 2013), that provides also the RV of the targets. The chemical abundances are derived from the measured EWs by using the code `GALA` (Mucciarelli et al., 2013). The line fitting is controlled line by line, with the purpose to identify possible lines with unsatisfactory fit or wrong continuum location.
A different approach is adopted for the species with available only blended lines characterized by hyperfine/isotopic structure (O, Sc, V, Mn, Co, Cu, Ba, La, Eu) or transitions located in noisy/complex spectral regions (Mg, Zn). Their abundances have been derived with our own code `SALVADOR` that performs a χ^2-minimization between the observed line and a grid of suitable synthetic spectra for which only the abundance of the investigated element can vary. Synthetic spectra are computed using the code `SYNTHE`.

A more detailed description of the procedure used for some problematic species is described in Section 3.4.

6.4.1 Error estimates

Abundance uncertainties have been computed taking into account the errors due to the measurement and the ones related to the adopted atmospheric parameters, summing each term in quadrature.
The internal errors due to the measurements have been derived with the same procedure described in Section 3.4.1, according to the method used to obtain the abundances.
The uncertainties arising from the atmospheric parameters have been computed deriving the abundance variation due to the change of only one parameter at a time, keeping the other ones fixed, a part from T_{eff} which affect the value of log g and v_t that had to be changed according to it. The applied variation of T_{eff} for UVES spectra depends on the uncertainties arising from the spectroscopic measurement, the value is different star by stars and of the order of 50 K. Instead, for GIRAFFE spectra, the uncertainty in T_{eff} comes from the photometry and it is assumed an error of 100 K for each target.
The log g value depends on T_{eff} (considered just before) and on the isochrone adopted for each GCs. Isochrone uncertainties derive from the choice of an age and a metallicity of the GC. Therefore, we compute the variation of log g coming from the isochrone change of 1 Gyr in age and 0.1 dex in metallicity, which are the typical errors of these parameters. In particular, the metallicity affect mainly the value of log g, implying its variation of about 0.07 dex, the adopted error for log g.
Finally, the variation applied to v_t is again different for GIRAFFE and UVES spectra, depending on the method used to derive its value. For UVES spectra, v_t is derived spectroscopically and the typical uncertainties are of the order of 0.08 km/s,

but different star by star. Instead, for GIRAFFE targets v_t have been derived from the log g-v_t relation (Mucciarelli & Bonifacio, 2020) and the variation applied to v_t is of 0.15 km/s, value computed taking into account the dependence from log g and the error linked to the relation.

The final errors in [Fe/H] and [X/Fe] abundance ratios are calculated using the equations 3.1 and 3.2 in Section 3.4.1.

6.5 Results

This work presents for the first time the detailed chemical composition of three GCs with different ages, with the twofold aim to study the chemical evolution of the SMC and to investigate the occurrence of MPs in these galaxies. The analysis was performed in a homogeneous way, with the advantage of removing most of the systematics (i.e. solar abundances, atomic data, model atmospheres), affecting the comparison of GCs abundances derived in different studies.
For all the analysed elements, the average abundance ratios for the SMC GCs are listed in Table 6.2, while the abundances derived for each star are listed in Tables 6.3 - 6.4. Note that there is no Zn abundances for NGC 121. Since the only available Zn line has a wavelength located at the beginning of the stellar spectrum, for this GC the spectra are too noisy and the continuum location results to be uncertain. Therefore we prefer to reject this line for NGC 121. Moreover, Cu abundances for NGC 121, available only for three stars, have higher errors in comparison with the ones associated to the other two SMC GCs for this element. Cu abundances are measured with the spectrum synthesis of the only available line in this spectral range, located at ∼5105.5 Å, a region particularly noisy for the spectra of NGC 121.

6.5.1 Age-metallicity relation

The study of the metallicity of these GCs with different ages, provides information about the evolution of the metallicity with the time. The oldest SMC GC, NGC 121, is ∼2 Gyr younger than the old MW and LMC clusters and with a metallicity of [Fe/H] = − 1.17 dex. The intermediate-age GC NGC 339 has a metallicity similar to the NGC 121, with [Fe/H] = − 1.24 dex. Finally NGC 419, the youngest one, has a metallicity significantly higher ([Fe/H] = − 0.58 dex).
We report our results in Fig. 6.2, where the Fe abundances are shown as a function of the age of the GCs (ages from Glatt et al., 2009). As shown, in the first 2 Gyr, the SMC reaches a metallicity of ∼ –1.2 dex, a value lower than the metallicity reached by the LMC (Pagel & Tautvaisiene, 1998; Harris & Zaritsky, 2009) and MW (Haywood et al., 2013; Snaith et al., 2015) at the same time, as attended for less massive systems. Later, the metallicity of the SMC remains nearly constant

until 6 Gyr ago, indicating that the galaxy experienced a lower SFR in that period. After then, the metallicity starts to increase again, reaching a [Fe/H]~ -0.6 dex in the following 4 Gyr. This increase is probably related to the first encounter between LMC and SMC, occurred likely 4 Gyr ago (Bekki et al., 2004; Bekki & Chiba, 2005), which triggered the main star formation episodes in the MCs (Harris & Zaritsky, 2009; Rubele et al., 2012; Nidever et al., 2020). We compare our results with the theoretical prediction of the AMR derived by Pagel & Tautvaisiene (1998), shown as black line in Fig. 6.2. Observations nicely agree with the theoretical model by Pagel & Tautvaisiene (1998), enforcing the scenario described above for the chemical enrichment of the SMC.
In the second panel of Fig. 6.2 is represented the metallicity distribution for SMC field stars (see Chapter 5). We can assume that the SMC field stars have experienced

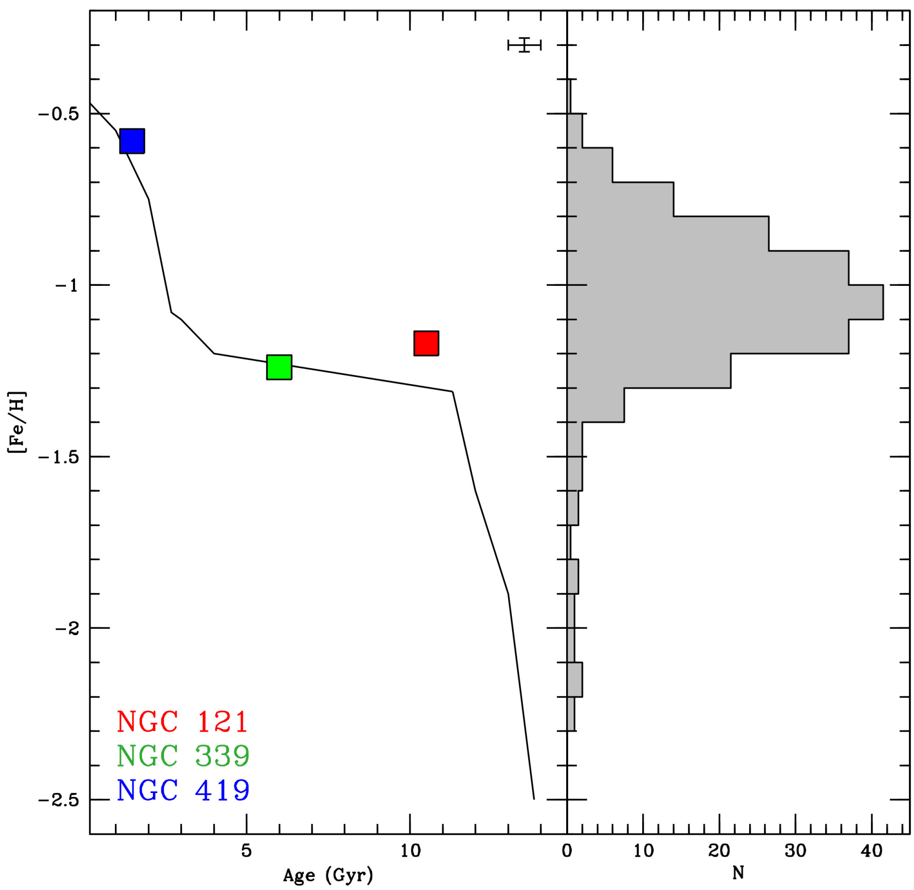

Figure 6.2: Left panel: average metallicity as a function of the age (Glatt et al., 2009) for the SMC GCs analysed in this work (colored squares). Theoretical AMR calculated by Pagel & Tautvaisiene (1998) is also reported (black line)
Right panel: metallicity distribution of the SMC field stars found in the study discussed in Chapter 5.

the same chemical enrichment of the SMC GCs, therefore we conclude that the most metal-poor field stars found in the previous sample had to be formed during the first 1-2 Gyr of the life of the galaxy, since they had to be older than NGC 121 according to their metallicities. Instead, the bulk of the stellar population formed most recently, nearly 3-4 Gyr ago according to the AMR of Pagel & Tautvaisiene (1998), corresponding to the beginning of the gravitational interaction between the Clouds, leading to the increase in metallicity.

6.5.2 Abundance ratios

To better characterize the chemical enrichment history of the SMC we measured the abundances for the main groups of elements (light, α, iron-peak, neutron-capture elements) of the three GCs. The mean values estimated for each GCs are reported in Fig. 6.3, where the abundance ratios are represented as a function of the atomic number, color coded according to the GCs.
In general, we can conclude that all the GCs have solar scaled α-abundances. The solar-scaled values suggest that these stars have been enriched by both SN Ia and SNe II and this is another evidence of the slow SFR characteristic of the first period of the galaxy. The iron-peak elements abundance ratios are more (for Mn and Cu) or less depleted in comparison to the solar values for all the SMC GCs, the same that happens for the light elements abundances, with Na more depleted than Al. The abundance ratios of the s-process neutron-capture elements are depleted for Y, nearly solar for Zr and super solar for Ba and La, while for Nd, which is produced from both neutron-capture processes, and for the r-process element Eu, the abundance ratio values are highly enhanced respect to the solar values. The last evidence is an indication that all the 3 environments from which the GCs formed experienced r-process pollution.

Moreover, we compared the mean abundance ratios derived for the GCs in this work, with the ones for SMC field stars derived in the work in Chapter 5. The two samples of stars give complementary information, since from GCs we can achieve simultaneously ages and metallicities, but field stars provide high statistics and we can obtain metallicities all over the galaxy.
In Figs. 6.4 - 6.7, the elemental abundance ratio as a function of the metallicity for all the analysed elements for SMC GCs (colored squares) and field stars (black dots). For all of them, the two samples of target display similar patterns. The assumption that the SMC field stars and GCs share similar chemical enrichment history is confirmed by the agreement between their abundances. Therefore we can properly use the metallicity of the field stars as a proxy of their age, in comparison with the GCs ones.

In addiction, the same figures show the abundance ratios derived for MW GCs analysed in the work described in Chapter 4 (grey squares) and literature abundances

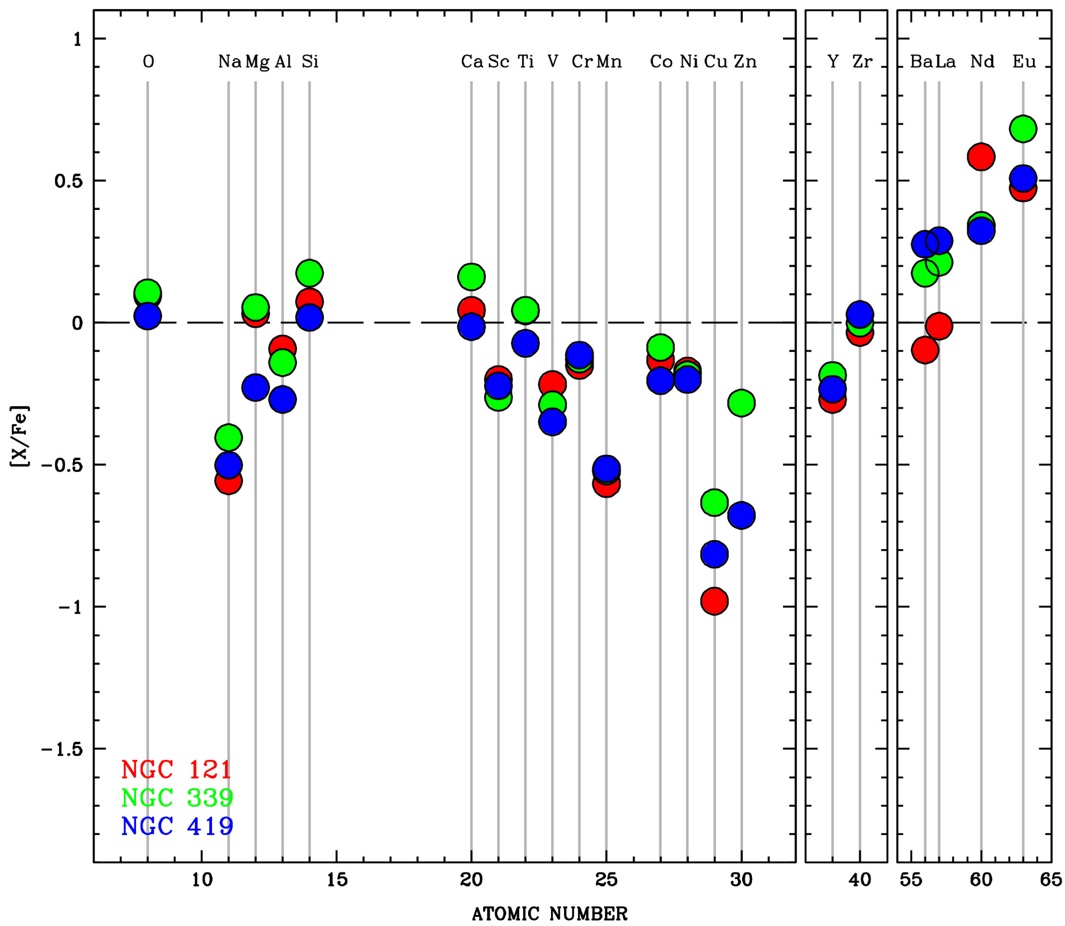

Figure 6.3: Mean abundance ratios of the analysed elements for NGC 121 (red circles), NGC 339 (green circles), and NGC 419 (blue circles).

for MW field stars as reference (grey dots, list of the used works in captions).

α-elements

In Fig. 6.4 is reported the abundance ratios of Si, Ca, Ti and the average abundances value among the three elements, as a function of the metallicity. We can observe an agreement between the abundances of SMC GCs and field stars. The α abundances are depleted in all the elements for the three GCs in comparison with the MW values. In particular, the α abundance values are similar to zero also for the oldest GC, indicating that the galaxy experienced a slower SFR.

Since α-elements are produced mainly in massive stars exploding as SNe II, their trend is an indication of a lower contribution by massive stars in the SMC, as we found also for the LMC in Chapter 3.

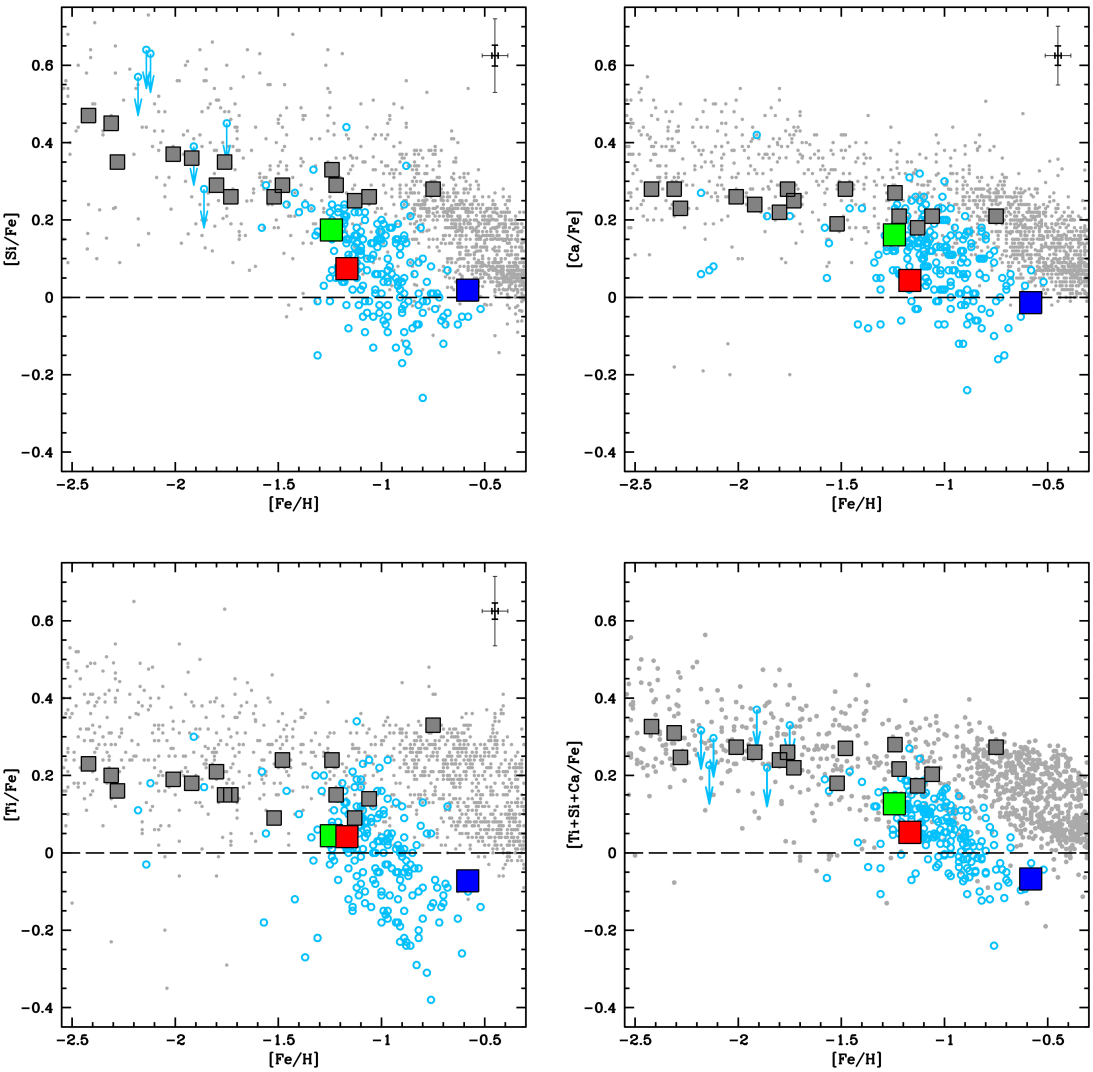

Figure 6.4: α-elements abundance ratios (Si, Ca, Ti and their mean value, from top left panel to bottom right panel, respectively) as a function of [Fe/H] for SMC GCs (colored squares: NGC 121 in red, NGC 339 in green and NGC 419 in blue), SMC field stars (light blue open dots), MW GCs (grey squares) and MW field stars (grey dots). Arrows indicate upper limits. SMC field stars and MW GCs data are from the works described in previous chapters (Chapter 5 and 4, respectively). MW field stars are from Edvardsson et al. (1993); Fulbright (2000); Stephens & Boesgaard (2002); Gratton et al. (2003); Reddy et al. (2003, 2006); Barklem et al. (2005); Bensby et al. (2005); Adibekyan et al. (2012); Roederer & Lawler (2012); Mishenina et al. (2013); Reggiani et al. (2017).
The abundance errors for the SMC GCs are reported as error bars, where the thin bar is the typical total uncertainty for individual stars and the thick bar is the error of the mean value of the GC.

iron-peak elements

They are mainly produced in SNe Ia, but contributions not negligible are also from SN II and HNe.
As visible in Figs. 6.5 - 6.6, where the iron-peak elements abundance ratios vs metallicity are represented, the SMC GCs abundances are in agreement with the SMC field stars ones for Sc, V, Ni and Cu. For the other elements (Cr, Mn, Co and Zn), field stars abundances are not available.
Looking at the comparison with the MW GCs, we have that the iron-peak elements have abundances lower than the MW ones, a part from Cr and Mn that have abundances similar to the MW GCs. Among the depleted elements, Sc, V and Zn are the ones with the highest differences respect to the MW stars with similar metallicities. Same results was found also for the LMC, as described in Chapter 3.
From these behaviours we can conclude that the contribution by massive stars in SMC was lower than in the MW, in agreement with the scenario derived from the α-elements abundances.

neutron-capture elements

The derived abundances for Y, Zr, Ba, La, Nd and Eu are reported in Fig. 6.7 as a function of the metallicity.
Regarding the elements for which we have SMC field stars abundances (Zr, Ba and La), their values agree with the SMC GCs ones.
From the comparison with the MW GCs abundances, we can see a good agreement for all the analysed neutron-capture elements (instead, for the LMC we detected enhanced Ba and La abundances, see Chapter 3). We can conclude that the SMC and the WM have experienced similar contribution from electron capture SNe (that mainly produced Y and Zr, see Kobayashi et al., 2020) and low mass (1-3 $M_{\odot}$) AGB stars (the main nucleosynthesis channels for the production of the s-process, Busso et al., 1999), and similar rate of NS mergers and collapsars, considered the main producers of r-process elements (Pian et al., 2017; Siegel et al., 2019).

6.5.3 Light elements abundance variations

In Fig. 6.8 are represented the [O/Fe]-[Na/Fe] and [Al/Fe]-[Mg/Fe] abundance ratios for the analysed stars, colored according to the GC of belongings. Our abundances are compared with the ones of MW GCs stars, described previously in the work in Chapter 4, and with the SMC field stars abundances derived in Chapter 5, but only in the O-Na plane, since Al abundances are not available for field stars.
While in the MW GCs stars is clearly visible the presence of MPs, with the second population having O and Mg depleted, and Na and Al enhanced in comparison to the first population, the same does not occur in SMC GCs stars. Concerning O and Na, NGC 121 and NGC 419 do not show evidence of intrinsic variations for these abundance ratios. Only for NGC 339 we observe a hint of intrinsic spread in [Na/Fe],

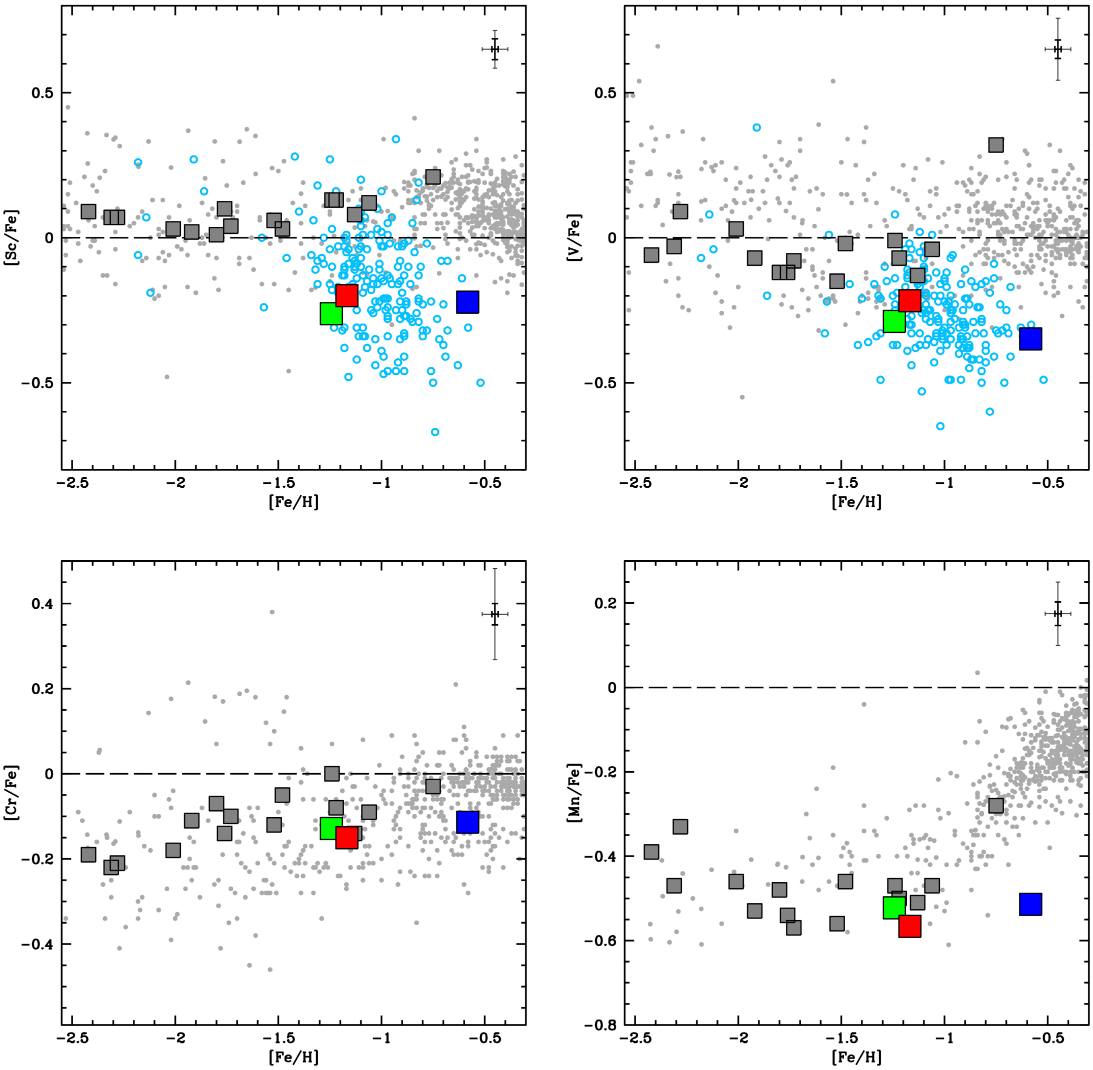

Figure 6.5: Iron-peak elements abundance ratios (Sc, V, Cr and Mn, from top left panel to bottom right panel, respectively) as a function of [Fe/H], for SMC and MW GCs and field stars. Same symbols and data as in figure 6.4. MW field stars data are from Fulbright (2000); Stephens & Boesgaard (2002); Gratton et al. (2003); Reddy et al. (2003, 2006); Bensby et al. (2005); Adibekyan et al. (2012); Roederer & Lawler (2012); Reggiani et al. (2017).

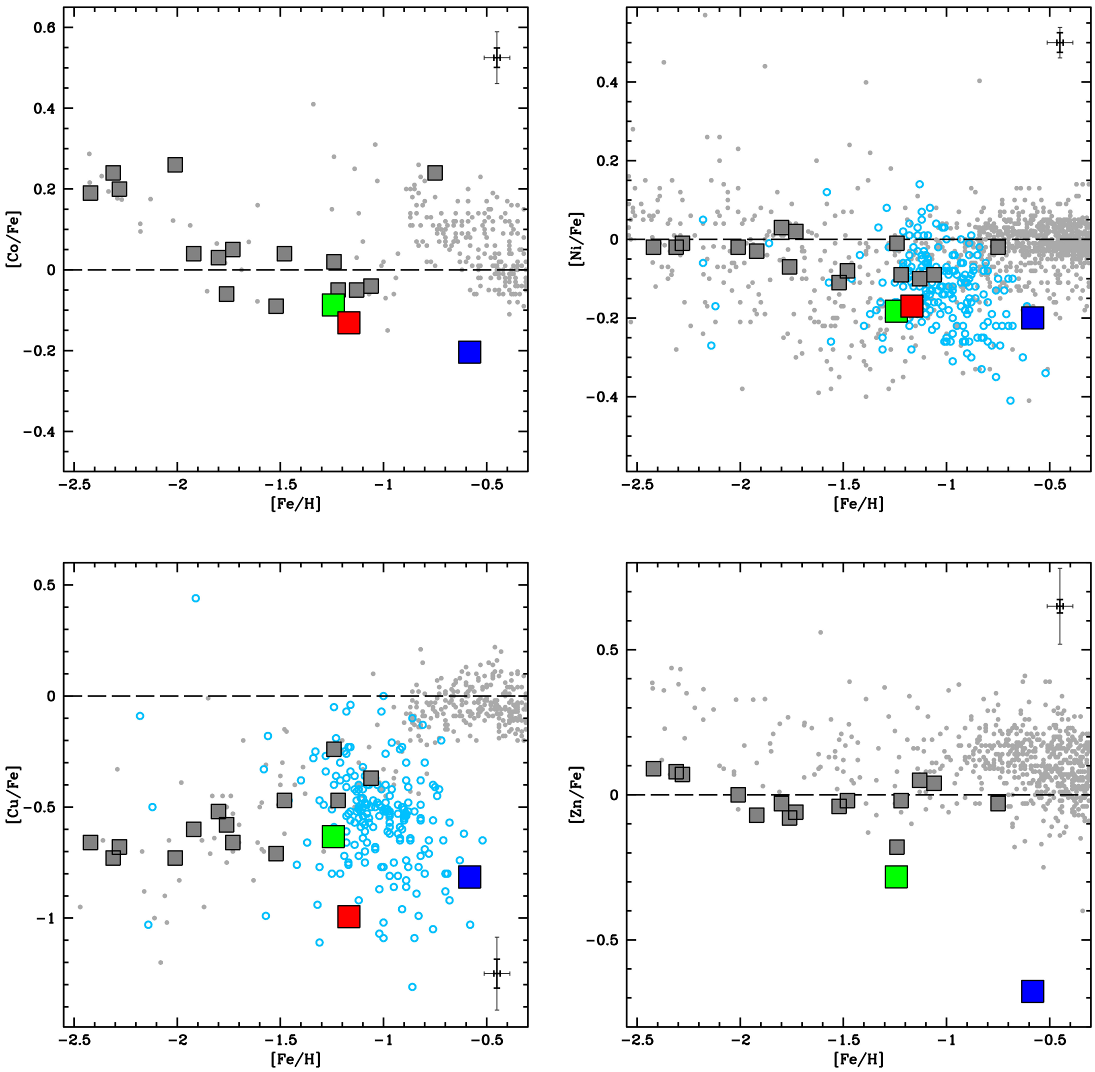

Figure 6.6: Iron-peak elements abundance ratios (Co, Ni, Cu and Zn, from top left panel to bottom right panel, respectively) as a function of [Fe/H], for SMC and MW GCs and field stars. Same symbols and data as in figure 6.4. MW field stars data are from Edvardsson et al. (1993); Fulbright (2000); Stephens & Boesgaard (2002); Gratton et al. (2003); Reddy et al. (2003, 2006); Bihain et al. (2004); Bensby et al. (2005); Nissen et al. (2007); Adibekyan et al. (2012); Roederer & Lawler (2012); Mishenina et al. (2013); Yan et al. (2015); Reggiani et al. (2017).

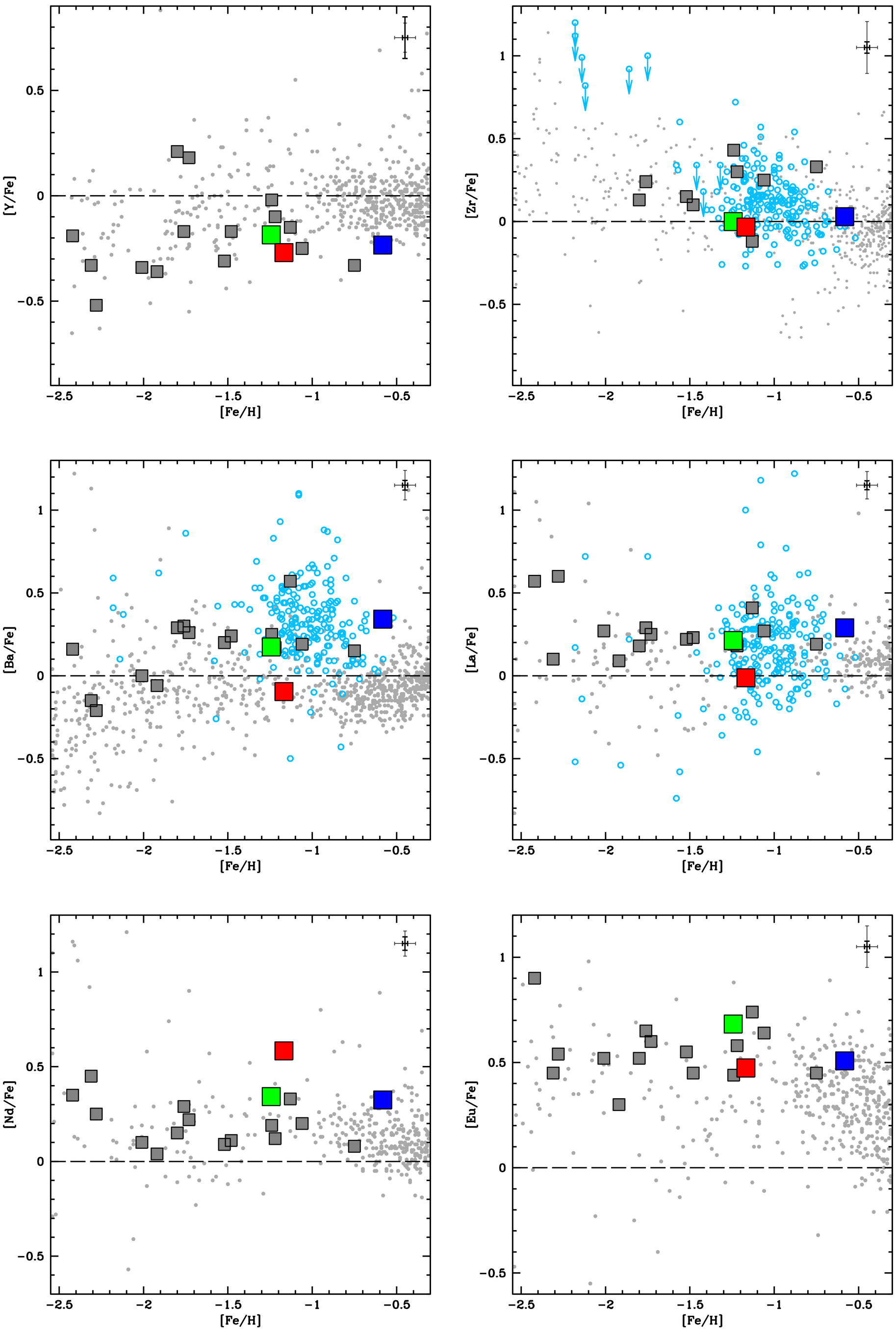

Figure 6.7: Neutron-capture elements abundance ratios (Y, Zr, Ba, La, Nd and Eu, from top left panel to bottom right panel, respectively) as a function of [Fe/H], for SMC and MW GCs and field stars. Same symbols and data as in figure 6.4. MW field stars data are from Edvardsson et al. (1993); Burris et al. (2000); Fulbright (2000); Stephens & Boesgaard (2002); Reddy et al. (2003, 2006); Barklem et al. (2005); Bensby et al. (2005); Roederer & Lawler (2012); Mishenina et al. (2013); Yan et al. (2015); Battistini & Bensby (2016); Reggiani et al. (2017); Forsberg et al. (2019)

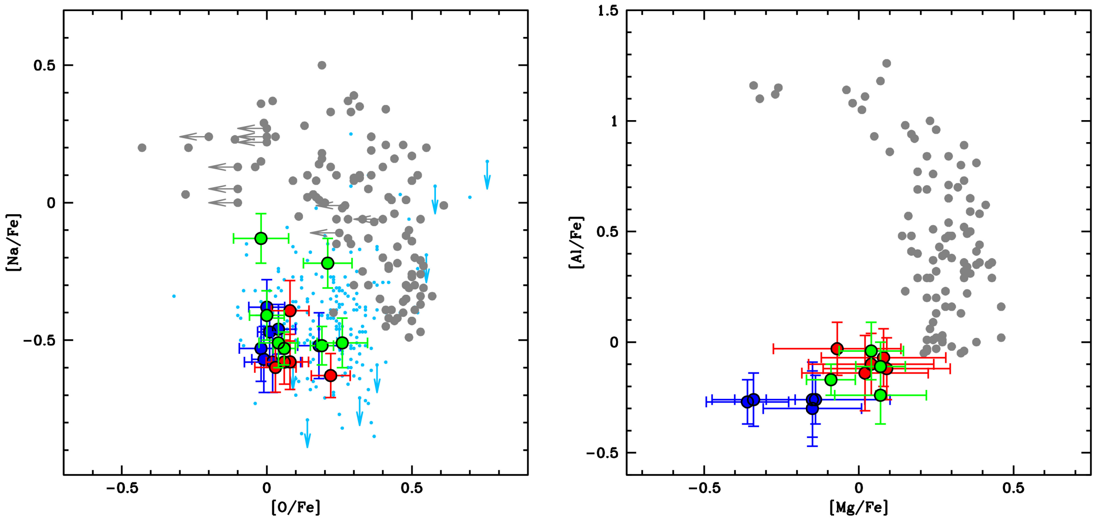

Figure 6.8: [Na/Fe] as a function of [O/Fe] in the left panel, [Al/Fe] as a function of [Mg/Fe] in the right panel. The symbols are: red circles for NGC 121, green circles for NGC 339, blue circles for NGC 419, grey dots for MW GCs from the work in Chapter 4 and light blue dots for SMC field stars from Chapter 5. Arrows indicate upper limits measurements. Error bars are given as the error on the measure for each star analysed in this work.

with two stars enhanced with respect to the other stars. However this difference is marginally statistically significant. Concerning Mg and Al, all the clusters exhibit homogeneous abundances.
Therefore, we can not confirm from our spectroscopic study the presence of multiple stellar populations in NGC 121 and NGC 339, as derived previously from photometric analysis (Dalessandro et al., 2016; Niederhofer et al., 2017a,b). The main reason of this opposite result can be find in the low number of analysed stars, but also the abundance variations in Na-O and Al-Mg in these GCs can be not so extended to be reveal by spectroscopic studies. But we confirm the lack of multiple stellar populations in NGC 419, as derived by Cabrera-Ziri et al. (2020).

6.6 Summary

We analysed high-resolution spectra of stars belonging to three SMC GCs, chosen in order to cover the entire range in age of the SMC GCs.

From the metallicity of the GCs, in relation with their ages, we confirmed the theoretical AMR. In particular we found that the metallicity reached a values of ~ -1.2 dex in the first 2 Gyr, keeping this value nearly constant until 6 Gyr ago. Later, the metallicity started to increase, reaching [Fe/H] ~ -0.6 dex nearly 1 Gyr ago.

Comparing the AMR with the metallicity distribution of SMC field stars, we conclude that the bulk of the SMC stellar populations formed nearly 3-4 Gyr ago (when the SMC started to be gravitationally bound with the LMC) and that the most metal-poor stars formed during the first burst of star formation that the galaxy experienced.

We derived the abundance ratios for elements belonging to the main groups and we compared them with the abundances of SMC field stars derived in Chapter 5. The two samples have similar abundances in all the elements, indicating that GCs and field stars experienced similar chemical enrichment.
We compare the SMC GCs abundances also with MW GCs ones, and we conclude that the SMC has experienced a slower SFR, a lower contribution by massive stars, and a similar contribution by electron capture SNe and low mass AGB stars, and similar rate of NS merger and collapsars.

Finally, analysing O and Na abundances in the GCs stars, we found no evidence of MPs.

Table 6.2: Average abundance ratios for the SMC GCs from the analysed stars. The error on the mean, the average standard error of the measure and the number of stars are also reported.

	NGC 121			NGC 339			NGC 419		
	mean	$\overline{err}$	$N_\star$	mean	$\overline{err}$	$N_\star$	mean	$\overline{err}$	$N_\star$
$[Fe/H]$	-1.17 ± 0.02	0.06	5	-1.24 ± 0.01	0.06	7	-0.58 ± 0.02	0.07	8
$[FeII/H]$	-1.25 ± 0.05	0.10	5	-1.33 ± 0.02	0.05	4	-0.67 ± 0.03	0.08	5
$[Na/Fe]$	-0.56 ± 0.04	0.09	5	-0.40 ± 0.06	0.08	7	-0.50 ± 0.03	0.10	7
$[Al/Fe]$	-0.09 ± 0.02	0.14	5	-0.14 ± 0.04	0.11	4	-0.27 ± 0.01	0.13	5
$[O/Fe]$	0.09 ± 0.03	0.07	5	0.11 ± 0.04	0.07	7	0.02 ± 0.02	0.07	8
$[Mg/Fe]$	0.03 ± 0.03	0.20	5	0.05 ± 0.04	0.13	7	-0.23 ± 0.05	0.17	5
$[Si/Fe]$	0.07 ± 0.04	0.10	5	0.17 ± 0.02	0.08	7	0.02 ± 0.02	0.10	8
$[Ca/Fe]$	0.04 ± 0.01	0.05	5	0.16 ± 0.03	0.07	7	-0.01 ± 0.03	0.10	8
$[Ti/Fe]$	0.04 ± 0.01	0.08	5	0.04 ± 0.02	0.08	7	-0.07 ± 0.03	0.11	8
$[Sc/Fe]$	-0.20 ± 0.02	0.07	5	-0.26 ± 0.06	0.07	4	-0.22 ± 0.03	0.06	5
$[V/Fe]$	-0.22 ± 0.03	0.08	5	-0.29 ± 0.03	0.11	7	-0.35 ± 0.04	0.13	8
$[Cr/Fe]$	-0.15 ± 0.03	0.13	5	-0.13 ± 0.03	0.08	7	-0.11 ± 0.01	0.11	8
$[Mn/Fe]$	-0.57 ± 0.03	0.11	5	-0.52 ± 0.02	0.05	4	-0.51 ± 0.04	0.07	5
$[Co/Fe]$	-0.13 ± 0.02	0.07	5	-0.09 ± 0.02	0.06	7	-0.20 ± 0.03	0.07	8
$[Ni/Fe]$	-0.17 ± 0.04	0.04	5	-0.18 ± 0.01	0.03	7	-0.20 ± 0.03	0.05	8
$[Cu/Fe]$	-0.98 ± 0.09	0.23	3	-0.63 ± 0.05	0.10	7	-0.82 ± 0.05	0.17	6
$[Zn/Fe]$	–	–	–	-0.28 ± 0.03	0.10	4	-0.68 ± 0.01	0.16	4
$[Y/Fe]$	-0.27 ± 0.15	0.06	2	-0.19 ± 0.10	0.07	4	-0.23 ± 0.05	0.07	5
$[Zr/Fe]$	-0.03 ± 0.05	0.15	5	-0.00 ± 0.02	0.14	7	0.03 ± 0.03	0.17	8
$[Ba/Fe]$	-0.10 ± 0.03	0.10	5	0.17 ± 0.03	0.08	7	0.28 ± 0.02	0.08	8
$[La/Fe]$	-0.01 ± 0.02	0.09	5	0.21 ± 0.04	0.08	7	0.29 ± 0.02	0.08	8
$[Nd/Fe]$	0.58 ± 0.04	0.09	5	0.34 ± 0.04	0.05	4	0.32 ± 0.03	0.06	5
$[Eu/Fe]$	0.47 ± 0.03	0.12	5	0.68 ± 0.02	0.09	4	0.51 ± 0.03	0.09	5

Table 6.3: Chemical abundances for the SMC GCs stars, first part.

ID	[Fe/H]	[FeII/H]	[Na/Fe]	[Al/Fe]	[O/Fe]	[Mg/Fe]	[Si/Fe]	[Ca/Fe]	[Ti/Fe]	[Sc/Fe]	[V/Fe]
						NGC 121					
9	-1.22 ± 0.04	-1.34 ± 0.12	-0.58 ± 0.10	-0.03 ± 0.12	0.08 ± 0.06	-0.07 ± 0.21	0.13 ± 0.08	0.02 ± 0.06	0.05 ± 0.09	-0.22 ± 0.06	-0.22 ± 0.07
14	-1.21 ± 0.06	-1.35 ± 0.11	-0.39 ± 0.11	-0.14 ± 0.17	0.08 ± 0.07	0.02 ± 0.20	0.16 ± 0.09	0.05 ± 0.06	0.02 ± 0.10	-0.13 ± 0.06	-0.18 ± 0.07
18	-1.13 ± 0.07	-1.19 ± 0.08	-0.60 ± 0.09	-0.10 ± 0.14	0.03 ± 0.07	0.04 ± 0.20	0.08 ± 0.10	0.06 ± 0.05	0.03 ± 0.07	-0.20 ± 0.09	-0.30 ± 0.12
31	-1.10 ± 0.06	-1.09 ± 0.10	-0.58 ± 0.08	-0.12 ± 0.14	0.06 ± 0.06	0.09 ± 0.21	0.05 ± 0.12	0.08 ± 0.05	0.07 ± 0.08	-0.21 ± 0.07	-0.12 ± 0.06
35	-1.18 ± 0.06	-1.28 ± 0.07	-0.63 ± 0.08	-0.07 ± 0.13	0.22 ± 0.07	0.08 ± 0.20	-0.05 ± 0.11	0.01 ± 0.04	0.04 ± 0.06	-0.23 ± 0.06	-0.26 ± 0.09
						NGC 339					
219	-1.26 ± 0.11	–	-0.51± 0.09	–	0.26 ± 0.09	0.18 ± 0.14	0.10 ± 0.12	0.18 ± 0.08	0.11 ± 0.12	–	-0.29 ± 0.16
466	-1.24 ± 0.08	–	-0.22± 0.09	–	0.21 ± 0.08	–	0.26 ± 0.14	0.30 ± 0.10	0.10 ± 0.15	–	-0.17 ± 0.18
535	-1.24 ± 0.02	-1.27 ± 0.06	-0.53 ± 0.06	-0.17 ± 0.07	0.06 ± 0.04	-0.09 ± 0.08	0.17 ± 0.04	0.05 ± 0.06	-0.05 ± 0.04	-0.28 ± 0.07	-0.40 ± 0.06
835	-1.24 ± 0.08	–	-0.13± 0.09	–	-0.02 ± 0.10	–	0.23 ± 0.12	0.22 ± 0.12	0.05 ± 0.14	–	-0.35 ± 0.18
893	-1.25 ± 0.03	-1.36 ± 0.05	-0.52 ± 0.07	-0.11 ± 0.11	0.19 ± 0.04	0.07 ± 0.08	0.10 ± 0.05	0.11 ± 0.05	0.02 ± 0.05	-0.32 ± 0.05	-0.32 ± 0.07
958	-1.20 ± 0.05	-1.32 ± 0.05	-0.51 ± 0.09	-0.24 ± 0.13	0.04 ± 0.07	0.07 ± 0.15	0.18 ± 0.06	0.11 ± 0.06	0.04 ± 0.05	-0.10 ± 0.09	-0.22 ± 0.06
1076	-1.27 ± 0.04	-1.38 ± 0.05	-0.41 ± 0.09	-0.04 ± 0.13	-0.00 ± 0.06	0.04 ± 0.10	0.18 ± 0.05	0.16 ± 0.04	0.04 ± 0.03	-0.35 ± 0.07	-0.27 ± 0.07
						NGC 419					
345	-0.54 ± 0.11	–	–	–	-0.03 ± 0.10	–	-0.08 ± 0.17	-0.01 ± 0.10	0.01 ± 0.13	–	-0.15 ± 0.17
616	-0.62 ± 0.09	–	-0.52± 0.12	–	0.18 ± 0.07	–	0.04 ± 0.13	0.01 ± 0.14	0.01 ± 0.15	–	-0.32 ± 0.17
727	-0.60 ± 0.05	-0.70 ± 0.07	-0.38 ± 0.10	-0.30 ± 0.17	0.00± 0.06	-0.15± 0.16	0.02 ± 0.08	0.04 ± 0.08	-0.08 ± 0.09	-0.19± 0.05	-0.42± 0.11
732	-0.53 ± 0.05	-0.67 ± 0.11	-0.57 ± 0.12	-0.26 ± 0.12	-0.01± 0.04	-0.34± 0.13	-0.04 ± 0.07	-0.07 ± 0.10	0.00 ± 0.10	-0.32± 0.06	-0.36± 0.12
852	-0.61 ± 0.05	-0.57 ± 0.09	-0.53 ± 0.12	-0.26 ± 0.17	-0.02± 0.08	-0.15± 0.25	0.11 ± 0.08	-0.09 ± 0.11	-0.22 ± 0.09	-0.12± 0.07	-0.52± 0.09
885	-0.55 ± 0.11	–	-0.58± 0.11	–	0.02 ± 0.10	–	0.07 ± 0.15	0.17 ± 0.14	0.00 ± 0.14	–	-0.31 ± 0.17
1384	-0.56 ± 0.04	-0.67 ± 0.08	-0.47 ± 0.10	-0.27 ± 0.10	0.01± 0.04	-0.36± 0.13	0.01 ± 0.06	-0.11 ± 0.08	-0.18 ± 0.08	-0.22± 0.05	-0.36± 0.09
1633	-0.65 ± 0.05	-0.72 ± 0.07	-0.46 ± 0.09	-0.26 ± 0.11	0.04± 0.06	-0.14± 0.16	0.02 ± 0.08	-0.05 ± 0.07	-0.12 ± 0.08	-0.26± 0.06	-0.35± 0.09

Table 6.4: Chemical abundances for the SMC GCs stars, second part.

ID	[Cr/Fe]	[Mn/Fe]	[Co/Fe]	[Ni/Fe]	[Cu/Fe]	[Zn/Fe]	[Y/Fe]	[Zr/Fe]	[Ba/Fe]	[La/Fe]	[Nd/Fe]	[Eu/Fe]
NGC 121												
9	-0.08 ± 0.14	-0.50 ± 0.09	-0.16 ± 0.05	-0.17 ± 0.03	-1.00 ± 0.22	–	-0.42 ± 0.15	-0.01 ± 0.14	-0.16 ± 0.09	0.04 ± 0.08	0.50 ± 0.09	0.45 ± 0.11
14	-0.07 ± 0.15	-0.55 ± 0.07	-0.10 ± 0.07	-0.17 ± 0.04	-1.13 ± 0.23	–	-0.12 ± 0.17	-0.09 ± 0.16	-0.10 ± 0.12	0.03 ± 0.08	0.50 ± 0.09	0.49 ± 0.12
18	-0.24 ± 0.10	-0.63 ± 0.12	-0.18 ± 0.08	-0.11 ± 0.03	-0.81 ± 0.23	–	–	-0.17 ± 0.14	-0.01 ± 0.09	-0.05 ± 0.10	0.66 ± 0.08	0.56 ± 0.12
31	-0.17 ± 0.13	-0.52 ± 0.15	-0.12 ± 0.06	-0.30 ± 0.04	–	–	–	0.15 ± 0.18	-0.03 ± 0.11	-0.08 ± 0.08	0.57 ± 0.10	0.50 ± 0.12
35	-0.19 ± 0.14	-0.64 ± 0.09	-0.11 ± 0.08	-0.10 ± 0.04	–	–	–	-0.05 ± 0.15	-0.18 ± 0.10	0.00 ± 0.09	0.69 ± 0.09	0.37 ± 0.11
NGC 339												
219	-0.22± 0.12	–	0.00 ± 0.09	-0.17 ± 0.05	-0.67 ± 0.12	–	–	-0.01 ± 0.20	0.33 ± 0.09	0.07 ± 0.11	–	–
466	-0.19± 0.13	–	-0.10 ± 0.09	-0.22 ± 0.04	-0.59 ± 0.12	–	–	0.01 ± 0.21	0.16 ± 0.10	0.36 ± 0.11	–	–
535	-0.18 ± 0.05	-0.53 ± 0.03	-0.17 ± 0.03	-0.21 ± 0.02	-0.65 ± 0.07	-0.24 ± 0.09	-0.24 ± 0.05	-0.00 ± 0.08	0.24 ± 0.06	0.19 ± 0.05	0.28 ± 0.04	0.67 ± 0.07
835	-0.02± 0.11	–	-0.07 ± 0.08	-0.14 ± 0.05	-0.63 ± 0.11	–	–	-0.09 ± 0.22	0.07 ± 0.11	0.32 ± 0.11	–	–
893	-0.11 ± 0.05	-0.53 ± 0.03	-0.17 ± 0.03	-0.22 ± 0.02	-0.44 ± 0.08	-0.33 ± 0.09	-0.22 ± 0.05	0.00 ± 0.09	0.09 ± 0.06	0.17 ± 0.05	0.31 ± 0.04	0.63 ± 0.07
958	-0.05 ± 0.06	-0.48 ± 0.09	-0.04 ± 0.05	-0.17 ± 0.02	-0.57 ± 0.11	-0.21 ± 0.14	0.09 ± 0.11	0.02 ± 0.11	0.18 ± 0.09	0.20 ± 0.07	0.45 ± 0.05	0.71 ± 0.11
1076	-0.13 ± 0.05	-0.55 ± 0.04	-0.06 ± 0.04	-0.15 ± 0.02	-0.88 ± 0.08	-0.35 ± 0.10	-0.37 ± 0.06	0.06 ± 0.09	0.15 ± 0.07	0.18 ± 0.07	0.33 ± 0.05	0.72 ± 0.10
NGC 419												
345	-0.18± 0.15	–	-0.19 ± 0.09	-0.07 ± 0.08	-0.67 ± 0.15	–	–	-0.01 ± 0.20	0.27 ± 0.08	0.39 ± 0.10	–	–
616	-0.11± 0.13	–	-0.05 ± 0.09	-0.15 ± 0.07	-0.65 ± 0.10	–	–	0.03 ± 0.20	0.28 ± 0.07	0.25 ± 0.09	–	–
727	-0.10 ± 0.08	-0.50± 0.08	-0.30± 0.05	-0.22 ± 0.03	-0.88 ± 0.15	-0.66 ± 0.15	-0.11 ± 0.08	0.09 ± 0.16	0.28 ± 0.08	0.29 ± 0.07	0.42 ± 0.06	0.54 ± 0.10
732	-0.06 ± 0.08	-0.51± 0.10	-0.23± 0.05	-0.28 ± 0.03	–	-0.70 ± 0.15	-0.33 ± 0.07	0.20 ± 0.16	0.34 ± 0.06	0.35 ± 0.07	0.31 ± 0.06	0.46 ± 0.07
852	-0.15 ± 0.08	-0.54± 0.08	-0.30± 0.05	-0.15 ± 0.04	-0.99 ± 0.32	-0.69 ± 0.19	-0.16 ± 0.08	-0.10 ± 0.15	0.29 ± 0.13	0.26 ± 0.09	0.35 ± 0.06	0.53 ± 0.12
885	-0.08± 0.20	–	-0.10 ± 0.10	-0.25 ± 0.08	-0.87 ± 0.15	–	–	-0.02 ± 0.20	0.20 ± 0.09	0.23 ± 0.11	–	–
1384	-0.12 ± 0.07	-0.38± 0.05	-0.25± 0.04	-0.26 ± 0.03	-0.83 ± 0.15	-0.66 ± 0.15	-0.36 ± 0.06	-0.02 ± 0.13	0.34 ± 0.06	0.24 ± 0.06	0.27 ± 0.05	0.57 ± 0.07
1633	-0.11± 0.08	-0.64± 0.05	-0.21± 0.05	-0.22 ± 0.03	–	–	-0.21 ± 0.08	0.06 ± 0.16	0.21 ± 0.10	0.30 ± 0.07	0.27 ± 0.08	0.44 ± 0.10

Chapter 7

The first unbiased Metallicity Distribution of Sagittarius dSph: preliminary results

Based on the results in
Minelli A., Bonifacio P., Mucciarelli A., Bellazzini M., Monaco L., 2022, in preparation

7.1 Introduction

The Sgr dwarf spheroidal galaxy is the most obvious example of the ongoing disruption of a satellite into a large galaxy, the MW. Nowadays, it is visible the remnant of the galaxy that in the past was possibly as massive as the LMC (as suggested by the results discussed in Chapter 3), and the two arms of its tidal streams.

Until now, extensive and detailed studies of the remnant of Sgr dSph are focused on the central few arcmin of its main body (Carretta et al., 2010b; Mucciarelli et al., 2017b; Alfaro-Cuello et al., 2019), where the surface density of the dwarf galaxy reaches its maximum. As explained in Section 2.3, this region hosts a complex and composite stellar nucleus and a massive metal-poor GC, namely M 54 (Monaco et al., 2004b; Bellazzini et al., 2008; Alfaro-Cuello et al., 2019), whose stellar content is not representative of the main body of Sgr dSph (Siegel et al., 2007; Mucciarelli et al., 2017b; Alfaro-Cuello et al., 2019). Moreover, Sgr lies at low Galactic longitude and latitude and the blue side of the RGB in its CMD is strongly affected by contamination of stars from the Bulge and the Thick Disc of the MW. As a result, we are still lacking an unbiased view of its metallicity distribution and of its main abundance patterns over the entire range of metallicity spanned by this system.

This problem can be solved thanks to *Gaia* proper motions, that allow us to effectively remove the contaminants from the CMD, selecting a clean sample of high-probability Sgr members over the whole color/metallicity range spanned by Sgr RGBs. In this Chapter are reported some preliminary results of the study of a sample of 452 Sgr spectra, selected in the central region of the Sgr main body using *Gaia* proper motions.

7.2 Spectroscopic dataset

The 452 observed RGB stars are located in four fields (Fig. 7.1) in the core of Sgr, outside of the nuclear region in order to avoid stars belonging to the Sgr stellar nucleus or to M 54. The Sgr CMD was clean retaining only stars with parallaxes compatible with the distance of Sgr and, especially, having proper motions within 0.5 mas/yr ($\sim$ 60 km s^{-1}) from the mean motion of the galaxy (as determined by Gaia Collaboration et al., 2018c). Among the remaining stars, candidate targets were selected in the magnitude range $16.0 < G < 17.4$ (approximately corresponding to $16.4 < V < 17.8$), in order to avoid stars so cool to have their spectra badly affected by TiO bands (Monaco et al., 2005), and also preventing the metallicity

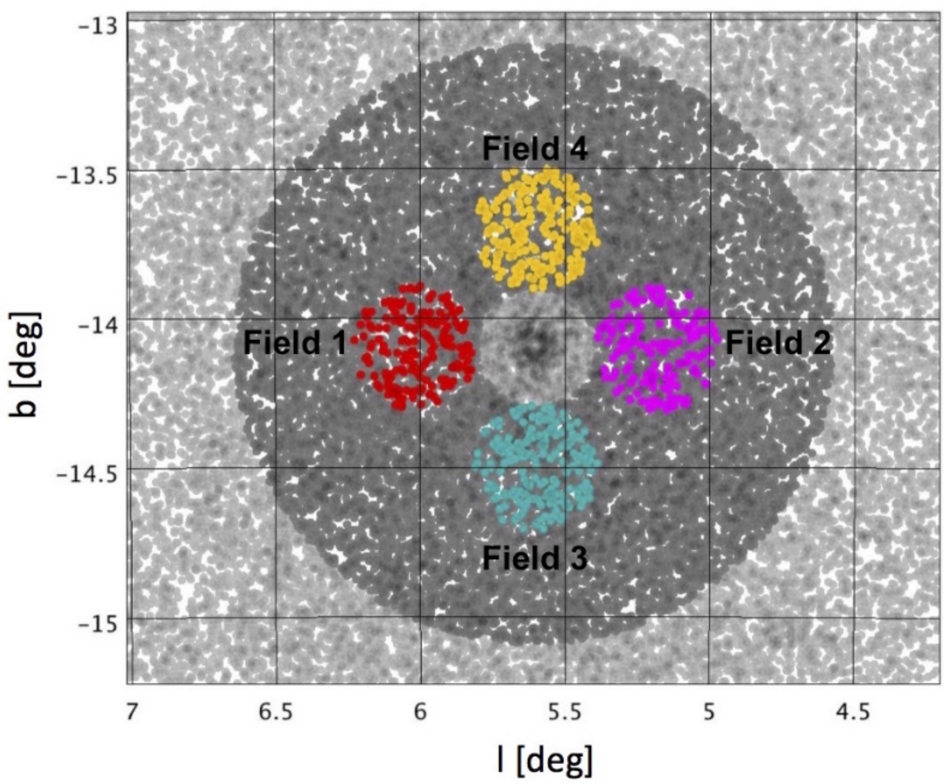

Figure 7.1: Map of the central region of Sgr from *Gaia* eDR2 parallax and proper motions selected stars. In dark grey the innermost 1.0 deg with the nuclear region excised. The eligible spectroscopic targets in the four FLAMES fields observed are shown as colored circles.

bias inherent to a selection in color. The observed targets are represented in the *Gaia* eDR3 CMD in Fig. 7.2 as red dots. This CMD is made with all the stars present in the central region of Sgr, without apply proper motion selection.
All the spectra have been acquired with the multi-object spectrograph GIRAFFE-FLAMES (Pasquini et al., 2002) mounted at the Very Large Telescope of ESO, with the HR21 setup (8484 – 9001 Å and a resolution of 18000). The observations are collected under the ESO program 105.20AH.001 (PI: Bellazzini), and took place between 28th June and 5th July 2021.
The spectra have been reduced with the dedicated ESO pipeline*, that performs the bias subtraction, flat-fielding, wavelength calibration, spectral extraction and order merging. For each target, two exposures have been acquired. The individual exposures have been sky-subtracted using the average spectrum of some close sky regions observed at the same time of the science targets, and then they are combined in a single spectrum for each star, in order to reach a SNR per pixel of at least 30 for the faintest stars.

*http://www.eso.org/sci/software/pipelines/

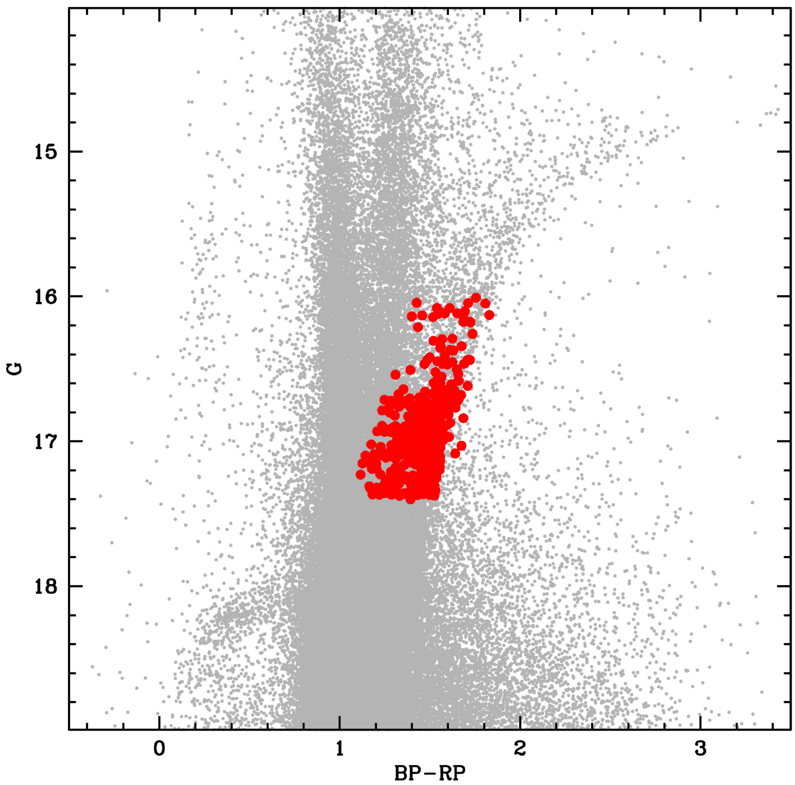

Figure 7.2: *Gaia* eDR3 CMD of the central region of Sgr without proper motion selection. Red dots are the targets observed in this work.

7.3 Atmospheric parameters

The adoption of a reliable $T_{\rm eff}$ is a crucial ingredient to derive the correct metallicity of the observed stars. Due to the small spectral coverage of the Sgr spectra, the number of Fe lines is too small (between 8 to 22 according to the brightness of the star) to prevent a robust spectroscopic determination of $T_{\rm eff}$. Therefore, we derived $T_{\rm eff}$ from the photometry.
For all the selected targets we have accurate *Gaia* eDR3 photometry, from which we can derive the atmospheric parameters in a homogeneous way.
We derive the atmospheric parameters iteratively, until the difference between the new and the old $T_{\rm eff}$ was smaller than ± 50 K and the difference between new and old log g was smaller than ± 0.05 dex. We create a grid in the parameter space defined using the `ATLAS9` model atmosphere grids by Mucciarelli et al., in preparation. The starting points are the stellar mass and the metallicity of the stars. $T_{\rm eff}$ was computed from the semi-empirical infrared flux method (BP-RP)-$T_{\rm eff}$ relation derived by Mucciarelli et al. (2021b). (BP-RP) where dereddened using E(BP-RP) derived by interpolating in the theoretical grid the E(B-V) from the reddening maps of Schlafly & Finkbeiner (2011). The value of E(B-V) are 0.122 ± 0.003, 0.126 ± 0.004, 0.133 ± 0.005, 0.138 ± 0.002 for field from 1 to 4 as in Fig. 7.1 respectively).
The bolomentric correction (BC_G) was derived by interpolate in $T_{\rm eff}$ using a grid of theoretical (BC_G) based on the synthetic spectra as above, and the value of log g was computed from the equation:

$$\log g = \log{(M/M_\odot)} + 4\log{(T_{eff}/T_\odot)} + 0.4(G_0 + BC_G) + 2\log p + \log\ L_\odot + \log g_\odot \tag{7.1}$$

where p is the parallax, derived adopting the distance modulus from Monaco et al. (2004a) and G_0 is the dereddened apparent G magnitude.
Finally the v_t have been derived from the relation of Mucciarelli & Bonifacio (2020), according to the log g and the metallicities of the stars.

Because the atmospheric parameters depend on the value measured for the metallicity, we repeat this procedure to derive the parameters using the metallicity obtained from the first chemical analysis.

7.4 Analysis and preliminary results

In this section it is reported a description of the methods adopted to derive the RVs and the metallicities of the analysed targets, and the results obtained until now. The analysis is still in progress, therefore the results reported here are only preliminary.

7.4.1 Radial Velocity

The first step in the spectral analysis is to derive the RV of each target. The RVs will be used to

1. identify the stars members of the Sgr main body;
2. perform a kinematic study of Sgr, in particular in combination with the metallicity;
3. infer the rate of success in the selection of member stars by using *Gaia* proper motions.

We tested different tools to derive RVs, such as cross-correlation, template matching, and the code `DAOSPEC` (Stetson & Pancino, 2008). The main difficulty in the RV measurement for these spectra arises from the presence of numerous spikes in the spectra that makes it hard to recognize the atomic lines. The spikes come from the operation of sky subtraction, because of the existence of numerous and deep telluric lines in the wavelength range of the available spectra.
Among all, the most promising tool is the template matching, in which a synthetic spectrum, computed for each star with the appropriate atmospheric parameters and metallicity, is shifted until the recognized spectra lines correspond to the ones in the observed spectra. This can be mainly done thanks to the presence of the prominent CaII triplet lines, located in this wavelength range, and not significantly affected by the spikes.
The RV of each star is derived from the wavelength shift value of the synthetic spectrum in comparison to the observed one.

The RV distribution for the analysed stars is reported in Fig. 7.3.
According to Ibata et al. (1997), we consider Sgr member the stars with RV between +100 km/s and +180 km/s. We found that all the observed stars can be considered belonging to the main body of Sgr according to their RV values. Therefore the rate of identification of Sgr member stars derived from the *Gaia* proper motions is equal to 100%. This result confirms the power of the adopted approach based on the *Gaia* eDR3 proper motions. This finding will be extremely useful for future survey devoted to study Sgr stars (for instance MOONS@VLT).

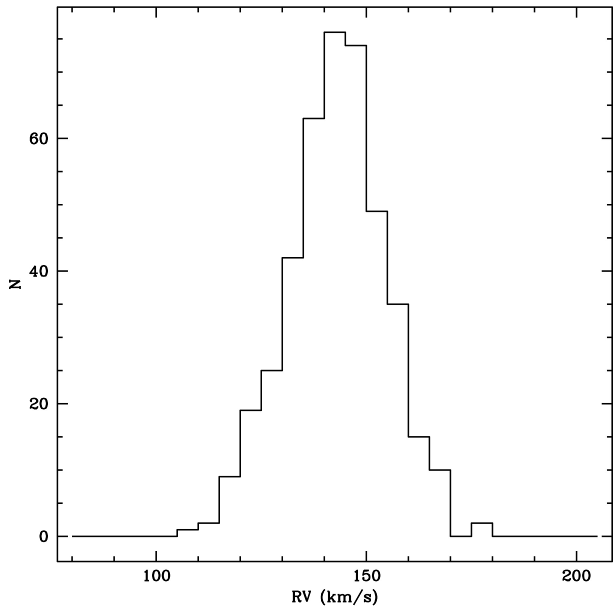

Figure 7.3: Radial velocity distribution of the analysed targets.

7.4.2 Metallicity Distribution

We measured the Fe abundances from nearly 15 Fe lines for each target. The selection of the linelist used to derive the metallicity was performed by comparing the observed spectrum of each star with a synthetic spectrum, computed with the appropriate atmospheric parameters and metallicity, in order to evaluate the level of blending and saturation of each transition. Synthetic spectra have been computed with the procedure described in Section 3.4.

The EWs of every lines belonging to the final linelist (improved for every star) have been measured with `DAOSPEC` (Stetson & Pancino, 2008) through the wrapper `4DAO` (Mucciarelli, 2013), forcing the RV to the value measured by the template matching. From the measured EWs, Fe abundances have been derived by using the code `GALA` (Mucciarelli et al., 2013).

In Fig. 7.4 is reported the metallicity distribution derived for the analysed stars. The distribution can be described as the sum of two Gaussian components, with the split at [Fe/H] $= -0.75$ dex, describing two different stellar populations: the metal-rich population has a mean metallicity of $\overline{[Fe/H]} = -0.25$ dex and a standard deviation of $\sigma = 0.21$ dex, while the metal-poor population has $\overline{[Fe/H]} = -1.12$ dex and $\sigma = 0.28$ dex.

One only star with [Fe/H] < -2.0 dex ([Fe/H] $= -2.29$ dex) has been found in the sample. Therefore, the fraction of very metal-poor stars in Sgr main body is $\sim 0.2\%$. An explanation of this very small fraction can be that the metal-poor population

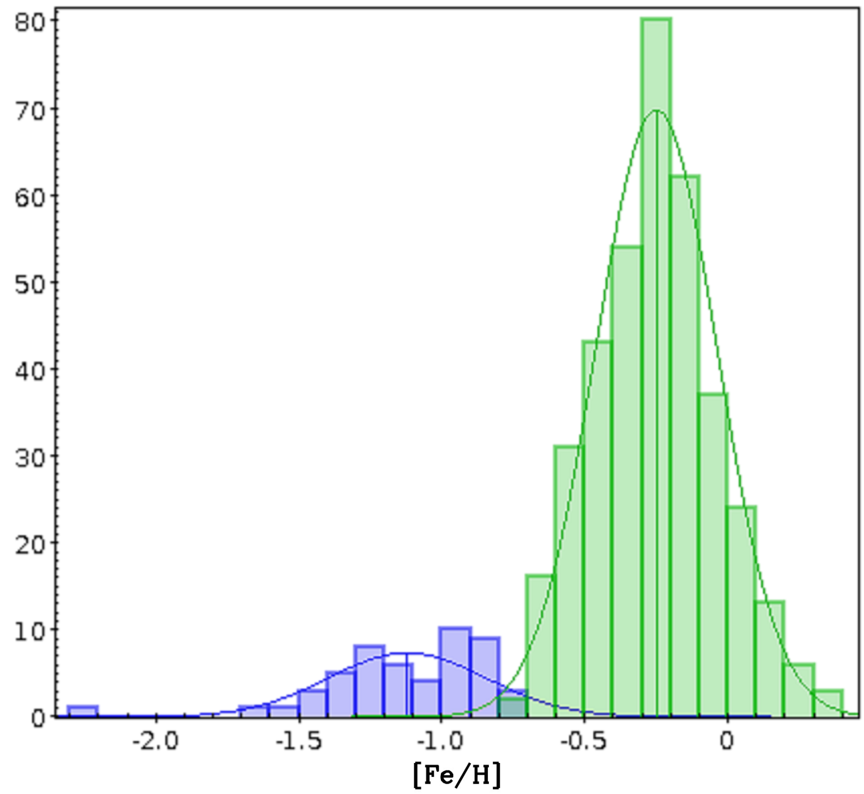

Figure 7.4: Metallicity distribution of Sgr stars analysed in this work. Two stellar populations are identified, a dominant metal-rich population (green Gaussian) and a metal-poor one (blue Gaussian).

have been stripped away from the galaxy due to the gravitational interaction with the MW. Indeed, the Sgr stream stars are on average more metal-poor than the main body ones (Monaco et al., 2007; Carlin et al., 2018; Hayes et al., 2020; Hasselquist et al., 2021). Moreover, it is also possible that the metal-poor stars are gathered in the most central region of the galaxy, because from previous studies there are evidence of a higher fraction of metal-poor stars (Mucciarelli et al., 2017b; Hansen et al., 2018; Chiti & Frebel, 2019).

We compare our metallicity distribution with the ones derived by Hayes et al. (2020) from *APOGEE* spectra of a large sample of Sgr stars belonging both to the main body and the streams, selected according to their angular momentum. The comparison is reported in Fig. 7.5, where the distributions are normalized to have the same area. It is clear that the main body stars are more metal-rich than the streams ones. There is a difference in the two main body metallicity distributions, with the peak of the ours that is about 0.2 dex more metallic than that by Hayes et al. (2020), but both distributions show a secondary stellar population moved toward the low metallicities.

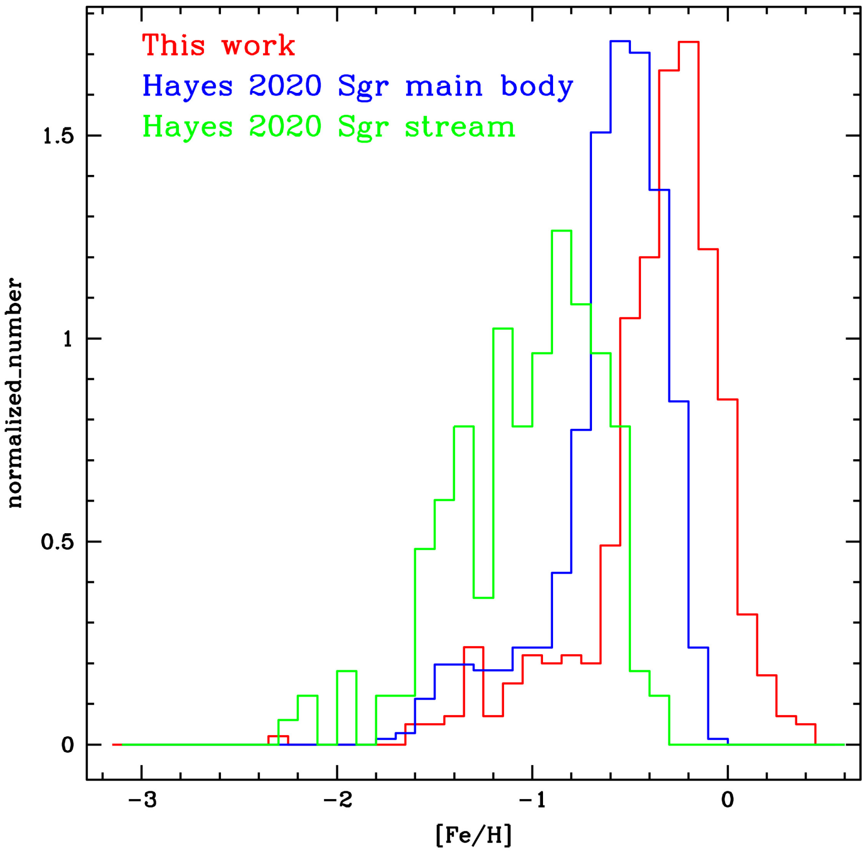

Figure 7.5: Comparison between the metallicity distribution derived in this work (red line) and the distributions derived by Hayes et al. (2020) for the main body (blue line) and stream stars (green line) of Sgr. The distributions are normalized to have the same area.

7.4.3 Substructures

An interesting investigation is the search for the presence of sub-populations, i.e. stellar populations distinct from the other Sgr stars. Putting together the information derived from the kinematic and the chemical studies, we look for stellar populations with similar metallicity that have kinematic properties different from the other stars. Taking into account the RVs, we are evaluating only one component of the motion of the star, not the entire kinetic energy. To have a proxy of the kinetic energy we compute the speed for each star, starting from RVs and the proper motion in right ascension and declination provided by *Gaia* eDR3, following the relation provided by Hobbs et al. (2021) (Section 4.1.7, equation 4.9):

$$speed = \sqrt{4.74047^2 \times \left[\left(\frac{pmra}{parallax} \right)^2 + \left(\frac{pmdec}{parallax} \right)^2 + RV^2 \right]} \qquad (7.2)$$

In Fig. 7.6, are reported the RVs and the speeds, scaled for their mean value in the distribution, as a function of the metallicities for each target. We divide the stars in 2 groups according to their metallicity. The metallicity cut is made at [Fe/H] = – 0.75 dex, according to the two Gaussian components identified in the metallicity distribution (see Fig. 7.4). We compute the mean RV and speed for each sub-population, represented as red squares in Fig. 7.6. Neither for RV-metallicity nor speed-metallicity plane, a significant difference between the two stellar populations is found.
Therefore, no evidence of substructures are visible in our Sgr sample.

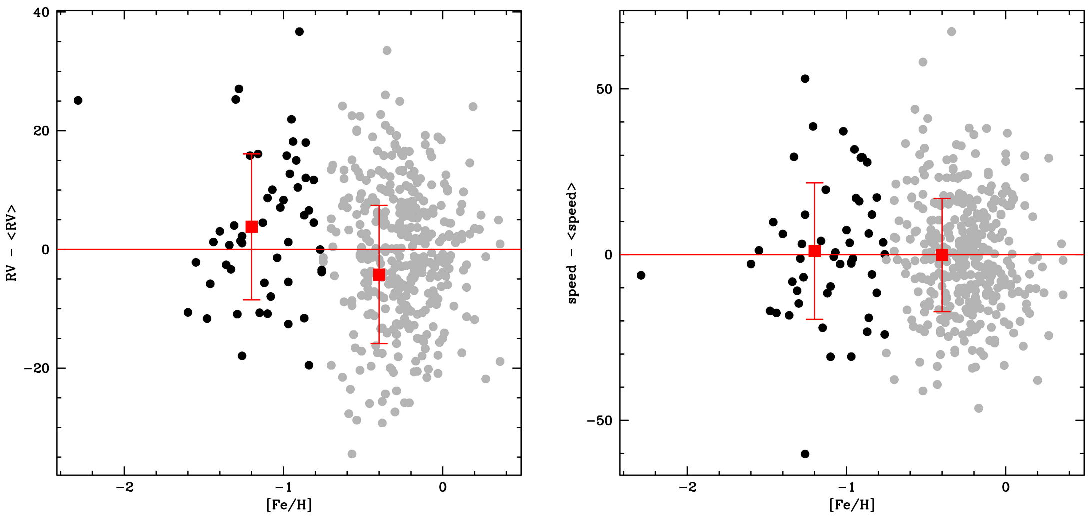

Figure 7.6: RV scaled for the mean RV of the distribution as a function of the metallicity for the analysed stars in the left panel. The same but for the computed speed values in the right panel. Black dots are metal-poor stars, grey dots metal-rich stars, split at [Fe/H] = – 0.75 dex. Red squares are the mean values of the considered sub-sample of targets, while the error bars are the measured standard deviations.

7.5 Summary

In this work we analysed a large sample of main body Sgr stars located in four fields in the central region of the galaxy. The targets are selected in an unbiased way using *Gaia* proper motions. Shown below the derived preliminary results:
(1) We derive a success rate of 100% in the selection of stars using *Gaia* proper motions.
(2) The metallicity distribution can be described as the sum of two Gaussian components, a metal-poor stellar population peaked at − 1.12 dex and the dominant metal-rich one, with the metallicity peak at − 0.25 dex.
(3) No evidence of stellar populations with metallicity or kinematical properties different from other Sgr stars is found.

The next step is to derive the abundances of other elements for which some atomic lines are present in the available spectra, such as Al, Mg, Ca, Ti and possibly Si and V.
Moreover, 30 spectra were observed with the high-resolution spectrograph UVES during the same observations of the GIRAFFE targets discussed here. These stars are located on the bright, blue (metal-poor) part of the Sgr RGB. With these spectra we will measure the abundance of elements from all the main groups providing a complete screening of the metal-poor Sgr stars.

Chapter 8

A new set of chisels for Galactic archaeology: Sc, V and Zn as taggers of accreted globular clusters

Based on the results published in
Minelli A., Mucciarelli A., Massari D., Bellazzini M., Romano D., Ferraro F. R., 2021, The Astrophysical Journal, 918, 32

8.1 Introduction

According to the generally accepted Λ-CDM cosmological model, large galaxies that we observe today were formed from the merging of small structures (White & Rees, 1978; Gaia Collaboration et al., 2018c). The MW is an excellent example of this assembly mechanism, since in the past it has experienced several merger events, many of which have been recently discovered thanks to the advent of the *Gaia* mission (e.g., Gaia-Enceladus-Sausage, Sequoia, Thamnos, see Helmi (2020) for a comprehensive review). During this assembly process, the MW accreted both field stars and GCs. In particular, about 50% - 60% of its current population of GCs has likely been accreted from different external progenitors, while the rest has likely formed in-situ (Massari et al., 2019; Forbes, 2020). So far, the accreted or in-situ origin of the GCs has been primarily assessed by using their dynamics, coupled with information on their age-metallicity relation (Kruijssen et al., 2019; Massari et al., 2019). However, the dynamical properties of some GCs do not allow a clear-cut classification.

Chemical tagging (Freeman & Bland-Hawthorn, 2002) is a powerful tool to reveal the origin of stars by means of their chemical patterns. In particular, it has been shown both theoretically (e.g. Matteucci & Brocato, 1990) and observationally (e.g.

Gaia Collaboration et al., 2018c; Fernández-Alvar et al., 2018), that abundance of α-elements is an efficient tool to distinguish stars born in the MW from those born in dwarf galaxies. Furthermore, the slow neutron-capture elements were observed to be enhanced in dwarf galaxies with respect to MW stars of similar metallicity (see e.g. Tolstoy et al., 2009).

As revealed by the comparison between LMC/Sgr and MW (see Chapter 3), the chemical abundance ratios of some iron-peak elements, namely Sc, V and Zn, can be used as diagnostics to identify possible extra-galactic stars in the metal-rich regime ([Fe/H] > -1 dex, see Section 3.5.3)).

These usually poorly explored abundance ratios are, thus, able to distinguish stars formed in low SFR environments, like those of dwarf galaxies, in the metal-rich regime, where more commonly investigated abundance ratios (like the explosive α-elements or neutron-capture elements) lose their sensitivity as a proxy of different stellar birth places.

Here, I present an application of the proposed tool for chemical tagging to four metal-rich GCs, namely NGC 5927, NGC 6496, NGC 6388 and NGC 6441. These GCs have similar metallicities ([Fe/H] ~ -0.5 dex) and they are thus located in the metallicity range where the iron-peak element abundance ratios should exhibit the largest discrepancy in case they have a different origin (see Section 3.5.3). According to their dynamical properties, the first two have been clearly identified as in-situ clusters (Massari et al., 2019). On the other hand, the other two seem to share an accreted origin, but their orbital properties make their classification more uncertain (see Massari et al., 2019; Kruijssen et al., 2020). These two clusters are usually associated each other, in particular because they exhibit extended blue horizontal branches (Rich et al., 1997), despite of their high metallicity, suggesting an high He content (Bellini et al., 2013).

8.2 Spectroscopic datasets

All the spectra have been acquired with the multi-object spectrograph UVES-FLAMES (Pasquini et al., 2002) mounted at the Very Large Telescope of ESO, using the grating 580 Red Arm CD#3, which provides a spectral resolution of R= 47000 and a spectral coverage between 4800 and 6800 Å. They have been reduced with the dedicated ESO pipelines*, including bias subtraction, flat-fielding, wavelength calibration, spectral extraction and order merging. For each individual spectrum, the sky background has been subtracted, using the spectra obtained observing empty sky regions.

Considering the high luminosity/low temperature and high metallicity of the observed stars, we check for the presence of TiO molecular bands that can affect the

*http://www.eso.org/sci/software/pipelines/

derived chemical abundances and we exclude the contaminated spectra.
The targets of our analysis are four GCs. Their data were collected as follows:

- *NGC 5927* – NGC 5927 is a disky MW GC (according to the classification adopted by Massari et al., 2019, disk clusters have the maximum height from the disk $Z_{max} < 5$ kpc and the orbital circularity $circ < 0.5$). It has a metallicity of [Fe/H] = – 0.47 ± 0.02 dex (Mura-Guzmán et al., 2018) and a mass of $2.75 \pm 0.02 \times 10^5\ M_\odot$(the value is taken from the current latest version of the GCs database by Holger Baumgardt, see Baumgardt & Hilker, 2018). The dataset for this GC is composed of five RGB stars, observed under the ESO-VLT program 079.B-0721 (PI: Feltzing).

- *NGC 6441* – This cluster has a metallicity of [Fe/H] = – 0.39 dex ± 0.04 dex (Gratton et al., 2006), a mass of $1.32 \pm 0.01 \times 10^6\ M_\odot$ (Baumgardt & Hilker, 2018) and despite its orbit currently place it in the Galactic Bulge, it likely has an accreted origin according to Massari et al. (2019). Among the four members identified by Gratton et al. (2006), we include in our analysis only the two giant stars observed under the ESO-VLT program: 073.D-0211 (PI: Carretta), whose spectra are not contaminated by TiO molecular bands.

- *NGC 6388* – This cluster has a similar orbit compared to that of NGC 6441, yet Massari et al. (2019) classify it as an in-situ Bulge GCs (these authors defines as bulge clusters those placed on highly bound orbits, with apocenter $apo < 3.5$ kpc). It has a mean metallicity of [Fe/H] = – 0.44 ± 0.01 dex (Carretta et al., 2007) and a mass of $1.25 \pm 0.01 \times 10^6\ M_\odot$ (Baumgardt & Hilker, 2018). Among NGC 6388 stars observed under the ESO-VLT program: 073.D-0211 (PI: Carretta), we analyzed the four giants that are cluster members according to their RV (Carretta et al., 2007) and whose spectra were not contaminated by TiO molecular bands.

- *NGC 6496* – Just like NGC 5927, NGC 6496 is a disky MW GC. It has a metallicity of [Fe/H] = – 0.46 ± 0.07 dex derived from low-resolution spectra (Carretta et al., 2009c) and a mass of $6.89 \pm 0.73 \times 10^4\ M_\odot$ (Baumgardt & Hilker, 2018). This dataset includes five RGB stars observed in the contest of the ESO-MIKiS survey (Ferraro et al., 2018), Large Programme 193.D-0232 (PI: Ferraro). The member stars are selected according to their RV.

The elements we focus on in our investigation are generally not affected by the chemical peculiarities associated to the so-called phenomenon of multi-populations in GCs (Bastian & Lardo, 2018). The only possible exception is Sc, which shows possible variations in massive GCs (Carretta & Bragaglia, 2021). NGC6441 and NGC6388 are indeed massive, but they do not show Sc variations according to the quoted analysis.

8.3 Analysis

The four target GCs are characterized by large values of color excess and differential reddening that make the atmospheric parameters of individual stars uncertain when derived from the photometry. Thanks to the large number of Fe I lines available in the UVES spectra, T_{eff} can be easily derived by imposing the excitation equilibrium. As discussed by Mucciarelli & Bellazzini (2020), for metal-rich giant stars spectroscopic temperatures are consistent with the photometric temperatures and the method can be adopted safely (at variance with the metal-poor stars where the spectroscopic temperatures are biased and systematically under-estimated, as shown in Fig. 9 of Mucciarelli & Bellazzini, 2020).

The log g is derived by using theoretical isochrones computed with the *Dartmouth Stellar Evolution Database* (Dotter et al., 2008), adopting for each GC an isochrone with appropriate age (Forbes & Bridges, 2010) and chemical mixture (we started with the literature value of [Fe/H] and [α/Fe], adapting in each interaction their value to the results of our analysis).

Finally, the v_t of the stars are derived spectroscopically, by minimizing the slope between the abundances from Fe I lines and the reduced equivalent widths.

The adopted atmospheric parameters for each stars are listed in Table 8.1.

Abundances of Si, Ca, Ti and Fe have been derived from the measured equivalent widths (EWs) of unblended lines using the code `GALA` (Mucciarelli et al., 2013). The

Table 8.1: Atmospheric parameters for the individual target stars.

star	T	log g	v_t
NGC 5927			
5039161	4400	1.97	1.40
5039423	4550	2.25	1.60
5040219	4550	2.25	1.30
5040282	4500	2.16	1.20
5041223	4500	2.16	1.40
NGC 6388			
77599	4100	1.33	1.60
83168	4150	1.42	1.50
108895	4000	1.16	1.50
110677	4000	1.16	1.50
NGC 6441			
7004463	3950	1.07	1.40
7004487	4050	1.24	1.20
NGC 6496			
14	4150	1.48	1.30
17	4150	1.48	1.30
18	4150	1.48	1.40
26	4400	1.94	1.40
159	4100	1.39	1.20

EWs have been measured with DAOSPEC (Stetson & Pancino, 2008) through the wrapper 4DAO (Mucciarelli, 2013). A line-by-line inspection has been performed in order to check the continuum location and the best-fit for each individual line.

The chemical abundances for the species for which only blended lines (Sc, V, Ba, La and Eu) or transitions located in noisy/complex spectral regions (Zn) are available, have been derived with our own code SALVADOR that performs a χ^2-minimization between the observed line and a grid of suitable synthetic spectra calculated on the fly using the code SYNTHE (Kurucz, 2005).

We exclude from our analysis those elements (O, Na, Mg and Al) involved in the multiple population phenomenon (Bastian & Lardo, 2018).

The procedure to select the lines used to derive the chemical abundances of the involved elements is described previously in Section 3.4, together with the typical number of lines generally used for each species. Atomic data for the selected lines are from the Kurucz/Castelli database, with more recent or more accurate data for some specific transition (see Mucciarelli et al., 2017a, for additional references related to Fe, Si, Ca, Ti, Ba and Eu lines). Atomic data for Sc and V lines are from MFW e NBS (Wiese & Fuhr, 1975; Martin et al., 1988b). For the Zn line at 4810 Å we adopt the oscillator strength by Roederer & Lawler (2012). Data for the La line at 6390 Å are from Lawler et al. (2001). Solar reference abundances are from Grevesse & Sauval (1998), for consistency with our previous work (see Chapter 3).

Errors in each abundance ratios have been calculated following the procedure described in Section 3.4.1 and propagating the uncertainties in astrophysical parameters into the chemical abundances.

8.4 Results and discussion

The objective of our analysis is to investigate whether the four GCs, all with a similar [Fe/H] ~ -0.5 dex, show any differences in their elemental abundances, with particular focus on the iron-peak elements that have proven to be effective in distinguishing accreted from in-situ stars in this metal-rich regime. To do so, we homogeneously analyse high-resolution spectra of RGB stars belonging to these Galactic GCs. The mean abundance ratios of the GCs for the analysed species are reported in Table 8.2, instead the abundances measured in individual stars are listed in Table 8.3.

Fig. 8.1 shows the measured abundance ratios for α-, iron-peak and neutron-capture elements, as a function of [Fe/H] for the stars analysed in the four target clusters. We can immediately appreciate that the α-elements Si and Ca show similar abundance ratios in all the four GCs. Slow (La and Ba) and rapid (Eu) neutron-capture elements, in addition to Ti, show a marginal discrepancy, with NGC 6388 and NGC 6441 being under-abundant compared to NGC 5927 and NGC 6496 at 1-2 sigma

Table 8.2: Mean abundance ratios, with the error on the mean and the average standard error of the measure for the four target clusters.

	NGC 5927		NGC 6388		NGC 6441		NGC 6496	
element	mean	$\overline{err}$	mean	$\overline{err}$	mean	$\overline{err}$	mean	$\overline{err}$
$[Fe/H]$	–0.46±0.01	0.05	–0.49±0.01	0.06	–0.54±0.06	0.04	–0.64±0.01	0.03
$[Si/Fe]$	+0.17±0.01	0.05	+0.24±0.05	0.07	+0.27±0.04	0.08	+0.29±0.01	0.04
$[Ca/Fe]$	+0.11±0.03	0.07	+0.11±0.02	0.11	+0.14±0.03	0.10	+0.20±0.04	0.05
$[Ti/Fe]$	+0.25±0.01	0.05	+0.12±0.05	0.11	+0.18±0.00	0.09	+0.28±0.03	0.05
$[Sc/Fe]$	+0.33±0.02	0.05	+0.01±0.02	0.06	+0.03±0.08	0.10	+0.38±0.01	0.06
$[V/Fe]$	+0.21±0.01	0.08	–0.25±0.05	0.14	–0.32±0.03	0.11	+0.17±0.02	0.12
$[Zn/Fe]$	+0.26±0.05	0.07	–0.12±0.04	0.08	–0.49±0.11	0.14	+0.29±0.07	0.14
$[Ba/Fe]$	+0.07±0.03	0.06	+0.05±0.03	0.07	–0.05±0.07	0.06	+0.22±0.04	0.07
$[La/Fe]$	+0.21±0.04	0.04	+0.12±0.02	0.07	+0.01±0.04	0.06	+0.26±0.02	0.05
$[Eu/Fe]$	+0.46±0.03	0.04	+0.34±0.04	0.04	+0.34±0.04	0.06	+0.51±0.01	0.05

level from the comparison between the mean abundance values and their standard deviation. On the other hand, a stark difference (at a significance level always larger than 3 sigma, up to $\sim$ 10 sigma) is found when considering the abundances of Sc, V and Zn. In particular NGC 6388 and NGC 6441 have abundance ratios for these iron-peak elements significantly lower than those measured in NGC 5927 and NGC 6496. We stress that these differences cannot be attributed to some systematics in the chemical analysis because the assumptions in the analysis of all the GCs are the same (i.e. the reference solar abundances, the atomic data, the model atmospheres, the method to derive the atmospheric parameters), and we analyse stars of similar spectral type. Therefore, the origin of the different [Sc/Fe], [V/Fe] and [Zn/Fe] chemical abundance ratios must be intrinsic, due to a real difference in the chemical enrichment path followed by the gas from which the two pairs of clusters formed.

Interesting enough, the differences in these abundance ratios for the two pairs of GC, match well those measured in our previous work (see Chapter 3) between LMC/Sgr and MW field stars of similar metallicity (overplotted in Figs. 8.1 as small filled circles). In particular, NGC 6388 and NGC 6441 exhibit [Sc/Fe], [V/Fe] and [Zn/Fe] abundances similar to those measured in LMC/Sgr stars, while NGC 5927 and NGC 6496 have abundances similar to those of MW stars. We remark that according to many results in the literature (Bensby et al., 2003, 2017; Battistini & Bensby, 2015; Duong et al., 2019; Griffith et al., 2021; Lucey et al., 2022) the iron-peak elements abundance ratios of MW disk and bulge stars are consistent with each other. All these works found abundance values similar to those of NGC 5927 and NGC 6496, but different from those of NGC 6388 and NGC 6441. We interpreted the low abundance ratios in LMC/Sgr stars in terms of a lower contribution from massive stars to the chemical enrichment, compared to that experienced by the MW (see Section 3.5.3). The reason for this would be that these elements are mainly produced by HNe, SNe II or electron-capture SNe with high-mass stellar progenitors. In particular, HNe (associated to stars more massive than $\sim$25-30 $M_{\odot}$)

would produce most of Zn, without a sizeable contribution from SN Ia (Romano et al., 2010; Kobayashi et al., 2020). Hence, the ratio [Zn/Fe] is expected to decrease significantly in galaxies with a low SFR, where the contribution by massive stars is reduced (Yan et al., 2017; Jeřábková et al., 2018).

In light of this finding, it is natural to conclude that both NGC 6388 and NGC 6441 should have formed from a gas poorly enriched by massive stars, at odds with what observed for the other two investigated clusters. Thus, the analysis presented here offers an independent confirmation that NGC 5927 and NGC 6496 formed in-situ, as already suggested by the kinematics (Massari et al., 2019), and identifies NGC 6388 and NGC 6441 as likely formed in an external environment, characterized by chemical enrichment histories influenced by a low SFR, and only later accreted by the MW. It is interesting to note, that of the two clusters identified here as accreted, the kinematics analysis by Massari et al. (2019) indicated only NGC 6441 as an accreted cluster associated to the Kraken merger event (see Kruijssen et al., 2020), while an unclear origin was indicated for NGC 6388. Therefore, in light of the similar chemical abundances of the two GCs, NGC 6388 should have formed from the same progenitor of NGC 6441 or at least from a system with a chemical enrichment history similar to that of Kraken.

Unlike Zn, whose nucleosynthesis in stars is pretty well understood (see previous paragraphs), the detailed nucleosynthetic paths leading to the stellar production of Sc and V still deserve investigation (see Cowan et al., 2020; Kobayashi et al., 2020, for recent reappraisals from the observational and theoretical point of view, respectively). Notably, different initial conditions of exploding white dwarfs leading to SN Ia may result in very different V yields (e.g. Shen et al., 2018; Leung & Nomoto, 2020) with sizable consequences on the predictions of chemical evolution models (Palla, 2021) that have still to be fully explored. Our results clearly highlight the importance of Sc, V and Zn as chemical taggers and will hopefully inspire further theoretical work.

8.4.1 Comparison with Carretta & Bragaglia (2022)

It was recently published an analysis of a large number of high-resolution stellar spectra belonging to NGC 6388 by Carretta & Bragaglia (2022). They derived the abundances of Sc for 185 stars, V for 35 stars and Zn for 31 stars. The resulting mean abundance ratios are [Sc/Fe] = − 0.02 dex (σ = 0.07 dex), [V/Fe] = 0.26 dex (σ = 0.14 dex), and [Zn/Fe] = 0.10 dex (σ = 0.24 dex). They compared their abundance ratios with literature values for MW field stars belonging to the disk and the bulge and no significant difference was found between NGC 6388 and the MW for the three species.

Their results conflict with our ones, and their abundance ratios display large difference respect to ours values apart from Sc, reaching a difference larger then 0.5 dex

for V. They explained their enhanced abundances as due to the differences in the adopted solar reference abundances and in the scale of atmospheric parameters. In particular, they demonstrated for Zn (the only element for which the comparison is feasible, since we used the same line) that taking differences into account the final [Zn/Fe] ratios would be virtually the same in the two works (see Appendix A of Carretta & Bragaglia, 2022). This is a further reinforcement to the importance to perform homogeneous analyses.
While Carretta & Bragaglia (2022) have a large number of analysed stars, they compared their abundances with the MW ones derived from different works, each of them with their own methods, atomic parameters, solar reference abundances and scale of the atmospheric parameters, making the comparison uncertain. Instead, the strength of our work is the homogeneous comparison, therefore the difference in the abundances measured in the MW GCs, also respect to MW, LMC and Sgr field stars, depend on the different chemical composition of the ISM from which the stars formed and not to possible systematics affecting the analyses.

8.5 Summary

The use of the iron-peak elemental abundances proposed in Minelli et al. (2021) (see Section 3.5.3) has allowed us to shed light on the origin of the metal-rich GCs NGC 6388 and NGC 6441, indicating also NGC 6388 as a possible accreted cluster from a progenitor similar to Kraken in spite of the fact that its dynamical properties were not sufficient to unambiguously determine its birth place. Moreover, this analysis offers an independent confirmation that NGC 5927 and NGC 6496 formed in-situ.

Table 8.3: Chemical abundance ratios and corresponding uncertainty for the individual target stars.

star	[Fe/H]	[Si/Fe]	[Ca/Fe]	[Ti/Fe]	[Sc/Fe]	[V/Fe]	[Zn/Fe]	[Ba/Fe]	[La/Fe]	[Eu/Fe]
					NGC 5927					
5039161	–0.42±0.04	+0.19±0.06	+0.10±0.08	+0.23±0.06	+0.28±0.05	+0.16±0.11	+0.07±0.07	+0.05±0.05	+0.08±0.06	+0.41±0.04
5039423	–0.47±0.05	+0.19±0.06	+0.06±0.07	+0.22±0.06	+0.32±0.05	+0.19±0.09	+0.22±0.09	+0.02±0.07	+0.22±0.04	+0.48±0.04
5040219	–0.51±0.04	+0.16±0.04	+0.10±0.06	+0.29±0.04	+0.36±0.04	+0.24±0.07	+0.32±0.07	+0.17±0.05	+0.28±0.04	+0.56±0.04
5040282	–0.44±0.04	+0.13±0.05	+0.20±0.06	+0.24±0.05	+0.33±0.04	+0.21±0.08	+0.40±0.07	+0.04±0.04	+0.24±0.04	+0.46±0.04
5041223	–0.47±0.05	+0.17±0.05	+0.07±0.07	+0.25±0.05	+0.38±0.05	+0.23±0.07	+0.30±0.07	+0.11±0.07	+0.24±0.04	+0.38±0.04
					NGC 6388					
77599	–0.49±0.09	+0.39±0.09	+0.17±0.12	+0.22±0.13	+0.01±0.05	–0.19±0.15	–0.07±0.09	–0.03±0.09	+0.16±0.05	+0.43±0.04
83168	–0.46±0.07	+0.19±0.09	+0.11±0.13	+0.15±0.13	+0.05±0.06	–0.17±0.17	–0.21±0.08	+0.08±0.08	+0.12±0.10	+0.31±0.04
108895	–0.51±0.03	+0.19±0.05	+0.09±0.09	+0.06±0.07	+0.02±0.04	–0.33±0.11	–0.12±0.06	+0.10±0.05	+0.07±0.04	+0.33±0.03
110677	–0.50±0.03	+0.19±0.06	+0.08±0.11	+0.03±0.10	–0.03±0.07	–0.32±0.13	–0.07±0.10	+0.05±0.06	+0.12±0.07	+0.27±0.04
					NGC 6441					
7004463	–0.48±0.03	+0.30±0.06	+0.16±0.11	+0.18±0.07	+0.11±0.10	–0.29±0.10	–0.38±0.14	+0.02±0.05	–0.03±0.05	+0.38±0.05
7004487	–0.59±0.04	+0.23±0.09	+0.11±0.09	+0.18±0.10	–0.05±0.09	–0.34±0.12	–0.60±0.14	–0.13±0.07	+0.04±0.07	+0.30±0.06
					NGC 6496					
14	–0.61±0.03	+0.31±0.04	+0.27±0.05	+0.34±0.05	+0.38±0.04	+0.25±0.12	+0.48±0.17	+0.27±0.06	+0.29±0.06	+0.52±0.05
17	–0.64±0.03	+0.29±0.05	+0.20±0.07	+0.31±0.06	+0.41±0.05	+0.19±0.15	+0.21±0.17	+0.29±0.06	+0.32±0.06	+0.48±0.05
18	–0.68±0.03	+0.27±0.05	+0.24±0.06	+0.29±0.05	+0.36±0.10	+0.17±0.14	+0.40±0.18	+0.08±0.11	+0.28±0.06	+0.48±0.06
26	–0.60±0.04	+0.30±0.04	+0.05±0.04	+0.19±0.06	+0.36±0.05	+0.10±0.07	+0.12±0.09	+0.21±0.05	+0.20±0.05	+0.55±0.04
159	–0.65±0.03	+0.28±0.04	+0.23±0.05	+0.29±0.05	+0.37±0.04	+0.16±0.12	+0.23±0.09	+0.26±0.05	+0.21±0.04	+0.50±0.03

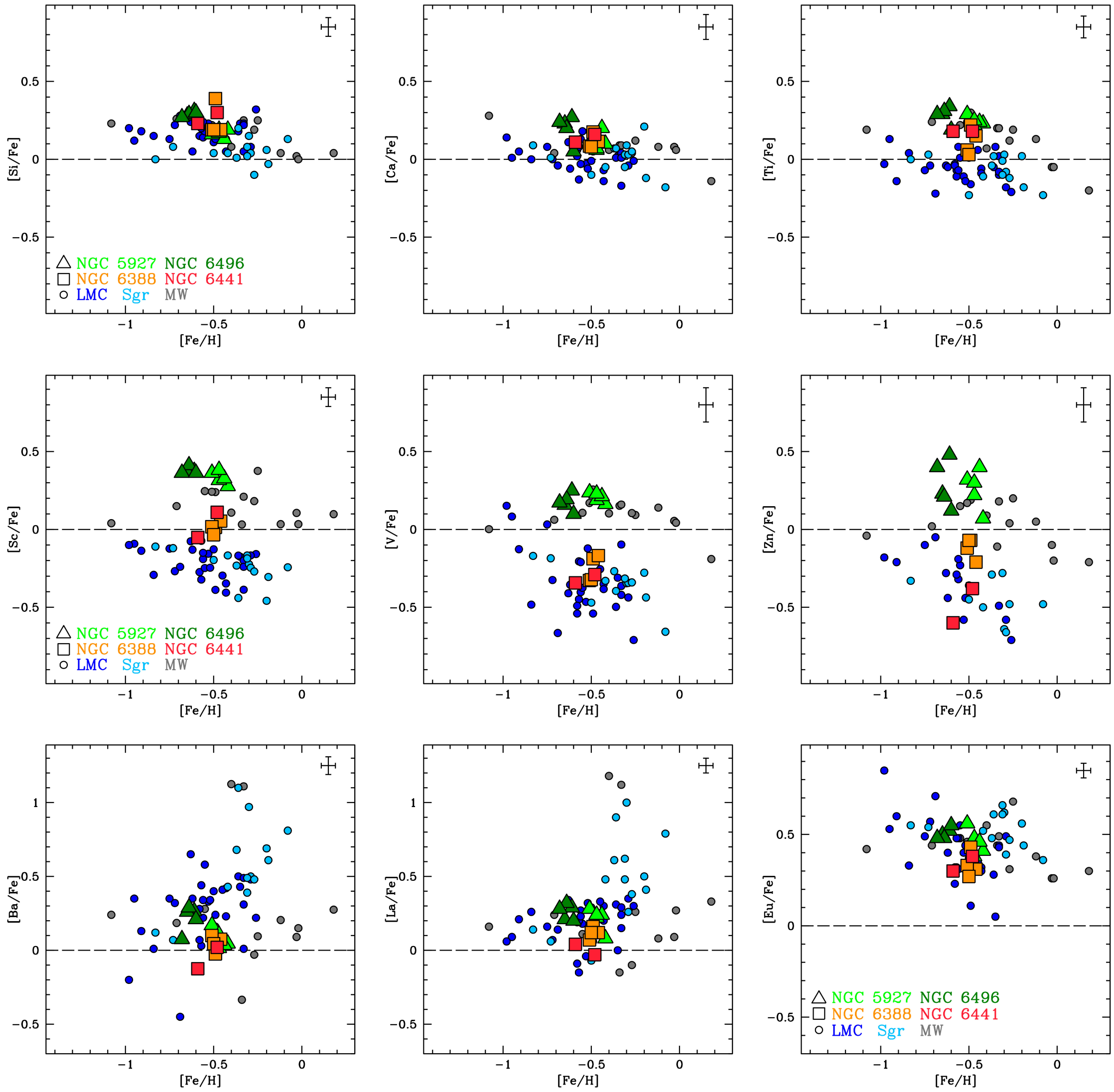

Figure 8.1: Behavior of the elemental abundance ratio as a function of [Fe/H] for NGC 5927 (light green triangles), NGC 6388 (orange squares), NGC 6441 (red squares), NGC 6496 (dark green triangles), with the data from my previous work (see Chapter 3) as reference: LMC (blue dots), Sgr (light blue dots) and MW (grey dots).
From panel left to panel right: first line, α elements [Si/Fe], [Ca/Fe] and [Ti/Fe] abundance ratios; second line, iron-peak elements [Sc/Fe], [V/Fe] and [Zn/Fe] abundance ratios; third line, neutron-capture elements [Ba/Fe], [La/Fe] and [Eu/Fe] abundance ratios.

Chapter 9

Conclusions and future perspectives

This Phd project has been focused on the chemical characterisation of the nearest MW satellites, namely LMC, SMC and Sgr. Their analysis allows to derive some important conclusions concerning the three galaxies:

- from the homogeneous comparison between LMC and Sgr, we derived a similar chemical composition of the two galaxies, that suggests similar chemical enrichment histories, as expected from the believed scenario where the progenitor of Sgr was a galaxy with a mass and a SFH similar to those of the LMC;

- comparing the abundances of LMC and Sgr stars with those of MW stars, we conclude that in these galaxies the contribution by massive stars to the chemical enrichment is less important with respect to the MW, coherently with the low SFR that LMC and Sgr experienced;

- thanks to the chemical tagging, we recognize NGC 2005 as an accreted LMC GC, originated in a galaxy that formed its stars with a much less efficient star formation compared to the LMC;

- we better characterised the chemical composition of the SMC, using both GCs and field stars, finding out that the galaxy experienced a low SFR at the beginning, followed by numerous recently bursts in the star formation, probably linked to the beginning of the gravitational interaction with the LMC. Moreover comparing the chemical composition of field stars and GCs, we conclude, in light of their comparable chemical composition, that they experienced a similar chemical enrichment history. Finally, comparing SMC abundances with the MW ones, we found that SMC experienced a slower SFR, a lower contribution by massive stars and similar contribution by low mass AGB stars;

- we derived an unbiased metallicity distribution for Sgr main body field stars, described as the sum of two Gaussian components (one metal-poor peaked at − 1.12 dex and the dominant metal-rich one peak at − 0.25 dex.), and we concluded that the percentage of metal-poor stars with [Fe/H]$<$ –2 dex is $\sim$ 0.2%;

- we derived a successful rate of 100% in the selection of Sgr member stars using *Gaia* proper motions;

- we proposed and tested the application of the chemical abundances of Sc, V and Zn as new diagnostics for the chemical tagging, in order to recognise stars or GCs accreted from systems with a lower SFR than the MW;

These results are important in light of future spectroscopic surveys, such as *MOONS*, that will give back a huge sample of star spectra, increasing enormously the number of data to analyse. They will allow to refine the observational strategy in terms of kind of objects to detect (i.e. field stars or GCs, that we know give complementary information), target selection (e.g. using *Gaia* proper motions, that we demonstrated to work efficiently in the case of Sgr stars), and spectral range for the observations (depending on the kind of elements that you want to observe, according to the conclusion that you want to reach, e.g. using Sc, V and Zn to recognize accreted stars).

Finally, we remark the importance to perform homogeneous chemical analyses, able to remove systematics related to different methods or reference values, in order to properly interpret the derived chemical abundances from stars for chemical tagging and for the comparison between different galaxies or different targets of the same system.

Bibliography

Adibekyan V. Z., Sousa S. G., Santos N. C., Delgado Mena E., González Hernández J. I., Israelian G., Mayor M., Khachatryan G., 2012, A&A, 545, A32

Alfaro-Cuello M., et al., 2019, ApJ, 886, 57

Alves D. R., 2004, New Astron. Rev., 48, 659

Andrae R., et al., 2018, A&A, 616, A8

Annibali F., Tosi M., 2022, Nature Astronomy, 6, 48

Arlandini C., Käppeler F., Wisshak K., Gallino R., Lugaro M., Busso M., Straniero O., 1999, ApJ, 525, 886

Bailer-Jones C. A. L., 2015, PASP, 127, 994

Barklem P. S., et al., 2005, A&A, 439, 129

Bastian N., Lardo C., 2018, ARA&A, 56, 83

Battistini C., Bensby T., 2015, A&A, 577, A9

Battistini C., Bensby T., 2016, A&A, 586, A49

Baumgardt H., Hilker M., 2018, MNRAS, 478, 1520

Bekki K., Chiba M., 2005, MNRAS, 356, 680

Bekki K., Couch W. J., Beasley M. A., Forbes D. A., Chiba M., Da Costa G. S., 2004, ApJ, 610, L93

Bellazzini M., Ferraro F. R., Buonanno R., 1999, MNRAS, 307, 619

Bellazzini M., Correnti M., Ferraro F. R., Monaco L., Montegriffo P., 2006, A&A, 446, L1

Bellazzini M., et al., 2008, AJ, 136, 1147

Bellini A., et al., 2013, ApJ, 765, 32

Belokurov V., et al., 2014, MNRAS, 437, 116

Bensby T., Feltzing S., Lundström I., 2003, A&A, 410, 527

Bensby T., Feltzing S., Lundström I., Ilyin I., 2005, A&A, 433, 185

Bensby T., Feltzing S., Oey M. S., 2014, A&A, 562, A71

Bensby T., et al., 2017, A&A, 605, A89

Bernstein R., Shectman S. A., Gunnels S. M., Mochnacki S., Athey A. E., 2003, in Iye M., Moorwood A. F. M., eds, Society of Photo-Optical Instrumentation Engineers (SPIE) Conference Series Vol. 4841, Instrument Design and Performance for Optical/Infrared Ground-based Telescopes. pp 1694–1704, doi:10.1117/12.461502

Bertaux J. L., Lallement R., Ferron S., Boonne C., Bodichon R., 2014, A&A, 564, A46

Besla G., 2015, preprint, (arXiv:1511.03346)

Besla G., Kallivayalil N., Hernquist L., Robertson B., Cox T. J., van der Marel R. P., Alcock C., 2007, ApJ, 668, 949

Besla G., Kallivayalil N., Hernquist L., van der Marel R. P., Cox T. J., Kereš D., 2010, ApJ, 721, L97

Bihain G., Israelian G., Rebolo R., Bonifacio P., Molaro P., 2004, A&A, 423, 777

Bonifacio P., Hill V., Molaro P., Pasquini L., Di Marcantonio P., Santin P., 2000, A&A, 359, 663

Bonifacio P., Sbordone L., Marconi G., Pasquini L., Hill V., 2004, A&A, 414, 503

Bragaglia A., Gratton R. G., Carretta E., D'Orazi V., Sneden C., Lucatello S., 2012, A&A, 548, A122

Brocato E., Castellani V., Ferraro F. R., Piersimoni A. M., Testa V., 1996, MNRAS, 282, 614

Brocato E., Castellani V., Di Carlo E., Raimondo G., Walker A. R., 2003, AJ, 125, 3111

Brown J. A., Wallerstein G., Zucker D., 1997, AJ, 114, 180

Brown J. A., Wallerstein G., Gonzalez G., 1999, AJ, 118, 1245

Burbidge E. M., Burbidge G. R., Fowler W. A., Hoyle F., 1957, Rev. Mod. Phys., 29, 547

Burris D. L., Pilachowski C. A., Armandroff T. E., Sneden C., Cowan J. J., Roe H., 2000, ApJ, 544, 302

Burton W. B., Lockman F. J., 1999, A&A, 349, 7

Busso M., Gallino R., Wasserburg G. J., 1999, ARA&A, 37, 239

Buzzoni A., Patelli L., Bellazzini M., Pecci F. F., Oliva E., 2010, MNRAS, 403, 1592

Cabrera-Ziri I., et al., 2020, MNRAS, 495, 375

Caffau E., Ludwig H. G., Steffen M., Freytag B., Bonifacio P., 2011, Sol. Phys., 268, 255

Cannon R. D., Croke B. F. W., Bell R. A., Hesser J. E., Stathakis R. A., 1998, MNRAS, 298, 601

Carlin J. L., Sheffield A. A., Cunha K., Smith V. V., 2018, ApJ, 859, L10

Carrera R., Gallart C., Hardy E., Aparicio A., Zinn R., 2008a, AJ, 135, 836

Carrera R., Gallart C., Aparicio A., Costa E., Méndez R. A., Noël N. E. D., 2008b, AJ, 136, 1039

Carrera R., Gallart C., Aparicio A., Hardy E., 2011, AJ, 142, 61

Carretta E., Bragaglia A., 2021, A&A, 646, A9

Carretta E., Bragaglia A., 2022, A&A, 660, L1

Carretta E., et al., 2007, A&A, 464, 967

Carretta E., et al., 2009a, A&A, 505, 117

Carretta E., Bragaglia A., Gratton R., Lucatello S., 2009b, A&A, 505, 139

Carretta E., Bragaglia A., Gratton R., D'Orazi V., Lucatello S., 2009c, A&A, 508, 695

Carretta E., Bragaglia A., Gratton R. G., Recio-Blanco A., Lucatello S., D'Orazi V., Cassisi S., 2010a, A&A, 516, A55

Carretta E., et al., 2010b, A&A, 520, A95

Casagrande L., et al., 2021, MNRAS, 507, 2684

Castelli F., Kurucz R. L., 2003, in Piskunov N., Weiss W. W., Gray D. F., eds, Vol. 210, Modelling of Stellar Atmospheres. p. A20 (`arXiv:astro-ph/0405087`)

Cayrel R., et al., 2004, A&A, 416, 1117

Chiappini C., Matteucci F., Romano D., 2001, ApJ, 554, 1044

Chiosi E., Vallenari A., 2007, A&A, 466, 165

Chiti A., Frebel A., 2019, ApJ, 875, 112

Cignoni M., Cole A. A., Tosi M., Gallagher J. S., Sabbi E., Anderson J., Grebel E. K., Nota A., 2012, ApJ, 754, 130

Cignoni M., Cole A. A., Tosi M., Gallagher J. S., Sabbi E., Anderson J., Grebel E. K., Nota A., 2013, ApJ, 775, 83

Cioni M. R. L., van der Marel R. P., Loup C., Habing H. J., 2000, A&A, 359, 601

Clayton D., 2003, Handbook of Isotopes in the Cosmos

Cohen J. G., 2004, AJ, 127, 1545

Cohen J. G., Huang W., 2009, ApJ, 701, 1053

Cohen J. G., Huang W., 2010, ApJ, 719, 931

Colavitti E., Matteucci F., Murante G., 2008, A&A, 483, 401

Cole A. A., Tolstoy E., Gallagher III J. S., Smecker-Hane T. A., 2005, AJ, 129, 1465

Cowan J. J., Sneden C., Roederer I. U., Lawler J. E., Hartog E. A. D., Sobeck J. S., Boesgaard A. M., 2020, ApJ, 890, 119

D'Onghia E., Fox A. J., 2016, ARA&A, 54, 363

Dalessandro E., Lapenna E., Mucciarelli A., Origlia L., Ferraro F. R., Lanzoni B., 2016, ApJ, 829, 77

Dekker H., D'Odorico S., Kaufer A., Delabre B., Kotzlowski H., 2000, in Iye M., Moorwood A. F., eds, Society of Photo-Optical Instrumentation Engineers (SPIE) Conference Series Vol. 4008, Optical and IR Telescope Instrumentation and Detectors. pp 534–545, doi:10.1117/12.395512

Dierickx M. I. P., Loeb A., 2017, ApJ, 847, 42

Dobbie P. D., Cole A. A., Subramaniam A., Keller S., 2014a, MNRAS, 442, 1663

Dobbie P. D., Cole A. A., Subramaniam A., Keller S., 2014b, MNRAS, 442, 1680

Dolphin A. E., 2002, MNRAS, 332, 91

Dolphin A. E., Walker A. R., Hodge P. W., Mateo M., Olszewski E. W., Schommer R. A., Suntzeff N. B., 2001, ApJ, 562, 303

Dotter A., Chaboyer B., Jevremović D., Kostov V., Baron E., Ferguson J. W., 2008, ApJS, 178, 89

Duong L., Asplund M., Nataf D. M., Freeman K. C., Ness M., 2019, MNRAS, 486, 5349

Edvardsson B., Andersen J., Gustafsson B., Lambert D. L., Nissen P. E., Tomkin J., 1993, A&A, 500, 391

Erkal D., Belokurov V. A., 2020, MNRAS, 495, 2554

Erkal D., et al., 2019, MNRAS, 487, 2685

Fernández-Alvar E., et al., 2018, ApJ, 852, 50

Ferraro F. R., Origlia L., Testa V., Maraston C., 2004, ApJ, 608, 772

Ferraro F. R., et al., 2018, ApJ, 860, 50

Forbes D. A., 2020, MNRAS, 493, 847

Forbes D. A., Bridges T., 2010, MNRAS, 404, 1203

Forsberg R., Jönsson H., Ryde N., Matteucci F., 2019, A&A, 631, A113

Frebel A., 2010, Astronomische Nachrichten, 331, 474

Freeman K., Bland-Hawthorn J., 2002, Annual Review of Astronomy and Astrophysics, 40, 487

Fuhr J. R., Wiese W. L., 2006, Journal of Physical and Chemical Reference Data, 35, 1669

Fuhr J. R., Martin G. A., Wiese W. L., 1988, Journal of Physical and Chemical Reference Data, 17

Fulbright J. P., 2000, AJ, 120, 1841

Gaia Collaboration et al., 2016, A&A, 595, A1

Gaia Collaboration et al., 2018a, A&A, 616, A1

Gaia Collaboration et al., 2018b, A&A, 616, A10

Gaia Collaboration et al., 2018c, A&A, 616, A12

Gaia Collaboration et al., 2021, A&A, 650, C3

Gallart C., et al., 2003, AJ, 125, 742

Gallart C., Stetson P. B., Meschin I. P., Pont F., Hardy E., 2008, ApJ, 682, L89

Geisler D., Bica E., Dottori H., Claria J. J., Piatti A. E., Santos Jr. J. F. C., 1997, AJ, 114, 1920

Geisler D., Smith V. V., Wallerstein G., Gonzalez G., Charbonnel C., 2005, AJ, 129, 1428

Gibbons S. L. J., Belokurov V., Evans N. W., 2017, MNRAS, 464, 794

Glatt K., et al., 2009, AJ, 138, 1403

González Hernández J. I., Bonifacio P., 2009, A&A, 497, 497

Graczyk D., et al., 2014, ApJ, 780, 59

Gratton R. G., Sneden C., Carretta E., Bragaglia A., 2000, A&A, 354, 169

Gratton R. G., Carretta E., Claudi R., Lucatello S., Barbieri M., 2003, A&A, 404, 187

Gratton R. G., Lucatello S., Bragaglia A., Carretta E., Momany Y., Pancino E., Valenti E., 2006, A&A, 455, 271

Grevesse N., Sauval A. J., 1998, Space Sci. Rev., 85, 161

Griffith E., et al., 2021, ApJ, 909, 77

Grocholski A. J., Cole A. A., Sarajedini A., Geisler D., Smith V. V., 2006, AJ, 132, 1630

Guglielmo M., Lewis G. F., Bland-Hawthorn J., 2014, MNRAS, 444, 1759

Guo Q., White S., Li C., Boylan-Kolchin M., 2010, MNRAS, 404, 1111

Hamanowicz A., et al., 2016, Acta Astron., 66, 197

Hammer F., Yang Y. B., Flores H., Puech M., Fouquet S., 2015, ApJ, 813, 110

Hanke M., Hansen C. J., Ludwig H.-G., Cristallo S., McWilliam A., Grebel E. K., Piersanti L., 2020, A&A, 635, A104

Hansen C. J., El-Souri M., Monaco L., Villanova S., Bonifacio P., Caffau E., Sbordone L., 2018, ApJ, 855, 83

Harris W. E., 1996, AJ, 112, 1487

Harris W. E., 2010, arXiv e-prints, p. arXiv:1012.3224

Harris J., Zaritsky D., 2004, AJ, 127, 1531

Harris J., Zaritsky D., 2006, AJ, 131, 2514

Harris J., Zaritsky D., 2009, AJ, 138, 1243

Hasselquist S., et al., 2017, ApJ, 845, 162

Hasselquist S., et al., 2021, arXiv e-prints, p. arXiv:2109.05130

Hayes C. R., et al., 2020, ApJ, 889, 63

Haywood M., Di Matteo P., Lehnert M. D., Katz D., Gómez A., 2013, A&A, 560, A109

Helmi A., 2020, Annual Review of Astronomy and Astrophysics, 58, 205

Hill V., 2010, in Cunha K., Spite M., Barbuy B., eds, Vol. 265, Chemical Abundances in the Universe: Connecting First Stars to Planets. pp 219–226, doi:10.1017/S1743921310000608

Hill V., Barbuy B., Spite M., 1997, A&A, 323, 461

Hill V., François P., Spite M., Primas F., Spite F., 2000, A&A, 364, L19

Hill V., et al., 2019, A&A, 626, A15

Hobbs D., et al., 2021, Gaia EDR3 documentation Chapter 4: Astrometric data, Gaia EDR3 documentation

Hollyhead K., et al., 2019, MNRAS, 484, 4718

Ibata R. A., Gilmore G., Irwin M. J., 1994, Nature, 370, 194

Ibata R. A., Wyse R. F. G., Gilmore G., Irwin M. J., Suntzeff N. B., 1997, AJ, 113, 634

Iwamoto K., Brachwitz F., Nomoto K., Kishimoto N., Umeda H., Hix W. R., Thielemann F.-K., 1999, ApJS, 125, 439

Jeřábková T., Hasani Zonoozi A., Kroupa P., Beccari G., Yan Z., Vazdekis A., Zhang Z. Y., 2018, A&A, 620, A39

Johnson J. A., Ivans I. I., Stetson P. B., 2006, ApJ, 640, 801

Kallivayalil N., van der Marel R. P., Alcock C., 2006, ApJ, 652, 1213

Kallivayalil N., van der Marel R. P., Besla G., Anderson J., Alcock C., 2013, ApJ, 764, 161

Kallivayalil N., et al., 2018, ApJ, 867, 19

Karakas A. I., 2010, MNRAS, 403, 1413

Karakas A. I., Lattanzio J. C., 2014, Publ. Astron. Soc. Australia, 31, e030

Kennicutt Robert C. J., 1998, ApJ, 498, 541

Kirby E. N., et al., 2010, ApJS, 191, 352

Kobayashi C., Nomoto K., 2009, ApJ, 707, 1466

Kobayashi C., Umeda H., Nomoto K., Tominaga N., Ohkubo T., 2006, ApJ, 653, 1145

Kobayashi C., Karakas A. I., Lugaro M., 2020, ApJ, 900, 179

Koch A., Grebel E. K., Gilmore G. F., Wyse R. F. G., Kleyna J. T., Harbeck D. R., Wilkinson M. I., Evans N. W., 2008, AJ, 135, 1580

Koribalski B., Johnston S., Otrupcek R., 1994, MNRAS, 270, L43

Kroupa P., 2002, in Grebel E. K., Brandner W., eds, Astronomical Society of the

Pacific Conference Series Vol. 285, Modes of Star Formation and the Origin of Field Populations. p. 86 (arXiv:astro-ph/0102155)

Kruijssen J. M. D., Pfeffer J. L., Reina-Campos M., Crain R. A., Bastian N., 2019, MNRAS, 486, 3180

Kruijssen J. M. D., et al., 2020, MNRAS, 498, 2472

Kurucz R. L., 1993, VizieR Online Data Catalog, 6039

Kurucz R. L., 2005, Memorie della Societa Astronomica Italiana Supplementi, 8, 14

Lach F., Röpke F. K., Seitenzahl I. R., Coté B., Gronow S., Ruiter A. J., 2020, A&A, 644, A118

Lapenna E., Mucciarelli A., Origlia L., Ferraro F. R., 2012, ApJ, 761, 33

Laporte C. F. P., Minchev I., Johnston K. V., Gómez F. A., 2019, MNRAS, 485, 3134

Larsen S. S., Brodie J. P., Strader J., 2012, A&A, 546, A53

Lawler J. E., Bonvallet G., Sneden C., 2001, ApJ, 556, 452

Layden A. C., Sarajedini A., 1997, ApJ, 486, L107

Layden A. C., Sarajedini A., 2000, AJ, 119, 1760

Lemasle B., et al., 2014, A&A, 572, A88

Letarte B., 2007, PhD thesis, University of Groningen

Letarte B., Hill V., Jablonka P., Tolstoy E., François P., Meylan G., 2006, A&A, 453, 547

Letarte B., et al., 2010, A&A, 523, A17

Leung S.-C., Nomoto K., 2018, ApJ, 861, 143

Leung S.-C., Nomoto K., 2020, ApJ, 888, 80

Leung G. Y. C., Leaman R., van de Ven G., Battaglia G., 2020, MNRAS, 493, 320

Limongi M., Chieffi A., 2003, ApJ, 592, 404

Lind K., Asplund M., Barklem P. S., Belyaev A. K., 2011, A&A, 528, A103

Lucey M., et al., 2022, MNRAS, 509, 122

Lugaro M., Karakas A. I., Stancliffe R. J., Rijs C., 2012, ApJ, 747, 2

Lupton R., 1993, Statistics in theory and practice, Princeton Univ

Mackey A. D., Gilmore G. F., 2003, MNRAS, 338, 85

Mackey A. D., Payne M. J., Gilmore G. F., 2006, MNRAS, 369, 921

Mackey D., et al., 2019, Nature, 574, 69

Marigo P., Girardi L., Bressan A., Groenewegen M. A. T., Silva L., Granato G. L., 2008, A&A, 482, 883

Martin G. A., Fuhr J. R., Wiese W. L., 1988a, Atomic transition probabilities. Scandium through Manganese

Martin G. A., Fuhr J. R., Wiese W. L., 1988b, Atomic transition probabilities. Scandium through Manganese

Martocchia S., et al., 2018, MNRAS, 473, 2688

Martocchia S., et al., 2019, MNRAS, 487, 5324

Massari D., Koppelman H. H., Helmi A., 2019, A&A, 630, L4

Mateluna R., Geisler D., Villanova S., Carraro G., Grocholski A., Sarajedini A., Cole A., Smith V., 2012, A&A, 548, A82

Matteucci F., Brocato E., 1990, ApJ, 365, 539

Matteucci F., Greggio L., 1986, A&A, 154, 279

Matteucci F., Recchi S., 2001, ApJ, 558, 351

Matteucci F., Romano D., Arcones A., Korobkin O., Rosswog S., 2014, MNRAS, 438, 2177

Mayer L., Governato F., Colpi M., Moore B., Quinn T., Wadsley J., Stadel J., Lake G., 2001, ApJ, 547, L123

McCall M. L., 2004, AJ, 128, 2144

McConnachie A. W., 2012, AJ, 144, 4

McCumber M. P., Garnett D. R., Dufour R. J., 2005, AJ, 130, 1083

McWilliam A., Smecker-Hane T. A., 2005, in Barnes Thomas G. I., Bash F. N., eds, Astronomical Society of the Pacific Conference Series Vol. 336, Cosmic Abundances as Records of Stellar Evolution and Nucleosynthesis. p. 221 (arXiv:astro-ph/0409083)

McWilliam A., Wallerstein G., Mottini M., 2013, ApJ, 778, 149

Meschin I., Gallart C., Aparicio A., Hidalgo S. L., Monelli M., Stetson P. B., Carrera R., 2014, MNRAS, 438, 1067

Milone A. P., et al., 2017, MNRAS, 464, 3636

Minelli A., Mucciarelli A., Romano D., Bellazzini M., Origlia L., Ferraro F. R., 2021, ApJ, 910, 114

Mishenina T. V., Pignatari M., Korotin S. A., Soubiran C., Charbonnel C., Thielemann F. K., Gorbaneva T. I., Basak N. Y., 2013, A&A, 552, A128

Monaco L., Bellazzini M., Ferraro F. R., Pancino E., 2003, ApJ, 597, L25

Monaco L., Bellazzini M., Ferraro F. R., Pancino E., 2004a, in Prada F., Martinez Delgado D., Mahoney T. J., eds, Astronomical Society of the Pacific Conference Series Vol. 327, Satellites and Tidal Streams. p. 190 (arXiv:astro-ph/0309044)

Monaco L., Bellazzini M., Ferraro F. R., Pancino E., 2004b, MNRAS, 353, 874

Monaco L., Bellazzini M., Bonifacio P., Ferraro F. R., Marconi G., Pancino E., Sbordone L., Zaggia S., 2005, A&A, 441, 141

Monaco L., Bellazzini M., Bonifacio P., Buzzoni A., Ferraro F. R., Marconi G., Sbordone L., Zaggia S., 2007, A&A, 464, 201

Mucciarelli A., 2011, A&A, 528, A44

Mucciarelli A., 2013, preprint, (`arXiv:1311.1403`)

Mucciarelli A., Bellazzini M., 2020, Research Notes of the American Astronomical Society, 4, 52

Mucciarelli A., Bonifacio P., 2020, A&A, 640, A87

Mucciarelli A., Carretta E., Origlia L., Ferraro F. R., 2008, AJ, 136, 375

Mucciarelli A., Origlia L., Maraston C., Ferraro F. R., 2009a, ApJ, 690, 288

Mucciarelli A., Origlia L., Ferraro F. R., Pancino E., 2009b, ApJ, 695, L134

Mucciarelli A., Origlia L., Ferraro F. R., 2010, ApJ, 717, 277

Mucciarelli A., et al., 2011, MNRAS, 413, 837

Mucciarelli A., Pancino E., Lovisi L., Ferraro F. R., Lapenna E., 2013, ApJ, 766, 78

Mucciarelli A., Monaco L., Bonifacio P., Saviane I., 2017a, A&A, 603, L7

Mucciarelli A., Bellazzini M., Ibata R., Romano D., Chapman S. C., Monaco L., 2017b, A&A, 605, A46

Mucciarelli A., Massari D., Minelli A., Romano D., Bellazzini M., Ferraro F. R., Matteucci F., Origlia L., 2021a, Nature Astronomy, 5, 1247

Mucciarelli A., Bellazzini M., Massari D., 2021b, A&A, 653, A90

Mura-Guzmán A., Villanova S., Muñoz C., Tang B., 2018, MNRAS, 474, 4541

Myeong G. C., Vasiliev E., Iorio G., Evans N. W., Belokurov V., 2019, MNRAS, 488, 1235

Neckel H., Labs D., 1984, Sol. Phys., 90, 205

Nidever D. L., et al., 2020, ApJ, 895, 88

Niederhofer F., et al., 2017a, MNRAS, 464, 94

Niederhofer F., et al., 2017b, MNRAS, 465, 4159

Niederste-Ostholt M., Belokurov V., Evans N. W., 2012, MNRAS, 422, 207

Nissen P. E., Akerman C., Asplund M., Fabbian D., Kerber F., Kaufl H. U., Pettini M., 2007, A&A, 469, 319

Noël N. E. D., Gallart C., Costa E., Méndez R. A., 2007, AJ, 133, 2037

Noël N. E. D., Aparicio A., Gallart C., Hidalgo S. L., Costa E., Méndez R. A., 2009, ApJ, 705, 1260

Nomoto K., Kobayashi C., Tominaga N., 2013, Annual Review of Astronomy and Astrophysics, 51, 457

Olsen K. A. G., Hodge P. W., Mateo M., Olszewski E. W., Schommer R. A., Suntzeff N. B., Walker A. R., 1998, MNRAS, 300, 665

Olsen K. A. G., Zaritsky D., Blum R. D., Boyer M. L., Gordon K. D., 2011, ApJ, 737, 29

Olszewski E. W., Schommer R. A., Suntzeff N. B., Harris H. C., 1991, AJ, 101, 515

Olszewski E. W., Suntzeff N. B., Mateo M., 1996, ARA&A, 34, 511

Pagel B. E. J., Tautvaisiene G., 1998, MNRAS, 299, 535

Palla M., 2021, MNRAS, 503, 3216

Pancino E., et al., 2017, A&A, 601, A112

Parisi M. C., Grocholski A. J., Geisler D., Sarajedini A., Clariá J. J., 2009, AJ, 138, 517

Parisi M. C., Geisler D., Clariá J. J., Villanova S., Marcionni N., Sarajedini A., Grocholski A. J., 2015, AJ, 149, 154

Parisi M. C., Geisler D., Carraro G., Clariá J. J., Villanova S., Gramajo L. V., Sarajedini A., Grocholski A. J., 2016, AJ, 152, 58

Pasquini L., et al., 2002, The Messenger, 110, 1

Patel E., et al., 2020, ApJ, 893, 121

Peñarrubia J., Gómez F. A., Besla G., Erkal D., Ma Y.-Z., 2016, MNRAS, 456, L54

Pian E., et al., 2017, Nature, 551, 67

Pietrinferni A., Cassisi S., Salaris M., Castelli F., 2004, ApJ, 612, 168

Pompéia L., et al., 2008, A&A, 480, 379

Prole D. J., et al., 2019, MNRAS, 484, 4865

Purcell C. W., Bullock J. S., Tollerud E. J., Rocha M., Chakrabarti S., 2011, Nature, 477, 301

Reddy B. E., Tomkin J., Lambert D. L., Allende Prieto C., 2003, MNRAS, 340, 304

Reddy B. E., Lambert D. L., Allende Prieto C., 2006, MNRAS, 367, 1329

Reggiani H., Meléndez J., Kobayashi C., Karakas A., Placco V., 2017, A&A, 608, A46

Reggiani H., Schlaufman K. C., Casey A. R., Simon J. D., Ji A. P., 2021, AJ, 162, 229

Reichert M., Hansen C. J., Hanke M., Skúladóttir Á., Arcones A., Grebel E. K., 2020, A&A, 641, A127

Rezaeikh S., Javadi A., Khosroshahi H., van Loon J. T., 2014, MNRAS, 445, 2214

Rich R. M., et al., 1997, ApJ, 484, L25

Ripepi V., et al., 2014, The Messenger, 157, 32

Ripepi V., et al., 2017, MNRAS, 472, 808

Roederer I. U., Lawler J. E., 2012, ApJ, 750, 76

Roederer I. U., Preston G. W., Thompson I. B., Shectman S. A., Sneden C., Burley

G. S., Kelson D. D., 2014, AJ, 147, 136

Romaniello M., et al., 2008, A&A, 488, 731

Romano D., Matteucci F., 2007, MNRAS, 378, L59

Romano D., Starkenburg E., 2013, MNRAS, 434, 471

Romano D., Karakas A. I., Tosi M., Matteucci F., 2010, A&A, 522, A32

Romano D., Bellazzini M., Starkenburg E., Leaman R., 2015, MNRAS, 446, 4220

Rubele S., et al., 2012, A&A, 537, A106

Ruiz-Lara T., Gallart C., Bernard E. J., Cassisi S., 2020, in XIV.0 Scientific Meeting (virtual) of the Spanish Astronomical Society. p. 185

Sabbi E., et al., 2009, ApJ, 703, 721

Sales L. V., Wang W., White S. D. M., Navarro J. F., 2013, MNRAS, 428, 573

Sbordone L., Bonifacio P., Castelli F., Kurucz R. L., 2004, Memorie della Societa Astronomica Italiana Supplementi, 5, 93

Sbordone L., Bonifacio P., Buonanno R., Marconi G., Monaco L., Zaggia S., 2007, A&A, 465, 815

Schiavon R. P., Caldwell N., Conroy C., Graves G. J., Strader J., MacArthur L. A., Courteau S., Harding P., 2013, ApJ, 776, L7

Schlafly E. F., Finkbeiner D. P., 2011, ApJ, 737, 103

Schmidt M., 1959, ApJ, 129, 243

Shen K. J., Kasen D., Miles B. J., Townsley D. M., 2018, ApJ, 854, 52

Shetrone M. D., Côté P., Sargent W. L. W., 2001, ApJ, 548, 592

Shetrone M., Venn K. A., Tolstoy E., Primas F., Hill V., Kaufer A., 2003, AJ, 125, 684

Siegel M. H., et al., 2007, ApJ, 667, L57

Siegel D. M., Barnes J., Metzger B. D., 2019, Nature, 569, 241

Simon J. D., 2018, ApJ, 863, 89

Simon J. D., 2019, ARA&A, 57, 375

Skowron D. M., et al., 2021, ApJS, 252, 23

Skrutskie M. F., et al., 2006, AJ, 131, 1163

Skúladóttir Á., Tolstoy E., Salvadori S., Hill V., Pettini M., 2017, A&A, 606, A71

Smiljanic R., et al., 2016, A&A, 589, A115

Smith G., Raggett D. S. J., 1981, Journal of Physics B Atomic Molecular Physics, 14, 4015

Smith V. V., et al., 2002, AJ, 124, 3241

Snaith O., Haywood M., Di Matteo P., Lehnert M. D., Combes F., Katz D., Gómez A., 2015, A&A, 578, A87

Song Y.-Y., Mateo M., Walker M. G., Roederer I. U., 2017, AJ, 153, 261

Soubiran C., Le Campion J.-F., Brouillet N., Chemin L., 2016, A&A, 591, A118

Spite F., Spite M., Francois P., 1989a, A&A, 210, 25

Spite M., Barbuy B., Spite F., 1989b, A&A, 222, 35

Stanimirović S., Staveley-Smith L., Jones P. A., 2004, ApJ, 604, 176

Stephens A., Boesgaard A. M., 2002, AJ, 123, 1647

Stetson P. B., Pancino E., 2008, PASP, 120, 1332

Stetson P. B., Pancino E., Zocchi A., Sanna N., Monelli M., 2019, MNRAS, 485, 3042

Tafelmeyer M., et al., 2010, A&A, 524, A58

Tepper-García T., Bland-Hawthorn J., 2018, MNRAS, 478, 5263

Tinsley B. M., 1979, ApJ, 229, 1046

Tolstoy E., Hill V., Tosi M., 2009, Annual Review of Astronomy and Astrophysics, 47, 371

Tully R. B., Courtois H. M., Sorce J. G., 2016, AJ, 152, 50

Ural U., Cescutti G., Koch A., Kleyna J., Feltzing S., Wilkinson M. I., 2015, MNRAS, 449, 761

Van der Swaelmen M., Hill V., Primas F., Cole A. A., 2013, A&A, 560, A44

Venn K. A., Irwin M., Shetrone M. D., Tout C. A., Hill V., Tolstoy E., 2004, AJ, 128, 1177

Wagner-Kaiser R., et al., 2017, MNRAS, 471, 3347

Wheeler J. C., Cowan J. J., Hillebrandt W., 1998, ApJ, 493, L101

White S. D. M., Rees M. J., 1978, MNRAS, 183, 341

Wiese W. L., Fuhr J. R., 1975, Journal of Physical and Chemical Reference Data, 4, 263

Woosley S. E., Weaver T. A., 1995, ApJS, 101, 181

Yan H. L., Shi J. R., Zhao G., 2015, ApJ, 802, 36

Yan Z., Jerabkova T., Kroupa P., 2017, A&A, 607, A126

Yan Z., Jerabkova T., Kroupa P., 2020, A&A, 637, A68

Zaritsky D., Harris J., Thompson I. B., Grebel E. K., Massey P., 2002, AJ, 123, 855

Zhao H., Ibata R. A., Lewis G. F., Irwin M. J., 2003, MNRAS, 339, 701

de Boer T. J. L., Belokurov V., Beers T. C., Lee Y. S., 2014, MNRAS, 443, 658

de Boer T. J. L., Belokurov V., Koposov S., 2015, MNRAS, 451, 3489

de Vaucouleurs G., de Vaucouleurs A., Corwin Jr. H. G., Buta R. J., Paturel G., Fouqué P., 1991, Third Reference Catalogue of Bright Galaxies. Volume I: Explanations and references. Volume II: Data for galaxies between 0^h and 12^h. Volume

III: Data for galaxies between 12^h and 24^h.
van den Bergh S., 1999, A&ARv, 9, 273
van der Marel R. P., 2001, AJ, 122, 1827
van der Marel R. P., Kallivayalil N., 2014, ApJ, 781, 121